Magnetic microscopy of domains and domain walls in ferromagnetic nanotubes

Michal Staňo

Communauté
UNIVERSITÉ Grenoble Alpes

THÈSE

Pour obtenir le grade de

DOCTEUR DE LA COMMUNAUTÉ UNIVERSITÉ GRENOBLE ALPES

Spécialité : **Nanophysique**

Arrêté ministériel : 25 mai 2016

Présentée par

Michal STAŇO

Thèse dirigée par **Dr. Olivier FRUCHART,** SPINTEC, Grenoble

préparée au sein du **CNRS, Institut Néel**
dans **l'École Doctorale de Physique**

Microscopie des domaines et parois de domaines dans les nanotubes ferromagnétiques

Thèse soutenue publiquement le **3 octobre 2017**,
devant le jury composé de :

Dr. Riccardo HERTEL Directeur de recherche CNRS, IPCMS, Strasbourg	Rapporteur
Prof. Hans-Josef HUG Professeur des universités, University of Basel, Basel Directeur de laboratoire, EMPA, Dübendorf	Rapporteur
Dr. Claire BARADUC Ingénieur-chercheuse, SPINTEC, Grenoble	Examinatrice
Dr. Bénédicte WAROT-FONROSE Chargée de recherche CNRS, CEMES, Toulouse	Examinatrice
Dr. Stefania PIZZINI Directrice de recherche CNRS, Institut Néel, Grenoble	Présidente

Communauté
UNIVERSITÉ Grenoble Alpes

THÈSE

Pour obtenir le grade de

DOCTEUR DE LA COMMUNAUTÉ UNIVERSITÉ GRENOBLE ALPES

Spécialité : **Nanophysique**

Arrêté ministériel : 25 mai 2016

Présentée par

Michal STAŇO

Thèse dirigée par **Dr. Olivier FRUCHART,** SPINTEC, Grenoble

préparée au sein du **CNRS, Institut Néel**
dans **l'École Doctorale de Physique**

Magnetic microscopy of domains and domain walls in ferromagnetic nanotubes

Thèse soutenue publiquement le **3 octobre 2017**,
devant le jury composé de :

Dr. Riccardo HERTEL Directeur de recherche CNRS, IPCMS, Strasbourg	Rapporteur
Prof. Hans-Josef HUG Professeur des universités, University of Basel, Basel Directeur de laboratoire, EMPA, Dübendorf	Rapporteur
Dr. Claire BARADUC Ingénieur-chercheuse, SPINTEC, Grenoble	Examinatrice
Dr. Bénédicte WAROT-FONROSE Chargée de recherche CNRS, CEMES, Toulouse	Examinatrice
Dr. Stefania PIZZINI Directrice de recherche CNRS, Institut Néel, Grenoble	Présidente

ABSTRACT

This thesis explores magnetic configurations, namely magnetic domains and domain walls (DWs) in single ferromagnetic metallic nanotubes (diameters 50–400 nm) by means of magnetic microscopies and numerical modelling. The work benefited from international collaboration with TU Darmstadt (synthesis), synchrotrons Elettra and Soleil as well as CNRS CEMES (magnetic imaging). Using electrochemical methods and nanoporous templates, we could fabricate Ni, NiCo, CoNiB, and NiFeB nanotubes as well as Ni wire-tube elements. For the imaging, we relied mainly on X-ray Magnetic Circular Dichroism coupled with PhotoEmission Electron Microscopy (XMCD-PEEM). We show the first experimental microscopy images of magnetic domains in metallic nanotubes. In long (30 µm) CoNiB tubes, we observed many azimuthal (flux-closure) magnetic domains separated by very narrow DWs. This is in contrast with literature and recent experiments where only axial domains appeared for similar geometry. By annealing, changing the chemical composition or just decreasing the nanotube diameter we could obtain also the axial domains. Therefore, tubes are versatile as magnetic domains can be prepared almost à la carte. We demonstrated switching of both axial and azimuthal domains with a magnetic field. We imaged also multilayered tubes – an equivalent of multilayered flat films that form a basic brick of current spintronics. We obtained two magnetic layers (exchange-) decoupled by an oxide spacer. Such a first-of-its-kind structure and its imaging paves the way towards 3D spintronics and magnetism based on vertical arrays of tubes.

KEYWORDS

Magnetic nanotube, micromagnetism, domain wall, XMCD-PEEM, electron holography, electrochemistry

RESUMÉ

Cette thèse explore les domaines magnétiques et les parois de domaine (PD), dans des nanotubes (NTs) métalliques ferromagnétiques individuels (diamètres 50-400 nm) au moyen de microscopies magnétiques et de modélisation numérique. Le travail a bénéficié d'une collaboration internationale avec TU Darmstadt (synthèse), les synchrotrons Elettra et Soleil ainsi que CNRS CEMES (imagerie magnétique). En utilisant des méthodes électrochimiques et des gabarits nanoporeux, nous avons fabriqué des NTs de Ni, NiCo, CoNiB et NiFeB ainsi que des éléments fil-tube de Ni. Pour l'imagerie, nous utilisons principalement le dichroïsme circulaire magnétique de rayons X associé à la microscopie à émission de photoelectrons (XMCD-PEEM). Nous avons réalisé les premières images microscopiques de domaines magnétiques dans les NTs. Dans des tubes CoNiB longs (30 µm), nous avons observé un grand nombre de domaines azimutaux séparés par des PD très étroites. Cela contraste avec la littérature et les expériences récentes où seuls des domaines axiaux apparaissent pour une géométrie similaire. Par recuit, en changeant la composition chimique ou simplement en diminuant le diamètre des NTs, nous avons également pu obtenir les domaines axiaux – préparation des domaines presque à la carte. Nous avons démontré le renversement des domaines axiaux et azimutaux avec un champ magnétique. En vue d'ouvrir la voie à des tubes multicouches - un équivalent de films plats multicouches qui forment une brique de base de la spintronique actuelle, nous avons obtenu deux couches magnétiques découplées par un intercalaire d'oxyde. Ces structures et leurs imagerie ouvrent la voie à la spintronique 3D basée sur des réseaux de tubes verticaux.

MOTS CLÉS

Nanotube magnétique, micromagnétisme, paroi de domaine, XMCD-PEEM, holographie électronique, électrochimie

ACKNOWLEDGEMENT

First of all, I thank Sandra Schaefer for a great collaboration, preparation of very good samples, information on electroless plating and polymeric membranes. Without her contribution the presented work would be much thinner. Last but not least, I appreciate nice stamps on the parcels with samples. Further, I acknowledge my supervisor, Olivier Fruchart, for giving me many nice (and challenging) opportunities as well as supplying means for their realization. I am grateful to Dr. Ricardo Hertel and Prof. Hans-Josef Hug for accepting to be referees of my work and reading through the (intricate) manuscript. Further I appreciate the comments and notes of other jury members: Claire Baraduc, Bénédicte Warrot-Fonrose, and Stefania Pizzini.

Great thanks goes to my colleagues from Institut Néel and Spintec. It is not possible to mention all of them, therefore I apologize to those who are not listed below. I thank to Márlio Bonfim and Jan Vogel for help with the focused MOKE setup, Ségolène Jamet for discussions on simulations and XMCD-PEEM simulation code, Daria Gusakova for unroll-tube script and discussion on micromagnetic simulations, Jean-Christophe Toussaint for development of simulation codes, Laurent Cagnon for transmission electron microscopy and some tips regarding (electro)chemistry, and Alexis Wartelle for numerous discussions and help not only with living in France. I am grateful to Nanofab (namely Bruno Fernandez and Jean-Francois Motte) and Optics and Microscopy (Simon Le Denmat, Sebastien Pairis) technological groups for their support and help with microfabrication (substrates, sample processing) and characterization (AFM, SEM), respectively; Cécile Nemiche for express printing of all the posters and the thesis.

Conducting the research would be impossible without occasional relax, Grenoble mountains, board games in K fée des jeux (avec fondant au chocolat), good meals in H2 restaurant, and support of my family in previous education and stages of life. I express my gratitude to Karol Nogajevski for being such a good mountain guide; the trip squads for nice hikes. I appreciate also help of my friends and colleagues from Brno: Viola Křižáková for coffee breaks, slack-line, discussions, very precise manuscript corrections and teaching me (reminding me of) some English rules. I highly appreciate a car power transformer (DC to AC) provided by Lukáš Flajšman enabling me to proceed with the manuscript during our trip in Canada (Canadian Rockies).

I am gratefull to Elettra and Soleil synchrotron facilities for allocating beamtime for the XPEEM and STXM experiments. A special thanks goes to Grande Onur and Grande Andrea, Bazovicca Center Hotel staff (soups) and Pizzeria Karis/Pesek. Scanning transmission electron microscopy microscopy was performed by Eric Gautier at Plateforme de Nanocaractérisation PFNC at CEA/Minatec (Grenoble). Electron holography experiments were conducted via the French research federation METSA with financial support from the CNRS-CEA METSA French network (FR CNRS 3507) on the CEMES Toulouse platform. I gratefully acknowledge PhD grant from the Laboratoire d'excellence LANEF in Grenoble (ANR-10-LABX-51-01). The manuscript was typeset using author-modified LaTeX code based on a template from Brno University of Technology.

CONTENTS

LIST OF FIGURES

LIST OF TABLES

1 INTRODUCTION

Research on magnetism in small dimensions (micro and nanomagnetism) has led to a revolution in data storage with high-capacity magnetic recording, e.g. hard disk drives (HDDs), and to new magnetic sensors (for magnetic field, rotation angle, angular speed), mostly focusing on thin films, nanoparticles and more recently on nanowires.

In 2004 IBM [1] proposed a concept of a non-volatile solid state memory (Fig. 1.1) based on shifting magnetic domain walls (DWs) in magnetic tracks – nanostrips [2]. Such memory would be fast, robust (not influenced by power outage, no mechanically moving parts), with low power consumption and in case of large arrays of vertical tracks it should provide also high storage density.

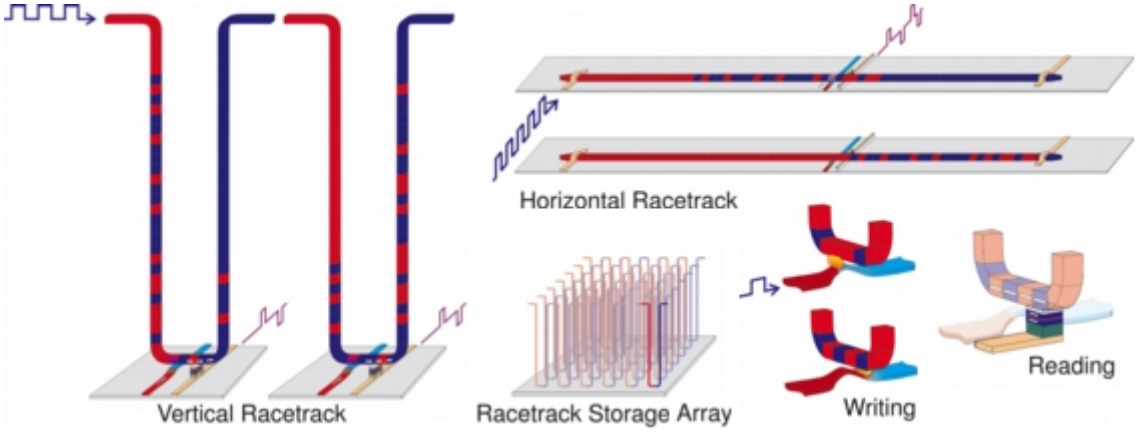

Fig. 1.1: Magnetic racetrack memory. The data are stored in magnetic tracks as domains with opposite magnetization direction. The concept has been demonstrated on a horizontal (planar) strip, but for the high density data storage one would be more interested in arrays of vertical tracks containing large number of closely spaced tracks. In ideal case data writing would be done electrically (e.g. with spin-polarized current to reduce the device consumption). Readout can be accomplished by measuring tunnel magnetoresistance of a junction connected to the track. Taken from [2].

Recently, also other types of memories (e.g. flash with tens of stacked layers) have gone into 3-dimensional architecture. Even in case of some HDD, there are few (2-3) magnetic recording layers that can be accessed independently [3, 4]. These are already on the market or will arrive soon. However, the racetrack memory still remains in laboratories or better to say as an idea. IBM and many other groups demonstrated the concept on a planar magnetic strip and contributed to fundamental understanding of domain wall motion in planar strips. However, even in a recent article [5], Parkin admits that going to 3D is a considerable challenge, mainly from the fabrication point of view. Study of magnetic tracks has focused

mainly on 2D strips prepared by lithography. Recently investigations of cylindrical nanowires prepared by (electro)chemical methods emerge [6]. Aside from cylindrical nanowires, there is a growing interest in other curved geometries (i.e. study of interplay of curvature and magnetism) [7] as well as in nanomagnets in 3D (three-dimensional nanomagnetism) [8]. These two (Fig. 1.2) largely overlap and bring new challenges as well as promise for new magnetic configurations, physics, and higher areal density of elements in devices.

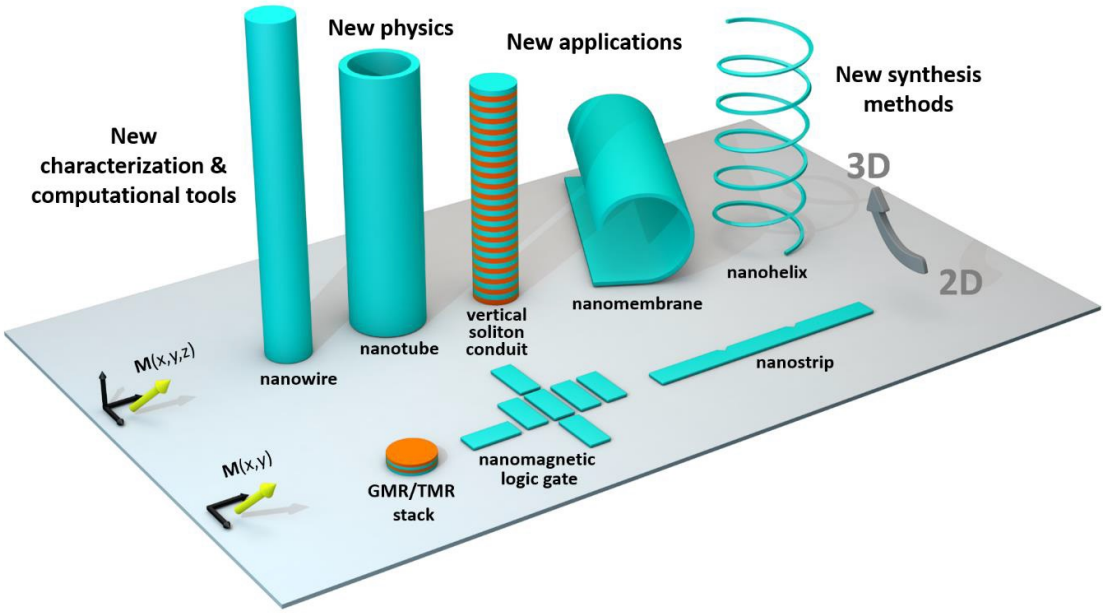

(a)

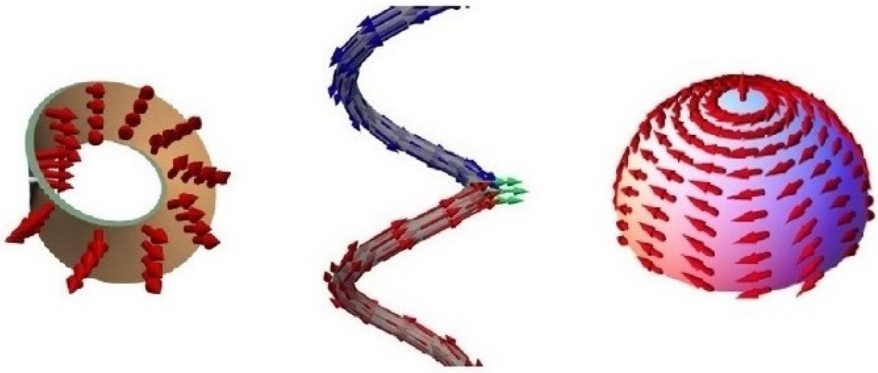

(b)

Fig. 1.2: (a) Three-dimensional nanomagnetism [8]. GMR/TMR stands for giant/tunnelling magnetoresistance utilized in sensors [9]. (b) Magnetism in curved geometries – examples (from the left): Möbius strip, nano-helix with a domain wall, and half-sphere (cap) with a vortex [7].

Magnetic nanowires and nanotubes

In nanomagnetism and spintronics, magnetic domain wall motion has been mainly investigated in flat strips prepared by lithography [5, 10]. However, magnetic nanotubes (NTs) and cylindrical nanowires (NWs) fabricated in vertical arrays by bottom-up methods are more suitable for the design of high density storage devices with 3D architecture.

Ten years after the initial proposal for the 3D racetrack memory, the focus is shifting from experiments on arrays of cylindrical nanowires to single-nanowire physics, based on transport [11], magnetometry [12], and imaging [13] involving the first experimental confirmations of DWs [14, 15]. These nanowires could provide a model situation for DW motion under magnetic field [16] or spin-polarized current [17] as fast ($> 1\,\mathrm{km/s}$) DW motion has been predicted in these wires [17]. However, DWs in magnetically-soft nanowires are of head-to-head or tail-to-tail type due to the axial magnetization in the domains, which is inherently associated with a large magnetostatic monopolar charge. The resulting long-range stray field could induce unwanted interactions (cross-talk) among densely-packed elements in a device. The newest solution, how to circumvent this issue, relies on artificial materials, so called synthetic antiferromagnets that generate no stray field. While the concept has been demonstrated for 2D flat nanostructures [5], the 3D implementation has not been realized so far.

Magnetic nanotubes, less exploited in comparison to the simple nanowire geometry, have been reported mainly in the context of biomedicine [18] and catalysis [19], while their individual magnetic properties have been largely overlooked. Yet theory and simulations predict similar physics of domain walls in nanotubes compared to cylindrical nanowires [20, 21], including fast ($> 1\,\mathrm{km/s}$) DW motion without Walker instabilities [22]. In terms of new physics and devices, nanotubes appear to be more suitable than solid nanowires. Indeed, their magnetic properties can be tuned by changing the tube wall thickness, and more complex architectures can be prepared based on core-shell structures [23]. These are analogous to multilayers in 2D spintronics (spin-electronics), such as magnetic layers separated by a thin non-magnetic spacer for sensors based on magnetoresistance effects [9] or synthetic antiferromagnets mentioned above.

Further, as it has been already done in case of nanowires [24–26], one can tune the magnetic properties and functionality of potential devices by modifying properties along the tubular structures (modifications could be used also for definition of bits in the racetrack memory):

- material: composition, segments from different elements [27], doping, irradiation ...

- geometrical change: diameter modulation [28], constriction, notches-defects, wire-tube elements [29, 30]
- core-shell structures [23] / multilayered tubes [31].

Why magnetic nanotubes?

In this work we are concerned only with magnetic properties and possible applications of nanotubes in spintronics. Aside from these, they have other properties interesting for different fields, e.g. large surface area – useful for catalysis. Further, both inner and outer surface can be functionalized and/or molecules (drugs) can be loaded inside the tube.

Magnetic nanotubes can bring new or enhanced phenomena due to their geometry, different topology compared to flat films, and possibility to create more complex structures and devices based on multilayered nanotubes (Fig. 1.3).

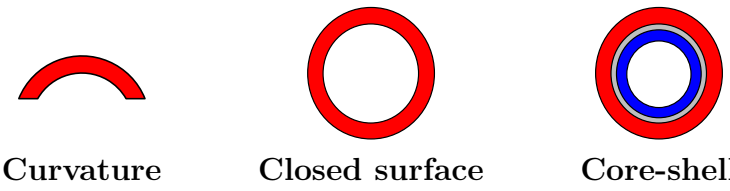

Fig. 1.3: Specific features of nanotubes – 3C: Curvature (curvature induced effects), Closed surface (different topology), and Core-shell geometry (multilayered tubes).

Namely curvature leads to breaking of an inversion symmetry: one can distinguish the inner and the outer surface. This does not happen for a perfect flat film, but only for multilayers – magnetic layer sandwiched in between two different (non-magnetic) layers. Therefore, in this regard, a magnetic tube (curved surface) is equivalent to a multilayered flat film/strip. In flat systems like $Pt/Co/AlO_x$ films (with ultrathin Co and thus perpendicular magnetization), breaking of the inversion symmetry is associated with promotion of chiral magnetic textures, fast propagation of magnetic domains [32], and non-reciprocity of spin wave propagation [33]. Similar phenomena indeed should arise in case of magnetic nanotubes (single magnetic layer, no additional layers needed): curvature induces magnetochirality [34], anisotropy and a so-called effective Dzyaloshinskii-Moriya interaction [7]. Recently, theoretical predictions of the non-reciprocity of spin wave propagation in the tubes have emerged as well [35, 36].

An open and exciting question is whether one can combine effects arising from both curvature and interfaces with different materials and make the effects (e.g. the effective Dzyaloshinskii-Moriya interaction) even stronger. Combination of such

core-shell structures with modification of properties along the structures as pointed above (material, geometry) could lead to e.g. novel magnonic (spin-wave) waveguides. Some core-shell nanowires have been already realized, such as spin-valves [37]. However, most of the possible stacks still awaits: synthetic antiferromagnets, structures with heavy metals (such as Pt) exploiting the Spin Hall effect [38, 39] or the Dzyaloshinskii-Moriya interaction (see section 2.2.1) [40]... Vertical arrays of such multilayered nanotubes could enable transfer of 2D spintronics to 3D and thus make spintronic devices more viable and competitive.

Chemists and material scientists can fabricate huge variety of nanostructures from different materials and with various shapes. This involves magnetic nanotubes, multi-layered tubes and core-shell nanowires. However, characterization of such structures is done by global measurements, typically by magnetometry on arrays or bundles of such structures. On the other hand, physicists can image and measure single nanostructures, but so far they have been focusing mostly on thin film elements prepared by lithography. More recently some of them moved on to the study of cylindrical nanowires prepared by chemical methods. In this work we bring together these two worlds. The author himself is a hybrid of an engineer, a physicist, and a chemist. We also build on a collaboration with expert chemists and material scientists from TU Darmstadt, in particular with Sandra Schaefer.

Organization of the manuscript

The presented manuscript is divided into 4 parts:

- I: Theoretical background & State of the art
- II: Methods & Instrumentation
- III: Results & Discussion – Magnetic nanotubes
- IV: Results & Discussion – Multilayered nanotubes

Thus, we will start with a review of theoretical background and information on what has been already done in the field of elongated magnetic nanostructures and nanotubes in particular. Part II describes techniques we used in our investigation as well as some related supporting information. Finally results (both experiments and numerical modelling) are discussed in parts III and IV, with part III being focused on magnetic nanotubes and the last one on more advanced core-shell structures (multilayered tubes).

Part I

Theoretical background & State of the art

2 MAGNETISM IN LOW DIMENSIONS

In this chapter, upon briefly discussing different magnetic orderings, we will focus on ferromagnets. We will treat them in the framework of a so-called micromagnetism. This continuum theory is especially suitable for the description of nanostructures which form usually too large systems to be addressed by (relativistic) quantum mechanics, however, still too small to be described by the phenomenological Maxwell's theory of electromagnetic fields. Micromagnetism bridges the gap between these two approaches - assuming continuum while taking some results derived from quantum mechanics. For basics of magnetism or other methods how to treat it, one may consult the following (text)books [41–43].

2.1 Magnetically-ordered materials

Below we briefly cover materials that are magnetically ordered. Note that the same materials may display different ordering and/or total magnetic moment depending on conditions such as crystallographic structure (influenced also by following parameters), temperature, stress, electric field etc. Magnetic ordering can be also different if the size of the material is decreased to nanometric dimensions; material defects play a role as well. We can distinguish 3 main groups of magnetically ordered materials: ferromagnets, ferrimagnets and antiferromagnets. Atoms in these have net magnetic moments and these moments strongly interacts creating regions with moments aligned (parallel) in one direction – so called domains (to be discussed below). In our work we will focus on materials exhibiting ferromagnetic behaviour.

Ferromagnets

The interaction of magnetic moments in ferromagnets leads to their preferential alignment parallel to the same direction. Therefore, ferromagnets can have a strong net magnetic moment. The volume density of the moment is referred to as magnetization. Despite strong magnetic moments, the whole ferromagnet can have a weak net moment due to the presence of ordered regions (domains) with different orientation of the common axis for the magnetic moments (e.g. demagnetized state).

Antiferromagnets

Magnetic moments in antiferromagnets have a common axis, but they are ordered in antiparallel directions leading to zero net magnetic moment. As such, antiferromagnets are uneasy to be influenced by the external magnetic field. On the other hand,

even antiferromagnets can be manipulated with spin polarized current and antiferromagnetic spintronics becomes a hot topic thanks to faster spin dynamics compared to ferromagnets [44, 45]. Typical time-scale for spin precession and reversal in antiferromagnet (dominated by strong exchange interaction) is in the picosecond range (THz frequency), whereas magnetization dynamics in ferromagnet happens mostly at nanosecond scale (GHz frequency). Currently, antiferromagnets are used in spin-valves to fix the magnetization in a ferromagnetic so-called reference layer through ferromagnetic/antiferromagnetic coupling (makes the ferromagnet magnetically harder).

Ferrimagnets

Ferrimagnets are usually composed of atoms forming 2 sub-latices from different elements, or same elements, but having different oxidation number, occupying different crystallographic site, ... Magnetic moments in one lattice are ordered in antiparallel direction with respect to the moments in the other lattice. The material still have some resulting magnetic moment as the magnitude of the moment of atoms from the two different sub-latices is not the same except at one particular temperature for some of them. At this point, so-called magnetic moment compensation temperature, temperature dependence of the magnetic moment magnitude leads to zero net magnetic moment. Such compensation is observed in garnets and rare-earth–transition-metal alloys, but not in magnetite.

Aside from this, ferrimagnets may have another compensation temperature. It is angular momentum compensation point where the net angular momentum vanishes. Recently ferrimagnets regained attention thanks to findings indicating very interesting properties near such temperature: ultra-fast magnetization switching similar to antiferromagnets [46] and possibility to achieve magnetic field-controlled antiferromagnetic spin dynamics [47]. Moreover, recent simulations show that domain-wall dynamics in ferrimagnets subject to Dzyaloshinskii-Moriya interaction (DMI) can be associated with emission of terahertz spin-waves [48]. One may thus think about spintronics based on ferrimagnets, as these unlike antiferromagnets can be more easily manipulated, especially by external magnetic field.

Synthetic antiferromagnets

Aside from above-mentioned materials present in nature, one can create artificial materials – synthetic antiferromagnets (SAFs) and ferrimagnets based on heterostructures composed of two (ferro)magnetic layers separated by a thin spacer. Example of such spacer is Ru, but other (transition) metals and even semiconductors/insulators can be used [49] (possibly different mechanism – spin polarized tunnelling).

Inter-layer magnetic Ruderman-Kittel-Kasuya-Yosida interaction (RKKY, indirect exchange), leads to parallel (ferromagnetic) or antiparallel ordering of magnetization in the two layers depending on the spacer nature and its thickness (typically around 1 nm). The interaction oscillates in between these two regimes and its strength decreases with the spacer thickness [50].

SAFs can be easier to prepare than genuine antiferromagnets and they have similar fast magnetization dynamics (also very fast domain wall motion) [51, 52]. In addition, SAFs offer more versatility in terms of tuning the magnetic moments and the Néel temperature (above this temperature there is no more antiferromagnetic order). In practice, it is difficult to obtain the same magnetic moments of the two magnetic layers, thus one obtains a synthetic ferrimagnet. Recent experiments on such structures in form of strips show promising results [53].

In this thesis we will restrict our exploration to ferromagnetic nanotubes and partially we will also touch tubular multilayers. But as will be shown later, antiferromagnetic nanotubes can be prepared and in theory ferrimagnetic tubes may be exploited as well. However, note that just ferromagnetic tubes alone are not so well explored from the experimental point of view not speaking of other possible magnetic orderings.

2.2 Micromagnetism

Micromagnetism, sometimes merged with nanomagnetism (magnetism at nanoscale), is suitable for the description of magnetism at mesoscopic scale – i.e. micro and nanostructures. The micromagnetism is a continuum theory of magnetism, where magnetization is supposed to be a continuous function of a position in space. In addition, it is assumed that the magnetization vector has a constant norm for homogeneous materials, thus only the direction of magnetization is allowed to change:

$$\vec{M}_\mathrm{s} = \vec{M}_\mathrm{s}(\vec{r}), \left\|\vec{M}_\mathrm{s}\right\| = \text{const.} \tag{2.1}$$

The topic will be covered only briefly without derivations and provision of deeper insight. Interested reader is encouraged to consult an excellent book *Magnetic Domains* [54] and other helpful resources [55, 56].

We used this approach in numerical modelling of magnetization in our nanostructures (tubes, wires).

2.2.1 Energies at play

There are various contributions to the total energy of a (micro)magnetic system, among them the most important ones are: exchange, magnetostatic (dipolar), Zeeman (energy in external magnetic field), magnetocrystalline anisotropy and magnetoelastic energy. The interplay of these energies determines the magnetization configuration of a sample and affects its evolution, dynamics.

Exchange energy

This contribution results from a purely quantum mechanical interaction between spins (more generally magnetic moments). In case of the direct Heisenberg exchange, the exchange energy of two spins $\vec{S}_1$, $\vec{S}_2$ reads [42]:

$$E_{\mathrm{ex,spin}} = -J_{1,2}\vec{S}_1 \cdot \vec{S}_2, \tag{2.2}$$

With constant J representing the value of exchange integral; for ferromagnets $J > 0$ and alignment of neighbouring spins in the same direction is preferred. In the micromagnetic continuum approach, if the magnetization in a ferromagnet deviates from the uniform one, an energy penalty in the form of an isotropic volume [1] exchange stiffness energy appears:

$$E_{\mathrm{ex}} = A \iiint\limits_{\text{ferromagnet}} \left(\vec{\nabla} \cdot \frac{\vec{M}}{M_{\mathrm{s}}} \right)^2 \mathrm{d}V, \tag{2.3}$$

where A is the exchange stiffness with dimension J/m. At zero temperature, still used in many simulations, its value is loosely related to the critical Curie temperature T_{c}: $A(T = 0\,\mathrm{K}) \approx \mathrm{k_B} T_{\mathrm{c}}/a_{\mathrm{L}}$, with $\mathrm{k_B}$ being Boltzmann's constant and a_{L} lattice parameter of the ferromagnetic crystal [54]. Typical value are of the order of 10 pJ/m: around 30 pJ/m for cobalt and 10 pJ/m for permalloy ($Ni_{80}Fe_{20}$) [43].

For minimization of the exchange energy, uniform magnetization $\vec{M}$ is preferred.

Generalized expression states:

$$E_{\mathrm{ex}} = \iiint\limits_{\text{ferromagnet}} \sum_{i,k,l} A_{kl} \frac{\partial}{\partial x_k} \left(\frac{M_i}{M_{\mathrm{s}}} \right) \frac{\partial}{\partial x_l} \left(\frac{M_i}{M_{\mathrm{s}}} \right) \mathrm{d}V. \tag{2.4}$$

Fortunately, symmetric tensor A_{kl} reduces to a simple scalar for cubic or isotropic materials, thus the isotropic stiffness expression (2.3) can be used [54].

[1] There exist also interface exchange coupling, when two different ferromagnets are in contact. This case is far beyond the scope of this work.

Asymmetric exchange (Dzyaloshinskii-Moriya interaction)

Above we discussed the common symmetric exchange interaction. However, asymmetric exchange, so-called Dzyaloshinskii-Moriya interaction [40, 57], exist as well and is extensively investigated in spintronics. Starting again from the atomistic description with 2 spins, the energy associated with this interaction reads:

$$E_{\mathrm{DM,atom}} = \vec{d}_{1,2} \cdot \left(\vec{S}_1 \times \vec{S}_2 \right), \tag{2.5}$$

with $\vec{d}_{1,2}$ being the Dzyaloshinskii-Moriya interaction vector for the atomic bond. While the symmetric exchange (2.2) favours co-linear spin arrangements (parallel and anti-parallel spins), the DMI promotes spin-canting and textures such as spin-spirals, (anti)skyrmions. The DMI is present in bulk materials that do not have space inversion symmetry and more important it may also arise at the interface of ferromagnetic thin films and materials with high spin-orbit coupling (e.g. $\mathrm{Pt/Co/AlO}_x$ multilayer – both interfaces play a role). As mentioned in the introduction, the DMI is associated with the breaking of the inversion symmetry, leading to magnetochirality, non-reciprocity of spin-wave propagation etc.

For ultra-thin films the DMI energy can be written in the micromagnetic continuum approximation as follows [58, 59]:

$$E_{\mathrm{DM}} = t \iint\limits_{\mathrm{film}} D \left[\left(m_x \frac{\partial m_z}{\partial x} - m_z \frac{\partial m_x}{\partial x} \right) + \left(m_y \frac{\partial m_z}{\partial y} - m_z \frac{\partial m_y}{\partial y} \right) \right] \mathrm{d}S, \tag{2.6}$$

where D is is the continuous effective DMI constant ($[D]$=J/m^2), t is the film thickness, $m_i = \frac{M_i}{M_\mathrm{s}}$ the normalized magnetization vector, and z is axis perpendicular to the film.

In case of our samples, magnetic tubes, we do not consider the DMI. Proper treatment of the DMI in magnetic tubes is beyond the scope of our work. Interested readers may consult a theoretical work by Goussev dealing with DMI in the tubes [60], note that the work claims some important differences for DMI in planar films (wires) and tubes. As already stated, effects similar to the one induced by DMI can arise from the curved geometry itself.

Zeeman energy

The Zeeman term describes energy of a magnetic moment in an external magnetic field. This contribution gives an energy penalty if the magnetization does not lie in the direction of the external applied field:

$$E_{\mathrm{Z}} = -\mu_0 \iiint\limits_{\mathrm{ferromagnet}} \vec{M} \cdot \vec{H}_{\mathrm{ext}} \, \mathrm{d}V. \tag{2.7}$$

Magnetostatic energy

Magnetostatic (dipolar) energy describes Zeeman-like mutual interactions of magnetic moments in a ferromagnet and reads:

$$E_{\mathrm{d}} = -\frac{1}{2}\mu_0 \iiint_V \vec{M} \cdot \vec{H}_{\mathrm{d}} \, \mathrm{d}V, \tag{2.8}$$

With integration taken over the ferromagnet volume V which defines a closed surface $\partial V \equiv S$.

Sometimes an energy density called dipolar constant $K_{\mathrm{d}} = \frac{1}{2}\mu_0 M_{\mathrm{s}}^2$ is used. While demagnetizing field $\vec{H}_{\mathrm{d}}$ has zero curl, it results from a potential: $\vec{H}_{\mathrm{d}} = -\vec{\nabla}\phi_{\mathrm{d}}$. Using this notation and the concept of magnetic charges, magnetostatic energy can be expressed in a different form [54]:

$$E_{\mathrm{d}} = \mu_0 M_{\mathrm{s}} \left(\iiint_V \rho_{\mathrm{m}} \phi_{\mathrm{d}} \, \mathrm{d}V + \oiint_{\partial V} \sigma_{\mathrm{m}} \phi_{\mathrm{d}} \, \mathrm{d}S \right). \tag{2.9}$$

In analogy with electrostatics [2], volume (ρ_{m}) and surface (σ_{m}) density of magnetic charges (shortly just charges) are defined as:

$$\rho_{\mathrm{m}} = -\mu_0 \vec{\nabla} \cdot \vec{M} = \mu_0 \vec{\nabla} \cdot \vec{H}, \tag{2.10}$$

$$\sigma_{\mathrm{m}} = \mu_0 \vec{n} \cdot \vec{M}. \tag{2.11}$$

Second part of (2.10) originates in inserting [3] material relation $\vec{B} = \mu_0 \vec{H} + \mu_0 \vec{M}$ into Maxwell equation $\vec{\nabla} \cdot \vec{B} = 0$. Vector $\vec{n}$ in (2.11) denotes outward-directed surface normal. Note that very often the volume magnetic charges are defined simply as $\rho_{\mathrm{m}} = \vec{\nabla} \cdot \vec{M}$.

To minimize E_{d}, we need to reduce both volume and surface charges, which leads to a so called charge avoidance principle. Surface charges can be avoided when the magnetization lies parallel to the sample edges, which can lead to a so called flux closure as will be shown later. The shape of the sample – integration region – has also a significant influence on the magnetization configuration. Sometimes we speak about shape anisotropy in this case and consider K_{d} as a anisotropy constant (see effective anisotropy below). However, the shape anisotropy is not related to other anisotropies like the magnetocrystalline one, which will be cover in the next section.

Magnetocrystalline anisotropy

In a crystal not all directions of the magnetization have the same energy. Due to crystal-field effects, coupling electron orbitals with the lattice, and coupling of electron orbitals with spins, some directions (or planes) with respect to the crystal axes

[2] $\vec{\nabla} \cdot \vec{E} = \frac{\rho_{\mathrm{e}}}{\epsilon_0}$ and therefore $\vec{\nabla} \cdot \vec{H} = \frac{\rho_{\mathrm{m}}}{\mu_0}$.

[3] $\left(\vec{\nabla} \cdot \vec{B} = 0\right) \wedge \left(\vec{B} = \mu_0 \vec{H} + \mu_0 \vec{M}\right) \Rightarrow -\mu_0 \vec{\nabla} \cdot \vec{M} = \mu_0 \vec{\nabla} \cdot \vec{H} = \rho_{\mathrm{m}}$.

are preferred. These are so called easy axes (or easy planes/surfaces). On the other hand, less favoured hard axes exist [56]. Rigorous treatment of magnetocrystalline anisotropy is quite complex as well as formulas used for its description, interested reader may consult references [41, 43, 54]. Very often volume density of magnetic anisotropy energy is given in terms of a set of angular functions. Here we will restrict ourselves to simple example of a uniaxial anisotropy found in hexagonal and orthorhombic crystals:

$$\epsilon_{\mathrm{mc,u}} = K_1 \sin^2\theta + K_2 \sin^4\theta + \cdots , \tag{2.12}$$

where K_i are anisotropy constants with dimension $\mathrm{J/m^3}$ and θ is angle between magnetization and the anisotropy axis. Anisotropy constants for higher power terms are usually negligible and sometimes only the first term is taken into account. Cobalt is a typical represent with $K_1 = 520\,\mathrm{kJ/m^3}$ and the c axis of the hexagonal crystal being the only easy axis [56].

Magnetoelastic coupling

So far we have spoken of an undeformed lattice. External stress results in strain and magnetoelastic contribution which is sometimes taken as a part of magnetocrystalline anisotropy. Local deformation may result from stress generated by the ferromagnetic material itself – magnetostriction [43]. Inverse magnetostriction (Villari effect) describes change in magnetization (and other magnetic properties) when the material is strained (external influence, stress).

2.2.2 Characteristic lengths

As a consequence of a competition of different interactions, characteristic quantities such as lengths arise. We will mention here only two of them [56]:

- anisotropy exchange length (Bloch parameter): $\Delta_{\mathrm{a}} = \sqrt{\frac{A}{K_{\mathrm{a}}}}$,
- dipolar exchange length (exchange length): $\Delta_{\mathrm{d}} = \sqrt{\frac{A}{K_{\mathrm{d}}}}$.

Δ_{a} is important for hard magnetic materials, where exchange and anisotropy (with anisotropy constant K_{a}) compete. This length corresponds to a width of a domain wall (discussed below) separating two domains. For soft magnets, Δ_{d} with exchange and dipolar energy competition is more relevant. Δ_{a} is roughly 1 nm for hard magnets and up to several hundreds nanometers for soft magnets. Δ_{d} lies near 10 nm for both types [56]. Therefore we see, that nanoscale is really important in magnetism. These exchange lengths have importance in micromagnetic simulations where small volumes of a magnetic body are supposed to be described by one magnetic moment.

2.2.3 Magnetization dynamics

Magnetization dynamics, i.e. the evolution of magnetization, is described by the Landau-Lifschitz-Gilbert (LLG) equation:

$$\frac{\mathrm{d}\vec{M}}{\mathrm{d}t} = \gamma_{\mathrm{G}}\vec{M} \times \vec{H}_{\mathrm{eff}} + \frac{\alpha_{\mathrm{G}}}{M_{\mathrm{s}}}\vec{M} \times \frac{\mathrm{d}\vec{M}}{\mathrm{d}t}. \tag{2.13}$$

The first term stands for Larmor precession of the magnetization around an effective magnetic field $\vec{H}_{\mathrm{eff}}$ (typically external magnetic field, but there could be other, internal, contributions such as magnetostatic, anisotropy, and exchange). $\gamma_{\mathrm{G}} = -\mu_0 g \frac{\mathrm{e}}{2m_{\mathrm{e}}}$ is the Gilbert gyromagnetic ratio, with e being the elementary charge and m_{e} the mass of the electron. The Landé g factor has value close to two for many ferromagnets [54]. The gyromagnetic ratio links magnetic moment $\vec{\mu}$ with angular momentum $\vec{L}$: $\vec{\mu} = \gamma\vec{L}$. As we know from mechanics, $\frac{\mathrm{d}\vec{L}}{\mathrm{d}t} = \vec{T}$, where $\vec{T}$ stands for torque. Thus all the terms on the right-hand-side of (2.13) can viewed as torques [4] multiplied by a constant.

In real magnetic systems there are losses that cause damping of the precessional motion. In the end, magnetization is oriented parallel with respect to $\vec{H}_{\mathrm{eff}}$, as expected [5]. This is described by the second term in (2.13) with α_{G} being the dimensionless empirical (phenomenological) Gilbert damping parameter with typical values for real materials $10^{-3} - 10^{-1}$. It describes further unspecified dissipative phenomena such as magnon scattering on lattice defects. Note that some damping-like torques can have opposite sign and lead to an effective negative damping constant α. Vectors and terms acting in the LLG equation are depicted in Figure 2.1.

The effective magnetic field is given by:

$$\vec{H}_{\mathrm{eff}} = -\frac{1}{\mu_0}\frac{\delta E}{\delta \vec{M}}, \tag{2.14}$$

where E is the total energy of the system under consideration. Particular energy contributions have been already described above.

New phenomena in magnetization dynamics such as spin transfer [62] and spin orbit torques [63, 64] or the Dzyaloshinskii–Moriya interaction [40, 57] can be incorporated into the LLG equation (2.13) as additional torques (on the right hand

[4] We recall that the torque acting on a magnetic dipole in an external magnetic field is given by $\vec{T}_{\mathrm{e}} = \vec{\mu} \times \mu_0\vec{H}$.

[5] Magnetization precessional dynamics can be viewed as analogue of a gyroscope in mechanics. Even though antiparallel alignment of $\vec{M}$ with respect to $\vec{H}_{\mathrm{eff}}$ in case of negative α_{G} might be a surprise, it has its mechanical analogy as well: special spinning tops having a low lying centre of gravity – *tippe tops*. Some readers may recall the photo in which even Wolfgang Pauli and Niels Bohr were fascinated by upside-down flip of the *tippe top* [61, Fig. 3.18].

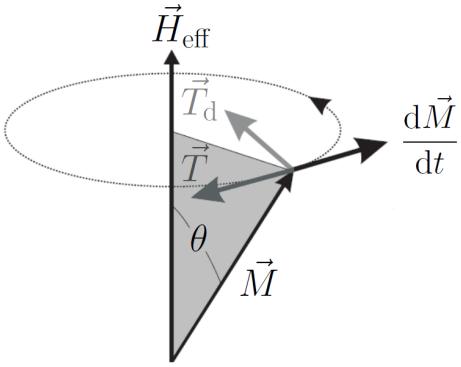

Fig. 2.1: Schematic picture of the dynamics of a magnetization vector (or magnetic moment) – graphical representation of the LLG equation. Torque $\vec{T} = \vec{M} \times \vec{H}_{\mathrm{eff}}$ acts on the magnetization $\vec{M}$ in an effective field $\vec{H}_{\mathrm{eff}}$. This leads to a precession of the magnetization around $\vec{H}_{\mathrm{eff}}$ in a direction opposing $\vec{T}$, because γ_{G} is negative. In case of non-zero damping α, a damping torque $\vec{T}_{\mathrm{d}}$ emerges. It is related to the second term in the LLG equation. For a common case of positive α it aligns the magnetization with the effective field. Therefore the end point of $\vec{M}$ goes in a spiral before it reaches final state (angle $\theta = 0$). Typical time-scale for this process is in the order of nanoseconds. Adapted from [61].

side of the LLG) [65], or included in the effective magnetic field $\vec{H}_{\mathrm{eff}}$ as new energy contributions, respectively.

2.3 Magnetic domains and domain walls

2.3.1 Origin of magnetic domains and domain walls

Usually only tiny nanomagnets (or magnets subjected to a strong uniform external field) are uniformly magnetized, larger magnets are split into several magnetic domains, regions with (almost) uniform magnetization, however, with different magnetization direction in the neighbouring regions (domains). The presence of domains results from competition of particular energy contributions, mainly exchange, magnetostatic, and anisotropy energy. It also depends on the magnetic history of the sample: during a hysteresis cycle, sample may display different amount, sizes and even types of domains. Usually larger number of domains can be obtained upon demagnetization of a sufficiently large sample. How the competition of different energies influences magnetization in a spheroidal particle is illustrated in Figure 2.2. Exchange energy alone favours uniform magnetization, thus only one domain is present – we speak of a single domain-state. If we consider also the magnetostatic interaction, a flux-closure pattern appears as a tendency to minimize surface charges

by keeping magnetization parallel to the particle edges. Anisotropy may favour only certain directions of the magnetization, e.g. in case of uniaxial anisotropy, two domains could be more favourable than the complete magnetic flux-closure. In such case, domains are separated by a boundary, a domain wall (DW). Domain theory is very complex and there is no single and simple origin of domain creation for all materials. It rather differs from case to case, depending on anisotropies, shape and size of sample, and magnetic history of the sample. Magnetostatic energy plays an important role in this case [54]. For rigorous treatment and nice pictures of various domains (bamboo, bubble, spike, labyrinth, saw-tooth, ...) consult the excellent book *Magnetic domains* [54].

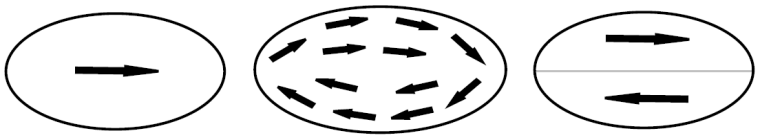

Fig. 2.2: Influence of energy contributions on a spheroidal particle. In first particle (from the left), only exchange is taken into account, thus uniform magnetization is present. In the middle flux-closure pattern results from competition of exchange and magnetostatic energy. On the right, particle with a considerable uniaxial anisotropy is split into two domains as intermediate directions of the magnetization are unfavourable. Gray line represents the the domain boundary – domain wall. Adapted from [43].

Here, we will focus on so-called 1D nanostructures – nanostrips, cylindrical nanowires, and mainly nanotubes – the main topic of the thesis. Even-though these are (especially in experiments) 3D objects, in some cases the magnetization and its dynamics can be approximated by a simple 1D model. We mention strips and nanowires as these have been already thoroughly investigated and some similarities can be found in case of nanotubes. Regarding nanotubes, most of the works are theory and simulations and only recently only few single tube experiments have emerged.

2.3.2 Domain walls in nanostrips

In nanostrips, usually prepared by lithography from thin films, magnetization tends to be in-plane. In this case two types of DWs can be observed: transverse and vortex (Fig. 2.3a,b). In nanostrips with magnetization perpendicular to the plane (e.g. very thin films) Néel and Bloch walls can be found (Fig. 2.3c,d). The DW type, Bloch vs Néel, depends mainly on the film thickness. The transition is reported around 20-40 nm for 180° DWs and magnetically-soft films. However, it can be affected by an additional magnetic anisotropy, such as magnetocrystalline [66].

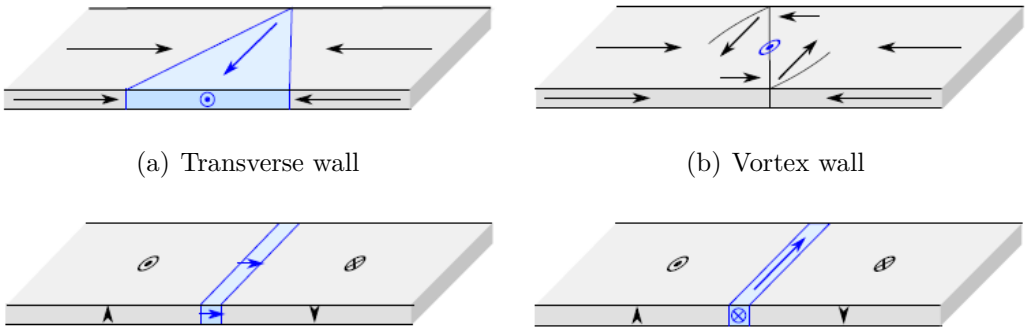

(a) Transverse wall (b) Vortex wall

(c) Néel wall (d) Bloch wall

Fig. 2.3: Scheme of domain walls in nanostrips. (a)-(b) Strips with in-plane magnetization with domain walls of (a) transverse and (b) vortex type. (c)-(d) Strips with out-of-plane magnetization with (c) Néel and (d) Bloch wall. Arrows depict local magnetization; domain wall region is highlighted with the blue colour. Schemes courtesy of Olivier Fruchart.

2.3.3 Domain walls in cylindrical nanowires

In cylindrical nanowires with axial domains, two DW types were predicted [16, 67, 68] and more recently also experimentally observed: transverse wall (TW) [14] and Bloch point wall (BPW) [15]. The first one has some similarities with both transverse and vortex walls in nanostrips. However, the other one has different topology and dynamics due to the magnetization curling around a Bloch point, a magnetic singularity where magnetization vanishes. TW wall is energetically more viable in nanowires with a smaller diameter, BPW in larger ones. The transition happens around seven times the (dipolar) exchange length, roughly 35 nm in case of permalloy. Note that TW, with magnetization curling on both sides, can be present in significantly thicker wires [14]. The wall type observed in experiments may also depend on the magnetic history of the sample.

2.3.4 Domain wall motion

Domain wall motion has been first (experimentally) investigated in thin films, flat nanostrips and more recently in nanowires. Only theoretical works exist in case of NTs (more in section 3.2). Various stimuli can be applied to displace a DW. Aside from magnetic field and (spin-polarized) current, one can use the following: spin-waves [69, 70], thermal gradients [71], non-uniform stress (in magnetostrictive materials) [72], and acoustic waves (creating stress) [73].

The motion, its dynamics and speed of DW propagation depend on the material,

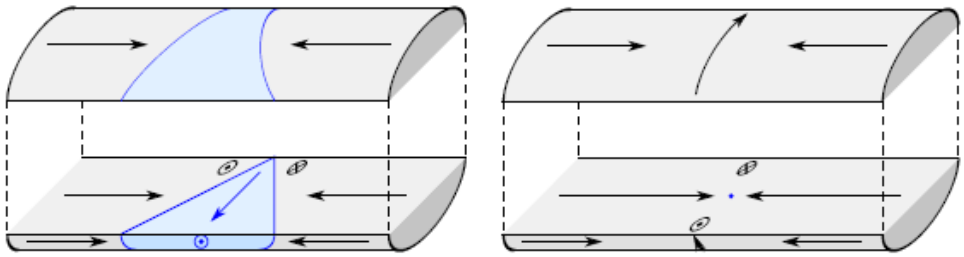

(a) Transverse wall (b) Bloch point wall

Fig. 2.4: Scheme of domain walls in cylindrical nanowires. (a) Transverse wall is preferred for smaller diameter wires, whereas (b) Bloch point Wall (sometimes called confusingly vortex wall) can be more likely found in larger ones (at least from the energy point of view). The BPW contains a magnetic singularity with vanishing magnetization, the Bloch point, in its centre, here represented with a small blue dot. Taken from [15].

nanostructure shape, DW type and configuration, and type of stimulus. One can expect differences between flat films and nanotubes as they have different topology.

In strips especially under magnetic field, the DW speed is limited by the Walker breakdown [74]: above certain field/current the DW becomes unstable and the speed drops (or at least changes its slope). This limit may be overcome or postponed towards stronger stimulus by changing structure shape, material (also heterostructures with interface phenomena), ... Note that controlled high-speed DW motion is important for potential solid state racetrack memories based on shifting the walls.

DWs in cylindrical NWs, especially the BPWs, are expected to move at high speeds under both magnetic field [16] and spin-polarized current [17] with speed predicted to be even $> 1\,\mathrm{km/s}$. So far no experimental confirmation of such a high speed has been reported. A comparison of current-driven DW motion for a nanowire and planar strip is given in Fig. 2.5. In magnetic nanotubes the situation should be similar to solid NWs with expectations for high DW speeds (more in section 3.2).

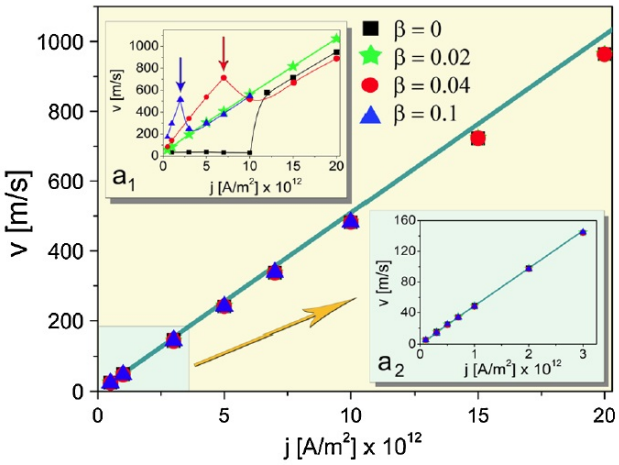

Fig. 2.5: Simulation – current-driven transverse wall motion in cylindrical wire and nanostrip (inset a_1). β is a so-called non-adiabatic spin-transfer parameter. In nanostrip so called Walker breakdown (arrows in the inset a_1) with decrease in speed appears. Taken from [17].

3 MAGNETIC NANOTUBES

Here we will restrict ourselves to ferromagnetic metallic tubes of Ni, Fe, Co, and their alloys/compounds and possibly their combination with other materials. We will not cover carbon nanotubes, for these an interested reader may consult a recent book *Magnetism in Carbon Nanostructures* [75].

In this chapter we discuss magnetic textures, mainly domains and domain walls, predicted in these tubes as well as some experiments reported on NTs. Further, we introduce some common methods for fabrication of such NTs or even multilayered (core-shell) structures. Last but not least, we provide an overview of what has been done on nanostructures with alternating wire (solid) and tube (hollow) segments.

3.1 Magnetic textures

One can think of various magnetic configurations in a nanotube. Some of these are schematically depicted in Fig. 3.1. Not all of them can be stable and other more complex states might be considered in case a special anisotropy is present.

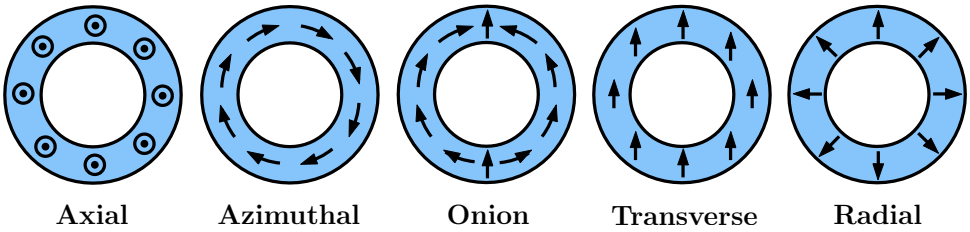

Fig. 3.1: Possible magnetization configurations in a tube. Only a tube cross-section is shown. Depending on the geometry, axial (longitudinal) and azimuthal (curling) states may span through the whole tube at remanence. In majority of elongated tubes, the so-called mixed state is present – axial magnetization with small curling at both tube ends. Under moderate external magnetic field applied in a transverse direction an onion state can develop. Upon further increase in the field magnitude it transforms into a transverse state. The last, radial state, is rather unfavourable due to high exchange energy (large spatial variation of the spins), still it could exist in small tube regions as a metastable domain wall (to be further discussed later).

3.1.1 Magnetization phase diagram

Escrig [76], Landeros [77], and Sun [21] and coworkers presented phase diagrams for magnetically soft NTs (considering exchange and magnetostatic energy) as a

function of tube diameter, tube wall thickness and length. In Fig. 3.2 one can see the diagram by Landeros.

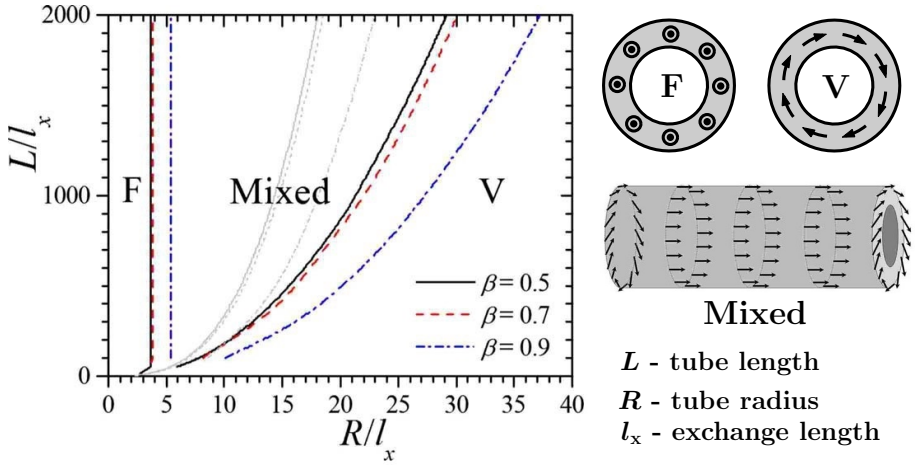

$\beta = R_{\text{inner}}/R_{\text{outer}}$; $\beta = 0$: solid wire; $\beta \to 1$: thin-walled tube

Fig. 3.2: Magnetization phase diagram of a soft magnetic tube. In nanotubes with very small diameter the magnetization is axial everywhere (here denoted as F - ferromagnetic state). For a tube with larger diameter, magnetization is still predominantly axial, but small curling develops at the tube ends (mixed state). Commonly F and mixed states are labelled as axially magnetized. Short tubes with larger diameter prefer to be in flux-closure state with azimuthal magnetization curling (V - vortex-like state). Favoured states depend also on the tube wall thickness with global curling being found rather in thicker tubes. Graph and notation taken from [77].

Depending on the geometry, one of the two following states is preferred: either axial magnetization (possibly with localized curling close to the tube ends – so-called mixed state), or curling along the entire tube (azimuthal/circular/flux-closure/vortex-like magnetization). The uniform azimuthal state is the ground state only for short tubes with a large diameter (small aspect ratio) and large tube wall thickness, all to be compared with the dipolar exchange length. Note that the models in [21, 76] overestimate the magnetostatic energy for the longitudinal magnetization state by disregarding the possibility of a creation of the end curling features [21, 77, 78] i.e. formation of the mixed state. In other words, in these works, tubes with axial magnetization occupy a smaller part of the phase diagram compared to Landeros' work [77]. Recently, the trends of geometrical dependence of the preferred state (axial, or azimuthal) were confirmed experimentally by Wyss et al. [79].

Other states such as transverse magnetization or onion state have been considered in theory, but these can be stabilized only under external transverse magnetic field [21]. A uniformly magnetized domain (axial or azimuthal) is more favourable

than multidomain state with DWs [21]; these may exist as a metastable state or in either large structures, or when additional anisotropy is present (e.g. magnetocrystalline).

There has been quite some debate regarding the axially magnetized tubes and also NWs with the end curling: is there a preference for the curling sense at the end? I.e. is the same or the opposite curling sense favoured at both tube ends? Recently it has been shown, that this supposed preference was an artefact caused by too large mesh cell size in the numerical computation [79]. Refined simulations with 1 nm cell size showed that magnetic energy of the two states is equal (within numerical precision), unless one considers tubes with aspect ratios approaching unity.

3.1.2 Azimuthal domains

So far most theoretical and experimental works have been concerned with tubes having axial magnetization. As stated above, such alignment of magnetization is expected for elongated NTs, unless they exhibit some anisotropy (e.g. magnetocrystalline, magnetoelastic).

Li and coworkers [80] prepared single-crystalline Co NTs by electroplating, graphical summary of their work is featured in Fig. 3.3. From global magnetometry on arrays of tubes, selective area electron diffraction and magnetic force microscopy (MFM) on single tubes they concluded that their tubes were in a flux-closure state (azimuthal magnetization) due to a magnetocrystalline easy axis being perpendicular to the tube axis. Magnetometry and diffraction indeed supported this finding; however, in our view the interpretation of the MFM results is questionable. In their electron microscopy images of tubes after template dissolution in sodium hydroxide, the tubes looked quite oxidized (hairy features on the surface, see the original image in [80]). Li et al. mentioned that from previous experiments they estimated the cobalt oxide layer thickness to be 3 nm, however, they refer to work on nanowires, not nanotubes. In case of NTs, especially thin-walled as in their case (10-15 nm), tubes are likely to be almost completely oxidized as both inner and outer tube surface is exposed to the hydroxide. We experienced the same problem in our experiments. Therefore, it is more probable that their weak signal measured in MFM comes from an electrostatic contribution (also long-range as magnetic interactions), especially as this contrast does not change after annealing and no contrast is expected for flux-closure.

Further, the flux-closure domains were reported by Wyss et al. [79] in short tubes using synchrotron magnetic microscopy (example in Fig. 3.4. In this thesis, we present similar observation, but with multiple domains and walls in significantly longer tubes – consult chapter 8. For information on the imaging technique see

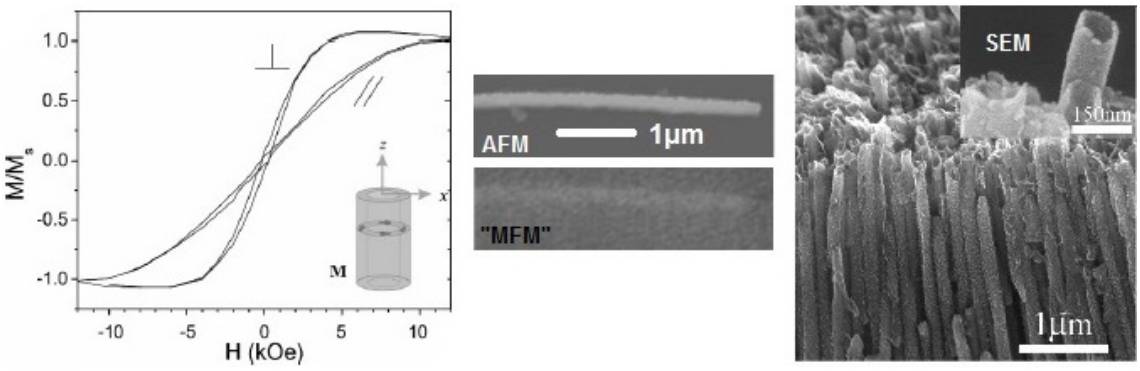

Fig. 3.3: Investigation of Co nanotubes with azimuthal domains by Li et al. [80]. From the left: magnetometry on an array of the tubes with magnetic easy axis being perpendicular to the tube axis, atomic and "magnetic" force microscopy investigation, and electron microscopy image of tubes after the template dissolution.

methods section 5.1.1.

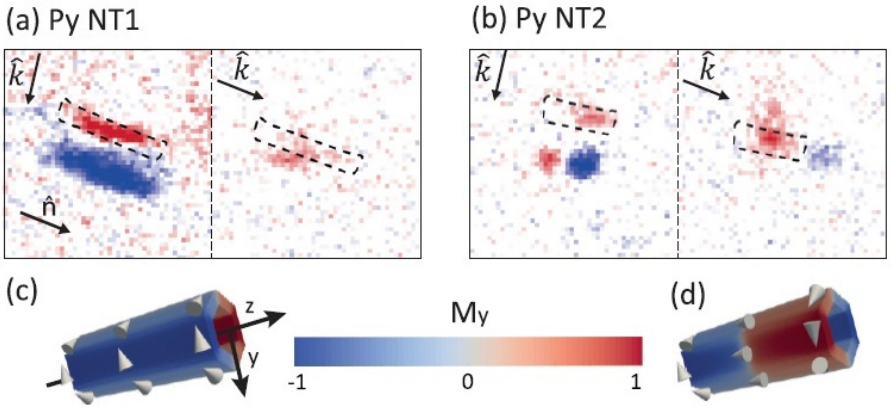

Fig. 3.4: X-ray magnetic circular dichroism - photoemission electron microscopy of permalloy tubes with azimuthal magnetization by Wyss et al. [79]. Magnetic images of of a permalloy tube (diameter around 250 nm, shell thickness 30 nm) for beam perpendicular and parallel to the tube axis for (a) 1.3-μm-long and (b) 0.7-μm-long tube. Technique maps projection of magnetization to the beam direction. Therefore in (a) a single domain is present, whereas (b) features two domains. (c)-(d) Probable magnetic states obtained from micromagnetic simulations (shorter tubes modelled).

3.2 Domain walls in magnetic nanotubes

Aside from coherent rotation of magnetization, the magnetization reversal in elongated NTs can proceed by nucleation and propagation of a DW [81]. In general,

all DWs in (magnetically soft) tubes are considered metastable [21], i.e. uniform axial/azimuthal domain has lower energy. So far mainly walls in tubes with axial magnetization have been considered (theory and simulations only, no experiments), still there are also several works dealing with walls between azimuthal domains. The latter is supposed to be found in tubes with small aspect ratios (mostly short tubes with large diameters, thus not very appealing for most of applications). Below we briefly mention walls predicted in magnetic NTs. Only few experiments ([79], and our work) show azimuthal domains in nanotubes and/or even DWs. So far no DW could be stabilized (or better to say trapped) and imaged in axially magnetized nanotubes.

3.2.1 Domain walls in nanotubes with axial domains

As mentioned above, due to their elongated shape, magnetic NTs are usually assumed to be axially magnetized. In such case, the DWs are predicted to be similar to the ones found in cylindrical NWs (see Fig. 3.5 and compare with the wire case in Fig. 2.4). Therefore, theory and simulations predict existence of transverse wall (TW) and vortex-like wall (VlW) [81], where the latter is a counterpart of the Bloch-point wall, but with no (micro)magnetic singularity (Bloch point) due to the hollow nature of the tube [20]. This makes the numerical modelling easier and more reliable. So far no direct experimental confirmation, e.g. imaging, of these DWs has been provided.

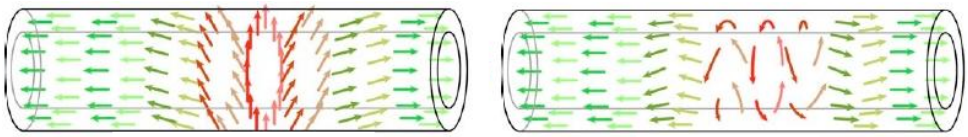

Transverse wall **Vortex-like wall**

Fig. 3.5: Scheme of domain walls predicted in nanotubes with axial domains: Transverse and Vortex-like walls, similar to domain walls in cylindrical nanowires (see Fig. 2.4). Image taken from [82].

The vortex wall is preferred for larger diameter and thin-walled tubes [81]. Most tubes prepared in experiment have such geometry, therefore VlW is more likely to be found in experimental imaging. In a thought experiment, the VlW in a tube can be "prepared" by rolling of a thin strip (film) with a TW lying in-plane of the strip.

TW in a tube is expected for diameters below 50 nm in case of nickel, permalloy and other elemental ferromagnets [81]. However, such NTs with tiny diameters are uneasy to fabricate. Allende et al. [83] modelled the angular dependence of the reversal modes, the TW could be found for larger diameters when the magnetic

field was applied close to a direction transverse to the tube axis. The predicted angular dependence of coercivity was experimentally confirmed by magnetometry on arrays of tubes [82, 84]. Later, Allende also modelled the propagation of TW in tiny diameter-modulated NTs [85].

As the VlW should be the most common one in tubes, both theory and numerical simulations focus on it. High speeds ($> 1\,\mathrm{km/s}$) have been predicted for such DWs subjected to axial magnetic field of just several mT (mobility $500\,\mathrm{km\ s^{-1}\ T^{-1}}$ for permalloy) [22]; similar to its BPW counterpart in cylindrical NWs [16]. Also it appears that, unlike in flat strips, the maximum speed is not limited by the Walker breakdown [74]. There is another so-called magnonic limit, i.e. interaction with spin waves created by the moving wall itself [22]. Under magnetic field, the DW dynamics depends on the chirality of the wall (respectively sense of circulation/curling of magnetization, type head-to-head or tail-to-tail) with respect to the applied field direction. Owing to the effect arising from the curved geometry [34], one chirality is preferred and higher speeds are achieved for a wall (VlW) with such a chirality. If we increase the field above certain threshold, the *bad* (unfavourable) chirality switches to the preferred one and high speed motion is recovered [86, 87], see Fig. 3.6. This is similar to what happens in cylindrical wires for Bloch point wall under magnetic field [16]. Similar chirality dependence was obtained in simulation for VlW motion in permalloy tube under azimuthal AC (almost 13 GHz) magnetic field with amplitude of 5 mT: speed above 300 m/s was found for the field having the same curling sense as the wall [88]. Note that such azimuthal field can be generated by a current-carrying wire inside the tube (i.e. producing Oersted field with the desired symmetry). This can be achieved in core-shell nanowires/multilayered tubes. Such structures could be fabricated starting from magnetic tubes in a template, e.g. via depositing thin insulating oxide (HfO_2) by atomic layer deposition and finally metallic core (Cu) by electroplating. Similar structures have been already prepared – see section 3.5.

The DW motion was also investigated under the current [89] (up to $10^{13}\,\mathrm{A/m^2}$ with DW speed of 1.2 km/s). Simulations yield speeds above $> 1\,\mathrm{km/s}$ (with DW mobilities comparable to the case of DWs in strips with out-of-plane magnetization and DMI), which should even increase with the tube diameter, and show a possibility to switch on purpose the wall chirality by current pulses [86]. Further, spin-wave-induced DW motion was predicted to reach speeds up to 660 m/s [90].

Most of the above-mentioned simulations were performed only for permalloy tubes without any anisotropy or special energy terms. Nevertheless, the latter was investigated as well: namely effect of magnetocrystalline anisotropy on the wall type, width, speed, and the dynamics as a whole [91]. In addition to the tube curvature giving rise to DMI-like effects [7], VlW motion with DMI was considered. DMI in tubes (with axial [sic!] magnetization in domains) seemed to promote narrower

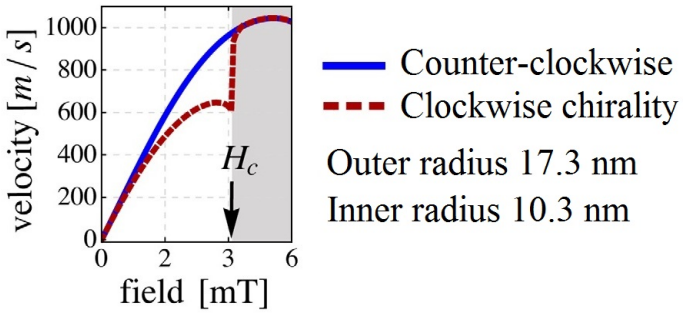

Fig. 3.6: Vortex-like wall speed under magnetic field for opposite chiralities [86]. Analytical modelling for permalloy nanotube. One wall chirality is preferred and the wall moves faster. The unfavourable chirality switches at a so-called chirality field H_c and the fast motion is recovered.

walls that propagate under current irrespective of the wall chirality. Under field, the speed was chirality dependent as in case without DMI [60].

3.2.2 Domain walls in nanotubes with azimuthal domains

Magnetic domains and associated domain walls in systems with azimuthal magnetization have been described (predicted) mostly in short tubes with large diameter, where azimuthal domains can exist even without special magnetic anisotropy. Lee et al. [92] modelled by micromagnetics a short permalloy tube (500 nm diameter, 1000 nm length and tube wall thickness 100 nm). As a relaxed state, they obtained 2 azimuthal domains separated by a DW that appears to have axial magnetization. Further, they introduced such tubes as a biaxial magnetic sensor and predicted anisotropic magnetoresistance of about 5 %. Experimental observation of such wall is claimed by Wyss et al. [79] and it is referred to as Néel wall due to a similarity of an unrolled tube with thin films. In case of these short tubes, one can discuss whether it is a Néel wall between azimuthal domains, or just axially magnetized tube with end curling with the opposite sense of circulation . . .

Betancourt et al. [93] also simulated magnetization in short (500 nm), large diameter (500 nm) permalloy tubes (tube wall thickness 50 nm). As the relaxed state they obtained two azimuthal domains separated by a cross-tie wall, i.e. counterpart of a magnetic structure with vortices and anti-vortices found in thin films/strips ([54], 3.6.4 Domain Walls in Thin Films). Further, they also probed motion of this narrow wall (supposedly 30 nm in width) in AC magnetic field (no DC component) applied in the azimuthal direction (Oersted field of a current-carrying wire inside the tube). The wall speed increased with the field magnitude and was around 70 m/s for 5.5 mT. Probably higher speeds can be obtained for larger fields. The maximum

speed occurred for frequency around 1 GHz with some slower motion observed up to 10 GHz. Similar wall appeared in a work on rolled-up nanomembranes by Streubel et al. [94]. Micromagnetic simulation of a Ni tube with diameter 300 nm including the magnetostriction resulted in azimuthal domains. Even though the DWs were not discussed in this case, they resembled the cross-tie ones.

In their theoretical paper [21], Sun and Pokrovsky briefly discussed the presence of two possible walls between azimuthal (vortex-like) domains, without giving any names or further description (schemes): "the magnetization rotates either in the plane ($\hat{\phi}$, $\hat{z}$), or in the plane ($\hat{\phi}$, $\hat{\rho}$)" with $\hat{\phi}$, $\hat{\rho}$, and $\hat{z}$ being unit vectors in azimuthal, radial, and axial direction, respectively. We identify these as the Néel (axial) and the Bloch (radial) walls, again in analogy with thin films. In section 9 we elaborate further on the walls types and provide images and micromagnetic simulations for all 3 walls (Néel, Bloch, and cross-tie). We provide both simulations and experimental images of tubes with DWs in the same section.

Based on 2D micromagnetic simulations, for low aspect ratio (< 15) tubes with uniaxial anisotropy (along tube) and large tube wall thickness, another more exotic configurations (Branch, Horse-saddle, ...) were reported [95]. However, these are of no interest in our work. It is also questionable whether all of them can be reproduced by full 3D simulations or even experiments.

3.3 Experiments on magnetic nanotubes

We have already mentioned some experiments performed on magnetic NTs and others will be discussed also in following sections. Nevertheless, here we provide a brief overview of experiments from the literature that we are aware of. We will describe experiments on tube arrays with nanostructures still in a template/matrix (e.g. nanoporous alumina) and measurements made on single (isolated) NTs. Note that from the experimental point of view it is much easier to study arrays of nanostructures, whereas in simulations usually only one or a few structures are modelled.

3.3.1 Experiments on nanotube arrays

The majority of experiments on NTs has been performed on NT-arrays. Such experiments are easier than inspection of individual tubes for several reasons. First, as tubes are commonly prepared in templates/matrices, one can use these directly without a need for further processing of the sample. The matrix makes the tubes more mechanically stable and partially protects them from the oxidation – but not the inner shell, unless additional protective layer is deposited or tube extremities are sealed. Such treatment is usually not applied, except for several works dealing

with tube fabrication via atomic layer deposition [28, 96] – here it is rather easy to deposit additional thin protective layer of silica or other oxides. Further, arrays, at least for magnetometry, provide higher magnetic moment and thus signal. The main disadvantage is that the measured quantity usually reflects average of many nanostructures with varying magnetic properties and geometry. Further, the behaviour of the tubes is influenced by magnetic dipolar interactions among them. Strength of such interactions can be estimated e.g. from so-called first order reversal curves [97] or modelled (numerically often only for several tubes, but in principle parts of the array can be effectively simulated using GPU-accelerated micromagnetic codes, such as mumax^3 [98]). Although some methods can access one tube in the template (e.g. magnetic force microscopy), one can detect only what happens close to the tube end, and there is still the influence of the neighbouring tubes.

The most common experiment on NT-arrays is magnetometry [96, 97, 99] using e.g. vibrating sample magnetometer (sometimes exploiting superconducting quantum interference device).

Bachmann et al. probed the geometry dependence of coercivity of magnetic tube arrays with the global magnetometry and found agreement with the theoretical prediction for magnetization reversal through nucleation and propagation of both transverse and vortex-like DWs [82]. Pathak and coworkers [100] performed magneto-optical measurement exploiting Kerr effect on arrays of Y-junction NWs with some tube segments, they could compare magnetization reversal at tube and wire ends. Tabasum carried out magnetic force microscopy, study of magnetization switching in a tube array and its comparison with arrays of NWs [101]. T. Wang [102], Li [103] and Kozlovskyi [104] studied Fe_3O_4, FeCo, and FeNi NT arrays, respectively, with Mössbauer spectroscopy, showing among others that magnetization lies predominantly along the tube axis (expected for elongated tubes). Z. K. Wang et al. [105] conducted Brillouin light scattering spectroscopy on an array of Ni nanorings (aspect ratio 1.5) and found spin wave frequency dependence on the axial magnetic field. Similar trend as in thin films was observed except for small fields ($< 50\,\mathrm{mT}$) where micromagnetic simulations predicted slightly different behaviour, but unfortunately measurement points were not available in this region to confirm such behaviour.

Even though we focus of this section on experiments, we will briefly mention related theoretical investigation of spin waves related to the experiments above. Magnons in NTs were described theoretically by Nguyen [106] confirming the trend schemed by Q. Wang (above). Gonzalez [107] worked further on the spin-wave dispersion relation. And more recently Hertel [34] and Otalora et al. elaborated more on possible modes and asymmetry in the spin wave dispersion relation and non-reciprocity of spin wave propagation in NTs [35, 36]. Most of these theoretical predictions still remain to be probed experimentally.

3.3.2 Experiments on single nanotubes

Experimental investigation of isolated NTs is much more challenging. This is also the reason why such experiments are still rather scarce. As porous templates are usually employed for the synthesis, one has to dissolve the template, purify a solution with NTs and transfer the tubes on a suitable substrate and obtain clean and isolated NTs (not clusters). In other instances (e.g. when fabricating tubes using nanopillars [79] or putting tubes on a microcantilever [108]) one even has to micro-manipulate the tubes onto a suitable place. Further, some substrate patterning or even lithography for electrical contacting could be necessary. Last but not least, individual NTs provide small magnetic signal (compared to solid NWs) and are also more prone to oxidation (both outer and inner surfaces exposed). Therefore, additional care should be taken to protect the tubes from oxidation. Further, tube with large diameters and very thin shell thickness may require fortification to avoid deformation (such elliptical cross-section instead of circular one). Both can be achieved at the same time by atomic layer deposition of a thin non-magnetic layer.

Regarding the reported experiments we will start with work of Li et al. [80] who studied individual single-crystalline Co NTs by magnetic force microscopy. They obtained weak uniform contrast which they interpreted as a sign of flux-closure domain (magnetization curling/winding along tube perimeter). However, given that the tubes were exposed to NaOH during the template dissolution, and as the NTs had thin walls (10-15 nm), it is more likely that the tubes were oxidized and weak contrast was of a non-magnetic origin (e.g. electrostatic interaction).

More convincing is an electron holography imaging of magnetic induction in short magnetic tubes of hexagonal cross-section performed in the group of Dunin-Borkowski [109]. They found axially magnetized tube with magnetization curling at the ends.

To the best of our knowledge, most experiments on single NTs have been done in the groups of Martino Poggio and Dirk Grundler (collaborating also with Dunin-Borkowski above, therefore similar samples with hexagonal cross-section were investigated). Namely they performed magnetoresistance measurements of Ni [110], Py and CoFeB [111] NTs; cantilever torque and SQUID magnetometry [108], and recently also magnetic imaging of CoFeB and permalloy NTs by synchrotron X-ray magnetic microscopy [79]. They imaged axially-magnetized tubes with end curling states (i.e. so-called mixed state, see e.g. Fig. 3.2) and azimuthal domain(s) in short tubes with a sign of the Néel wall in some of them.

Note also, that so far no DWs in axially magnetized tubes have been experimentally observed, not speaking of studying their displacement or even dynamics (under magnetic field or current).

In this thesis, we enrich these single tube investigations with similar synchrotron imaging (with higher resolution), but this time showing multiple well-defined domains and domain walls; magnetooptical measurements (with focused laser beam) and magnetic force microscopy with clear magnetic signal; all in chapter 8. Further, our electron holography investigation of higher aspect ratio CoNiB and NiFeB tubes can be found in sections 8.3.5 and 8.3.3.

3.4 Fabrication of magnetic nanotubes

The nanotube fabrication relies mostly on bottom up, (electro)chemical, methods and use of templates (filling nanoholes or coating nanopilars). Chemical-based synthesis is utilized either for the whole deposition process, or at least for the template synthesis. Such template, e.g. if in the form of vertical pillars, can be coated by physical (vapour) deposition [111]. There exist also template-free chemical syntheses [112], but template-assisted process is preferred as it provides better control on geometry of the nanostructures. Further, it is possible to employ lithography, top-down approach, to prepare tubular structures. However, such way is so far inefficient, time consuming, and very limited in terms of geometrical parameters.

Various structures can be used as a template. The first division might be into porous membranes (with holes; deposition inside) and (arrays of) pillars/wires (deposition on the outside surface). Note that for example biological microtubuli [113] or other tubes (e.g. carbon NTs) can serve as both (deposition inside/outside). There are other suitable bio-templates such as viruses (Tobacco mosaic virus [114]), but in most cases membranes with arrays of pores are preferred (easier processing and manipulation of larger amount of structures). These include porous alumina, mica, and track-etched polymeric templates – PolyCarbonate (PC), PolyEthylene Terephthalate (PET) or even Kapton (chemically resistant – difficult to dissolve). In this work we use both most common types of porous templates – (nano)porous polycarbonate [115] and alumina [116]; both are further discussed in methods section 4.1. The preparation of polycarbonate templates is also discussed in methods section 4.4.1.

Below we provide more information on nanotube and core-shell nanostructure preparation. Other information on the fabrication can be found in references [117–119].

3.4.1 Lithography

Top-down approaches, e.g. based on electron-beam lithography together with sputtering or evaporation of a magnetic material, provide only tubes with small aspect

ratios (short tubes with large diameters). One should rather speak about rings as the length (given by thickness of a film being patterned by the lithography) is of the same order as the diameter. In addition, both diameter and tube wall thickness is limited to larger values (resolution limit of the lithography), therefore so far the process could not be down-scaled. Moreover, the deposition can be rather long and expensive and cannot deliver such a high amount of NTs as bottom-up techniques. To give an example: Huang et al. [120] prepared short permalloy tubes with diameter of 300 nm, tube wall thickness 20 nm, and height 160-600 nm using electron-beam lithography together with ion-beam milling.

3.4.2 Electrodeposition

Electroplating in porous templates can yield tubes with diameters as small as 25 nm [121] based on porous working electrode [122, 123], modified template pore walls [124] or other particular conditions (pH, current density, over-potential). The material is of high quality, even single crystals can be obtained [80], but wire-vs-tube growth instabilities occur [125]. In addition, in some depositions, the tubes become thicker during the growth and they eventually transform into solid wires as their length increases. One can prepare conductive deposits: pure metals and alloys. Semiconductors can be prepared as well, insulators (oxides) only after post-processing.

The problem with obtaining both NWs and NTs upon electrodeposition in cylindrical nanopores can be overcome to some extent by using a template with tubular nanoholes - these can be prepared e.g. by deposition and controlled shrinking of polymeric NWs inside porous alumina [126]. Such approach offers better control over the tube wall thickness, but it cannot be applied to very high aspect ratio structures as the inner polymeric wire would collapse and block the pore.

More information with references are in the methods section 4.2, results of our electroplating are discussed in sections 7.1 and 7.2.

3.4.3 Electroless deposition

Electroless plating of magnetic (nano)tubes [127–129] provides good control over the tube thickness [130], diameters down to 100 nm using porous templates [19] and 50 nm in case of biotemplates [113]. Various materials can be deposited, oxides, magnetic and non-magnetic metals. Similar to atomic layer deposition (below) the growth can be conformal and even high aspect ratio pores can be filled. The technique is also suitable for deposition of multilayers [31], which we demonstrate in

chapter 11. More details on the plating process are mentioned in section 4.4. Most of the tubes we investigate in our work are fabricated using this deposition method.

3.4.4 Atomic layer deposition

Atomic layer deposition (ALD) [96, 131] provides a great control over the tube wall thickness, but the resulting material, in most cases oxide, is quite granular and magnetically imperfect [23]. One can deposit a huge variety of different materials [132], including also rather pure metals and especially transition metals such as Fe, Co, Ni, and Cu [133]. To the best of our knowledge so far only ferromagnetic oxides that were reduced after the deposition (or as an additional ALD cycle) [96], have been used for the magnetic nanotube preparation by ALD. Maybe the above-mentioned metal deposition, using molecular hydrogen as a precursor, could provide better materials from the magnetic point of view. Yet, there could be some issues, we are not aware of, that prohibit such depositions in very high-aspect ratio pores as even more recent works still deal with ferromagnets prepared either by reduction of ALD oxides [134, 135], or the oxides (e.g. iron oxides) are studied directly [82, 84]. Conformal deposition of iron oxides was also utilized to prepare tubes with varying diameters [28] (i.e. with protrusions and constrictions), similar to recent works on cylindrical NWs where these modulations are intended to created pinning sites for DWs.

3.4.5 Sol-gel and similar chemical methods

Sol-gel depositions commonly results in deposition of complex compounds that needs to be further processed (thermal treatment, typically few hundreds of °C) to form oxides and eventually, e.g. after reduction in hydrogen atmosphere, ferromagnetic metals. In this way, Fe [136], Ni or CoFe [137] NTs were deposited. The preparation of solutions is in general more complex than in case of electroplating and even than electroless baths. On the other hand, higher aspect ratio structures were prepared (up to aspect ratio 1000 and diameters down to 50 nm). In addition, some of the prepared complex oxides can be very interesting - multiferroic and antiferromagnetic compounds can be synthesised as will be mentioned in section 3.5 below.

3.4.6 Other methods

There are many other ways how to obtain NTs. We have already mentioned physical (but can be also chemical) deposition on vertical pillars [79]. One may also prepare tube-like structures or Swiss-rolls by rolling strained thin sheets (micrometric diameters) [138, 139] using lithography and strain engineering. Further it is

possible to exploit Kirkendall-Based route [140], hydrothermal approaches, thermal decomposition - these and other methods can be found in a review [118].

3.5 Core-shell structures

Aside from simple tubes, multilayered tubes and core-shell NWs are of significant interest: the combination of different materials and geometry provides better control over the magnetic properties as well as effects exploited in planar (2D) spintronics (also other fields, but here we restrict ourselves to magnetism). These include often combination of magnetic and non-magnetic layers (both electrical conductors and insulators) for Giant MagnetoResistance (GMR), spin-valves, etc. One can also think about the combination of ferromagnets and heavy metals such as platinum for Spin Hall Effect and/or Dzyaloshinskii–Moriya interaction.

Similar to nanotube fabrication, there are two main fabrication routes: coating (sputter-deposition, evaporation, ...) of vertical pillars (commonly grown by Vapour-Liquid-Solid deposition using catalyst particles) and deposition in porous templates combining chemical methods.

The former method is rather simple and enables fabrication of very nice structures such as core-shell nanowire spin valves [37], CoO (10 nm)/Co (5 nm)/Cu (5 nm)/Co (5 nm), deposited through sputter deposition around the chemical vapour-deposited Ni NWs. These core-shell wire exhibited a giant magnetoresistance effect of 9%, comparable to the same multilayers in the form of a planar film. Vertical and fully 3D core-shell nanostructures can be grown also by Focused Electron Beam Induced Deposition (FEBID), such as Co-C NWs with Pt shell [141].

Examples using the later approach, combination of chemical methods follow:

- sequential electrochemical steps
  Co/NiO/Ni (inner tube) [142]; Ni shell + Cu core [143]
- electrochemical and atomic layer deposition
  Fe_3O_4 (ALD shell)/SiO_2/Ni (electroplated core) [23, 144]
- electroless plating
  Ni/Co and Ni/CoNiFe multilayered tubes [31]
  Ni shell deposited on Cu nanowires in solution [145]
- sol–gel and electrochemical deposition
  $FeTiO_3$ (antiferromagnetic shell) + Ni or $Ni_{80}Fe_{20}$ core [146]
  $BiFe_{0.95}Co_{0.05}O_3$ (multiferroic shell) + permalloy core [147]
  Cr_2O_3 (antiferromagnetic shell) + Ni or Fe core [148]
- electrochemical co-deposition with phase separation
  Ni shell + Cu core [149–151]

Core-shell NWs, also with (rather short) segments from different materials can be prepared by a so-called coaxial lithography presented by Ozel and coworkers [152]. This approach combines chemical depositions with many steps and can be thus quite tedious, still very nice results can be obtained.

To conclude, multilayered nanotubes (and/or core-shell nanowires) can be prepared by several different techniques, mostly by combination of (bottom-up) chemical methods in porous templates. Many interesting heterostructures have been prepared, but in most cases no magnetic characterization has been performed, except for magnetometry on arrays of structures. The only exception (aside from the tubular spin valve), to the best of our knowledge, is a pioneering work by Kimling and coworkers [23]: single core-shell NWs, where two magnetic layers were separated by SiO_2 spacer, were investigated using polarized synchrotron X-rays, utilizing so-called shadow X-ray Magnetic Circular Dichroism Photo-Emission Electron Microscopy (XMCD-PEEM, for information on the technique see section 5.1.1 or [153]). The stack of layers consisted of $Fe_3O_4/SiO_2/Ni$. Unfortunately, the iron oxide shell prepared by ALD had inhomogeneous magnetization due to the granular structure of the material.

In our work we also touched the issue of multilayers tubes (even with a non-magnetic spacer), this time prepared by electroless plating that yields high-quality nanocrystalline materials. We probed the tubes with the shadow XMCD-PEEM. The results of our investigation are summarized in chapter 11.

3.6 Wire-tube nanoelements

One of the possibilities how to modify the magnetic properties and energy landscape for DWs is to alternate wire and tube segments in a single nanostructure (Fig. 3.7). Such structures have been considered in simulations and first trials for their experimental fabrication exist as will be detailed below. During our nanotube electroplating trials we obtained such nanostructures with multiple wire and tube segment with a sharp transition (section 7.2.1) and longer tubular segments than reported in the literature. Further, we also tried to investigate them with electron holography and other magnetic microscopies.

Fig. 3.7: Scheme of a nanostructure with alternating wire and tube segments.

3.6.1 Fabrication of wire-tube elements

In principle it is possible to fabricate tube-wire elements in a controlled manner with defined lengths of the segments, however such deposition process is extremely challenging and has not been fully realized. Summary of the relevant literature is given below.

One can produce such structures by coaxial lithography [152], but it is quite time consuming as many fabrication steps are needed; further the length of the segments is limited (probably max few µm, much shorter segments have been realized).

Philippe and Michler [29] presented a theoretical kinetic model for electrodeposition of tubes, wires and even wire-tube elements. They supported the model with experimental deposition of Co nanostructures in porous alumina and found very good agreement. In the other words, they could model and later fabricate desired nanostructure based on pH, applied potential and initial pore diameter. However, even in their model they showed that the tube wall thickness increases with the deposition time, i.e. as the length of the tubes growths, tubes transform into solid wires. Therefore this limits the tube length in their process to few microns. Still their work is outstanding as many works dealing with nanotube fabrication are based just on a "black magic" or trial and error approach. Further on, they could fabricate wire-tube nanostructures with a defined periodicity of the segments by sweeping the deposition potential, however experimental realization included segments with diameter of 60 nm and length of only ≤ 30 nm. Still using their model, it might be possible to realize longer segments, at least for large diameter structures. Note that no magnetic characterization was performed in their work.

Arshad [154] fabricated tube-wire Co-Pt nanostructure (diameter 200 nm) by electroplating, where the growth started as a tube (thickness 30 nm) and after 1 µm it continued with the wire segment (1-19 µm depending on the plating duration). The transition was rather continuous, i.e. not sharp and only one tube-wire segment was realized. On the other hand, at least global magnetometry measurement on arrays of these structures was carried out (or better to say arrays containing also such structures), yielding angular dependence of the coercivity.

3.6.2 Numerical simulations of wire-tube elements

Theoretical and numerical study started with consideration of one wire-tube transition and investigation of coercivity and magnetization reversal of such structure with magnetic field [155] and later also electrical current [156]. Soon the modelled structure was extended to more segments: wire-tube-wire (we called it twire) or tube-wire-tube (wube). Here the DW nucleation and motion was studied by Monte Carlo simulations, also considering segments from different materials (Ni, Co) [30].

Further work included simulations of coercivity and remanence as a function of geometry [157], later extended to full hysteresis loops and angular dependence of magnetic properties [158].

All previously mentioned works focused on isolated tubes; later magnetostatic interactions between wire-tube nanostructures were considered – numerically for a hexagonal "array" of 7 nanostructures [159] and analytically for two elements [160].

Part II

Methods & Instrumentation

In this part we will rather briefly cover techniques used in experiments and numerical simulations. Experiments involve fabrication of samples, magnetic nanotubes, by bottom-up (electro)chemical methods using porous templates. Further, we cover their experimental investigation using a variety of techniques for structural and magnetic characterization. Finally, we describe micromagnetic simulations of magnetization in tubes as well as numerical modelling of contrast obtained by magnetic microscopies, both for comparison and easier interpretation of the experimental images.

4 FABRICATION

In this section we will briefly cover the main electrochemical methods used for NT synthesis – electroplating and electroless plating. Further, we will mention templates used in order to get nanostructures of defined diameter (and length in case of electroless deposition). Last but not least, we feature atomic layer deposition, used mainly for the template processing and partially also protection of the synthesised NTs.

4.1 Templates

In order to obtain nanostructures of well-defined shape, we used templates with cylindrical holes (pores); namely we employed nanoporous alumina (mostly for electroplating) and porous track-etched polycarbonate (see Fig. 4.1). Both lab-made and commercial templates were employed. Alumina membranes were fabricated by the classical two-step anodization process [116] either by the author, or Laurent Cagnon. We utilized also commercial templates from SmartMembranes. Polycarbonate templates were used mainly for electroless plating and they will be further described in section 4.4.1. A brief summary of some advantages and drawback of both template types is given below after few words on fabrication of templates.

4.1.1 Fabrication of templates

Nanoporous alumina is prepared by electrochemical anodic oxidation of high purity Al sheets (best annealed with low roughness – mechanically and electrochemically polished) in acidic solutions. Under certain conditions (acid, concentration/pH, applied voltage) aluminium oxide with hexagonally ordered straight nanoholes can be obtained directed by the hydrogen evolution, volume expansion of the oxide and related stress and electrical field strength. Ordering can be improved by a patterning the Al substrate or by Al reanodization after etching out the previously formed layer. It also improves with the anodizing time: the initial layer is disordered (and pore might be branched – see Fig. 7.7) as the pores nucleate at local defects and only after certain time (pore length) the self-ordering is achieved. The pore diameter and spacing is almost linearly proportional to the applied voltage and the diameter can be adjusted by chemical etching or atomic layer deposition of alumina inside the pores. Thickness of the membrane can range from hundreds of nanometres to tens of micrometres depending on the anodization time and the Al substrate. Voltage can be changed during the growth leading to diameter modulations of the pores. By a particular substrate patterning one can also get pores with triangular, rectangular

cross-section, provided that they are not too long (otherwise more natural cylindrical pores are recovered). More info can be found in book *Nanoporous alumina* [161].

Fabrication of polycarbonate templates is further discussed in section 4.4.1. Therefore, we mention here only the basic principle. Accelerated high energy ions (particles) are passed through a polycarbonate sheet (thickness typical in micrometers). Ion tracks through the material make it less chemically resistant. Therefore, upon immersion of such treated sheet into strong basis (NaOH, KOH), one can etch pores. The pore size depends on the nature of the ions and their energy, etchant, and the etching time. Pore density is proportional to the fluence of ions and its is in most cases lower than for as prepared alumina membranes. Usually, a wide beam of ions from a laboratory source is not perfectly collimated (typical irradiated surface area is at least several cm^2) which leads to pores that are not straight and that do not point in the same direction. Higher quality templates can be obtained exploiting ions from large scale ion/particle accelerators.

Porous alumina vs ion track-etched polycarbonate

Polycarbonate membranes can be very easily and rapidly dissolved in e.g. dichloromethane (within seconds). Such solvent does not oxidize the fabricated magnetic nanostructures. From our experience it is also easier to obtain cleaner sample using these templates, i.e. with smaller amount of impurities coming mainly from template dissolution residues. This is of particular importance for synchrotron experiments performed under ultra-high vacuum and high voltage applied between the sample and microscope objective (such as in X-ray photoemission electron microscopy). Further, preparation and handling of membranes with thickness of several microns does not rise a significant problem. The main drawback is a small temperature stability window – this limits processing and measurement of NTs that are still in the template. Further, especially commercial membranes have a quite rough surface that translates into poor surface quality of the deposited nanostructures. In addition, other defects can occur: pores are not straight and sometimes intersect other pores.

The main advantage of nanoporous alumina is the hexagonally-ordered array of straight pores and possibility to engineer the template parameters: both diameter and pore spacing (pitch) can be controlled and adjusted almost independently. In addition, one can have pores with different diameters along their length which also translates into deposited nanotubes/nanowires. In particular, one can create diameter modulations, protrusions, and constrictions in order to tune the magnetic properties and create nucleation and pinning sites for magnetic domain walls. Filled alumina membranes can withstand a wide range of temperatures from liquid helium

magnetometry on tube array up to annealing of structures in the membrane. As a ceramics, alumina is more sturdy (higher hardness), but also fragile, specially with thickness of several microns. The biggest drawback is that due to its chemical resistance it can be dissolved only in strong acids and basis. In most cases, these attack the deposited magnetic nanostructures (oxidation if not dissolution), also in general the dissolution takes a longer time (typically from tens of minutes to several hours). Therefore, a special care or additional protective layers are needed, in particular for thin-walled NTs.

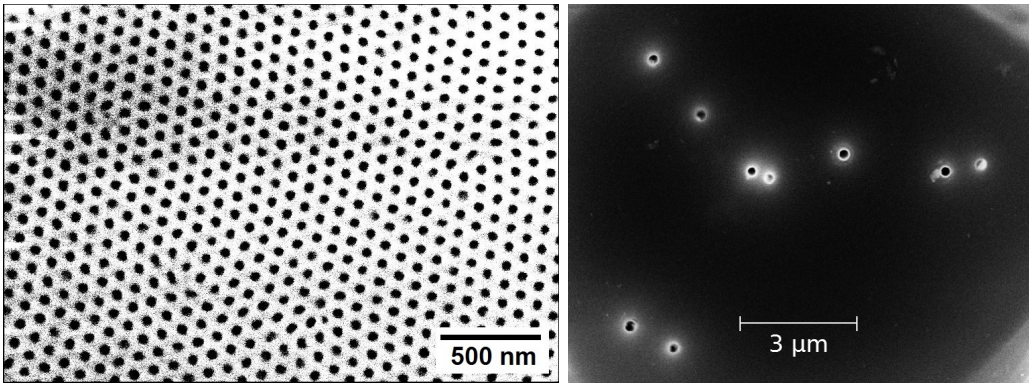

(a) porous alumina (b) porous polycarbonate

Fig. 4.1: Scanning electron microscopy images of nanoporous membranes (top view). (a) Nanoporous alumina (bare, empty), (b) porous polycarbonate membrane (already filled with tubes; otherwise the contrast is rather poor).

4.2 Electrodeposition

An electrochemical cell for the electroplating of metallic layers consists of at least two conductors, e.g. sheets of metal, immersed in a electrolyte – ionic conductor. An example of such an electrolyte is a solution or melt of a metallic salt plus some additives. By applying a voltage across these two electrodes it is possible to shift the Fermi level of electrons in electrodes, i.e. the electrochemical potential $\overline{\mu}$, and reduce metal cations from the electrolyte at the surface of negatively biased electrode – so called cathode. Commonly, a three-electrode electrochemical cell is used. The electrode where the desired reaction, reduction, takes place is named working electrode (WE), the second one counter electrode (CE, here anode). The CE is usually from a chemically inert material such as platinum, which prevents unwanted interference with the desired reaction. A complementary redox reaction, oxidation, takes place at the CE. The third electrode, reference electrode (RE), serves as a

reference for measurement of the WE electrical potential. For more information on electroplating and electrochemistry in general consult references [162, 163].

To get cylindrical nanostructures we used nanoporous alumina templates. The template itself is (and needs to be) an electrical insulator. The bottom side of the template (with more ordered pores) is covered with an evaporated Au layer (with a 3-5 nm thick Ti seed layer) that serves as the WE. Therefore, the nanostructures grow from the bottom. Typically electroplating in such pores covered with thick compact electrode yields solid nanowires. To promote the tube growth, the Au layer is so thin (with respect to the pore diameter) that it does not completely cover the pore opening [122, 123]. I.e. at the pore extremity it forms an annulus and not a solid disk. The Au side of the template is attached to a larger Cu plate, contact being made with an Agar silver paint (AGG302, Agar Scientific). Unwanted deposition of metals is avoided by covering other areas with chemically-resistant insulating tape (e.g. Kapton; non-conductive resin can be applied as well). For the electrochemical cell setup and scheme of the working electrode see Figure 4.2.

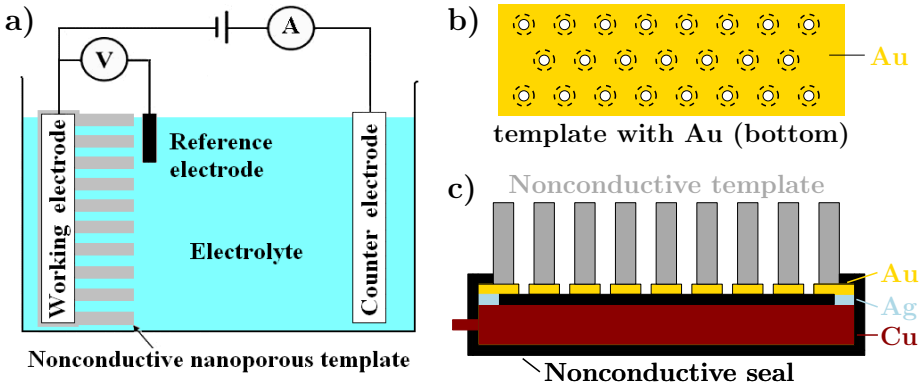

Fig. 4.2: Electroplating of tubes in nanopores. a) Scheme of an electrochemical cell for plating in nanopores. The only contact of a plating solution with the working electrode should be through the pores. This requires either electrical insulation of the rest of the electrode, or exposition of only one side of the electrode. Otherwise a film would be deposited on the backside of the electrode. b) Bottom view of a porous template covered with thin layer of Au serving. Dashed circles show the pore position. Therefore, there pores are not completely closed with the Au layer (there is Au annulus instead of disk at the bottom of each pore). c) Scheme of the template attached to Cu macro-electrode.

All our depositions were conducted at ambient conditions and room temperature. As the external current source we used a VersaSTAT 3 potentiostat (Princeton Applied Research), the electrodes are summarized below:

- **working electrode**: porous Au layer at the bottom of a nanoporous template (alumina, polycarbonate),
- **counter electrode**: platinum mesh (higher surface area than the working electrode),
- **reference electrode**: saturated calomel electrode (SCE).

Further details will be given in the following sub-sections dealing with particular depositions. We will focus only on the depositions that are discussed in the results section: preparation of NiCo NTs (section 7.1) and Ni wire-tubes (section 7.2.1). Aside from these, we also tried Ni/Cu co-deposition with phase separation (Ni shell and Cu core) [129] and electrodeposition of Ni tubes via current pulses [164], but in these cases, we obtained at best only few poor tubes with high roughness. Last but not least, we tested also NiFe NT plating according to Zhang [165], but we obtained nanowires instead of nanotubes.

4.2.1 Ni wire-tube elements

Similar to Proenca's work [123] we used a nanoporous alumina template; in our case commercial SmartPor50 (SmartMembranes) with pore diameter around 50 nm. However, several slight changes were employed. First, we evaporated 50 nm of Au (3 nm Ti seed layer) instead of 40 nm to serve as the porous working electrode. Further, the electrode was sealed at the bottom with a non-conductive tape instead of a resin (see Fig. 4.2). Without such a sealing the yield of tubes is smaller: first, the electrolyte can interact with the silver paint and decrease the adhesion and electrical contact with the underlying Cu macro-electrode. Second, the penetration of the electrolyte below the porous Au layer leads to deposition of continuous magnetic film that eventually closes the holes in the Au layer and may lead to deposition of solid wires instead of tubes. Electrical contact was made at the sample Au electrode edges with the silver paint. The deposition was conducted at room temperature (instead of 35°C) at -1.55 V vs SCE for 20 min without any stirring (instead of 250 RPM). The electrolyte, Watts bath, consisted of 1.14 M $NiSO_4$, 0.19 M $NiCl_2$, and 0.73 M H_3BO_3. Note that Proenca reported only deposition of nanowires, or nanotubes, i.e. no wire-tube elements.

4.2.2 NiCo nanotubes

We tried CoNi NT electrodeposition following the work by Zhang [166]. We used a lab-made nanoporous alumina template with the pore diameter 80-90 nm. We deposited a thin porous electrode (3 nm Ti + 10 nm Au) on the bottom side of the template by electron beam evaporator. Further, we sealed the bottom of the porous

electrode with Kapton tape. The electroplating was conducted at room temperature, −2.0 V vs SCE for 30 min. We used a fresh electrolyte with pH 2.5 with the following composition: 0.05 M $CoSO_4$, 0.05 M $NiSO_4$, and 0.1 M H_3BO_3.

4.3 Atomic layer deposition

Atomic Layer Deposition (ALD) [131, 132] was used for deposition of thin oxide layers, mainly AlO_x and HfO_x, serving as a mechanical reinforcement of NTs, a protective layer, and as a non-magnetic spacer in trials for deposition of multilayered tubes. Further, we used it also for the reduction of the pore diameter of the alumina templates. We utilized Savannah ALD (Cambridge NanoTech). Note that most of our tubes were without protective ALD coating as our main investigation method is based on emission of photoelectrons from the sample surface and additional non-conductive layer can decrease their yield and lead to electric charging effects.

4.4 Electroless plating

Electroless plating (autocatalytic deposition) relies on the reduction of metallic ions from the liquid electrolyte by means of a reducing agent – chemical substance providing electrons for the reduction. Unlike in electroplating, no external current source is needed and samples do not have to be electrically conductive. Therefore, almost any surface can be coated, even though some (e.g. non-conductive ones) may have to be chemically modified – using so called sensitization and activation procedures described below. Further, the deposition is conformal like in case of atomic layer deposition and high-aspect ratio structures (pillars, nanopores) can be covered with the deposit. A large variety of materials can be deposited: metals, alloys, metalloids, oxides, ... Being based on a rather simple "beaker" chemistry and owing to its versatility, the technique is used in industry, particularly in microelectronics. Further information on electroless plating can be found in references [162, 167, 168].

The choice of the reducing agent depends on the metal to be plated as well as on the chemical resistance of the substrate. Many reducing agents contain boron (e.g. dimethylamino borane – our case) or phosphorous (sodium hypophosphite). A portion (from few to tens of percent) of these elements is incorporated in the deposit and by changing their content, many material properties can be influenced (grain size, electrical conductivity, hardness, ...). Amount of B (P) depends on the deposition process, mainly on the pH and reducing agent concentration. Almost pure metals can be obtained using hydrazine or formaldehyde.

The method has been also employed for magnetic (nano)tube fabrication [127–129]. The technique provides good control over the tube thickness [130] (proportional to the plating time), diameters down to 100 nm using porous templates [19] and 50 nm in case of biotemplates [113]. The grain size of the deposit can be decreased upon increase of the B or P content ([169], p. 122).

We used tubes prepared by this method in most of our experiments. First we relied on a supply of tubes from Sandra Schaefer in TU Darmstadt (samples labelled with SS, consult Tab. 4.1), later we fabricated also our own NTs following the same procedure.

Tab. 4.1: Survey of electroless-deposited samples from TU Darmstadt. Only samples used in our work are featured.

Sample	Diameter	Length	Description
SS53	300 nm	≤30 µm	CoNiB tubes
SS123	390 nm	≤30 µm	NiFeB tubes
SS124	150 nm	≤10 µm	CoNiB tubes
SS125	100 nm	≤10 µm	CoNiB tubes
SS126	80 nm	≤10 µm	CoNiB tubes
SS147	400 nm	≤20 µm	multilayered tubes: NiFeB/(Pd)/CoNiB
SS148	400 nm	≤20 µm	multilayered tubes: NiFeB/SnO_x/CoNiB

4.4.1 Templates

As a shape-giving template, ion-track etched polycarbonate membranes were used. The track formation and track etching process is explained in literature [115]. For all the samples denotated with **SS** (fabricated by Sandra Schaefer) lab-made templates were prepared as follows. A polycarbonate foil (Pokalon from LOFO, High Tech Film GmbH) was irradiated with Au^{26+} ions at the GSI Helmholtzzentrum für Schwerionenforschung GmbH (Darmstadt). An example of irradiation parameters for 300 nm pore diameter follows: fluence 10^7 ions/cm^2; kinetic energy of the projectile 11.4 MeV per nucleon. The latent ion tracks were etched out at 50°C in a 6M stirred sodium hydroxide solution. The etching time was adjusted depending on the desired pore diameter, 11 min were used for pore size around 300 nm (sample SS53). The as-prepared templates with cylindrical pores were washed with water and dried. The length of the tubes is determined by the template thickness (pore length); for smaller pore size (80-150 nm) we used mainly 10 µm-thick foils, whereas for larger pores (300-400 nm) we employed templates with thickness of 20 or even

30 µm. Thus, for smaller pores we used smaller template thickness as plating in higher aspect ratio pores is more challenging.

In some cases, we observed a narrowing of the pore diameter close to the template surfaces, which led to cigar shaped structures upon filling the template. This effect occurs when the irradiated polycarbonate film is not etched directly after irradiation, but after some time (months). Ageing results in partial "healing" of the polymer and modifications that are more pronounced close to the template surface. Modifications make the pore ends more resistant to the chemical etching resulting in narrower diameters.

For the samples synthesized at Institut Néel (see section 7.3), we used commercial templates Osmonics Poretics (K01CP01300) with the following characteristics: nominal pore diameter 0.1 µm, membrane thickness ≤ 7 µm, and $1.5 \cdot 10^8$ pores/cm^2. Such porosity is still rather large and may result in unwanted defects (e.g. intersecting pores).

One can also employ nanoporous alumina templates, the electroless plating procedure is basically the same as for polycarbonate (see below), except that at the beginning the pore walls are modified with e.g. 3-AminoPropylTriEthoxySilane (APTES) [129]. We successfully performed tests of such depositions, consult Fig. 7.7.

4.4.2 Fabrication procedure

The deposition of NTs inside porous polycarbonate membranes consists of several steps. First, the porous template is sensitized with a $SnCl_2$ solution (42 mM $SnCl_2$ and 71 mM trifluoroacetic acid in 1:1 methanol:water) and activated with a $PdCl_2$ solution (11.3 mM $PdCl_2$, 33.9 mM KCl) [127]. The goal of the activation procedure is to bind tiny Pd particles (less than few nm in size) on the pore walls that will catalyse the deposition of the desired material (metal). The procedure (sensitization follow by the activation) is repeated three times in order to obtain better surface coverage with the Pd particles (poor coverage could lead to holes and increase in roughness of the deposited layer). After the three cycles of sensitization (45 min first, then only 15 min each) plus activation (4 min each cycle), the template is washed with ethanol and water, then immersed in the electroless plating bath. The deposition takes place at room temperature. It starts at the pore walls on the catalytic Pd seed particles and continues radially towards the pore centre (Fig. 4.3). During the synthesis, hydrogen gas evolves at the template surface as a part of the deposition reaction. The composition of plating solutions for various materials (metals) is given below. In general, it consists of the metal source (metallic salt), reducing agent, and additives: pH buffers keeping the same (very similar) acidity/alkalinity of the solution; complexing agents – partially binding metallic ions and increasing

stability of the plating bath. In an unstable plating bath, the metal precipitates in the solution volume, instead of being preferentially deposited on the Pd-covered surface.

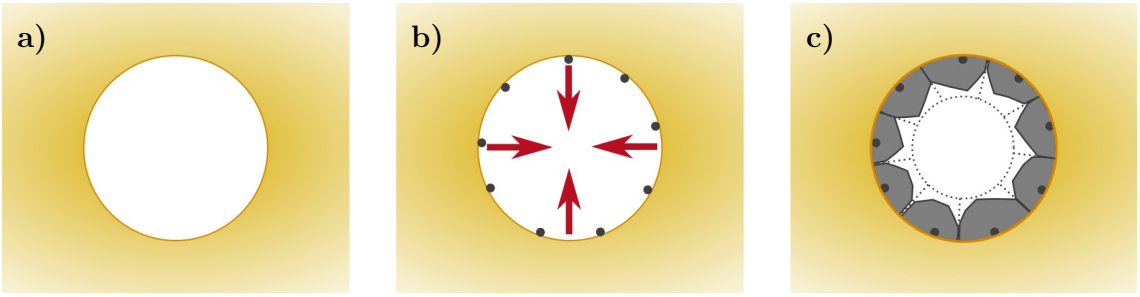

Fig. 4.3: Scheme of radial metal tube growth in a pore during the electroless plating. Cross-section of a cylindrical pore in the polycarbonate foil. a) Empty pore. b) Functionalized polymer surface with Pd seeds on the pore walls. The arrows show the growth direction of the desired metal (e.g. Co, Ni, Fe). c) Metal grows radially from the pore wall inwards. The final state is indicated by the dotted lines. Image courtesy of Sandra Schaefer.

CoNiB plating bath [127]

- metal source: 100 mM $NiSO_4 \cdot 7H_2O$, 30 mM $CoSO_4 \cdot 7H_2O$
- complexing agent+pH buffer: 100 mM trisodium citrate dihydrate
- reducing agent: 100 mM DiMethylAmine Borane (DMAB)

The solution seems to be stable even for weeks, but a decrease in the deposition rate is expected over time.

NiFeB plating bath

- metal source: 100 mM $NiSO_4 \cdot 7H_2O$, 30 mM $FeSO_4 \cdot 7H_2O$
- complexing agent+pH buffer: 100 mM trisodium citrate dihydrate
- reducing agent: 100 mM DMAB

SnO_x plating bath

- metal source: 100 mM $SnSO_4$
- reducing agent: 100 mM DMAB

Synthesis proceeds with a slightly different mechanism: so-called chemical bath deposition (no Pd or other seeds are needed). It results in deposition of tin oxide instead of the metal alone. It is similar to TiO_2 deposition already reported in [170]. The typical deposition rate is very low (1 nm/h), which on the other hand enables synthesis of conformal continuous films and better control over the thickness.

Cu plating bath [171]

- metal source: 30 mM $CuSO_4 \cdot 5H_2O$

- complexing agent: 35 mM EthyleneDiamineTetraacetic Acid (EDTA)
- pH buffer: 380 mM TriEthanolAmine (TEA)
- reducing agent: 100 mM DMAB

Despite EDTA being a strong complexing agent, the bath is not very stable and Cu precipitates in the solution within few hours, therefore a fresh solution should be used. Stability could be increased by increasing the EDTA concentration and it should also depend on the pH. Different recipes using formaldehyde or sodium borohydride as the reducing agent exist as well.

4.4.3 Multilayered tubes

Multilayered tubes were prepared by Sandra Schaefer (TU Darmstadt) using subsequent deposition of different layers. In general, one has to keep in mind that the chemistry used for the synthesis of a new layer may modify (or even attack) the previous layer(s), which may restrict the choice of materials.

We summarize the steps for fabrication of SS148 NiFeB/SnO_x/CoNiB trilayered tubes in Fig. 4.4.

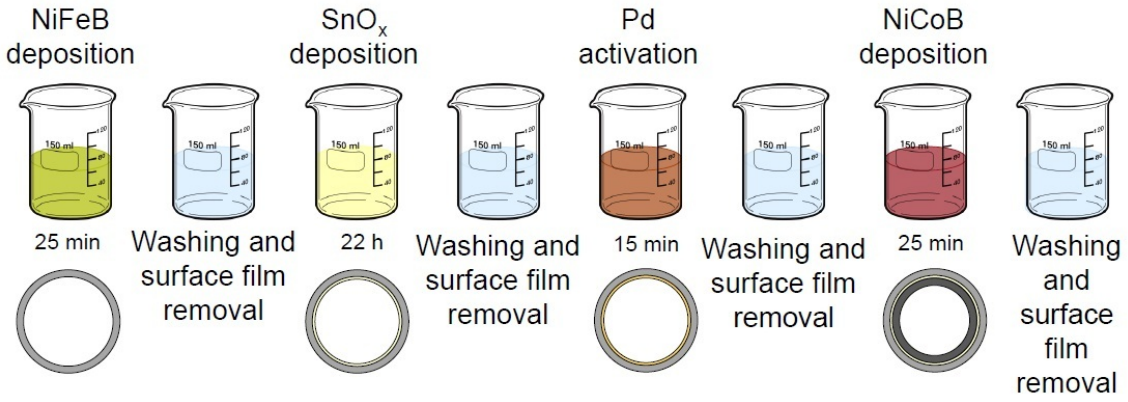

Fig. 4.4: Scheme of the preparation process for the multilayered tubes (here SS148 NiFeB/SnO_x/CoNiB). Porous membrane is first sensitized and activated ($3\times$) and subsequently it is immersed in different aqueous solutions. After deposition of each layer, film formed on top/bottom part of the membrane is removed by a gentle mechanical polishing. Image courtesy of Sandra Schaefer.

SS147 with a Pd spacer was prepared in a similar way, just the CoNiB deposition is longer (65 min as the deposition rate appeared to be lower) and the oxide spacer deposition is replaced by Pd plating procedure as follows:

Pd plating bath [172]

- metal source: 4 mM $PdCl_2$

- complexing agent+ligand: 38 mM pentane-2,4-dione (acetylacetonate), 47 mM 4-(DiMethylAmino)Pyridine (DMAP)
- reducing agent: 80 mM hydrazine monohydrate

The bath was heated to 50°C and the polycarbonate membrane with NiFeB tubes was immersed in the solution for 1 h. As the reaction rate seemed to be slow, the temperature was raised to 70°C and the deposition run for another 1 h.

4.5 Sample preparation for measurements

After the nanostructure deposition in templates, the template is washed with demineralized water and dried. The metallic film deposited on the top/bottom surfaces of the template is removed by a gentle mechanic polishing using a fine sand paper. For measurements requiring isolated tubes, the polycarbonate template is dissolved in dichloromethane and the tubes are rinsed several times (at least 3 times) with the same solvent. Alumina membranes are dissolved (as mentioned above) in 1 M sodium hydroxide and rinsed with water (3× or more) and then isopropyl alcohol (3× or more). Typically, a piece of a template with area of few mm^2 is immersed in 0.5 mL of the etchant. The insufficiently rinsed structures are later (after dispersion on a substrate)) covered with rest of the template dissolution process. Depending on the measurement technique, the tubes are dispersed either on a doped Si substrate with alignment marks (for XMCD-PEEM, magnetic force microscopy or magnetooptics with focused laser), or on a Cu grid with a thin lacey carbon film (for transmission electron microscopies and electron holography) or on a 100 nm-thick SiN membrane (for scanning transmission X-ray microscopy). For the dispersion, several µL are (repeatedly) transferred onto the substrate using a micropipette. For alignment of the tubes we insert a permanent magnet below the substrate with the field direction colinear with the airflow inside the hood. For a set of orthogonal tubes (Fig. 4.5b), the process is done twice with substrate rotation by 90° vs the magnet and in both cases with weak airflow 45° to the field direction. Images of the tubes on some of these substrates can be found in section 5.1.3.

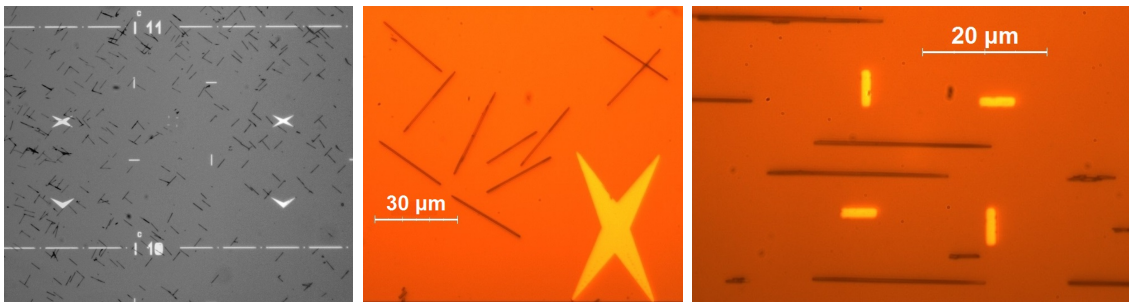

(a) (b) (c)

Fig. 4.5: Optical images of magnetic tubes dispersed on Si substrates with alignment marks. (a) overview of a substrate with two orthogonal sets of tubes, (b) detail of another area (rotated by 90°). (c) Another sample with tubes now all aligned along the same direction. Alignment of the tubes is promoted by a permanent magnet placed below the substrate during the dispersion of tubes from a solution.

5 CHARACTERIZATION

In this chapter we will describe shortly the techniques used for magnetic, structural, and topographical characterization of the samples. Aside from electron microscopy, related analytic techniques and electron holography, we cover synchrotron observations with circularly polarized X-ray beam, scanning probe microscopy, and magnetometry.

In the majority of the magnetic measurements the samples were AC demagnetized in a transverse direction (vs tube axis) before imaging. In case of VSM-SQUID sample was demagnetizated along the direction of field applied during acquisition of the hysteresis loops.

5.1 Synchrotron X-ray microscopies

For the determination of magnetization in our tubes we utilize mainly synchrotron-based magnetic microscopies relaying on X-ray Magnetic Circular Dichroism (XMCD), a difference in absorption for left and right circularly-polarized light. Aside from the helicity (circular polarization) of the photons (carrying thus angular momentum), the absorption depends on the sample magnetization with respect to the beam propagation direction. For iron group elements the effect is strong at the L_3 and L_2 absorption edges (See Fig. 5.1a).

The effect can be detected either in a direct transmission of photons (scanning or wide-field transmission X-ray microscopy) or via collection of photoelectrons (photoemission electron microscopy – PEEM) – see Fig. 5.2. The amount of created photoelectrons is assumed to be proportional to the absorbed photons (of sufficient energy). In case of very thin films, the photoelectron yield is proportional to the absorption, however, for thicker samples only a part of photoelectrons can leave the sample and contribute to the detected signal. In our experimental study we utilize mostly the X-PEEM technique.

The XMCD microscopies are element sensitive, in our work we focus on L_3 and L_2 absorption edges of transition metals forming our ferromagnetic tubes – mostly Co and Fe (Ni gives usually a weaker XMCD contrast even if the sample is Ni-rich due to the smaller number of holes in the absorption band). As the precise energy of the absorption edge can differ (even up to a few eV) from sample to sample (even among tubes on the same substrate) due to local environment of the probed atoms (e.g. degree of oxidation), one usually start with determining the edge energy via X-ray Absorption Spectroscopy (XAS). Further, there might be instrument (calibration) related energy shift. In XAS, the energy of the beam is scanned while we monitor the photon absorption (or photoelectron yield). In

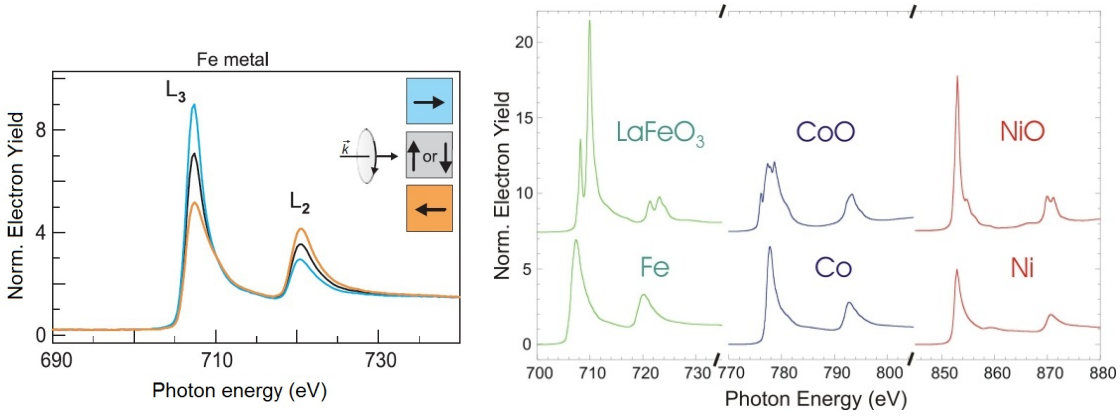

(a) XMCD

(b) XAS of Fe, Co, Ni, and some of their oxides

Fig. 5.1: X-ray absorption spectroscopy of iron group elements detected via photoelectron yield. (a) Demonstration of X-ray Magnetic Circular Dichroism: photon absorption depends on the magnetization direction in a sample with respect to the circularly polarized beam. The same is obtained for a fixed magnetization direction, while changing from a right to a left circularly-polarized beam. Only around the L-edges there is a significant difference in absorption reflecting magnetic configuration of the sample. Taken from [173]. (b) Example of a X-ray absorption spectroscopy for some pure 3d metals and some of their oxides. Source: [174].

Fig. 5.1b we see a textbook case of a spectrum for Fe, Co, Ni and their oxides. XAS is a very good measure of the sample quality as the oxidized sample has broader and multiple peaks, sometimes shifted in energy. More information on XMCD can be found in a review by Fisher & Ohldag [175] or book by Stöhr & Siegmann [173]. Below we will mention some aspects related to the particular XMCD microscopies.

5.1.1 X-ray PhotoEmission Electron Microscopy (X-PEEM)

In order to image magnetic domains and walls in the tubes (and also nanowires), we use X-ray Magnetic Circular Dichroism - PhotoEmission Electron Microscopy (XMCD-PEEM) [176, 177]. This photon-in, electron-out mostly surface-sensitive (but integrated volume information available as well in some cases, see below) and element-sensitive technique maps the component of magnetization parallel to the X-ray beam propagation direction. We use the so-called shadow geometry on isolated tubes dispersed on a doped Si substrate (Fig. 5.3), as pioneered by Kimling et al. [23] and further developed in our group [153].

The sample is irradiated with a monochromatic X-ray beam arriving 16° from the substrate plane, with illumination size of several tens of micrometers. Excited

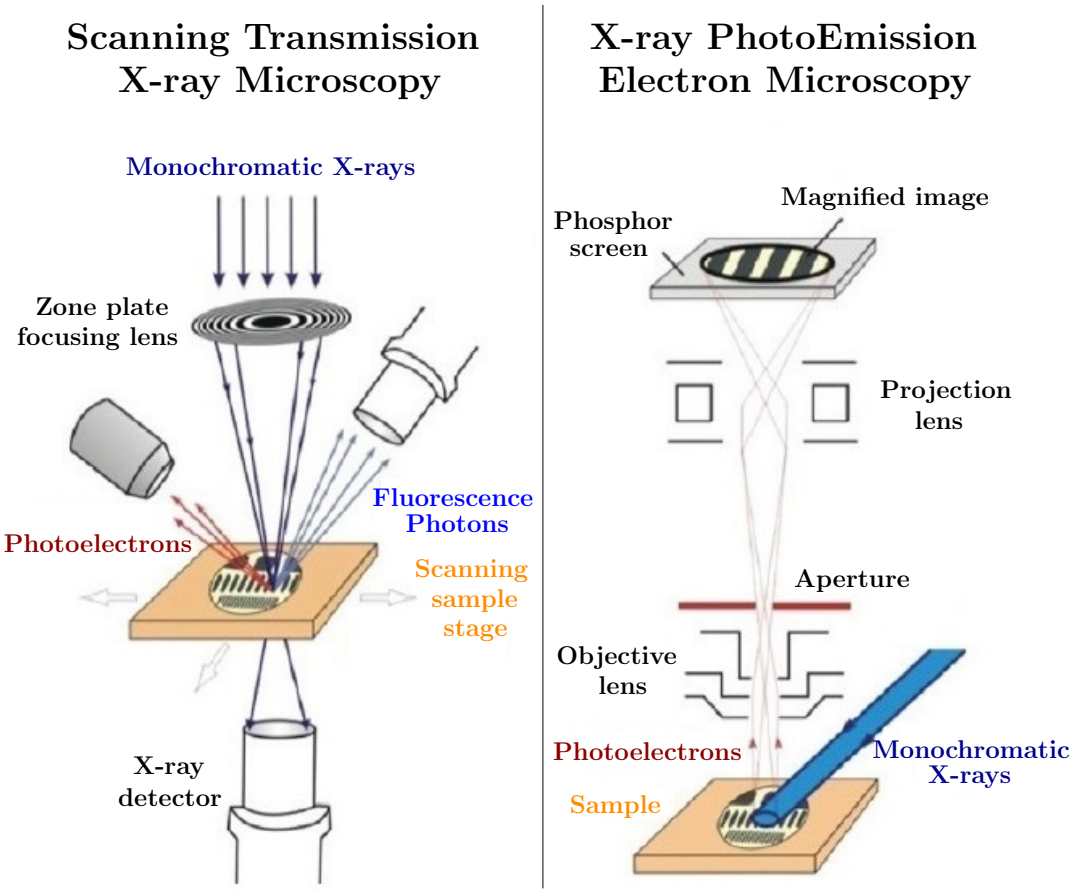

Fig. 5.2: Magnetic X-ray microscopies: Taken from [175] (original image is in [173]).

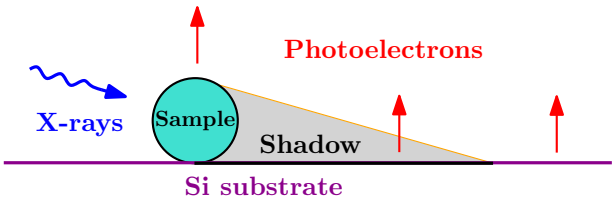

Fig. 5.3: Shadow XMCD-PEEM scheme. X-rays with energy matching the absorption edge of the sample (e.g. Co-L_3 for Co-rich sample) arrive 16° from the supporting Si substrate. The photons are absorbed and emit photoelectrons. This happens mainly at the sample (e.g. tube) surface (resonant absorption). Absorption of photons leads to creation of a geometrical shadow behind the sample. If the sample is not too thick (maximum few hundreds of nanometres depending on the material and X-ray energy), some photons are transmitted through the sample; these photons create additional photoelectrons upon being absorbed by the supporting substrate (non-resonant absorption) in the shadow area. Other parts of the substrate irradiated by the X-rays also emit photoelectrons (but smaller amount than the sample surface).

photoelectrons are collected by PEEM from both sample surface and the substrate, including area with a geometrical shadow behind the sample (created by X-rays only partially transmitted through the sample) [23]. To facilitate collection of the photoelectrons, the technique is implemented under ultra-high vacuum and there is a voltage difference of 20 kV between the sample and the microscope objective.

The energy of photons is tuned to the L_3 absorption edge of cobalt (around 778 eV) or Fe (around 708 eV) depending on the sample composition. An instructional X-PEEM image of CoNiB tubes on Si substrate taken with X-ray energy matching Co-L_3 edge can be found in Fig. 5.4.

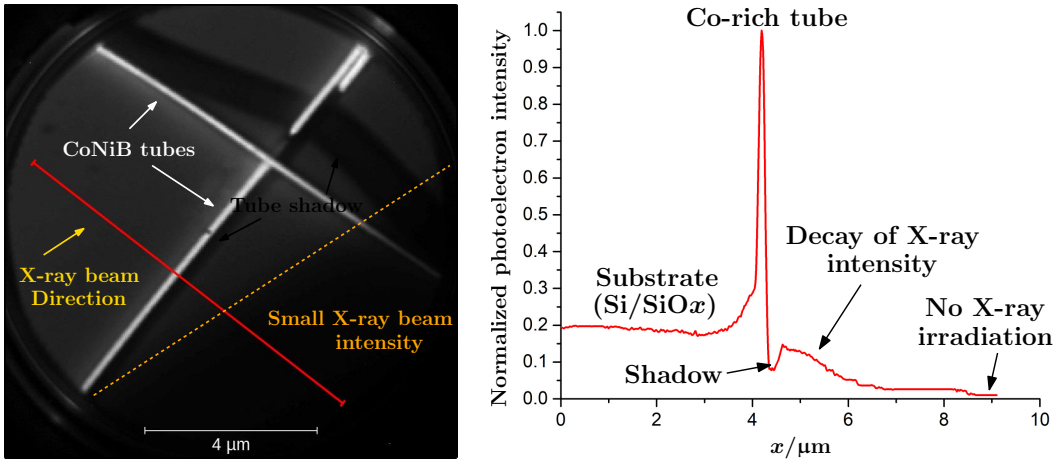

Fig. 5.4: X-PEEM image of partially irradiated sample with intensity line profile. X-ray photon energy tuned to Co-L_3 absorption edge. (a) X-PEEM image of Si substrate (+native SiO_x layer) with CoNiB tubes (bright) and their shadows. The bottom right part is irradiated with only few photons and thus the photoelectron intensity is also very low. (b) Line profile along the red solid line displayed in (a). The photoelectron yield is the highest on the tube, yet there is still significant intensity both from the substrate and the tube shadow area – compared to the almost non-irradiated area on the right.

Here only part of the sample is irradiated by the X-ray beam (for demonstration, otherwise the beam should be centred on the sample with rather homogeneous intensity), which leads to a small intensity and dark area in the bottom right part of the resulting image. This is done on purpose by a partial closure of beam exit slit and displacement of the beam spot on the sample. In the image, CoNiB tubes appear bright (resonant absorption of X-ray and thus large amount of created photoelectrons). Further, there is the shadow behind each tube – best visible in the top right part with a full shadow of a tube lying across (and on top of) another

tube. The shadow is brighter in its centre with confirms the hollow character of the tube. In most cases, a part of the shadow is obstructed by the tube (sample) itself. However, in principle tubes can be placed on a pre-patterned substrate (elevated non-magnetic pads, e.g. from Au) in order to recover the full shadow.

The photoelectron intensity profile along the red line is shown in Fig. 5.4b. The intensity is normalized to the maximum, obtained from the tube surface. Very important fact for our magnetic imaging (as will be discussed below) is that the photoelectron yield from the Si substrate is significant. Even-though the X-ray energy is tuned for Co-L_3 (around 778 eV), thus far away from both L and K edges of Si, the non-resonant absorption of X-rays and subsequent photoelectron emission gives about 20 % of photoelectron signal from the sample. In the geometrical shadow this value is clearly smaller, yet still non-negligible compared to the part of the sample (bottom-right) that is not irradiated by the X-rays. To the right of the tube (in the profile) the photoelectron yield decays due to smaller amount of incoming X-ray photons (partially closed slit). Note again that for the proper imaging the X-ray beam must be centred on the point of interest and the X-ray irradiation should be rather homogeneous across the whole region of interest (in such a case the photoelectron signal from the substrate can be slightly smaller with respect to the tube).

In order to obtain the magnetic information, 2 (sets of) X-PEEM images are acquired, one for each circular polarization of the X-ray beam. The XMCD magnetic image is obtained as normalized difference of these two:

$$\frac{I_{\circlearrowleft} - I_{\circlearrowright}}{I_{\circlearrowleft} + I_{\circlearrowright}}. \tag{5.1}$$

The resonant X-ray absorption of the sample (tube) depends on the polarization and magnetization direction with respect to the beam propagation direction. On the other hand, the absorption of X-rays by the Si substrate does not depend on the beam polarization. Thus in XMCD, the substrate does not contribute to the magnetic image and creates grey, non-magnetic background. However, there is one exception: the shadow area on the substrate. While the substrate is non-magnetic and its absorption of photons is independent of the beam polarization, the amount of created photoelectrons does depend on the intensity of incoming X-ray photons. And this amount of photons transmitted through the sample (tube) depends on the beam polarization – for one circular beam polarization more X-ray photons are absorbed and thus less photons will hit the substrate behind the tube, i.e. in the shadow area. Thus, the shadow reflects magnetic volumic information integrated along the photon path. Due to the integration, the interpretation of magnetic contrast in the shadow might not be as straight-forward as in the case of signal coming from

the tube surface. However, one can compare it with numerical modelling of the (shadow) XMCD-PEEM contrast that has been developed in our group [153]. Such modelling also enables in principle quantitative analysis of the images.

The XMCD-PEEM technique has a spatial resolution around 30-40 nm for the magnetic imaging (depends on sample and parameters). Note that in the shadow the resolution is improved up to a factor of 3.6 ($1/\sin 16°$) along the beam direction, because the shadow is stretched due to the small incidence angle of the beam. While XMCD-PEEM is basically surface-sensitive technique (photoelectrons have small energy and cannot escape from the sample/substrate volume), thanks to the shadow we can also (indirectly) obtain information on the magnetization in the volume of the sample, in particular when comparing experimental XMCD-PEEM images with numerical modelling for several micromagnetic configurations [153].

By tuning the focus point of the microscope (adjusting a current flowing through the objective lenses) and by optimizing a so-called start voltage (STV, an additional voltage bias applied to the sample which determines the kinetic energy of the collected photoelectrons) one can focus either on the tube surface, shadow, or a comprise of both (depends also on the geometry – for larger tube diameter the intermediate focus will not be as good as clear focus on either tube, or the shadow). Further information can be found in reference [153].

Typically, for one resulting XMCD-PEEM image, 30-60 images are acquired for both circular polarizations of the beam with acquisition time of few seconds for each image in order to improve the signal to noise ratio. Stack of images for the same polarization are drift-corrected, co-added (averaged), and finally two obtained images (one for each polarization) are again drift-corrected and the XMCD image is calculated as their normalized difference. The amount of averaged images and the acquisition time is a compromise between high signal-to-noise ratio, low resulting image blurring caused by sample drift (mainly mechanical) and total time needed for the acquisition of images. The experiments were performed at the Nanospectroscopy (synchrotron Elettra) and HERMES (synchrotron SOLEIL) beamlines.

Annealing

The in-situ annealing was performed at Elettra under ultra-high vacuum, however in a chamber distinct from the X-PEEM microscope chamber (preparatory chamber connected to the PEEM). We ramped the temperature to the desired value, keeping it at least for 30 min (except for 300°C – only 10 min), and then we cooled the sample down to room temperature. The annealing was repeated several times with gradual increase in the target annealing temperature. The imaging was performed after each annealing step. The temperature control was not very precise as we used a small

current-heated filament in the cartridge at the back of the sample. The temperature was estimated based on previous and similar filament heating experiments, and on a comparison with annealing of twin samples in a more controlled environment. This implies an uncertainty of ±50°C.

Application of magnetic field

Magnetic field was applied using a dedicated sample cartridge with a coil fitted in the cartridge below the sample. The coil is powered by an external current source that enable either continuous operation or current pulses of duration in ms or longer. The field direction is always perpendicular to the X-ray beam due to the sample holder construction. During our first experiments with this setup, the magnetization of the sample could be switched with extremely low field values ($< 0.1\,\mathrm{mT}$). A detailed inspection and testing revealed that the problem was in the current source supplying current for the coil and the way it had been programmed. As the current source was not bi-directional, one had to switch the current leads to apply field in the opposite direction. For this, the source was turned off as well as the high-voltage rack (remind: there is 20 kV between sample and the objective lenses of the microscope). After turning the source on again, during initialization, there was a current spike of about 5 A (producing field around 100 mT) (see Fig. 5.5). Therefore, this spike reversed the magnetization in the sample (magnetic NTs), the desired fields values applied afterwards had thus no effect on the sample. The effect of this spike on azimuthal magnetic domains in tubes is discussed in section 11.2.2.

The spike was later suppressed by reprogramming the supply by the beamline scientists and reliable imaging after application of magnetic field (for 0.5 s or longer) or even in the magnetic field could be conducted. In the results section (experimental results) we will state whether spike or just DC field was applied.

We also performed imaging under applied magnetic field. In this case, the collected photoelectrons and thus the obtained image was affected by the field. Typically upon increasing the field (in 1 mT steps) the field of view moved. We tried to compensate this by introducing additional electron beam shift, tuning stigmator coils, STV, etc. Both field and tweaking of the settings led to decrease of the signal/noise and deterioration of the spatial resolution. Later we found out that it was sufficient to adjust excitation of the main objective lenses.

5.1.2 Scanning Transmission X-ray Microscopy (STXM)

This technique relies on the transmission of X-rays through a thin sample that must be placed on a thin, X-ray transparent substrate (in our case 100 nm-thick SiN membrane). The X-ray beam is focused by diffractive Fresnel zone plate optics to a

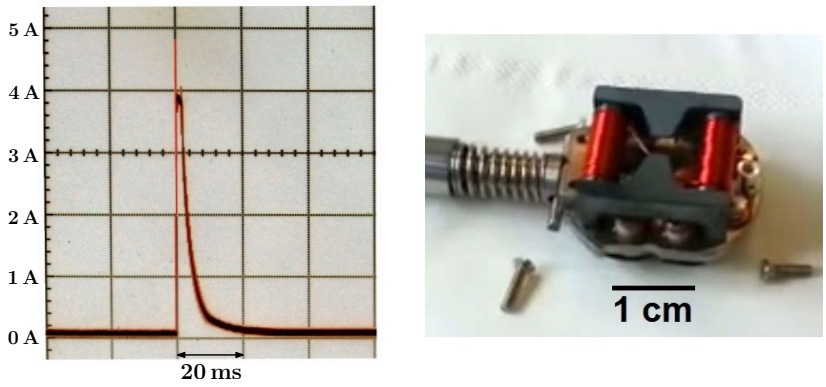

(a) current spike (b) field cartridge

Fig. 5.5: X-PEEM field cartridge: current spike during electromagnet initialization. (a) Current spike before setting the desired current for the coil producing field in XMCD-PEEM experiments. Photo courtesy of Andrea Locatelli. (b) Photo of the custom designed X-PEEM cartridge (Nanospectroscopy beamline, Elettra) with coil windings. The sample is inserted on top of the pole pieces and covered with a metallic cap with a small opening (around 5 mm).

spot of 30 nm, which defines the resolution of the technique. Scanning by the sample (on piezo-stage) is performed in order to reconstruct pixel by pixel a larger image. Magnetic imaging relies again on XMCD at L_3 edges. The contrast is very similar to the one obtained by XMCD-PEEM in the shadow. Imaging can be performed under higher magnetic fields (typically hundreds of mT, even above 1 T possible) as we detect directly photons that are not affected by the field. We used STXM at the HERMES beamline to obtain images of CoNiB tubes under increasing axial magnetic field to extract the strength of the anisotropy field related to the azimuthal anisotropy (section 8.3.1). Magnetic field is created by a set of 4 rotatable permanent rod magnets whose mutual orientation is controlled by motors. The setup enables application of magnetic field up to 200 mT in the sample (substrate) plane.

5.1.3 Substrates for synchrotron experiments

For STXM, the tubes are dispersed on thin silicon nitride (Si_3N_4) membranes (100 nm or 200 nm), whose thick Si frames are glued onto a metallic plate – see Fig. 5.6. We tried both commercial membranes (window size 1.0 mm and thickness 100 nm) provided by Synchrotron Soleil and lab-made substrates with Au alignment marks (window size 0.7 mm, thickness 200 nm, Au marks with thickness of 40 nm).

In case of XMCD-PEEM, we used larger n-doped Si substrates (up to 1 cm edge) with Au alignment marks such as shown in Fig. 4.5. The same substrates (and

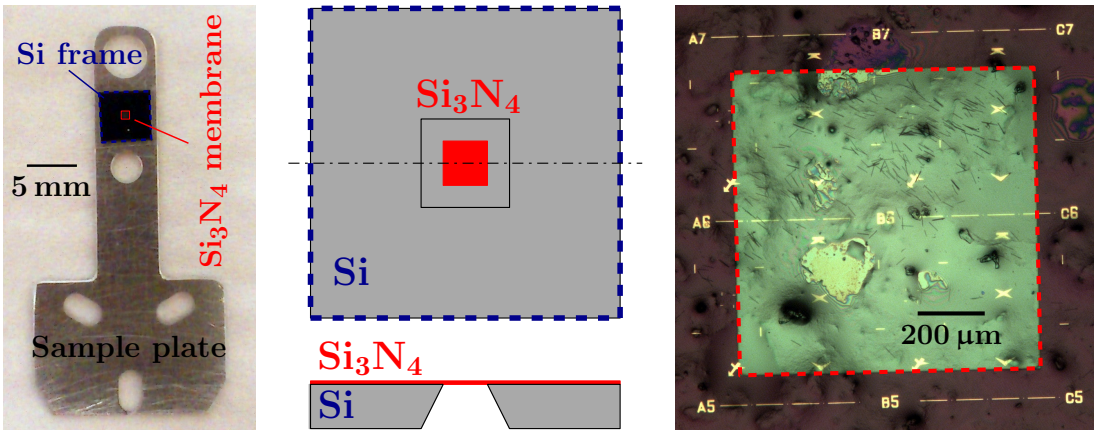

(a) sample plate (b) membrane scheme (c) custom Si_3N_4 + Au marks

Fig. 5.6: Si_3N_4 membranes for STXM. a) Photo of a metallic sample plate with the membrane (edge of the Si support frame is 5 mm), X-rays arrive perpendicular to the plane. b) Scheme of the Si_3N_4 membrane on the Si support frame (bottom and cross-section side view). c) Optical image (top view) of a custom-made Si_3N_4 membrane (Nanofab, Institut Néel) with Au (40 nm) alignment marks. The brighter inner square highlighted by the dashed red square corresponds to the membrane "window" (membrane edge 0.7 mm, thickness 200 nm). There are magnetic tubes dispersed on top of the membrane as well as many impurities from the template dissolution. These impurities (extreme case shown, cleaner samples with aligned tubes were used as well) are not an issue for STXM, however, for XMCD-PEEM such sample would be unusable.

sometimes also the same samples) were used for magnetic force microscopy and magneto-optical measurements with focused laser. The substrates were designed by Alexis Wartelle and fabricated by Bruno Fernandez (Nanofab, Institut Néel).

5.2 Atomic & Magnetic force microscopy

Atomic Force Microscopy (AFM) senses interaction between sharp tip and a sample. The interaction is commonly detected through displacement or change in oscillation (amplitude, phase, frequency) of a microlever that bears the sharp tip. Aside from short-ranged van der Waals interaction providing basically the sample topography, one can employ a tip with a magnetic coating to probe magnetic longer-range interaction as well.

More about AFM can be found in a very nice book by Eaton and West [178]. For further information on Magnetic Force Microscopy (MFM) one can consult ([179], chapters 11 and 12), ([54], section 2.6.1) or author's master thesis [180].

Two main instruments were used for the investigation of our samples: NT-MDT Ntegra Aura (imaging under field possible) and HR-MFM Nanoscan (imaging under vacuum).

5.2.1 NT-MDT Ntegra Aura with Px controller

The Ntegra Aura microscope is specifically designed for magnetic force microscopy (no magnetic sample holder, no microscope parts affected by the field in the sample area) and enables application of magnetic field during the imaging. One can use either a standard commercial base with coils for in-plane field (up to approx 200 mT, pole pieces and gap dependent) and custom-made coils, or a dedicated home-made base for measurement with out-of-plane magnetic field (even above 1 T).

Classical two pass tapping/lift mode technique introduced by Digital Instruments [181] was used for the imaging. During the first pass, the oscillation amplitude change was tracked showing (predominantly) the sample topography, whereas the phase shift of the oscillating cantilever was recorded in the second pass at elevated (lift) height, reflecting longer range interactions (mostly magnetic, but also electrostatic).

5.2.2 HR-MFM Nanoscan

The microscope from Nanoscan dedicated to high resolution MFM imaging at Institut Néel was operated under secondary vacuum ($1 \cdot 10^{-4}$ Pa) in order to benefit from higher sensitivity and (thermal) stability. The low pressure significantly increases

the quality factor of the mechanical cantilever (smaller damping, see Fig. 5.7) and thus enhances the probe sensitivity in case of amplitude or phase shift detection. The cantilever oscillates close to its resonance frequency with amplitude of oscillation around 10 nm. We used frequency modulation with Phase-Lock Loop (PLL) [182]. Therefore we keep the phase of the oscillator and track the shift of the resonance frequency upon interaction with the sample (the shift is proportional to the force gradient, in the first approximation). In such a case the low pressure (low damping, high quality factor) does not enhance the signal itself, but decreases the noise (see e.g. [182]).

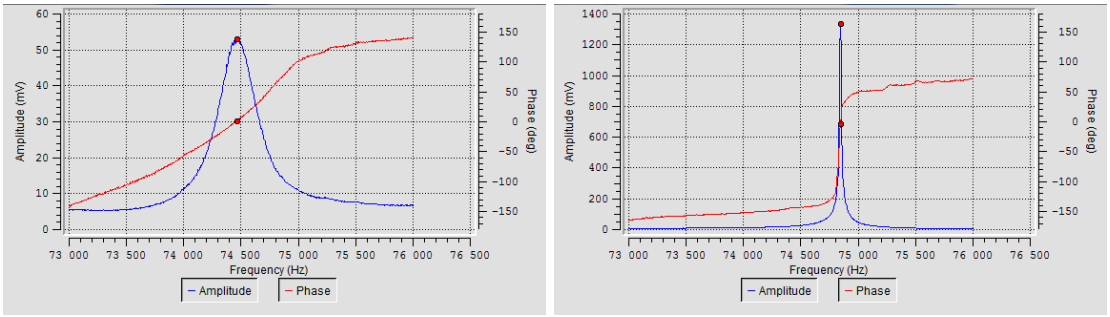

(a) Ambient pressure (b) Under vacuum

Fig. 5.7: Resonance of Olympus AC240TS cantilever at ambient pressure and under vacuum ($4 \cdot 10^{-3}$ Pa). The frequency range is the same in both cases. However, for the same driving force, the resonant amplitude is significantly larger under vacuum. Note also that the resonant frequency shifts with the density of the surrounding medium. It decreases with the increasing medium density [183].

First, we define a base for the height by a certain setpoint, e.g. -2 Hz frequency shift and sample electrical bias 1400 mV on a supporting Si substrate (empty flat area). Note that real sample-probe distance is both tip and sample dependent in such a case. We locate our structure using Electric Force Microscopy (EFM), then we (partially) compensate the sample tilt and measure the electric Contact Potential Difference (CPD) [184]. With respect to our base (which itself is far from the real sample surface) we define the lift height. Finally, we lift the probe by the selected height, switch off the z-feedback loop (z-vertical direction), compensate the CPD by biasing the tip and we perform scan of our structure while monitoring the frequency shift. If everything is set properly, the signal should reflect mainly the magnetic interaction. During the image scan, the probe moves at typically 4-5 µm/s.

5.2.3 Probes

As probes we used commercial non-magnetic probes that were lab-coated with custom magnetic layers. More specifically we employed Asylum AC240TS non-magnetic probes (typically 2 N/m stiffness, 70 kHz resonance frequency – 1st harmonics) lab-coated with thin layer of CoCr, typically 10 or 20 nm, capped with 4 nm protective layer (SiO_x, AlO_x). The thickness given here corresponds to a layer deposited on a flat substrate, the layer on the tip may differ.

5.3 Electron microscopies

Here we shortly discuss electron microscopies and related techniques employed for characterization of our samples. Namely we will cover scanning electron microscopy and associated chemical analysis through detection of characteristic X-rays, and transmission electron microscopy. Electron holography will be mentioned in a separate section 5.4.

5.3.1 Scanning Electron Microscopy

Scanning Electron Microscopy (SEM) together with Energy-Dispersive X-ray spectroscopy (EDX) were used for structural and chemical analysis of the prepared nanostructures, respectively. SEM probes the sample with a focused beam of electrons and several outputs can be obtained. Most commonly, scattered and secondary-emitted electrons from the sample are collected. Back-scattered electrons have energy close to the primary beam, they give also a chemical contrast as their yield is proportional to the atomic number of present elements; last but not least, they can be less affected by the sample charging compared to the low energy secondary electrons.

If the energy of the beam is sufficient, at least few hundreds of eV, transitions between core-electron energy levels of the sample atoms can be excited. The then empty core-shell levels are filled with electrons from higher levels accompanied by emission of characteristic X-rays and Auger electrons (prevailing for light elements with low atomic number).

The X-rays can be probed with Energy Dispersive X-ray Spectroscopy (EDX) and from the characteristic radiation (well-defined photon energy given by the difference in energy levels) one can determine the elemental composition of the sample. Aside from the characteristic radiation, we always detect also a continuous background, Bremsstrahlung (braking radiation), associated with deceleration of the primary beam of electrons while interacting with the sample.

All SEM images and EDX measurements were performed by the author on a Zeiss Ultra+ microscope with Bruker QuanTax EDX system. The chemical analysis with EDX was conducted using different primary electron beam energies. Both clusters and single tubes on a Si substrate were probed, as well as single tubes on a grid for Transmission Electron Microscopy (TEM) with a lacey carbon film.

Primary beam energies of 15 and 20 keV were used for efficient excitation of K_α lines of iron group elements and thus more precise determination of ratio of metals. Much lower energies (≤ 5 keV, namely 3.0, 4.5, and 5.0 keV) and single tubes on the TEM grid were used in order to detect boron (B-K_α: 183 eV).

Light elements such as boron are very difficult to detect with EDX, for some systems even impossible. Several ingredients are needed for boron detection: low primary beam energy (otherwise the boron signal is hidden in the background), silicon drift detector with a very light window transmitting B-K_α radiation [185]. Even with these the excitation of characteristic X-rays is low, the window absorption high and the detector efficiency low. In addition, part of the B-K_α can be absorbed by other sample atoms and carbon layer (unavoidable contamination, especially as the tubes come from the polycarbonate template). The best results were obtained on single tubes suspended above vacuum – no substrate contribution.

5.3.2 Transmission Electron Microscopy

If not stated otherwise, TEM images were acquired at 300 keV electron beam energy together with Laurent Cagnon using a Philips CM300 FEG-TEM. For acquisition of Selected Area Electron Diffraction (SAED) patterns we used an aperture that restricts irradiation of the sample by the electron beam to an area with 240 nm in diameter. This enable local acquisition of electron diffraction patterns. The patterns displayed in the results section are good representatives (but not averages) of the data acquired on several parts of the sample (nanowire/tube).

5.4 Electron holography

Electron holography is a powerful quantitative technique that enables to map various quantities with lateral resolution of few nanometres with prospects for atomic resolution. It can be used for mapping magnetic induction in and around a magnetic nanostructure, visualization of doping in semiconductors, determination of the thickness of a thin film, measurement of the so called mean inner potential etc. [186–189].

First, we will briefly introduce some theoretical background of the technique, then we will describe the instrument used for the imaging, and finally we discuss

samples and their preparation for the imaging. We demonstrate the imaging capabilities and phase maps interpretation on CoNi nanowires in order to provide a short "tutorial" before discussing more complex patterns obtained on tubes (in the results section). Simulation of electron holography phase maps are described in a separate numerical modelling section 6.4. The results of the imaging can be found in sections 5.4.4 (tutorial, basic results on nanowires), B.4 (DWs in diameter modulated wires), 7.2.2 (twires), 8.3.5 (CoNiB tubes), and 8.3.3 (NiFeB tubes).

5.4.1 Theoretical background

Electron holography enables us to determine quantitatively both the amplitude and the phase of an electron wave that passes through a thin sample, thanks to interference and its numerical analysis. In a so-called off-axis holography (used in our experiments), nearly planar electron waves pass partially through the sample (influenced by the sample - object wave), partially through vacuum (unaffected – reference wave) – see Fig. 5.8.

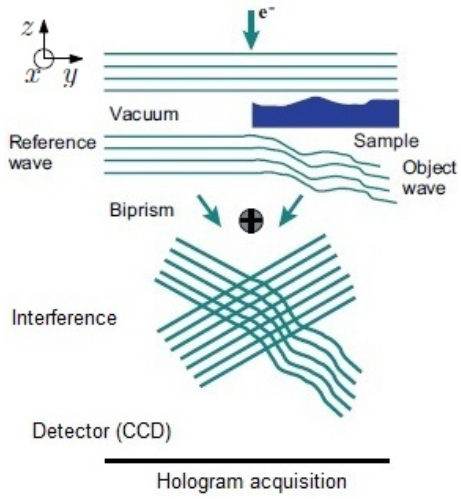

Fig. 5.8: Scheme of electron holography. Adapted from [189].

These two waves are forced to interfere via a positively charged thin metallic (Pt) wire, so called (Möllenstedt–Düker) biprism. On a detector (CCD camera) we acquire a hologram, i.e. a classical TEM image with superimposed interference fringes. Numerically one can reconstruct a map of the electron wave phase shift ϕ. This shift, with respect to the vacuum reference wave, is influenced by both electric and magnetic potentials and reads (neglecting dynamical diffraction) [187]:

$$\phi = \int_{\tau} \vec{k} \cdot \mathrm{d}\vec{s} = \phi_{\mathrm{e}} + \phi_{\mathrm{m}} = \frac{\mathrm{e}}{\hbar} \frac{1}{v} \int_{\tau} V(x,y,z)\mathrm{d}s - \frac{\mathrm{e}}{\hbar} \int_{\tau} \vec{A}(x,y,z) \cdot \mathrm{d}\vec{s}, \tag{5.2}$$

where $\vec{k}$ is the relativistic electron wave vector determined for example from the Klein-Gordon-Flock equation or the more general Dirac equation (relativistic versions of the Schrödinger equation for spin equal to 0 and 1/2, respectively), e is the elementary charge, $\hbar$ the reduced Planck constant, v the relativistic electron velocity, $V(x, y, z)$ stands for electrostatic potential and $\vec{A}$ represents the magnetic vector potential (magnetic induction $\vec{B} = \vec{\nabla} \times \vec{A}$). The integration is taken along the electron path represented by a curve τ. Note, that even for a region with zero magnetic/electric field there is some effect on the electron (charged particle in general), provided that the associated potentials are non-zero – recall the Ehrenberg–Siday–Aharonov–Bohm effect.

For a given accelerating voltage in the transmission electron microscope (e.g. 300 kV), terms in front of the first integral on the right hand side of (5.2) are constant and usually grouped together in a parameter labelled c_E (see also appendix B.1; interaction constant σ in Lichte's review [187]).

As the electron beam is usually supposed to travel along z direction, we can rewrite (5.2) assuming homogeneous sample composition and no external charges, nor fields:

$$\phi(x, y) = \mathrm{c}_E t(x, y) V_0 - \frac{\mathrm{e}}{\hbar} \int_\tau A_z(x, y, z) \mathrm{d}z, \tag{5.3}$$

with

- $\mathrm{c}_E = \frac{\mathrm{e}}{\hbar} \frac{1}{v}$, interaction constant depending on electron energy through $v = v(E)$, $\mathrm{c}_{300\,\mathrm{keV}} = 6.5262 \cdot 10^6$ rad/(V · m),
- $t(x, y)$ – sample thickness (in general electron path length through the sample),
- V_0 – electrostatic Mean Inner Potential (MIP, volume averaged electrostatic potential),
- A_z – z (along the beam)-component of magnetic vector potential – depends only on in-plane magnetic induction B_x, B_y (components perpendicular to the beam direction).

The integral in (5.3) is taken from $-\infty$ to $+\infty$, but in practise one takes just the sample surrounding. In a simple case, the electrostatic contribution ϕ_e to the phase shift is given by the sample thickness and (mostly constant) MIP. In general, the MIP can vary within the sample (used for visualization of different doping levels in semiconductors by electron holography), but for metals of uniform composition it can be well-approximated by a constant. The values of the MIP were calculated with various models for many elements, see e.g. [190]. The values can also be measured, even with the electron holography itself provided that we know other parameters (e.g. sample thickness). This is rather easy for non-magnetic elements with well defined sample shape and slightly more challenging for magnetic metals. Example

of such measurements are covered in a thesis by Signoretti [191], where MIP values were determined for electrodeposited cylindrical nanowires, composed of Co, Cu, Ag, and Ni respectively. These values for metals are usually around 20 V (both from experiments and various calculations).

The magnetic part of the phase shift can give information about the magnetic flux. The difference between ϕ_m at two arbitrary points [x_1,y_1] and [x_2,y_2] in a phase image,

$$\Delta\phi_\mathrm{m} = \phi_\mathrm{m}(x_1, y_1) - \phi_\mathrm{m}(x_2, y_2) = -\frac{\mathrm{e}}{\hbar}\int_\tau \left(A_z(x_1, y_1, z) - A_z(x_2, y_2, z)\right) \mathrm{dz}, \quad (5.4)$$

can be rewritten in the form of a loop integral along a rectangular loop Ψ given by 2 parallel electron trajectories going through the two points and joint at infinity by lines perpendicular to the trajectories [188]. Using Stokes' theorem, we finally arrive at the expression with the magnetic flux Φ_m encompassed by the loop Ψ and containing the induction $\vec{B} = \left(\vec{\nabla} \times \vec{A}\right)$:

$$\Delta\phi_\mathrm{m} = -\frac{\mathrm{e}}{\hbar}\oint_{\Psi=\partial\Sigma} \vec{A} \cdot \mathrm{d}\vec{l} = -\frac{\mathrm{e}}{\hbar}\iint_\Sigma \left(\vec{\nabla} \times \vec{A}\right) \cdot \mathrm{d}\vec{S} = -\frac{\mathrm{e}}{\hbar}\iint_\Sigma \vec{B} \cdot \mathrm{d}\vec{S} = -\frac{\mathrm{e}}{\hbar}\Phi_\mathrm{m}, \quad (5.5)$$

Where $\vec{S}$ is a normal to the surface Σ encompassed by the loop Ψ, therefore normal to the electron (beam) direction. Therefore only in-plane (perpendicular to the electron beam) magnetic induction components contribute to the magnetic phase shift. This implies that the sample needs to be tilted to get information about the remaining induction component. For a thin film of thickness t with a rectangular cross-section, normal electron beam incidence and homogeneous in-plane magnetization (and thus induction), the magnetic shift equals $\Delta\phi_\mathrm{m}(x) = -\mathrm{e}/\hbar\, Btx$, with x being coordinate in-plane of the film.

Phase maps acquired with the tilted sample might be needed for proper assignment of the magnetic configuration – different magnetization patterns can give rise to similar phase maps. It is possible to remove the electrostatic contribution and thus obtain pure magnetic information by subtracting images acquired with opposite sample magnetization (magnetization reversal), flipping the sample upside-down [192], taking holograms at different acceleration voltage, etc. [193]. More information on electron holography can be found in reviews [187–189].

5.4.2 Instrumentation & data processing

Concerning the instrumentation, a transmission electron microscope with a highly coherent electron source is required (cold cathode, FEG=Field Emission Gun) in

order to obtain the interference and good visibility (contrast) of the interference fringes. Further, at least one electron biprism is needed to get the interference; a second one, optional, can serve for better tuning of the fringe spacing, field of view etc. Last but not least, a good camera is needed for the hologram acquisition. To gain information on the out-of-plane magnetic induction, the sample holder needs to be tilted with respect to the incoming beam. In our case the sample tilt is limited to 60° at best. Larger sample tilt could come in handy. In the ideal case the sample holder should support rotation/tilt up to 360 ° to enable tomography [194, 195] – full 3D field reconstruction. This would also eliminate the necessity for removing and reinserting the sample from and into the vacuum (for example in case of the sample flipping).

Magnetic field can be applied in-situ via excitation of objective lenses (otherwise turned off in order not to influence the sample magnetization) to produce an out-of-plane field (along the electron beam). Sample can be tilted if an in-plane (e.g. along tube/wire) field component is required.

In our case, the electron holography imaging was conducted on the I^2TEM microscope (Lorentz mode; using a transfer lens corrector as imaging lenses) at CNRS CEMES (Toulouse, France) within the framework of the French METSA research federation. The microscope was operated at 300 keV electron energy by Aurélien Masseboeuf and partly also by Christophe Gatel. A double biprism was used to enlarge the field of view and remove Fresnel fringes. Off-axis holography was employed, phase reconstruction was done by inverse fast Fourier transform of one of the side-bands of the hologram power spectrum (after centring and windowing). Data were processed by the author in Gatan's DigitalMicrograph software with holography scripts provided by Aurélien Masseboeuf (CEMES, Toulouse) except for the removal of the electrostatic contribution that was done by Aurélien Masseboeuf himself following a procedure of Tonomura [192] (acquiring another hologram with the sample flipped upside-down).

Experimental phase maps were compared with simulations performed by the author using a dedicated code described in section 6.4.

5.4.3 Samples

We employed electron holography for the investigation of several samples. We started with a system having a known magnetization state – $Ni_{60}Co_{40}$ cylindrical nanowires with diameter modulation prepared by electroplating (fabricated by Sebastian Bochmann, FAU Erlangen, Germany). Recently, there has been an increasing number of reports on electron holography investigation of cylindrical magnetic nanowires. However, most of these works deal with uniformly-magnetized wires

or alternating magnetic and non-magnetic segments (e.g. Co/Cu) – this has been already done in 1996 by Beeli et al. [196]. Biziere et al. [14] observed transverse domain walls in NWs and provided support of numerical simulations of the magnetic phase maps. Further, some DWs have been reported in the study by Ivanov and coworkers [26]. In our work, we could not only prepare and identify a DW, but also displace it with a magnetic field (section B.4).

Later, we moved to more challenging samples: our own electroplated Ni tube-wire nanostructures with smaller diameter (around 60 nm). We also investigated magnetic (nano)tubes from CoNiB and NiFeB prepared by electroless plating at TU Darmstadt (by Sandra Schaefer). To the best of our knowledge the only observation of ferromagnetic nanotubes by electron holography has been performed in the group of Dunin-Borkowski [109] using small aspect ratio (5) CoFeB nanotubes: *diameter* (hexagonal cross-section) around 200 nm and length of 1 µm. They found axial magnetization with opposite curling sense at the ends of the tube. In our work, we look at higher aspect ratio tubes (50-100) from different materials.

As substrates we used Cu TEM grids (window size 50 µm) with lacey carbon film. Such carbon films have many holes, which increases the chance that at least part of the wire/tube is suspended in vacuum (no substrate contribution) during the observation. This facilitates the electrostatic part removal. Nanostructures were transferred on the grid from a suspension (nanostructures in isopropyl alcohol). For NiCo nanowires we used the grid as a filter and forced the liquid to flow through with a syringe. In this way, large amounts of nanostructures could be collected, if the syringe piston was moved slowly (otherwise the film could be damaged and windows in the grid are empty). When we tried to repeat the procedure for the electroless-deposited tubes, we obtained many damaged tubes (broken, *unrolled*, ...). Therefore, in case of tubes we used a micropipette to transfer several droplets of the solution with tubes on the grid. The solvent was left to evaporate. This resulted in a much lower density of structures (it could be increased for higher density of structures in the solution/solvent), but they retained the tubular shape and the sample was slightly cleaner.

An optical microscopy image of the grid and example of structures dispersed on the porous C film are given in Fig. 5.9. Prior to the electron holography investigation, in some cases, suitable structures (isolated, parts suspended, low amount of structural defects) were identified based on optical and scanning electron microscopy imaging. Just with the optical microscope one can locate nanowires (diameter of the thin section around 120 nm), but one cannot tell for sure whether it is a single wire or a bundle (couple, triplet) as they are well below the resolution of the optical microscope.

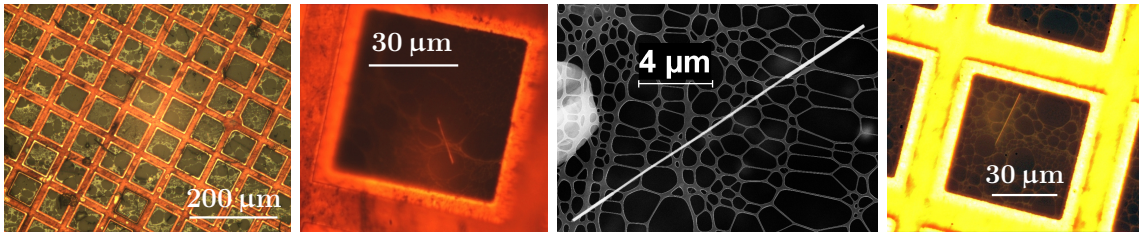

(a) (b) (c) (d)

Fig. 5.9: Nanostructures on TEM grids for electron holography imaging. (a) Optical image of a larger part of the Cu grid. The size of each window is around 55 µm. (b) closer look with optics on a NiCo nanowire on the porous carbon film at the bottom of the window. (c) Scanning electron microscopy of another NiCo diameter modulated nanowire. (d) Optical image of a CoNiB tube on the film.

5.4.4 Electron holography tutorial on NiCo nanowires

As pointed above, we start our electron holography investigations with $Ni_{60}Co_{40}$ electroplated cylindrical nanowires, a system with known magnetization state – axial magnetization – from previous synchrotron investigations, magnetic force microscopy, and by comparison with work on similar nanowires from NiFe [15, 197]. Larger amount of Co in the alloy could lead to a preference for transverse and vortex domains [198]. In our $Ni_{60}Co_{40}$ we nucleate and displace magnetic domain walls. Further, we use the domain walls for a testing of the code for numerical modelling of the phase maps and identification of the domain wall type and configuration. All this is featured in section B.4. Here, we will only use the sample to demonstrate the capabilities of the technique and basic interpretation of the phase maps.

A typical nanowire geometry is depicted in Fig. 5.10. The nanowire has three segments with a narrow central section (120-150 nm diameter) and two thicker segments (200 nm diameter or even more) on either side. The thin section is 10 µm long and the total length is at least 20 µm. Due to the fabrication procedure [199], the two diameter modulations (part where the diameter changes) are different: one transition is sharper, whereas the other one smoother. The aim of this geometry is to be able to nucleate, trap and confine a domain wall in the thin section. Some nanowires are covered with a non-magnetic remnants of the template dissolution process.

The nanowires are rather thick, but still exploitable for electron holography, even in the thick segments. An example of a hologram and the reconstructed phase map of the nanowire close to the sharp modulation is captured in Fig. 5.11. It shows the sample hologram (Fig. 5.11a) with a complicated interference fringe pattern as

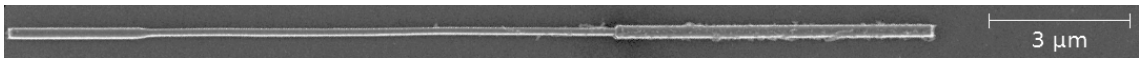

Fig. 5.10: Example of the NiCo diameter-modulated nanowire on a Si substrate. The central, thin section has diameter around 150 nm and length 10 µm. This part is positioned in between two thicker segments (200 nm in diameter or even more). Note the non-magnetic impurities on the right side of the wire originating from the template dissolution process.

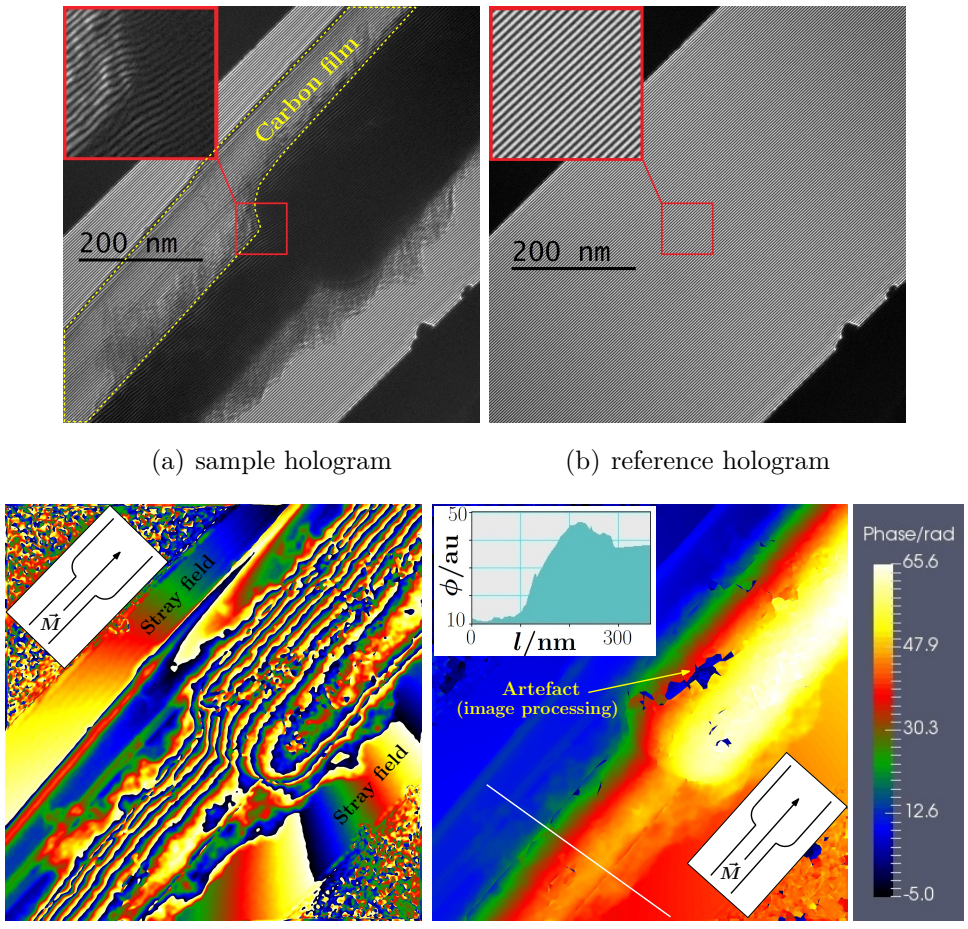

(a) sample hologram (b) reference hologram

(c) wrapped phase (d) unwrapped phase (continuous)

Fig. 5.11: Electron holography of a NiCo nanowire – from hologram to phase map. (a) Nanowire and (b) reference (without sample) holograms with insets showing a closer look on the fringes. (c) Reconstructed phase maps: (c) wrapped phase (in $[0,2\pi]$ interval) with contour lines following the magnetic induction direction and (d) continuous (unwrapped) phase with the inset showing a line profile across the wire.

well as a reference hologram (Fig. 5.11b, without the sample) used for correction of imperfections of the biprism and the imaging system. Note that the field of view is limited to the bright band in the hologram image. Reconstructed phase maps involve both electrostatic and magnetic contributions. Two phase maps are displayed: one with wrapped phase (confined in $[0,2\pi]$ interval) and processed, continuous (unwrapped) phase. The magnetization lies along the nanowire axis, except at the diameter transition (and wire ends). The magnetic induction follows the nanowire shape as can be seen on contour lines in wrapped phase map (Fig. 5.11c). Magnetization is supposed to follow as well, except for diameter modulation and other part where a stray field emanates from the sample. The inset in (Fig. 5.11d) shows a line profile across the wire. Here we can recognize the electrostatic part proportional to the cylindrical nanowire thickness as well as the slope rising to the right which is a pattern associated to the axial magnetization. Maps for different contributions (electrostatic only, magnetic only and combined) are discussed further in the text, see e.g. Fig. S8.

Before proceeding to domain wall studies or more complex samples, we verified that we can clearly see the difference between images with opposite nanowire magnetization (wire saturated with external magnetic field in 2 known opposite directions) – see Fig. 5.12.

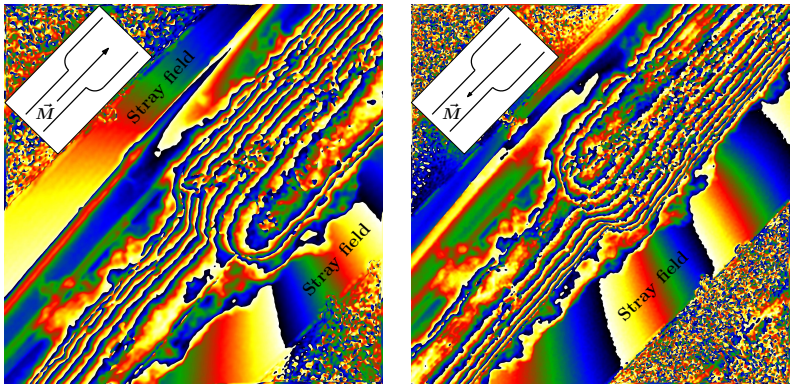

Fig. 5.12: Phase maps of a NiCo nanowire (close to the diameter modulation) with two opposite magnetization directions (upon saturation with external magnetic field). Opposite axial magnetization gives rise to opposite slope of the phase across the wire, which translates into contour lines that are concentrated on one, or the other side of the wire. Note also the stray field emanating from the transition (to the bottom right of the wire).

Magnetic signal (magnetic contribution to phase shift of the electron wave) was distinguishable even without removing the electrostatic contribution. Opposite magnetization direction could be recognized just in a live phase imaging (crude preview

obtained within several seconds) thanks to a different phase gradient across the wire detonated by contour lines (concentrated at opposite sides of the wire). This is crucial for fast identification of a domain wall presence and its position. Note that the magnetization is non-uniform in the diameter modulation, this gives rise to magnetic charges and a stray field emanating from this nanowire section (Fig. 5.12). The stray field is also manifested on the phase maps outside the wire near the modulation. This is more visible to the bottom right in Fig. 5.12. There is a carbon film (part of the substrate) on the other side of the wire (visible in Fig. 5.11a), which partially conceals the stray field lines.

More elaborated imaging with domain walls in nanowires and comparison with numerical modelling is described in section B.4, investigation of twires in 7.2.2, and finally study of tubes is covered in sections 8.3.5 (CoNiB tubes) and 8.3.3 (NiFeB tubes).

5.5 Magnetometry

We measured hysteresis loops of magnetic NTs both for their arrays (global magnetometry) and also single tubes (local magneto-optics with focused laser beam).

5.5.1 VSM-SQUID

For global magnetometry, measurement of arrays of (nano)tubes still in a template, we used a Quantum design MPMS SQUID VSM (Magnetic Property Measurement System - Superconducting Quantum Interference Device - Vibrating Sample Magnetometer). Samples were placed on a quartz or straw holder. After introduction into the measurement chamber and before acquisition of hysteresis loops, the sample was AC demagnetized along the applied field direction.

A cleaned empty holder was measured first (for each new sample to verify the holder cleanliness), its contribution was insignificant. Therefore, it was not necessary to remove such contribution. Further, we also considered a possible contribution of the template: both alumina and polycarbonate provided only weak diamagnetic contribution, which was disregarded as well in further studies.

5.5.2 Magneto-optics with focused laser beam

Single tubes dispersed on a Si substrate were probed by the Magneto-Optical Kerr Effect (MOKE) that relies on a change of polarization plane and ellipticity of a polarized light upon a reflection from a magnetic sample. The technique is rather surface sensitive, providing information from the depth up to approximately 30 nm

(depending on material, wavelength, etc.). The MOKE was implemented in the longitudinal configuration with a focused He-Ne ($\lambda = 632.8\,\mathrm{nm}$) laser (100x objective, laser spot 1 µm). The field was swept as a triangular wave signal, with frequency 1.1 Hz, and field calibration uncertainty max $\pm 5\,\mathrm{mT}$. In order to limit the potential effect of heating, the laser power was set to 0.2 mW. Commonly even few mW laser power is used for the investigation of magnetic nanostructures. In our measurements, such laser power leads to more squared loops (heat assisted switching) and prolongated exposure can damage our samples – see appendix A.2. The sample with tubes is placed on a piezostage, therefore the focused beam can be precisely positioned on a particular tube. Further information on the field of magneto-optics can be found in a book by Štefan Višňovský [200].

6 SIMULATIONS

To support our experimental observations and also to get better insight into the magnetic systems under investigation, we run numerical micromagnetic simulations of magnetization distribution in our samples – nanotubes and nanowires. Further, we employed modelling of the contrast expected for employed experimental techniques – namely electron holography and synchrotron based experiments with circularly polarized X-rays (XMCD-PEEM, STXM).

6.1 Micromagnetics

We used the following micromagnetic codes:

- Object Oriented MicroMagnetic Framework (OOMMF) [201]
- Finite Element LLG Object Oriented Development (FeeLLGood) [202, 203]

All micromagnetic simulations were performed at 0 K. Most simulations are done on permalloy or permalloy-like structures (for both nanowires and nanonotubes), therefore considering only exchange, magnetostatic and possibly Zeeman energy. As for simulation parameters we thus use exchange stiffness $A = 13{\cdot}10^{-12}$ J/m and spontaneous magnetization $\mu_0 M_\mathrm{s} = 1$ T if not stated otherwise. For the tubes with azimuthal (flux-closure) magnetization we also added an effective uniaxial anisotropy. We considered two ways for obtaining the azimuthal magnetization:

- point-wise varying easy axis that follow the azimuthal direction in every cell (implemented in OOMMF)
- constant hard axis along the tube axis (easily used in any code, exploited in FeeLLGood and thus presented in most cases shown here)

Below we provide additional information related to the used micromagnetic codes.

6.2 Object Oriented MicroMagnetic Framework

OOMMF is a public micromagnetic solver from NIST [201]. This finite difference code (discretization in parallelepipeds, commonly cubes) can solve the problem either by a numerical integration of the LLG equation or by minimizing the energy functional.

We used OOMMF (version 1.2a4; 1.2a6 for tubes with larger diameters) mainly for the first tests at the beginning of each set of new simulations (NTs, NTs with azimuthal anisotropy, multilayered tubes) where we profited from the code versatility. Later we used FeeLLGood for the better description of curved geometries and

also in order to benefit for its post-processing tools for modelling of experimental measurement techniques (more below).

Visualization of micromagnetic configurations was done mainly using native mmdisp tool. In some cases, the tool ovf2vtk [204] was employed for conversion of OOMMF format (OVF) to Visualisation ToolKit (VTK) file format for the visualization in ParaView software [205]. In these cases a threshold filter on magnetization vector magnitude had to be imposed in ParaView in order to remove zero-length vector artefacts (zero-length vectors oriented in one direction displayed on top of the real magnetic configuration).

6.3 FeeLLGood

FeeLLGood [202, 203] is a finite element code developed at Institut Néel by Jean-Christophe Toussaint. Further information on the code and its development can be found in PhD theses of Adrien Vaysset [206] and Ségolène Jamet [207]. For our simulations we employed version STDW 20150821 (using ScalFMM library [208] in computation of magnetostatic interactions). As we are dealing with finite elements, the geometry creation and meshing is not as straightforward as in finite differences. We address these points below, mainly utilizing Gmsh (free finite element mesh generator and geometry editor) [209]. Visualization of the resulting micromagnetic configurations as well as outcomes of the post-processing codes was done in ParaView [205].

6.3.1 Geometry and meshing

Simple geometries (wire, tube) were prepared directly in Gmsh using built-in scripts for extrusion of a disk or an annulus to prepare nanowires or nanotubes, respectively. When we tried to create a more complex system, such as coaxial (multi-layered) tubes, in Gmsh by extrusion of two 2D concentric annuli, the resulting geometry (combination of structured and unstructured grid) could not be meshed properly. We tried different meshing methods (Frontal, Delaunay) and various mesh post-processing (smoothing steps, mesh optimization), but without success (Gmsh program even got frozen or completely crashed for some combinations, others caused problems in the micromagnetic code itself).

In order to overcome this obstacle, we created the geometry in an external Computer-Aided Design (CAD) software. We used FreeCAD [210], but in principle any CAD can be used provided that the geometry can be exported to format that can be read by Gmsh. We successfully performed this step by exporting to brep (boundary representation) format (stp or iges should work as well). One then

only needs to define physical volume(s) and surfaces. For more complex geometries it is more convenient to use external CAD with much more user friendly interface than Gmsh one. On the other hand, even slight changes of geometry (i.e. different diameters, length, ...) require repeated exporting/importing of the geometry as well as specifying maximum element size (tetrahedron edge).

Even a mesh prepared using a CAD geometry caused some errors in the micromagnetic simulations. Finally, this problem was solved by performing more mesh post-processing which should improve the mesh quality. Experimentally we found that meshing in Gmsh with *3 smoothing steps* and *1 Lloyd smoothing step* followed by a common *Optimize 3D (Netgen)* works well. Other post-processing may do the job as well, but here we will stick to the one mentioned above.

In case of simple wire or tube geometry, we employed the Delaunay 3D meshing method and used only Optimize 3D (Netgen) procedure (no smoothing).

In all cases, the mesh represented by a sparse matrix is subject to Cuthill–McKee (CMK) ordering algorithm to decrease the bandwidth of the band matrix (script implemented by Jean-Christophe Toussaint) to ease and speed up the numerical computation.

Note on element size - mesh smoothing

Mesh smoothing not only *improves* the mesh, but may also result in a slight change in the size of some elements (changes in positions of nodes). It seems that the maximum element size is slightly increased upon the smoothing. In an example below (tube wall thickness of 15 nm), the maximum element size is slightly bigger than the desired value of 4 nm but still well below 4.5 nm. This difference was remarkable when we compared a tube prepared using just Gmsh and two coaxial tubes created in the FreeCAD and smoothing the mesh as described above. The non-smoothed tube had more nodes than both coaxial tubes together as can be seen in Fig. 6.1. Gmsh script with Lc=4 nm without the smoothing generates smaller elements, sometimes maybe even unnecessarily small.

6.3.2 Initial magnetic configuration

As an initial magnetic configuration one may use either the state from previous simulations or utilize a c++ script that assigns a unit magnetization vector to each node of the mesh based on a given analytical expression. In order to define different magnetization regions (e.g. two opposite domains and a DW), simple (nested) *if* conditions are applied. An example is given in the annex section C.

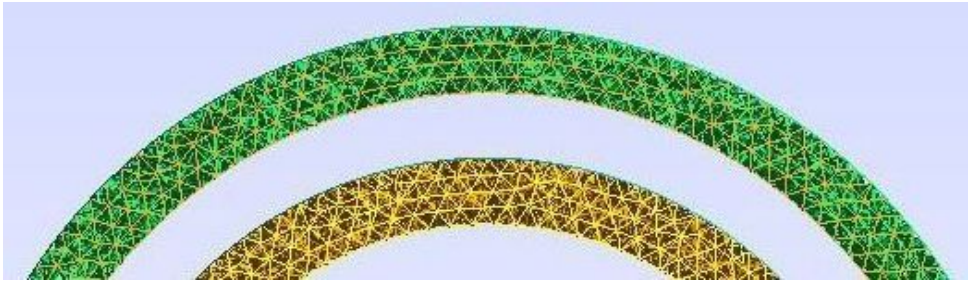

(a) 2 tubes, from FreeCAD, with smoothing

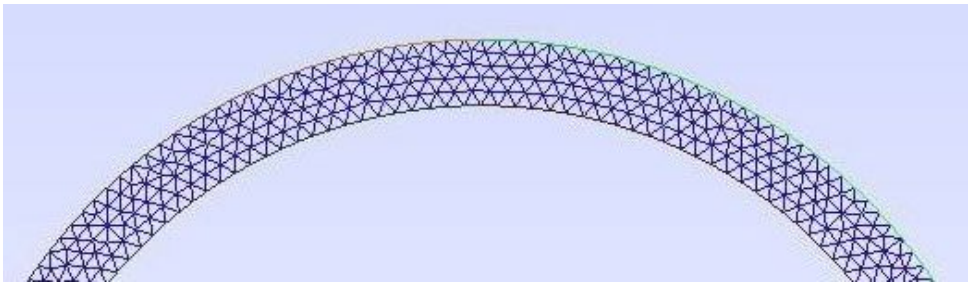

(b) Outer tube, Gmsh script, no smoothing

Fig. 6.1: Effect of mesh smoothing on element size. Comparison of a mesh (a) based on external CAD geometry and max element size 4 and (b) generated by Gmsh script with Lc=4 nm. There is a quite big difference between these two methods, probably due to the mesh post-processing in the first case. It is quite remarkable that the whole mesh in (a) involving both tubes has less elements/nodes than only the outer tube produced purely using Gmsh. Only one part of the front surface mesh is shown.

Initial configuration for coaxial tubes

Three main initial micromagnetic configurations were considered in case of two coaxial nanotubes separated by a vacuum spacer (chapter 10):

- (pseudo)random (boost library) – random $\vec{M}$ at each node
- (axial) antiparallel – $\vec{M}$ in one tube opposite to the other one
- (axial) parallel – $\vec{M}$ along the same direction in both tubes

Pseudo-random magnetization has been generated using the boost library [211], in particular Mersenne Twister (pseudorandom number generator mt19937) with the current time as a seed. Example of such initial configuration is given in Fig. 10.2.

6.3.3 Post-processing codes

Further we used extensions of FeeLLGood developed by Jean-Christophe Toussaint and Ségolène Jamet. These post-processing tools enable modelling of experimental contrast for several techniques, namely electron holography and XMCD-PEEM.

These are detailed in sections below.

6.4 Electron-holography code

Electron holography phase maps are not always easy to interpret. In order to facilitate this task we performed a numerical modelling of the phase shift maps. First we compute a relaxed 3D micromagnetic configuration using the FeeLLGood code (finite elements). In this way, we prepare one or several possible micromagnetic configurations we expect to appear in our system. The relaxed micromagnetic configuration is then used as an input for the calculation of the electron holography phase maps. Our technique combines both computational efficiency and precision which is uncommon for a numerical method, mainly due to the transformation of a 3D problem to a 2D one. Instead of performing the calculation in the whole (x,y,z) space like in [14], the magnetic phase shift is proportional to the z-component of the magnetic vector potential produced by a 2D equivalent magnetic system whose in-plane magnetization components are given by the path integral $\int_{\tau} (M_y, -M_x)\,\mathrm{d}z$, where z denotes the beam direction. The latter expression corresponds to the integrated (along the electron path) in-plane magnetization of the 3D original system rotated by 90 ° around the beam axis. This can be done for different sample tilts/rotations and both magnetic and electrostatic contributions to the electron phase shift.

For the 2D projection we use a frontal meshing method, the mesh has order 2 and it is optimized in a similar way to the 3D mesh used in micromagnetic simulations. The maximum cell size is 8 nm (but order 2, so effectively 4 nm), finer mesh of 4-5 nm was used for more refined modelling. But no significant difference has been found for the samples we model.

In experiments it is not always easy to obtain pure magnetic contrast. Therefore the idea is to include the electrostatic contribution in the numeric simulations. In such a case, we assume the electrostatic contribution to be proportional to the sample thickness and to the volume-averaged Mean Inner Potential of 22 V with the constant of proportionality $\mathrm{c}_{300\,\mathrm{keV}} = 6.5262 \cdot 10^6$ rad/(V · m) [187].

Unfortunately, in the current version of the code (v. 20151117), the electrostatic contribution can be modelled properly only for solid objects. In case of a tube the code assumes the thickness to be equal to the outer diameter and it disregards the inner hollow part. However, it is possible to take the hollow part into account: one can just subtract simulation of the electrostatic phase (setting $M_\mathrm{s} = 0$) calculated for a solid wire corresponding geometrically to the inner hollow part of the tube (see Fig. S4). In order to avoid artefacts, the same 2D mesh is used for the projection

of both tube and the "inner wire".

6.4.1 NiCo nanowires

As for the micromagnetic simulation of the nanowires only exchange and dipolar interactions were taken into account (thus neglecting magnetocrystalline anisotropy) with the following parameters: saturation polarization $\mu_0 M_s = 1\,T$ and exchange stiffness $A = 10^{-11}\,J/m$. The wire diameter is 120 nm, same as in the experiment (central thin section of the wires). The tetrahedron size was 5 nm or smaller. We consider a wire with the length sufficiently longer than the DW width, however much shorter than in the experiment. Magnetic charges are removed at either end, thus mimicking an infinitely long wire. In wire we considered two axial domains with a DW (either TW, or BPW). The computation was done for different wire tilts and domain wall orientation (azimuth for the TW) for both magnetic and electrostatic contribution.

6.4.2 Tubes

In the case of tubes, we focussed on azimuthal domains separated by the Néel, Bloch or cross-tie walls, that were obtained by previous relaxation of micromagnetic configurations. For the relaxation we started with axial magnetization in the DW for the Néel wall and with radial magnetization for the other two. The cross-tie is obtained for thinner tube shells and smaller effective anisotropy constants. We considered permalloy-like material with uniaxial anisotropy having hard axis along the tube axis to promote the azimuthal domains.

Note that the simulations presented here are crude. They are based on a small tube for the Bloch wall – diameter 50 nm, tube wall thickness of 10 nm; Néel and cross-tie walls (4 pairs of vortices and antivortices) were modelled in a larger tube with diameter 250 nm and 20 nm tube wall thickness. The micromagnetic configuration is prepared in FeeLLGood with mesh size 4 nm or smaller. For the electron holography projection, the 2D mesh element size was 6 or even 8 nm (for the cross-tie in the larger tube), a smaller size can be used for more refined results. Still the above-mentioned mesh size should be fine as it is a 2nd order mesh; test with smaller mesh did not reveal any significant difference.

6.5 XMCD-PEEM code

The implementation of the shadow-XMCD contrast modelling (including X-ray absorption, photoelectron emission, and their detection) is detailed in the work of

Jamet et al. [153, 207]. As an input magnetic configuration one can use either an analytical expression for the magnetization distribution, or a relaxed micromagnetic configuration (computed with the above-mentioned FeeLLGood code).

For comparison with experiments on CoNiB tubes (imaging performed at Co-L_3 edge), we assume the X-ray linear absorption coefficients μ to be those for pure cobalt multiplied by the atomic fraction of cobalt in the tube material. We disregard the boron influence and also suppose that Ni absorption at the Co-L_3 edge is negligible as we are well below the Ni-L absorption edges. Namely we used $\mu_+ = 0.038\,\mathrm{nm}^{-1}$ and $\mu_- = 0.064\,\mathrm{nm}^{-1}$ for two opposite circular polarizations of the X-ray beam (data for pure elements extracted from Nakajima's work[212]).

Some tests and qualitative comparisons were made also for permalloy(-like) nanostructures ($Ni_{80}Fe_{20}$). In these cases, we consider XMCD at Fe-L_3 and the X-ray linear absorption coefficients are $\mu_+ = 0.010\,\mathrm{nm}^{-1}$ and $\mu_- = 0.018\,\mathrm{nm}^{-1}$ [153], i.e. we again neglect Ni absorption (we are below Ni L edges) and take proportion of Fe into account. Basically, a larger difference between the coefficients is equivalent to a larger thickness of the magnetic material (e.g. tube wall thickness). As we do not aim to do quantitative, but only qualitative comparison with the experiments, the exact values are not of high importance. Further, quantitative comparison is anyhow challenging due to fine experimental features such as background level contrast affecting relative intensity from the surface with respect to the shadow. Nevertheless, one should note that larger material thickness or μ may lead to some changes: namely different proportion of the XMCD intensity coming from the nanostructure surface and from the shadow, as well as inversion of contrast at the edge of a nanostructure surface [153].

Part III

Results & Discussion
Magnetic nanotubes

7 SYNTHESIS OF NANOTUBES

Below we will describe the results of our attempts for synthesis of magnetic nanotubes. Tubes prepared at TU Darmstadt [127] will not be covered in this section. We used two electrochemical methods to prepare the tubes: electroplating where electrons for reduction of metallic ions (from an aqueous solution) are supplied by an external current source, and electroless plating where electrons are provided in a reaction with the so-called reducing agent. More information on the deposition process can be found in the methods, chapter 4.

7.1 Electroplating of NiCo nanotubes

Using electroplating we prepared nanotubes from NiCo and Ni, as well as Ni nanostructures with alternating wire and tube segments. These were obtained by employing a thin porous working electrode (see methods, section 4.2). We also tried to fabricate Ni/Cu core-shell nanowires [129] and Ni nanotubes by electrochemical etching of the Cu core, and pulsed electrodeposition of Ni [164]. However, in our case such nanotube preparations turned out to be highly unreliable and yielded at best very poor tubular-like structures with high roughness. Therefore we will focus below on the two afore-mentioned nanotube fabrication procedures (electrodeposition of NiCo and Ni with porous working electrode). In this section we will deal only with NiCo nanostructures, Ni tubes and wire-tube elements are described in section 7.2.

Following the article by Zhang [166] we electroplated NiCo inside nanoporous alumina membranes starting from the porous Au electrode at the bottom (pore diameter 80-90 nm). Among the fabricated structures, a vast majority consists of nanotubes with extremely thin walls (few nm) as revealed by transmission electron microscopy (Fig. 7.1). Due to prolonged exposition of the magnetic material to sodium hydroxide during the template dissolution, we expect these tubes to be almost completely oxidized, therefore of no use (if one does not want to study antiferromagnetic tubes). Aside from these structures we identified a few nanowires and several tubes with significantly thicker walls (10-20 nm).

Nanowires and nanotubes formed during the deposition had different chemical composition and crystallinity. Nanowires appeared to be Co-rich and well crystallized with a preferred texture, some parts almost monocrystalline (Fig. 7.2a). On the other hand, the nanotubes were polycrystalline without any preferred crystallographic direction (Fig. 7.2b) and they contained almost an equal amount of Ni and Co (some tubes were even slightly richer in Ni). We tried to image both NiCo nanowires and nanotubes with magnetic force microscopy and XMCD-PEEM. For

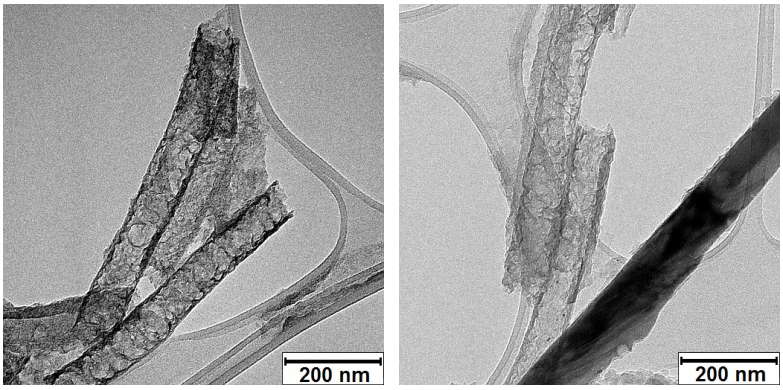

(a) (b)

Fig. 7.1: Transmission electron microscopy of electroplated NiCo nanostructures. (a) The vast majority of structures are nanotubes with a very thin wall (few nanometers). (b) Direct comparison between hollow nanotubes and a solid nanowire obtained in the same batch. Only a few nanowires were found.

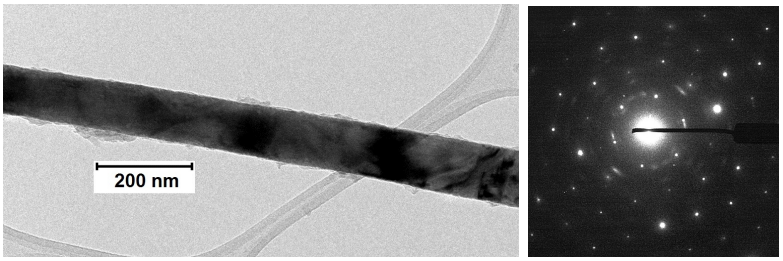

(a) Nanowire (diameter $\approx 100\,\mathrm{nm}$)

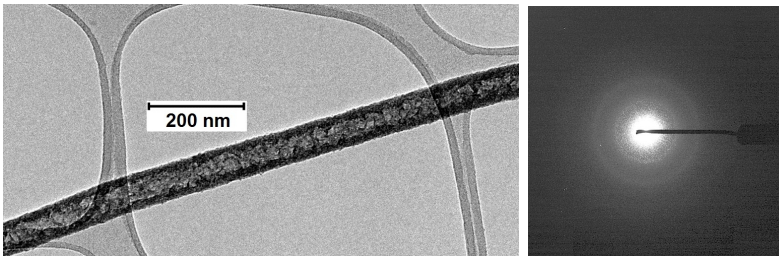

(b) Nanotube (diameter $\approx 70\,\mathrm{nm}$, tube wall 10-18 nm)

Fig. 7.2: Different NiCo nanostructures electroplated in the same template: (a) nanowire and (b) nanotube. Transmission electron microscopy images with selective area electron diffraction on the right. All observed nanowires were well crystallised with some being close to monocrystals. On the other hand, all probed tubes were polycrystalline.

NTs we obtained very weak signal only from XMCD-PEEM, however with no clear magnetic pattern, and nothing with MFM. This is consistent with our expectation that the NTs are significantly oxidized. On the other hand, for nanowires we obtained clear signal with both technique, showing a multidomain structure (Fig 7.3).

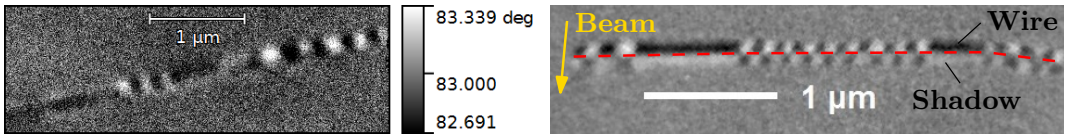

(a) MFM (b) XMCD-PEEM at Co-L_3 (another wire)

Fig. 7.3: Magnetic domains in Co-rich NiCo nanowires (diameter 100 nm) visualized by magnetic microscopies. (a) MFM and (b) XMCD-PEEM at Co-L_3 of another nanowire, contrast range 10 %; beam arrives from the top close to perpendicular to the wire – i.e. we see contrast on the wire surface and just behind it inverted contrast in the shadow (separated by the red dashed line). Strong contrast with the transverse beam direction indicates that magnetization has significant transverse component.

In both MFM one can identify two domain types: elongated domains with weaker contrast that sometimes appear to be dipolar (in direction traverse to the wire axis) and smaller domains with slightly stronger contrast that form series with alternating contrast and thus magnetization direction. Both types can be associated to transverse magnetization, just with different orientation: stronger contrast can result from short domains having significant out-of-plane magnetization component, weaker dipolar contrast can arisein case of transverse magnetization lying in-plane with respect to the supporting substrate. The XMCD-PEEM image of another wire from the same sample also show similar patterns (elongated domains and smaller alternating ones). As the X-ray beam is nearly perpendicular to the wire axis, the magnetization in the domains is indeed predominantly transverse.

Similar images by MFM has been already acquired by several groups. As for XMCD-PEEM, there is a recent observation of a similar patterns by Bran et al. [198]. According to their work, short domains, e.g. seen as checker board pattern in parts of Fig 7.3b should correspond to a transverse magnetization with alternating direction (component along and antiparallel to the beam, leading to magnetic flux-closure), whereas the elongated domains rather to vortex ones (but here one would expect almost no contrast in MFM). Note that just from such image alone one cannot clearly tell apart transverse and vortex domain. Without more details on the supposed vortex showing gradual contrast change in the shadow, it can rather transverse magnetization in the elongated domain, maybe just wit slightly different

orientation. Still such elongated transverse magnetization would be unfavourable, nevertheless possible as a metastable state.

7.2 Ni twires – wire-tube nanoelements

In this section we will describe results of synthesis and briefly also measurements performed on tube-wire nanoelements – twires. We have already discussed what has been done on twires in the literature in section 3.6.

7.2.1 Electroplating of Ni wire-tube nanoelements

When we tried to fabricate Ni nanotubes following the electroplating procedure published by Proenca et al. [123], we obtained mainly nanowires. TEM observations revealed also possible remains of destroyed tubes and most importantly several structures with wire and tube segments (Fig. 7.4).

It is striking that for our Ni twires the transition between the nanowire and the nanotube segment is very sharp. Some structures feature multiple transitions of this kind (Fig. 7.4c). The tube segments in such twires have length ranging from hundreds of nanometres to few microns (longest one observed: 2.2 µm, but there could be even longer ones). We attribute the presence of these twires to local instabilities during the deposition – local change of pH, concentration of the solution, defect, ... Following the kinetic model by Philippe and Michler [29] it could be possible to achieve an improved control over the deposition process.

7.2.2 Further TEM and electron holography on Ni twire

For the electron holography imaging, we found a rather nice twire, a nanostructure with a tube segment between two wire parts– consult Fig 7.5(a). From higher resolution TEM images we could see that the tube wall thickness is not completely uniform, it is below 10 nm, 5-7 nm in most cases. According to selected area electron diffraction, both tube and wire parts are polycrystalline with some wire parts being close to monocrystalline. Damaged tube-like structure to the right of our twire [Fig 7.5(a)] showed no diffraction at all.

Unfortunately, no clear magnetic signal was observed in a quick phase map preview even for the nanowire parts, unlike for the NiCo wires mentioned above. Only after removing the electrostatic contribution, we could see that magnetization is axial and more or less uniform along the wire and there is a stray field emanating from the wire-tube transition as captured in Fig 7.5(c). Unfortunately, small tube

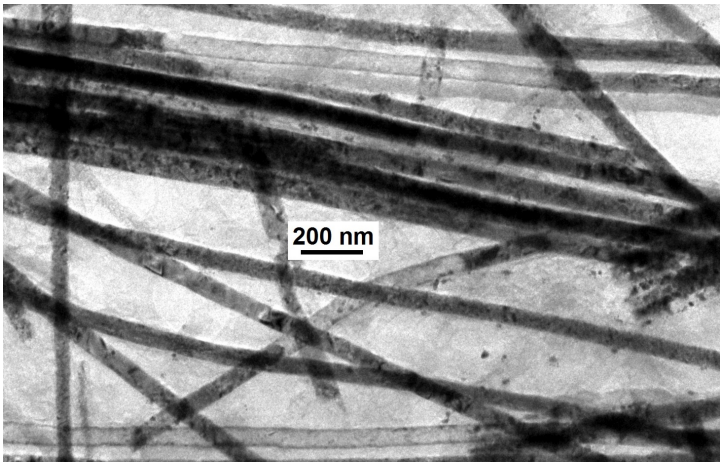

(a) Ni nanowires and twires

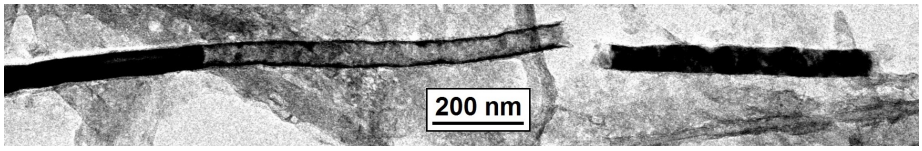

(b) Broken twire

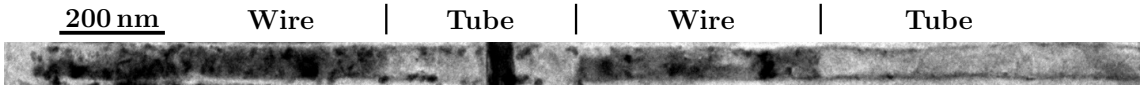

(c) Wire-Tube-Wire-Tube

Fig. 7.4: Transmission electron microscopy images of Ni twires (wire-tube nanoelements) after long dissolution of the template (one day). (a) The majority of nanostructures is formed by solid nanowires, further there are some nanotubes and small portion of tube-wire elements (twires). (b) Broken twire: as the tube wall thickness is very small, many tubes and twires are damaged (if not completely destroyed) during processing of the solution with nanostructures after the template dissolution. (c) Example of a twire with alternating segments (wire-tube-wire-tube). A small nanowire lies across the first tube segment.

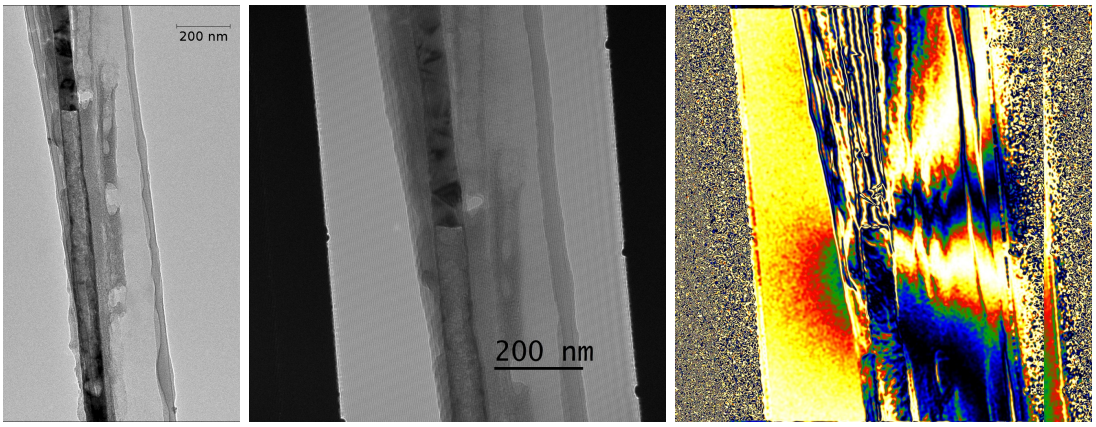

(a) TEM (b) Hologram (c) Amplified magnetic phase

Fig. 7.5: Electron holography on wire-tube-wire Ni nanostructure. (a) TEM image of the whole tube part with wire segments at both ends that extend microns in both directions. (b) Hologram of the upper wire-tube transition and (c) corresponding "amplified" magnetic phase shift reconstruction – $\cos(3\phi_{\mathrm{m}})$ is displayed instead of the magnetic phase ϕ_{m}. Here we can observe stray field coming from the wire-tube transition (mainly to the right of the structure). Except for the transition, magnetization seems to be uniform, along the wire axis. Unfortunately, we cannot say much about the tube part. Low tube wall thickness, together with possible oxidation and lower Ni magnetic moment provides only a feeble signal.

wall thickness (below 10 nm, sometimes just 5 nm) and possible sample oxidation prohibited us from obtaining clear (magnetic) information on the tube part.

7.2.3 Summary of twire investigation

We could fabricate Ni twires (diameters 60-80 nm) with multiple nanowire and nanotube segments (e.g. wire-tube-wire-tube) with extremely sharp transition and longer (at least 2.2 µm) tubular segments than reported in the literature. On the other hand, in our case the yield of such intriguing nanostructures is very low (mostly nanowires are obtained) and basically uncontrolled, so there is still room for improvement (e.g. following the work of Philippe and Michler [29]). But our work shows that it is possible to realize nanostructures with multiple and sufficiently long segments. Similar twires could serve as an experimental playground to test results obtained by simulations on wire-tube elements, including the domain wall nucleation and motion in such systems [30].

For electron holography we had a nice twire (wire-tube-wire), but it was difficult to get magnetic signal just from the nanowire part, not speaking of the tube – see Fig. 7.5. The tube wall thickness below 10 nm (sometimes just only 5 nm) together with possible oxidation, and low spontaneous magnetization compared to other ferromagnets, provided feeble, hard to detect magnetic signal. Thicker tube walls and/or different material should be considered as well as reducing the exposition of the sample to sodium hydroxide during the template dissolution (avoiding sample oxidation).

7.3 Electroless depositions at Institut Néel

As already stated in the methods, we acquired various electroless-plated samples thanks to the collaboration with expert chemists and material scientists from TU Darmstadt. Successful syntheses, capabilities and suitability of the electroless deposition technique for nanotube fabrication led us to a decision to try similar production also at Institut Néel. This would enable us to meet more specific needs and also investigate or further process the NTs while they are still fresh (without oxidation or other modification). Last but not least, collaboration with TU Darmstadt would concentrate rather on more complex (multilayered) NTs, that are currently beyond our reach. Therefore, we attempted to prepare nanotubes using the same procedure as described in the methods section 4.4.

After initial trials on flat substrates (Pd films on Si, bare Si), we proceeded with 20 min long CoNiB deposition in commercial porous membranes (Osmonics Poretics) with quoted pore diameter of 0.1 µm and template thickness of several microns. The

resulting nanotubes (Figure 7.6) had diameters ranging from 100 nm to 200 nm and tube wall thickness around 40 nm. Due to high density of pores in the membrane ($1.5 \cdot 10^8$ pores/cm^2), several defects appeared – mainly intersecting tubes. Further, the tube surface was more rough that in case of tubes prepared at TU Darmstadt using higher quality lab-made templates. The nanotubes were rather short, up to 6-7 microns in length. Still several isolated tubes on a Si substrate could be obtained. Example of their investigation by magnetic force microscopy is given in Fig. 8.25.

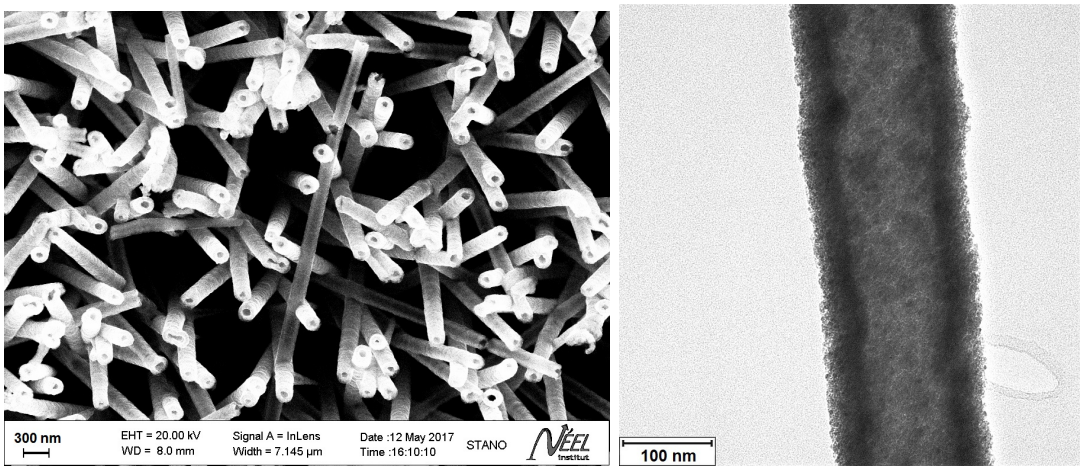

(a) Bundle of CoNiB nanotubes (b) Isolated nanotube

Fig. 7.6: CoNiB nanotubes electroless-deposited at Institut Néel in commercial templates. (a) Scanning electron microscopy of a bundle of the tubes. (b) Transmission electron microscopy of an isolated tube, image courtesy of Laurent Cagnon.

As in future we would like to investigate multilayered tubes and core-shell structures (e.g. CoNiB/Cu for current injection), we also prepared Cu nanotubes (30 min deposition, pH 7.8, see Methods for details) using the same templates types.

The above mentioned nanotubes are very short and therefore quite challenging for making electrical contacts or any domain wall experiments. As the length is limited by the template, different membranes with larger thickness / pore length and also smaller porosity (reducing number of intersecting pores/tubes) would be needed for future experiments.

We also performed successful deposition tests in more ordered alumina membranes (but still having some defects). However, further work is needed in this regard. An example of our first tubes in alumina membrane is shown Fig. 7.7.

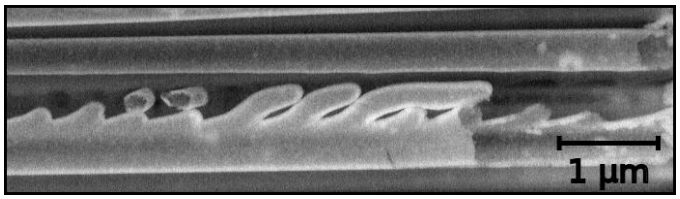

Fig. 7.7: Electroless-deposited CoNiB tubes in porous alumina membrane with a pore branching. Scanning electron microscopy image of a cross-section of porous alumina membrane filled with CoNiB tubes by electroless plating. Backscattered electron detection is employed, this highlight the tube wall (shell) and demonstrates the tubular character of the whole structure. Below a straight tube (top) there is a tube with several pore branching. These parts are filled with CoNiB tubular arms. Three full arm are visible, several others seem to be broken during cutting the membrane for cross-section observation. Even though here it is a defect, it show viability of electroless plating for fabrication on tubes with modulated diameter (protrusion, constrictions).

7.4 Summary of nanotube depositions

We could fabricated NiCo nanotubes by electroplating using porous working electrode according to Zhang [166]. However, some wires were present as well. This problem, wire vs tube growth instability is known [125], even-though not always reported. Our electroplated tubes (diameter around 100 nm) had very thin tube walls, mostly well below 10 nm, but still some were slightly thicker, having 10-18 nm.

Electroplating of Ni in smaller diameter pores (nominal pore size 50 nm) with porous electrode yielded mostly nanowires, some nanotubes and more interestingly also several twires (tube-wire elements) – for more information see section 7.2.1.

Therefore, in our view, the electroplating is viable, but so far not reliable for controlled nanotube fabrication. Also in most cases the tube wall is rather thin, so it might be necessary to protect the tube from oxidation by e.g. atomic layer deposition of layers like SiO_x. Still it has great potential, especially when employed in the coaxial lithography [152].

Our collaboration with TU Darmstadt yielded nice nanotubes prepared by another electrochemical method, electroless plating. As here the deposition start from the pore surface and not the electrode at the bottom of the pore, one gets naturally nanotubes. Thus the technique is more reliable (robust) as for nanotube preparation and the tube wall thickness can be easily controlled by the plating time. We started our own production of nanotubes by the electroless plating at Institut Néel. We could successfully fabricate CoNiB and Cu nanotubes with diameters 100-200 nm. These can be later combined (magnetic shell + Cu metallic core) for studies with current injection (also Cu may be replaced by Pt for spin-current manipulation of

the magnetization). Compared to electroless nanotubes supplied by Sandra Schaefer from TU Darmstadt, ours were more rough and with higher amount of defects. This was mainly caused by the use of an old commercial membrane (template) usually used for filtration and thus not optimized for deposition of nanostructures with uniform geometry.

8 DOMAINS IN CoNiB (NANO)TUBES

In this part (next 2 chapters) we will focus on the characterization of electroless-deposited CoNiB tubes, mainly the SS53 sample fabricated at TU Darmstadt. We will start with structural and chemical analysis and we will continue with magnetic characterization involving synchrotron XMCD experiments, as well as global and local magnetometry; electron holography and magnetic force microscopy. Aside from experiments, we will also provide numerical modelling, both of the micromagnetic configurations and also of the XMCD contrast in the XMCD-PEEM images. We will also give a brief comparison with smaller diameter nanotubes (both ours and from TU Darmstadt) and tubes from a different material – NiFeB.

8.1 Geometry, structure, and chemical composition

Electroless-plated SS53 CoNiB tubes have diameters 300-400 nm, length up to 30 µm and tube wall (shell) thickness approximately 30 nm. With the transmission electron microscopy we observe that the tubes are nanocrystalline (Fig. 8.1a,b) with the following microstructure (Fig. 8.1c,d): 1-2 nm thick boundaries separate 10 nm grains (clusters), themselves displaying an internal structure at the scale of 2 nm. According to preliminary high-resolution chemical analysis (electron energy loss spectroscopy done by Eric Gautier from Spintec), the boundaries are rich in lighter elements (oxygen detected, possibly also boron is concentrated here). A similar microstructure, with *macrograins* embedded in a boron-rich matrix, has been already reported in case of NiB nanoparticles [213].

Regarding the chemical composition, we obtained the proportion of the metals using EDX at higher primary electron beam energy (15-20 keV). The tubes are cobalt rich with Co:Ni ratio approximately 4:1. For boron detection we had to use lower primary beam energies; an example of such EDX spectrum of a single tube acquired with 4.5 keV primary beam energy is shown in Fig. 8.2. The presence of boron is clear (also for primary beam energy of 3.0 keV and 5.0 keV). The boron comes from the reducing agent used during the deposition. It influences the microstructure of the deposit, with higher boron content leading to finer grains and eventually to amorphous material [169].

As for the quantification of the boron presence, we could not obtain reliable results with EDX due to very low counts on the detector. Depending on the primary beam energy and quantification method, the figure for boron content ranged from a few up to almost 30 % at. In the literature, X-ray Photoelectron Spectroscopy (XPS)

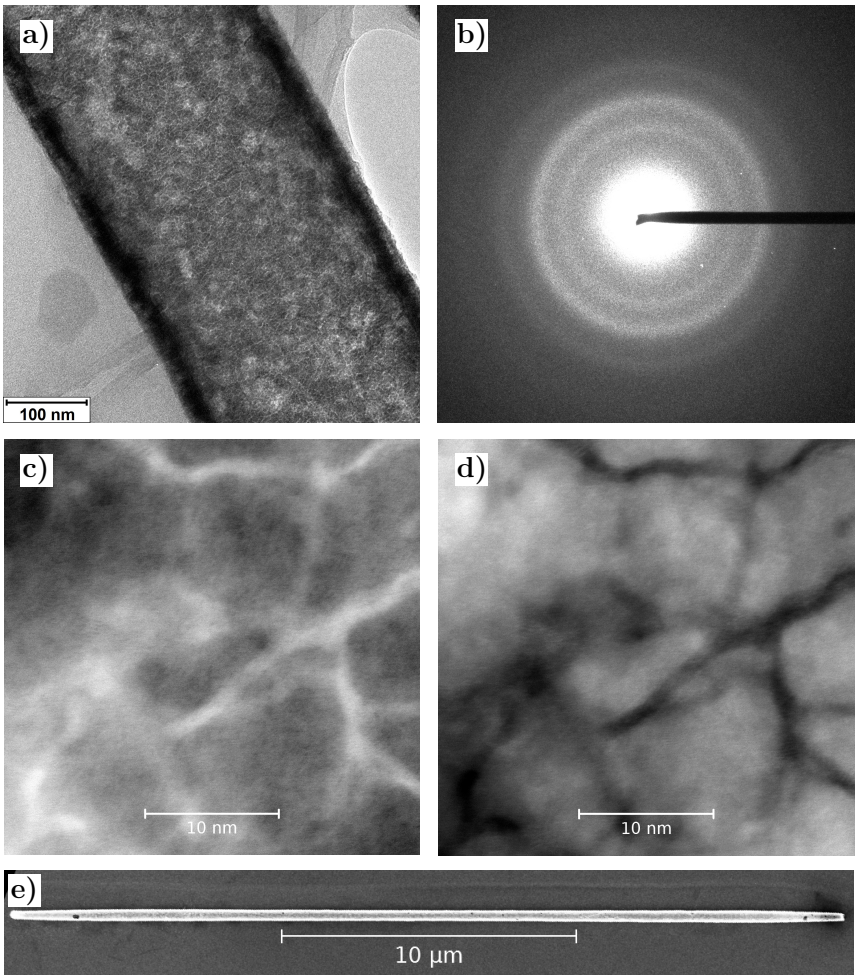

Fig. 8.1: Structure of electroless-deposited CoNiB nanotubes (SS53 sample). a) Transmission electron microscopy image of a nanocrystalline CoNiB tube and b) corresponding selected area (240 nm in diameter) electron diffraction pattern showing diffusive rings originating from nanograins with all possible crystallographic orientations. c) Closer look on the grains with scanning transmission electron microscopy in bright and d) dark field (Z contrast, heavier elements appear brighter). e) Scanning electron microscopy image of a whole tube (another tube, same batch). STEM images courtesy of Eric Gautier.

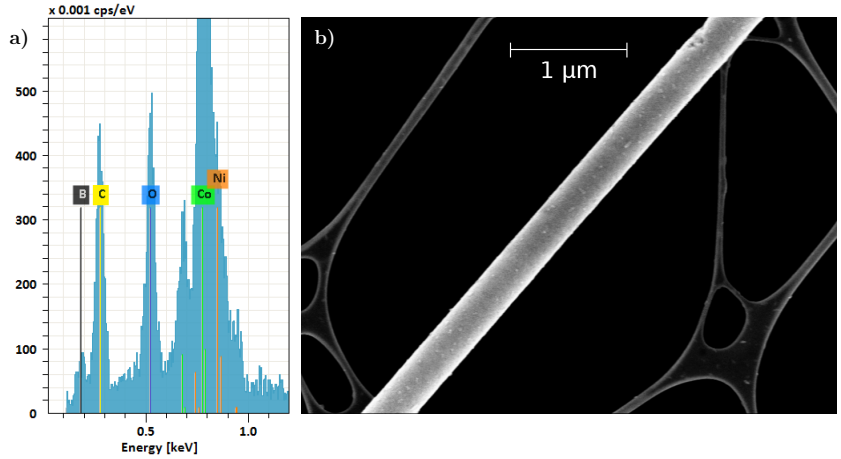

Fig. 8.2: Chemical analysis using EDX. a) EDX spectrum acquired with low primary beam energy (4.5 keV) showing the boron presence aside from expected Co and Ni, as well as C and O coming mainly from the template dissolution and possibly partial tube oxidation for the last-mentioned element. b) Electron microscopy image of the investigated tube on a lacey carbon film. The EDX spectrum is taken in the middle of the tube. Similar results were obtained at different locations (points) as well as when averaging over a larger tube area.

on significantly larger tubes (same concentration of the reducing agent) suggested a negligible B content [127], while Richardson et al. [99] found with XPS around 25% at of boron in electroless-deposited tubes using the same reducing agent (DMAB). They measured similar content for different deposited metals and alloys, concentration of metallic salts in the bath. The Boron content increased with lower pH of the plating bath; it should be also influenced by the concentration of the boron containing reducing agent (DMAB). In our case, on one hand the concentration of boron species in solution was lower (decreases B in the deposit), on the other hand the pH of the bath is slightly lower (increases B in the deposit). Altogether we expect a similar or slightly lower amount of boron in our tubes than reported by Richardson (25% at). Recent preliminary electron energy loss spectroscopy analysis performed at CNRS CEMES suggests that boron content is around 10 %. Further, the Ni content is slightly lower, suggesting that tubes are even richer in cobalt. However, this local analysis has been performed only on few small areas of a tube, whereas for EDX we have data both from small areas and average values along a tube or clusters of tubes.

Aside from above-mentioned elements (Co, Ni, B), sometimes traces of Pd (seed particles in the deposition) and Sn (template modified with Sn species) were detected with EDX as well. In theory, Pd particles if still present on the outer tube wall, could influence tube magnetic properties (via surface anisotropy or even the

DMI). However, in our case we suppose that such effects are negligible due to low Pd content (Pd partially replaced with Co and Ni during the plating process). On the other hand, one can prepare thicker layer of Pt or Pd in order to study such potentially interesting effects. The presence of C and O in EDX spectrum is attributed mainly to the dissolution of the polymeric template, TEM grid with the C film, and unavoidable partial carbon contamination and surface oxidation. To summarize the analysis, both the electroless-deposited tubes and thin films have approximate composition $(Co_{80}Ni_{20})B$ and are formed of very fine nanograins.

Further, we also analysed CoNiB tubes by X-ray absorption spectroscopy in the energy range covering both Co-L_3 and Co-L_2 absorption edges. We do not detected the X-ray absorption directly, but through a collection of photoelectrons emitted upon absorption of X-rays (X-PEEM technique). An example of such spectrum is given in Fig. 8.3 together with X-PEEM images of the tube acquired at different X-ray beam energies. The photoelectron signal in the shadow is inverted with respect to the tube surface: higher photon absorption in the tube means higher yield of photoelectrons from the surface, but also smaller amount of transmitted photons that create smaller number of photoelectrons from the substrate surface in the shadow area. From the shape of the peaks (dips) we can conclude that the tubes are metallic without significant oxidation (see comparison of cobalt and cobalt oxide spectra in Fig. 5.1b). Aside from analysis of the whole tube, we also inspected separately signal coming from the tube surface, as well as different parts of the shadow. Close to the shadow rim, the dip (inverse peak) is broader indicating slight oxidation in this area. As both tube (top) surface and centre of the shadow (volume information) are rather sharp, it is the inner tube surface that is partially oxidized and leads to broadening of the dip acquired from the rim of the shadow. This is not surprising given that after the fabrication, tubes stay inside polymeric matrix and only the inner surfaces of the tubes are directly exposed to the air. In magnetic imaging described later we even see a grey line (no-magnetic signal) in the shadow area corresponding to inner surface (Fig. 8.4a, Fig. 8.7-top).

XAS is also used for a precise determination of Co-L_3 edge for magnetic imaging using XMCD-PEEM that will be featured in next sections. The energy of the edge is taken from the dip in the shadow that reflects the integrated volume information, rather than from the tube surface. There are two main reasons for this choice: the shadow contains important information and the energy of the edge determined from the tube surface can be shifted due to presence of impurities and/or oxidation. In the above-mentioned case, the photoelectron peak on the surface coincides with the dip in the shadow, but generally it is not the case, especially as the surface is sometimes oxidized. For this reason, during synchrotron investigation we collect XAS on many tubes, sometimes repeatedly for the same tube (e.g. after annealing).

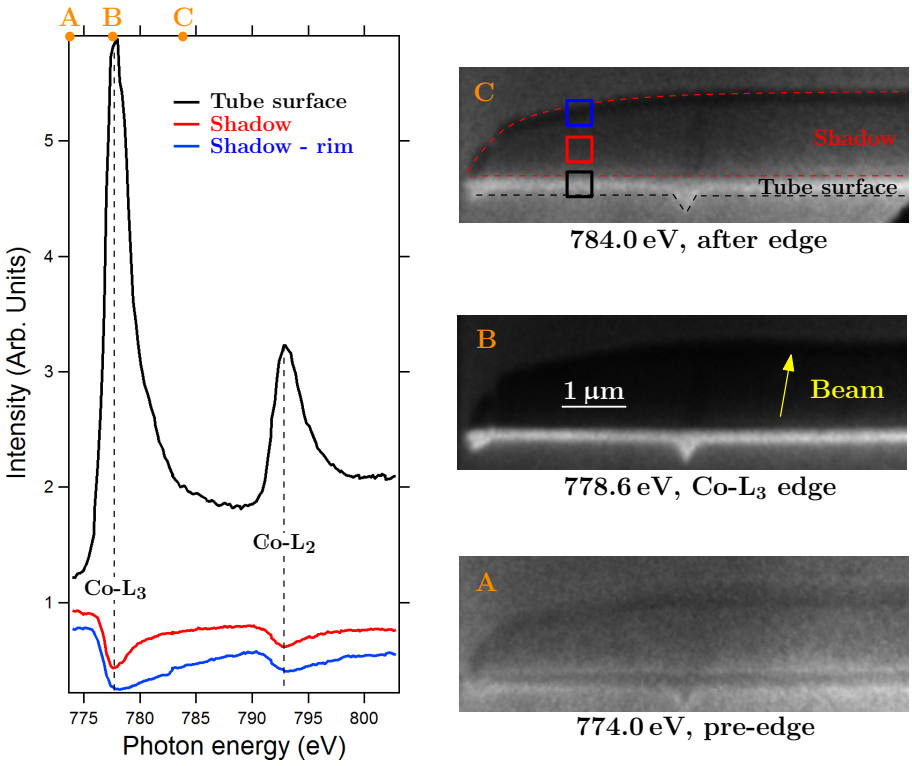

Fig. 8.3: X-ray absorption spectroscopy on a CoNiB tube detected via photoelectron collection. Curves for three different sample areas are featured: tube surface, shadow and rim of the shadow. X-PEEM images for different photon energies are on the right (pre-edge, edge, and post edge). Note that the curves in the graphs are averaged from almost the whole tube surface/shadow/shadow rim, examples of smaller parts of these areas are given in X-PEEM image C (post edge).

8.2 Azimuthal domains

One of the first measurements performed on fresh electroless-deposited tubes from Darmstadt was magnetic force microscopy. Given the elongated tube geometry and based on magnetization phase diagrams already discussed in section 3.1.1, we supposed that tubes should be axially magnetized (or more precisely in the so-called mixed state). The imaging relying on the 2-pass tapping-lift mode (Ntegra Aura microscope) turned out to be difficult due to the large diameter of the tubes (around 300 nm) and small shell thickness. First trials resulted even in damaged tubes – holes created by the tip or even completely cut tubes (consult Fig. S1). Therefore, we were forced to scan slowly (<4 µm/s) and with a high feedback gain in order to avoid tube damage. Even with such parameters, we were unable to recover any clear magnetic signal from these tubes at remanence. Some weak magnetic signal could be detected at tube end only when imaging under external magnetic field applied along the tube (switching polarity when reverting the field direction).

As arrays of tubes were strongly attracted by a permanent magnet, the MFM images showing no or very weak magnetic signal were quite puzzling. Therefore, we moved on to synchrotron investigation of the tubes as it is more sensitive and may provide more direct information on the orientation of magnetic moments. Fig. 8.4a displays an XMCD-PEEM image of two orthogonal tubes. Surprisingly, the magnetic contrast is insignificant for the tube aligned parallel to the X-ray beam direction, while it is much stronger when the beam is transverse to the tube axis. This shows that magnetization is not axial as expected from theory for long soft magnetic tubes [21], but it is perpendicular to the tube axis. Examination of the shadow reveals an inversion of contrast for X-rays having gone through the top and bottom parts of the tube (Fig. 8.4b), whereas uniform transverse magnetization would give rise to a monopolar contrast [153]. This proves that magnetization is not uniformly transverse in the tubes but azimuthal, curling around the tube axis. Similar contrast patterns have been reported for (localized) curling in nanowires[13, 15]. Now, the difficulty with obtaining magnetic contrast in MFM is understandable. The azimuthal, flux-closure, domains produce no stray field. Still there should be something to measure – stray field from the domain walls as we know that there are many domains in the CoNiB tubes. However, this dipolar field can be quite weak as will be discussed later.

We imaged the azimuthal domains also with scanning transmission X-ray microscopy (STXM) with the beam perpendicular to the tube axis (and the whole supporting Si_3N_4 substrate) – see Fig. 8.5. We could already infer the domains just with one beam circular polarization. The obtained XMCD contrast is analogous to XMCD-PEEM contrast in the shadow (also transmission).

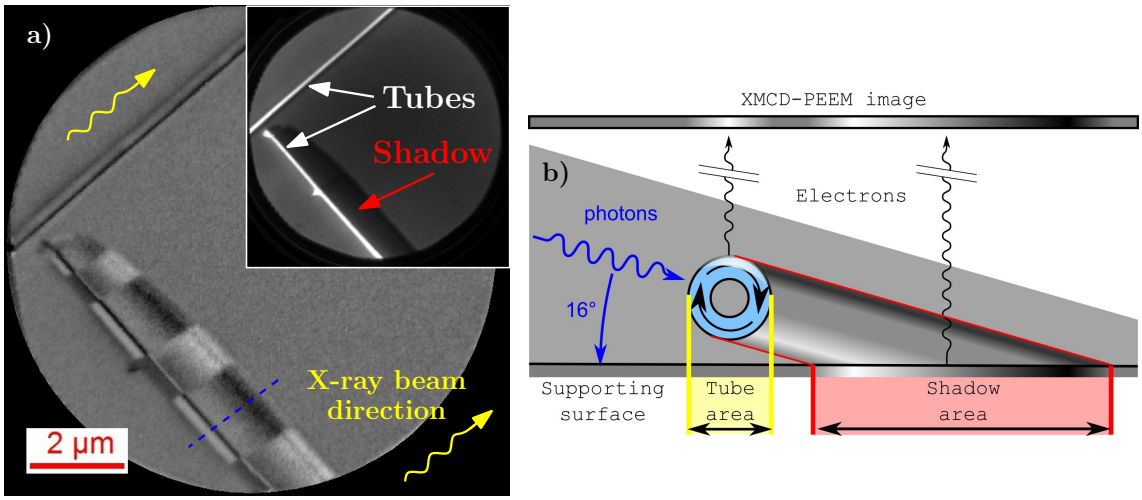

Fig. 8.4: Magnetic azimuthal flux-closure domains. a) XMCD-PEEM (Co-L_3 edge) image of two orthogonal tubes. The tube almost along the beam (top) gives rise to almost zero contrast, whereas strong contrast is observed for the tube perpendicular to the beam, revealing domains with azimuthal magnetization. The grey line in the shadow close to the rim comes from oxidation of the inner tube surface (nonmagnetic). The inset shows a photoemission electron microscopy image of the tubes. b) Scheme with the azimuthal magnetization and XMCD-PEEM contrast corresponding to a line profile of an azimuthal domain marked by a blue, dashed line in a). Note that in the experiment the tubes lie on the substrate and only part of the shadow can be observed. Sometimes contrast inversion can be seen also at the back side of the tube area as detailed and explained in [153].

Note that the tube is multidomain: the sense (sign) of the circulation of the flux-closure alternates along the tube axis. Such tubes provide a key advantage over longitudinally-magnetized systems in the context of devices like the racetrack memory (Fig. 8.6a), as flux-closure domains would drastically reduce the interaction between neighbouring elements via their stray field. The density of domains can be very high, 5/µm or more, upon demagnetization (Fig. 8.6b). The possibilities of using tubular racetracks instead of vertical strips or solid wires are further discussed in chapter 12 (Conclusion & Perspective).

(a) Circular Left (-)

(b) Circular Right (+)

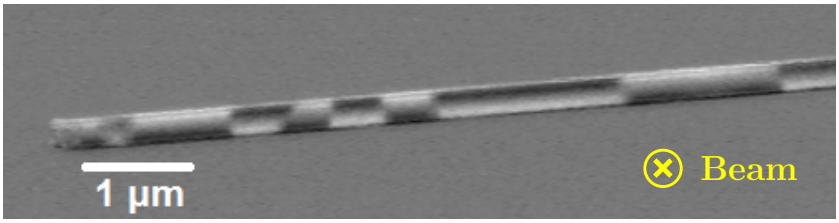

(c) X-ray Magnetic Circular Dichroism

Fig. 8.5: Scanning transmission X-ray microscopy of a CoNiB tube (SS53, tube Analena) at the Co-L_3 edge (778.1 eV). Even with a single circular polarization one can see a strong magnetic contrast (difference in absorption): (a) Image for circular left, (b) circular right polarization. (c) illustrates the XMCD (difference of the two beam polarizations). Images obtained on the same batch of tubes one year after the first XMCD-PEEM beamtime.

8.3 Magnetic anisotropy

Let us now turn to the reason for azimuthal magnetization. We find very similar domains following either AC-field demagnetization along the transverse direction, or saturation along the tube axis. Therefore, the azimuthal curling seems to be the ground state for this material and geometry. Recently, Wyss and coworkers [79] observed with XMCD-PEEM CoFeB and NiFe nanotubes (around 300 nm in diameter, 30 nm tube wall thickness, formed by sputtering on semiconducting nanowires with a hexagonal cross-section). They found the curling state (*global vortex*) only for tubes shorter than 1-2 µm (our tubes have 20-30 µm); longer tubes displayed axial

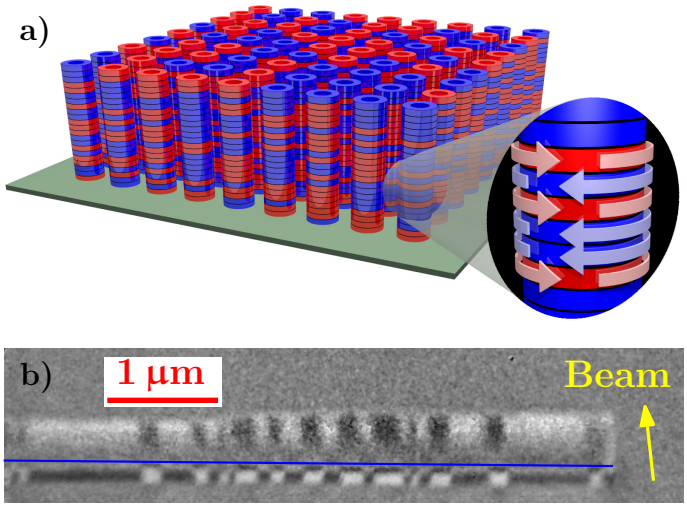

Fig. 8.6: Tubular magnetic racetracks. a) Scheme: bits of information would be coded by azimuthal domains with opposite circulation of magnetization. Flux-closure domains significantly reduce the stray field and thus the cross-talk in a dense array of tubes in a potential memory device. b) Experimental shadow XMCD-PEEM image of a CoNiB tube (on Si substrate) with many azimuthal domains. The field of view features 28 domains, with some of them being very narrow, not speaking of the domain walls themselves. The blue solid line is the approximate boundary between signal coming from the tube surface (below) and shadow (above the line).

magnetization with the curling only at the tube ends as expected from theory [21]. Similarly, our tubes should display axial magnetization (consult magnetization phase diagrams in [21, 76, 77]). Thus, we argue that an additional contribution, magnetic anisotropy, has to be present to promote alignment of magnetization in the azimuthal direction.

First, we provide arguments for describing and extracting the strength of the microscopic magnetic anisotropy favouring azimuthal magnetization. We start with addressing a question: What is the functional form relevant to describe the volume density of magnetic anisotropy, as none of the three local directions are equivalent (radial $\hat{\boldsymbol{r}}$, azimuthal $\hat{\boldsymbol{\phi}}$ and axial $\hat{\boldsymbol{z}}$)? Given the large aspect ratio of our tubes, we assume that the local shape anisotropy (i.e. magnetostatic energy) is the dominant energy term. This is also justified later by showing that an anisotropy field determined from hysteresis loops is small compared to spontaneous induction (tens of mT and about 1 T, respectively). Further, we suppose zero radial magnetization ($m_r = 0$) in magnetic domains ($m = \frac{M}{M_\mathrm{s}}$). Thus, describing the anisotropy with terms $-K_\phi m_\phi^2$ or $K_\phi m_z^2$ should be equivalent, because $m_\phi^2 + m_z^2 \approx 1$. $K_\phi > 0$ favours azimuthal magnetization.

On the basis of the moderate wall thickness (30 nm compared to 300 nm diameter for our CoNiB tubes; in general valid for thin-walled tubes), we assume that radius-dependent variations are averaged out and taken into account in an effective uniform value of K_ϕ. A first contribution to K_ϕ is magnetic anisotropy related to the (crystal) lattice K_m: magnetocrystalline, magnetoelastic or interface anisotropy (to be discussed later in the text). A second contribution is related to the exchange energy, whose volume density reads, for $m_r = 0$ [21, 214]: $E_\mathrm{ex} = (A/R^2)m_\phi^2$ with A being the exchange stiffness constant and R the tube radius. The term reflects curvature-induced anisotropy that forces $\vec{m}$ to deviated from the azimuthal direction (and lie e.g. in the axial direction): curvature induces a spatial variation of magnetization for a uniform m_ϕ, due to the non-uniformity of $\hat{\boldsymbol{\phi}}$. Uniform m_z is associated with no spatial variation, so it does not contribute. The exchange contribution leads to axial magnetization in nanotubes with small diameters as already shown in the magnetization phase diagrams (see Fig. 3.2). The total anisotropy coefficient is $K_\phi = K_\mathrm{m} - A/R^2$. This can be converted into an anisotropy field $H_K = 2K_\phi/(\mu_0 M_\mathrm{s})$. Measuring the latter experimentally allows one to estimate the microscopic anisotropy energy coefficient: $K_\mathrm{m} = A/R^2 + \mu_0 M_\mathrm{s} H_K/2$.

Now we will introduce measurements of CoNiB tubes under external magnetic field, enabling determination of the anisotropy field and thus estimation of the anisotropy coefficient K_m. Later we return to the question of origin of the anisotropy (magnetocrystalline, magnetetoelastic, interface, ...), effect of a thermal annealing, material composition and geometry on the magnetization direction in the domains.

8.3.1 Strength of the azimuthal anisotropy

In order to determine the magnitude (strength) of the azimuthal anisotropy and to gain further information on the magnetic properties of our tubes we performed experiments under magnetic field both on arrays of tubes (global magnetometry) and isolated tubes (synchrotron XMCD and magnetooptics with focused laser). We will focus on experiments with magnetic field applied in the axial direction, which should correspond to a hard magnetic axis. In such case the saturation field (i.e. field needed to align the magnetization in the axial direction) should be related to the anisotropy field.

XMCD imaging under magnetic field

First we carried out XMCD-PEEM imaging (detection via photoelectrons) at Elettra under external magnetic field with the beam transverse to the tube axis. Even imaging in few mT was challenging and required microscope alignment (after each change of the field) as the photoelectrons are influenced by the applied field. We applied magnetic field close to along the tubes and increased its value and observed a progressive loss of the contrast upon imaging (Fig. 8.7). This suggests that magnetization rotates towards the axis, perpendicular to the beam direction. Thus, there is smaller projection of magnetization onto the beam direction. We could acquire reasonable images up to 10 mT. At higher field values (up to 13 mT), the signal acquisition was very difficult (poor signal/noise, deteriorated spatial resolution). At the limiting field (13 mT) the tubes still displayed signs of the azimuthal domains, indicating that higher field should be applied to achieve the saturation. After the first application of the field, we observed (dis)appearance of small domains, we suspect that this may come from the current spike discussed in the methods (no spike during increase of the field).

Due to the limitations of XMCD-PEEM under the field (photoelectrons affected by the field), we later employed STXM with direct detection of transmitted photon to probe tube behaviour in higher fields. Note that even though photons are not affected by the field, the electronics – especially some types of X-ray detectors (photomultipliers) – could be influenced if not shielded properly (altered or even no signal at all). Summary of this investigation is displayed in Fig. 8.8. With the increasing field magnitude, we detected the expected gradual loss of the signal. Images under magnetic field applied in the opposite direction are very similar to the ones presented here. Approximately 25 mT were required for the tube saturation in the axial direction. After removing the field, at remanence, the tubes mostly return to the flux-closure domain pattern with a very small remanent magnetization.

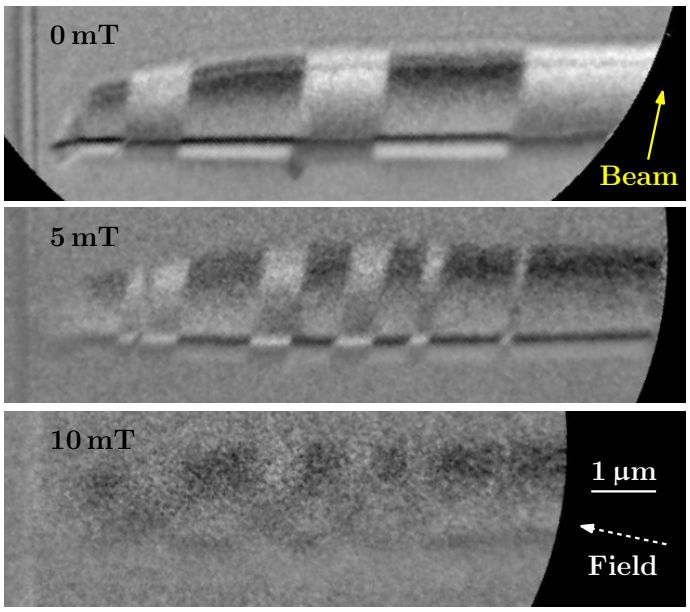

Fig. 8.7: XMCD-PEEM imaging of a CoNiB tube under external magnetic field. The yellow arrow (solid shaft) shows the beam direction and the white one (dashed shaft) the applied field direction. Images are aligned on the left side (vertical bar and left end of the tube). As the original field of view shifts with the field, it is not easy to recover exactly the same field of view (this lead to the black regions on the right).

We observed also some deviations from the expected contrast in the domains (e.g. red circles in the STXM image). They were most prominent at remanence (zero field after previous magnetization along the tube), but present also under smaller field values. These deviation consisted of triangular or trapezoidal areas of completely opposite contrast than in the domain. Upon different magnetic history their size and position changed, they were not present for the initially AC demagnetized tubes (see Fig. 8.5). In addition, the transition between domains is not as sharp as in the previous XMCD-PEEM imaging. This we attribute to sample ageing (STXM done 1 year after the first XMCD-PEEM) manifested mainly by more pronounced sample oxidation (determined from XAS). Further, in some tubes we found regions with weaker contrast that may indicate more pronounced oxidation or axial magnetization component (i.e. component now perpendicular to the beam direction). Therefore, the magnetic state of these aged tubes after remagnetization seems to be far more complex (also with several different domain boundary patterns) than for AC demagnetized fresh tubes. We still lack the complete understanding of the magnetic state.

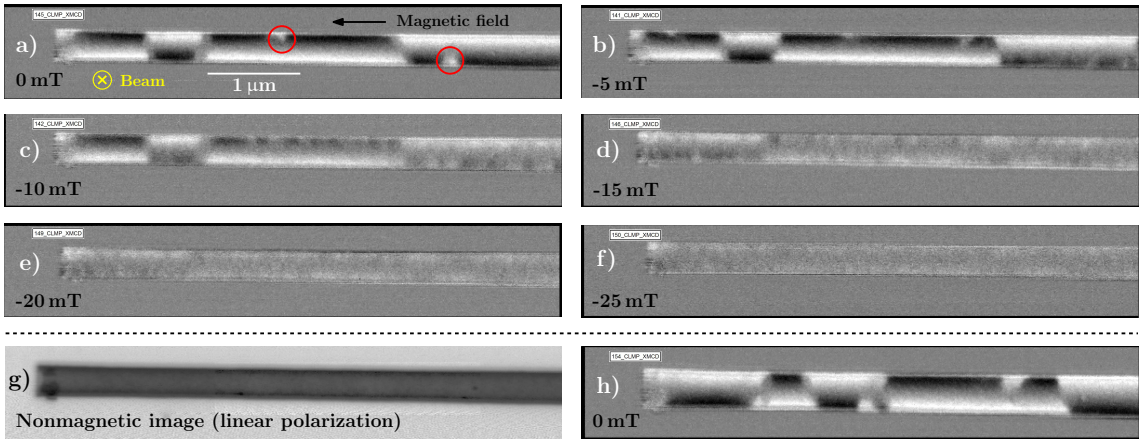

Fig. 8.8: STXM under external axial magnetic field. a)-f) XMCD magnetic images (same contrast range 15%) under axial magnetic field. With increasing field magnitude, the STXM contrast vanishes, showing that magnetization rotates towards the axial direction. Approximately 25 mT is needed for the saturation of tubes along the axial direction. Field of view a)-g) $6.0 \times 1.0\,\mu m^2$ and h) $6.0 \times 0.8\,\mu m^2$. g) Nonmagnetic STXM image (linear polarization of X-rays) highlighting the tubular structure. h) XMCD image after removing the magnetic field (after sequence a-f, image size $6.0 \times 0.8\,\mu m^2$).

Magneto-optics with focused laser

Aside from the X-ray microscopies, we also measured isolated tubes dispersed on a Si substrate via the Magneto-Optical Kerr Effect (MOKE), implemented in the

longitudinal configuration with a focused He-Ne ($\lambda = 632.8\,\mathrm{nm}$) laser (spot $1\,\mu\mathrm{m}$). The field was swept as a triangular wave signal, with frequency 1.1 Hz, and field calibration uncertainty max $\pm 5\,\mathrm{mT}$. For the measurements presented below, the laser power was 1.1 mW, for some measurements we used just 0.2 mW. Fig. 8.9 shows hysteresis loops obtained on the tubes. Some loops are slanted (Fig. 8.9a) with almost no remanence (tube axis = hard axis for magnetization) which is consistent with the synchrotron data, where magnetization is azimuthal at remanence (perpendicular to the tube axis) and under axial field gradually rotates towards the axis (see Fig. 8.8). However, in some cases (different tubes, even different tube part in one instance) the loops are quite squared (Fig. 8.9b).

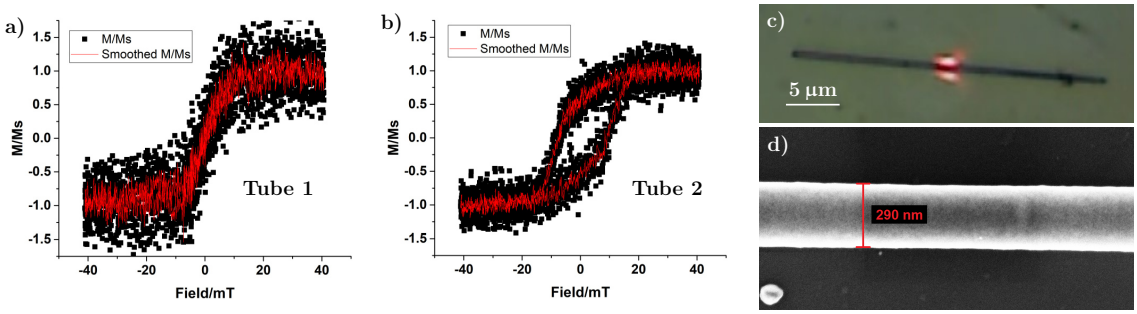

Fig. 8.9: Magnetometry on a single tube - magnetooptics with focused laser. Hysteresis loops for the axial magnetic field (longitudinal MOKE): a) slanted curve, b) rather squared loop obtained on another tube. Average of 100 loops with a short acquisition time (0.9 s). Data processed in OriginPro: line subtracted, normalized, smoothed: average of 7 adjacent points (red curve) – original curve had 5000 points (black points). c) Optical image (magnification 100x) of a tube with the diffracted laser spot, the magnetic field is applied in the horizontal direction, close to parallel to the tube axis. d) Scanning electron microscopy image of a central part of the tube from c).

This was also the case when one tube (previously non-irradiated) was probed with just 0.2 mW laser power – close to the minimum power we can apply and measure some magnetic signal for tubes in our setup. We assume that the loop squareness is caused by a laser heating due to a bad thermal contact with the substrate for some tubes. As tubes are dispersed from a solution, template dissolution products may create a halo around structures and decrease the thermal conductivity of the contact. In addition, in case of tubes (cylindrical objects in general) the contact area is rather small. Hysteresis loops acquired with higher laser power show larger squareness. Further, the signal is higher, but less stable (drift). For the power of several mW and longer time exposure, we noticed that some of our tubes are damaged – see annex A.2. Only several tubes were measured with MOKE

compared to several tens of tubes investigated by higher resolution X-ray microscopies. Therefore, in the determination of the anisotropy strength we rely on the X-ray microscopy (STXM under field). Nevertheless, in case of the slanted curves the saturation field is comparable to the one obtained from STXM (Fig. 8.8).

Magnetometry on tube array

Fig. 8.10a shows a hysteresis loop obtained by VSM-SQUID for an array of CoNiB tubes in a polycarbonate matrix with magnetic field applied along the tubes. The pore density is very low (Fig. 8.10b) and the hollow nature of tubes reduces the total magnetic moment compared with wires of identical (outer) diameter. Thus we expect weak magnetostatic interactions, contrary to the case of anodized alumina templates and solid nanowires [215].

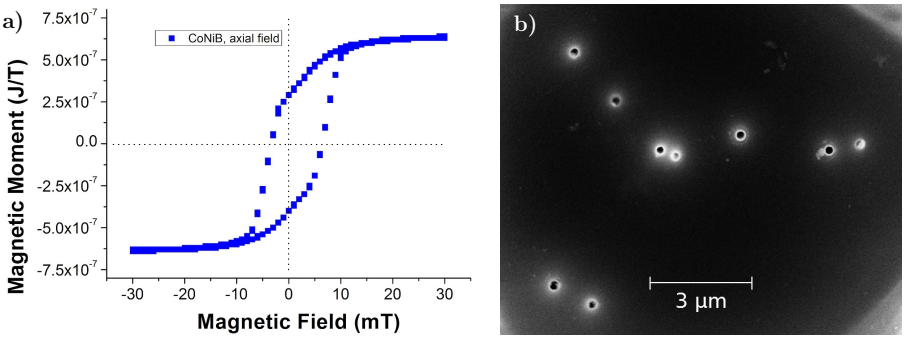

Fig. 8.10: Magnetometry on array of CoNiB tubes (axial field). a) Hysteresis loop on a sparse array (low density, low interactions) of CoNiB tubes in the polycarbonate template, measured by VSM-SQUID at room temperature. The field is applied parallel to the tube axis. Note the large remanence (not consistent with azimuthal magnetization). The slight shift of the loop towards positive fields is rather a problem of the instrument calibration than real effect (such as exchange bias). b) Scanning electron microscopy, top view of a part of the measured template illustrating the low density of pores.

Note that the hysteresis loop obtained on the array of tubes (still in the template) is rather squared with significant remanence. This opposes the measurement on tubes isolated from the template, where X-ray microscopies displayed magnetic states (azimuthal domains) with very low remanence. Also some loops acquired with focused magneto-optics on isolated tubes were slanted, unlike the ensemble of tubes. Therefore, aside from the possible interactions between the tubes we cannot rule out that liberation of tubes from the template and laying them on a supporting substrate can alter their properties. Note that the template with the array of tubes is already polished, thus the difference is not caused by a polishing-induced

strain. On the other hand, the polishing is not perfect and parts of the top/bottom film on the template are still present (few patches visible also in Fig. 8.10b). Despite this unpolished area being small, we cannot rule out its contribution in the magnetometry.

Determination of the anisotropy strength

Experimentally, we estimated the anisotropy field H_K based on the series of scanning transmission X-ray microscopy images acquired under different external magnetic field applied along the tube axis (Fig. 8.8). Upon increasing the field, the domain contrast decreases, which shows that magnetization gradually rotates towards the axial direction. Therefore, such behaviour would correspond to hysteresis loop measured for hard axis – slanted curve with zero remanence (such as in Fig. 8.9a). In such case the anisotropy and saturation fields are closely related. Even-though the method cannot give a precise measurement of the anisotropy, it still enables us to obtain reasonable estimate of the anisotropy. It is difficult to extract quantitatively the direction of magnetization in series of STXM, because of the exponential decay of photon intensity inside matter, uncertainties in the dichroic coefficient, and the existence of a background intensity in the image. We can only provide an estimate of the H_K from the fields where all contrast vanishes in the corresponding images. We find $\mu_0 H_K \approx 25\,\mathrm{mT}$.

As regards the conversion of H_K to the anisotropy constant, we do not have a direct measurement of the exchange stiffness of our material, however for example $Co_{80}B_{20}$ has $A \approx 10\,\mathrm{pJ/m}$ [216]. This value may be different in our case, but the order of magnitude should be correct. Besides, the tube diameter is large, so that the exchange penalty correction to the anisotropy is rather small, less than few mT of equivalent field, which might be well within the error/spread of the experimentally determined anisotropy field. Further, similar to the curvature-induced anisotropy (exchange contribution), curvature-induced effective Dzyaloshinskii-Moriya interaction is expected to be negligible as it also scales with the curvature, being more pronounced for tube diameters below 100 nm. Therefore, we arrive at an estimate of the anisotropy constant $K_\mathrm{m} \approx 10\,\mathrm{kJ/m^3}$. However, this value may be affected by a sample ageing (discussed further in section 8.3.5). The one-year-old sample, initially used for XMCD-PEEM and later for STXM, shows less sharp azimuthal domains and a weak axial component of the magnetization, although it has been kept under primary vacuum. Therefore, the initial value (giving well defined azimuthal domains with Bloch like domain walls), may have been higher (i.e. tens of $\mathrm{kJ/m^3}$).

8.3.2 Origin of the azimuthal anisotropy

As our tubes are cobalt-rich, the first contribution coming to mind is the magnetocrystalline anisotropy. However, as our tubes are nanocrystalline with a random texture (see diffraction rings in Fig. 8.1b), we rule out the magnetocrystalline contribution. There must be another source of magnetic energy, for which the degeneracy between the axial $\hat{\boldsymbol{z}}$ and the azimuthal $\hat{\boldsymbol{\phi}}$ direction is lifted. While both directions are normal to the radial direction $\hat{\boldsymbol{r}}$, and are thus locally similar to two the in-plane direction for a thin film, the difference is the existence of curvature along the azimuthal direction. We consider below two possible sources of magnetic anisotropy that could arise from the direction-dependent curvature: intergranular interface anisotropy and magneto-elastic coupling (inverse magnetostriction). Owing to the radial growth process (Fig. 4.3), grains are expected to have their shape and size varying differently along the two directions. We detail below handwaving models, and show that both sources could in some cases provide a strength of anisotropy whose order of magnitude is consistent with the experimental data.

Interface anisotropy

As our samples are nanocrystalline, the proportion of atoms in the vicinity of a grain/cluster boundary is not negligible, so that interface anisotropy K_s with e.g. boron-rich grain boundaries could arise. We consider a tube with outer diameter 250 nm and wall thickness 25 nm. Assuming an isotropic grain size l_0 upon nucleation from the outer diameter, the azimuthal grain size l_ϕ at the inner diameter should be reduced by 20 % (outer radius 125 nm, inner one 100 nm and thus (125 nm-100 nm)/125 nm=0.2; the grain size along the azimuth is directly proportional to the radius). We further assume that the grain size along the tube axis l_z stays almost constant (some small tensile strain is possible as a result of compressive strain in the radial direction). Thus on the average along the radius the anisotropy of grain size $\delta = \frac{\langle l_z\rangle - \langle l_\phi\rangle}{(\langle l_z\rangle + \langle l_\phi\rangle)/2}$ is 0.1, yielding a slightly wedge-shaped grain (such as in Fig. 4.3c); $\langle l_\phi\rangle = 0.9 l_0$, $\langle l_z\rangle = 1 l_0$ being average grain sizes along the azimuth and the tube axis, respectively, and l_0 is the grain size on the outer surface. Transmission electron microscopy suggests that the grain size is of the order of $t = 10$ nm. The anisotropic contribution of K_s to the effective volume magnetic anisotropy K_eff is $2\delta K_\mathrm{s}/t$. Considering $K_\mathrm{s} \approx 0.2\,\mathrm{mJ/m^2}$ as an estimate (values nearly one order of magnitude higher may exist at some interfaces, for instance between 3d elements and some oxides [217]), one finds: $K_\mathrm{eff} \approx 4 \cdot 10^3\,\mathrm{J/m^3}$. Expressed as the anisotropy field: $H_\mathrm{eff} \approx 2K_\mathrm{eff}/(\mu_0 M_\mathrm{s}) = 8 \cdot 10^3\,\mathrm{A/m}$ or $\mu_0 H_\mathrm{eff} \approx 10\,\mathrm{mT}$. This is of the same order of magnitude as the measured value of 25 mT. Another contribution of interface anisotropy may be due to the curvature of the outer and inner parts of the grains,

so that the orientation of atomic bounds is on the average slightly different along the axial and azimuthal directions. A proper modelling would, however, require advanced information about the structure of the interface, which is not available.

Magnetoelastic anisotropy

Borides of 3d ferromagnetic elements are known to display sizeable magnetoelastic effects [218] (except for few particular compositions, e.g. $(Ni_{80}Fe_{20})B$ with almost zero magnetostriction), and electroless plating is also known to deliver strained materials. It is probable that the expected wedged shape of the grains described above (also see Fig. 4.3c), induce a building of higher compressive strain ϵ along $\hat{\boldsymbol{\phi}}$ while the grain grows inward, because there is less and less space to accommodate incoming atoms. Tensile strain along $\hat{\boldsymbol{z}}$ may be expected from elastic theory, as a reaction to the compressive along $\hat{\boldsymbol{\phi}}$. An extra isotropic strain in the ($\hat{\boldsymbol{\phi}}$, $\hat{\boldsymbol{z}}$) plane may also be expected from the electroless deposition. Further strain may come from the rapid dissolution of the polycarbonate template used for the fabrication of tubes. The saturation magnetostriction of Co-rich CoNi borides is of the order of $\lambda \approx -6 \cdot 10^{-6}$, more values with references can be found in Tab. 8.1. For 3d metals the combination of elastic coefficients $c_{11} - c_{12}$ is of the order of $10^{-11}\,\mathrm{N/m^2}$, or $10^{-11}\,\mathrm{J/m^3}$. Thus, the linear magnetoelastic coefficient is $B_1 \approx -10^6\,\mathrm{J/m^3}$. An anisotropy of strain of $0.4\,\%$ would therefore be required to account for the observed microscopic anisotropy.

Considering our fabrication method, material and comparison with NiFeB tubes in the following section, we would like to put forward the magnetoelastic coupling as more likely source of the anisotropy. Most of electroless-deposited films are strained, even on a flat substrate. Fig. 8.11 shows an extreme case of thicker CoNiB film we deposited on a Si substrate. Internal stress was relaxed by formation of micro- and nano-cracks, delaminating parts of the film and partially rolling it, sometimes forming "Swiss rolls". Streubel et al. [94] used more controlled strain engineering to fabricate similar "microtubes" (but with better defined geometry). Some degree of strain is expected also for smaller thickness; curved tube surface [34] and radial deposition in confined pores (Fig. 4.3) can only enhance this effect.

To conclude this part, electroless-grown materials are expected to develop nanograins with some anisotropic structure features along the radial and azimuthal directions, associated with the local curvature of the supporting surface, be it shape or strain. The resulting contribution to magnetic anisotropy could arise from both interface anisotropy and magnetoelastic coupling. Realistic figures show that both sources could explain the experimental results. Having in mind comparison with NiFeB tubes below, we would put forward the magnetoelasticity. However, without

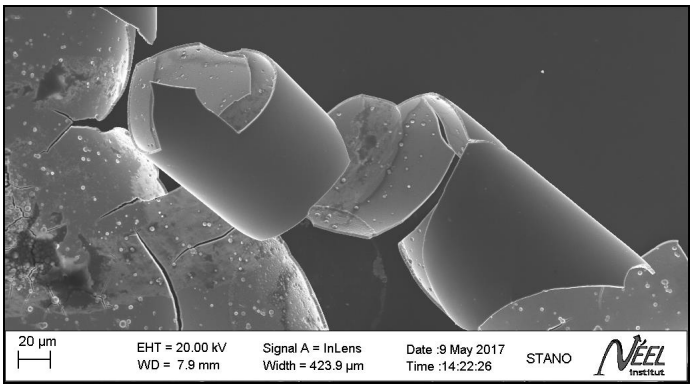

Fig. 8.11: Thick CoNiB electroless-deposited film on a Si substrate. The internal stress is relaxed by cracks in the film as well as delamination and rolling parts of the film, sometimes forming Swiss rolls or tube-like structures. Here an extreme case with 2 µm thick film is shown, but some degree of internal strain is expected for smaller thickness (delamination and rolling was not observed for films below 100 nm provided by TU Darmstadt).

further knowledge on the structural anisotropy of the nanograins, which would be challenging to access, it is not possible to decide unambiguously which phenomenon is dominating.

8.3.3 Comparison with NiFeB tubes

For comparison we also considered nanocrystalline electroless-plated tubes with very similar geometry (diameter 350-390 nm) but from $(Ni_{80}Fe_{20})B$. These proved to be axially magnetized (Fig. 8.12, see also electron holography in Fig 8.13). The difference between the two materials is the strength of the magnetostriction, which is sizeable and negative for $(Co_{80}Ni_{20})B$ (Tab. 8.1), and nearly vanishing and positive for $(Ni_{80}Fe_{20})B$ [218]. In addition, Fe-based alloys are also known to display lower interfacial anisotropy. In other words, both above-discussed anisotropy sources are expected to be weaker in magnitude for NiFeB tubes. Thus, it is not surprising to recover the axial magnetic state predicted by theory in tubes made of a magnetically-soft material.

We further investigated NiFeB tubes (SS123 sample from TU Darmstadt) with electron holography. Based upon previous synchrotron measurements on NiFeB shells, we expected uniform axial magnetization everywhere. Indeed phase maps indicating axial component of the magnetic induction were acquired. With the help of magnetic field we could saturate the tube along the two opposite axial directions (imaging at remanence) and we observed phase gradients similar to the case of

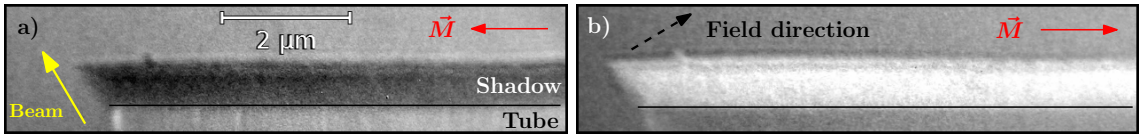

Fig. 8.12: XMCD-PEEM images of an electroless-deposited NiFeB shell magnetized axially sequentially along two opposite directions. The beam arrives from the bottom in the direction depicted by the yellow arrow. Only the shadow area (information from the volume) is clearly visible due to selected focus on the shadow and partial oxidation of the outer tube surface. The tube is axially magnetized with a magnetization component a) parallel and b) anti-parallel to the X-ray beam (images at zero field). The magnetization was switched between the 2 images by applying 16 mT along black dashed arrow featured in (b). Switching field of these tubes seems to be 10-16 mT (unfortunately, we cannot apply the field exactly along the tube axis). The grey line along the tube, close to the rim of the shadow is a sign of non-magnetic inner layer which serves as a mechanical fortification, protection from oxidation.

Tab. 8.1: Saturation magnetostriction λ_s for some Co-rich CoNiB compounds.

material	λ_s	reference
$(Co_{80}Ni_{20})_{80}B_{20}$	$-5 \cdot 10^{-6}$	[218]
$Co_{80-x}Ni_xB_{20}$	$-7 \cdot 10^{-6}$ for $x \in (0; 12)$	[219]
$(Co_{80}Ni_{20})_{77}B_{23}$	$-8 \cdot 10^{-6}$	[220]

nanowires (Fig. 8.13).

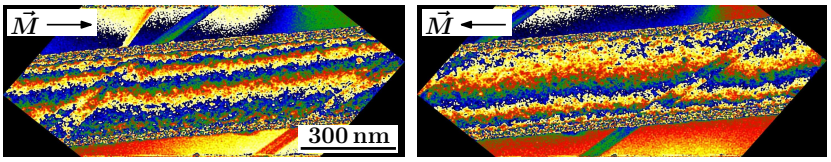

Fig. 8.13: Electron holography on a NiFeB SS123 electroless tube (diameter around 300 nm) with opposite magnetization. Wrapped phase maps show the tube saturated by external magnetic field in two opposite axial direction. Both electrostatic and magnetic parts are present. Compare with the nanowire case in Fig. 5.12.

Initially, magnetization at the tube ends was mostly uniform, pointing along the tube axis; similar behaviour was observed in XMCD-PEEM experiments. But after applying the transverse field, the end curling appeared (Fig. 8.14, right end), similar to the one observed by Diehle et al. [109] and with extend matching the predictions in [79] for the given tube diameter. The interesting point is that the end curling is expected to develop in such larger diameter tubes, as the mixed state (axial magnetization with end curling) has lower energy than having axial magnetization everywhere (see the limitation of the "F" state to small diameters in Fig. 3.2). Further, we continued also as in case of the nanowires with modulated diameter: we tried to nucleate a DW with a transverse magnetic field having also a small axial component. We did not observe well-separated opposite domains with a domain wall in between. Instead, complex phase patterns were present. This might be caused by the large tube diameter (300-400 nm). Experiments on nanotubes with smaller diameter and pure axial field could provide better results.

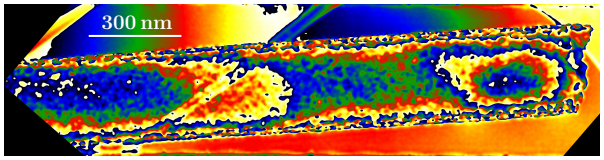

Fig. 8.14: Electron holography on a NiFeB SS123 electroless tube (diameter around 300 nm) after saturation in a nearly transverse direction. Image at remanence close to the tube end. Both electrostatic and magnetic parts are present. On the right end of the tube one can see pattern that could be assigned to end curling typically present in large diameter tubes. To the left we expected pattern for axial magnetization such as in Fig. 8.13, i.e. with contour lines along the tube. However, a different pattern is present instead.

8.3.4 Annealing

In order to investigate further the electroless CoNiB material,its magnetic properties in tubular geometry and the role of the granular structure or the strain in the observed azimuthal anisotropy, we annealed the tubes at various temperatures and examined their magnetization state after cooling to room temperature. Further we also imaged their morphology with the scanning electron microscopy.

XMCD-PEEM investigation of annealed tubes

As can be seen in Fig. 8.15, the XMCD-PEEM contrast associated with the azimuthal domains becomes weaker and finally disappears with the increasing annealing temperature. We attribute the loss of the contrast to a gradual rotation of magnetization towards the axial direction. The final weak uniform contrast is determined by the close-to-perpendicular direction of the longitudinal magnetization with respect to the beam direction. Other possible explanations could include transverse magnetization close-to-perpendicular to the beam direction and/or decrease of magnetic moment caused by oxidation. Both cases are highly improbable, as an external magnetic field would be required to sustain the transverse magnetization and similar electroless-deposited materials are known to increase their magnetic moment upon annealing [99]. Finally, X-ray absorption spectroscopy performed on the annealed tubes does not show any indication of significant oxidation (such as broad & multiple peaks).

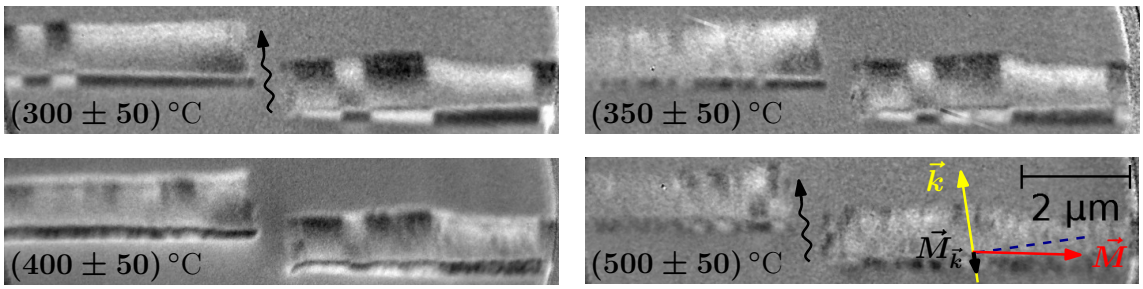

Fig. 8.15: Changing the magnetic anisotropy upon gradual annealing of CoNiB tubes. XMCD-PEEM images (same contrast range [-13%..13%]) of the same tubes after annealing at increasing temperature. All images are taken after cooling down to room temperature. The X-ray beam arrives close to perpendicular to the tube axis as indicated by the arrow.

Azimuthal magnetization persists only at the ends of some tubes (Fig. 8.15 left tube 350°C). Such so-called end curling state is expected from the locally high demagnetizing field[21, 78]. It has been already found for nanowires with axial

magnetization[221] and recently observed by Wyss et al. in axially magnetized nanotubes [79].

Note that the degree of the transformation is not the same for all tubes for a given temperature (Fig. 8.15), possibly due to a slightly different tube wall thickness. Moreover, above 450°C some tubes exhibit defects – mainly holes (see section 8.3.4). These imperfections translate also into inhomogeneities in the magnetic configuration.

During the annealing a few parameters affecting the anisotropy change (some of them are linked): grain size increases (grain boundaries change) and the strain is reduced. Both effects are consistent with the reduction of the azimuthal anisotropy and thus presence of axial magnetization. Note that the magnetoelastic coupling itself can be affected by the annealing as well as the composition and crystallography.

Magnetization reversal in annealed tubes

After the in-situ annealing, magnetization of the CoNiB tubes is longitudinal. We remounted the sample on the field sample cartridge (with a coil fitted below the sample) to apply magnetic field to these tubes. Several mT applied along the tube axis should be sufficient to fully reverse the magnetization direction (Fig. 8.16). The contrast on the tube as well as in the shadow is weak, due to the small projection of the magnetization to the beam direction (other possibilities – transverse magnetization and oxidation – were discussed above and excluded). Unfortunately, we cannot provide a more precise figure as for the switching field value due to technical issues (current/field spike) discussed in section 5.1.1. Fort the left tube one can see stronger contrast at the tube end – this is so called end (azimuthal) curling of the mixed state (see Fig. 3.2). Here the curling sense switched with the change in axial magnetization direction from antiparallel to parallel to the beam. However, as has been recently shown by Wyss et al., both curling senses should have the same energy for high-aspect ratio tubes [79].

We also tried to image the annealed tubes with magnetic force microscopy. We could detect magnetic charges at the tube ends, suggesting axial magnetization in accordance with XCMD-PEEM investigation of the annealed tubes.

Defects arising from annealing

Upon annealing under vacuum in the PEEM preparatory chamber, defects (holes) appeared in the shell of some CoNiB tubes, for temperatures typically above 450°C. These holes are visible both in X-PEEM and subsequent scanning electron microscopy images (Fig. 8.17a, here an extreme case being shown). Not all tubes had the same density of holes upon the same annealing (Fig. 8.17b), which may

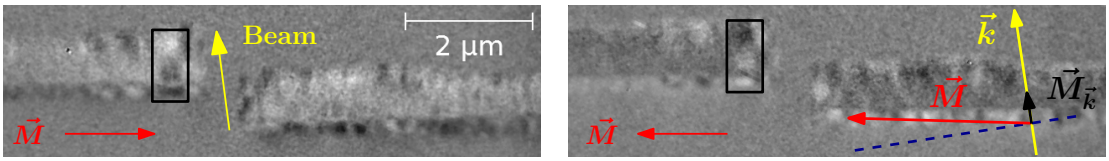

Fig. 8.16: Magnetic switching of annealed tubes with axial magnetization. The magnetization in the axially-magnetized tubes can be reversed by applying a magnetic field along the tube axis, as seen from the left to the right image. The beam arrives from the bottom of the image, and is close to perpendicular to the tube axes, so that the magnetic contrast is rather weak. Still one can distinguish the switch, both on the tube and in the shadow. In both images the left tube displays some azimuthal curling close to its end (highlight by black frame), as seen in the shadow. After the field application this curling switches as well. Both tubes display several defects (holes) due to over-annealing.

come from variation in the tube wall (shell) thickness. Some tubes do not display any visible damage.

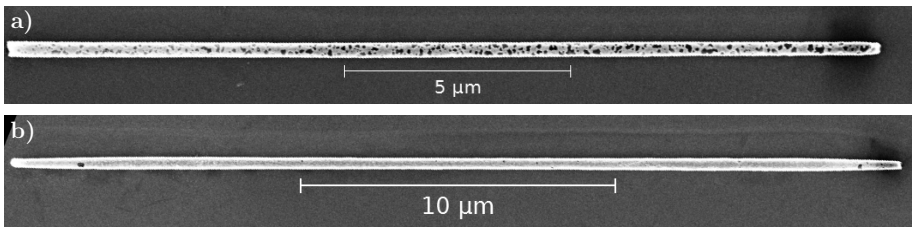

Fig. 8.17: Defects upon in-situ annealing at (500 ± 50)°C. SEM images of two tubes lying on the same substrate, displaying very different amount of defects after the annealing. The difference may come from a variation in the shell thickness. Both tubes displayed axial magnetization.

As the calibration of temperature for the in-situ annealing is not accurate, for comparison we performed annealing experiments in a separate vacuum furnace with a better control over the temperature as both the substrate and the environment are at the same temperature. Even the furnace annealing (at least 30 min, secondary vacuum) provided tubes both with and without significant defects for temperatures 450°C, 500°C, 550°C, and 600°C. Still more defects in a larger ratio of tubes appear with increasing temperature, especially above 550°C. For a lower temperature, 400°C, no significant defects were present, but on the other hand the transformation to axial magnetization was not complete. At 550°C most of the tubes were severely damaged with many holes, only a minority of tubes was rather intact and some tubes survived also up to 600°C. Therefore, the optimal annealing temperature seems to be 450°C-500°C. Further, we tried shorter (15 min) and longer (150 min)

annealing time for 450°C. 15 min led to almost no defects, but the increase of the grains size with respect to the as-deposited sample was very small, suggesting that longer annealing is needed. Longer (150 min) experiment produced slightly more defects such as tubes broken in places where there were already some small defects.

Now we will briefly mention possible differences in experimental conditions between annealing done inside the PEEM system (in-situ annealing) and the vacuum furnace annealing but we do not suppose that they play a significant role. The PEEM preparation chamber is operated under ultra-high vacuum. However, during the annealing the pressure increases substantially and it is of the same order of magnitude as the pressure in the vacuum furnace (secondary vacuum, $< 10^{-4}$ Pa). The main difference might be X-ray beam irradiation of some tubes before the annealing, in particular effect of the X-rays on the tubes and impurities that cover them (breaking bonds, graphitizing hydrocarbons, etc.). As only part of the sample was irradiated, but the whole sample was annealed, we could conclude that there is no big difference between irradiated tubes and tubes not exposed to X-rays (based on electron microscopy images of both sets of tubes). As we used twin samples on the same substrates in both (in-situ, furnace) annealing experiments, we suppose that both are comparable.

The presence of larger defects (especially above 450°C) can be an issue as they lead to inhomogeneity in the magnetic configuration. We tried to tackle this problem by fortifying the tubes with an additional inner (non-magnetic) layer deposited either by electroless plating or atomic layer deposition (ALD). It seems that the amount of defects in such tubes upon annealing is lower. Alternatively it is possible to perform the ALD after dispersion of tubes on the substrate – this improves not only mechanical stability, but also protects the tubes from further oxidation. But we refrained from such treatment as the electrically-insulating oxide cover layer can cause problems (charging) in collection of the photoelectrons in XMCD-PEEM unless it is very thin.

8.3.5 Sample ageing

In this section we will look further at aged CoNiB tubes. These are the tubes from the same batch as the ones investigated with XMCD-PEEM. However, at the time of the measurements presented below, they were almost one and half years old, i.e. even older than tubes observed with STXM where some changes in the magnetic state were already noticed. Despite being kept under primary vacuum for most of the time, they are partially oxidized (determined from X-ray absorption spectroscopy), mainly the inner surface as we could already observe in the shadow of XMCD-PEEM images for some tubes (e.g. Fig. 8.7 – grey line in the tube shadow of the

top tube). The outer surface is better protected as the tubes were stored still in the polycarbonate template. The ageing seems to have an effect on the anisotropy and magnetic configuration in the tubes as will be shown in following images obtained by electron holography and magnetic force microscopy.

Electron holography on aged CoNiB tubes

For a tube with azimuthal domains and thus perfect flux-closure we would expect no magnetic signal in electron holography phase maps. Magnetization perpendicular to the beam is opposite in upper and bottom part of the tube and thus its contribution cancels out; magnetization along the beam does not affect the electron wave (there is no Lorentz force on the electron). Therefore, the signal, if present, could come only from domain walls or defects. However, as mentioned above, we have indications that there is some axial magnetization component in the domains that should be visible in the phase maps.

In our electron holography experiments, unlike in simulations (see annex section B.3), a contrast clearly not of electrostatic origin (compare with Fig. S4) was observed almost everywhere in several tubes, indicating the presence of an in-plane/axial component of the magnetization (see Fig. 8.18).

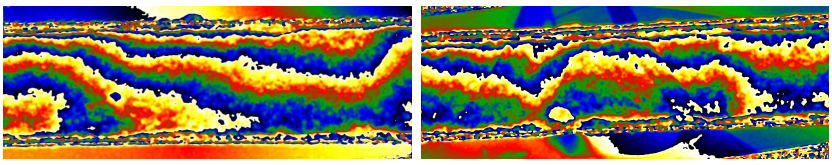

Fig. 8.18: Experimental wrapped phase maps (both magnetic and electrostatic part) of CoNiB electroless tubes (SS53, diameter 300 nm). On many places clear axial component of magnetic induction can be seen (compare to for example previous experiments on nanowires – Fig. 5.12). Also several strange pattern appeared, these are at least partially of magnetic origin.

Further in some cases, we could remove the electrostatic part by processing images with a flipped sample (magnetic contribution reverses, electrostatic one remains the same) and obtain pure non-zero magnetic contribution (e.g. Fig 8.19), sometimes even displaying weak stray field from some tube parts – tube ends and also from parts far from the ends or structural defects (domain walls?).

Therefore, flux-closure is indeed not perfect, which we relate to the sample ageing. If we assume that the spontaneous induction did not decreased significantly (approx. 1 T for fresh CoNiB thin films), then the integrated measured induction would correspond to a magnetization being predominantly 80° from the tube axis.

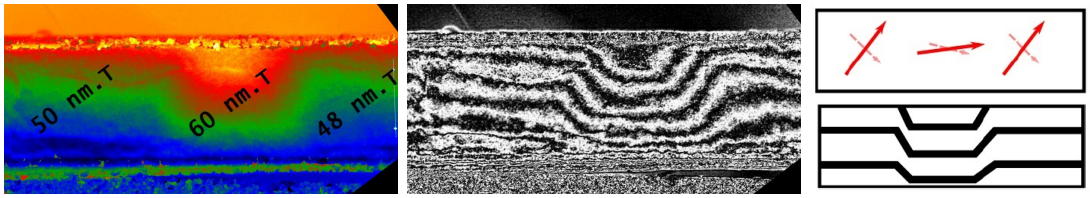

(a) (b) (c)

Fig. 8.19: Electron holography – magnetic phase maps for a CoNiB tube part (tube diameter around 300 nm, shell thickness 30 nm). (a) continuous magnetic phase map with integrated in-plane magnetic induction values. (b) corresponding area with amplified magnetic phase – $\cos\phi$. (c) Small scheme indicating possible deviation of magnetization from in-plane (axial, horizontal) direction, the modelling is tentative and the angle could be exaggerated.

However, the integrated in-plane induction varies along the tube. As both the diameter and shell thickness seem to be rather uniform, it may reflect that the magnetization has a larger in-plane component – see model by Aurélien Masseboeuf in Fig. 8.20.

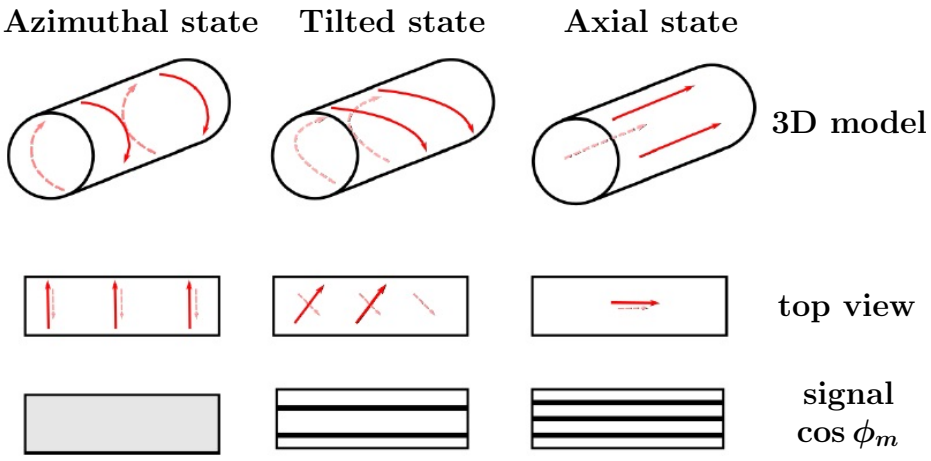

Fig. 8.20: Electron holography – expected magnetic phase for different magnetic configurations in a tube. A schematic model by Aurélien Masseboeuf depicting expected amplified magnetic phase ($\cos\phi$ instead of ϕ) for magnetic configuration having different axial magnetization component.

In addition, several different phase patterns appeared, some of them might be ascribed to domains walls (Fig. 8.21, note that both magnetic and electrostatic parts are present), but probably not simply to Bloch walls. Even after removal of the electrostatic contribution (available only for some tube parts), it will not be easy to assign a magnetic configuration to the obtained phase maps.

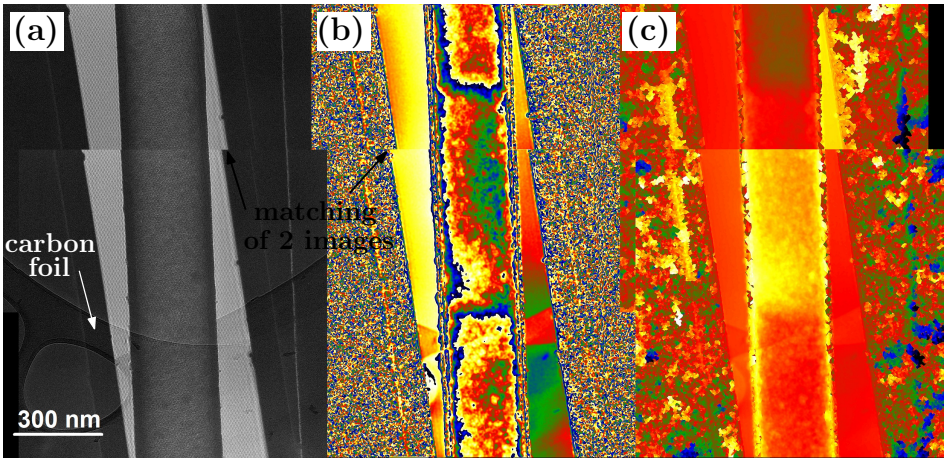

Fig. 8.21: Electron holography on another CoNiB SS53 electroless tube (diameter around 300 nm). (a) hologram, (b) reconstructed wrapped phase phase, and (c) unwrapped phase. In the phase maps both magnetic and electrostatic parts are included. Very sharp changes are observed with spacing compatible with the domain size previously observed with synchrotron techniques. However, the contrast is compatible with no walls we modelled. The magnetic origin of these is supported by the fact that on the hologram we cannot see such abrupt change in the structure/tube geometry. The figures are composed of two sets of consequent images, this leads to and offset in unwrapped phase (c).

We also applied external magnetic field before acquiring images. It had very little influence on the magnetic configuration as already observed with synchrotron XMCD.

To summarize this section: in aged (almost 1.5 years) CoNiB electroless tubes we observed some axial component of magnetization in many parts of the tubes (indicating decrease of the azimuthal anisotropy strength) as well as some strange phase patterns which could be in some cases ascribed to domains wall. However, they do not look like simple Bloch walls, nor other common wall types.

MFM of aged tubes under vacuum

After some time we returned to magnetic force microscopy investigation of now aged (almost 1.5 years) SS53 CoNiB electroless tubes (initially with azimuthal domains and Bloch walls as will be detailed in next chapter). As we now know that tubes are predominantly magnetized along the azimuthal direction forming multiple flux-closure domains, we expected only signal coming from the domain walls (azimuthal domains create no stray field). As we were unable to detect any magnetic signal using the Ntegra microscope operated at ambient conditions, we switch to the Nanoscan instrument operating under secondary vacuum (10^{-4} Pa) and thus better signal-to-noise ratio. First we tried high resolution MFM single pass non-contact imaging with slow feedback-response. However, the large height of the structure made such imaging impossible. Most of the signal was simply coming from the electrostatic interaction or topography (van der Waals interaction). We tried imaging under different tip/sample electrical bias, but not with fully compensated electrostatic contribution.

We could have tried common two-pass tapping mode with the lift as on the NTegra microscope, but we wanted to avoid being too close to the sample as the tapping may damage the probe and the probe exchange is quite time consuming due to the need to reach the low pressure in the chamber. Therefore, we decided to perform single pass constant height mode imaging with additional lift as suggested by the microscope manufacturer and described in the methods section 5.2.2.

We have imaged two CoNiB electroless tubes (reminder: diameter and thus height around 300 nm). Both are measured with the same probe coated with 10 nm CoCr. Due to sample ageing we can expect less sharp domains and more complex magnetic structure than initially observed with XMCD-PEEM.

Fig. 8.22 shows a measurement of the first tube. The top image features EFM done with -2 Hz setpoint and sample bias 1400 mV. It serves mainly for localization of the structure. The bottom image (same area) is the constant height MFM with lift of 30 nm and compensated CPD (580 mV). As the potential is determined in the

tube centre, it is possible that it varies along the tube. However, we suppose that such variations are not very large – measurement in few different points showed a difference of maximum few tens of mV. Therefore, the observed alternating contrast along the tube cannot be assigned just to such variations in the CPD.

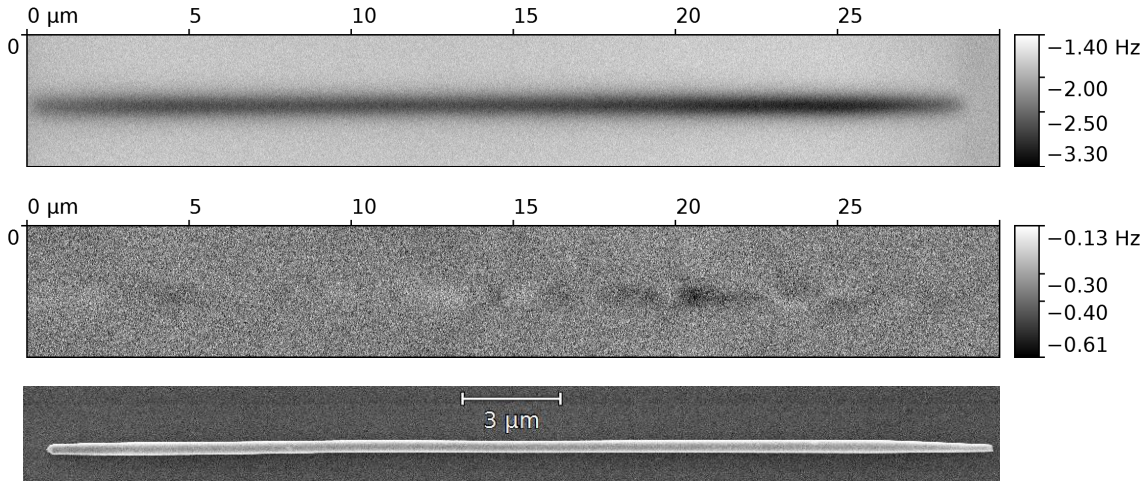

Fig. 8.22: CoNiB aged tube 1. From top: electric force microscopy for sample localization, constant height MFM, and electron microscopy image of the tube

As for the contrast, we observe alternation of darker and brighter segments along the tube. Given the large distance from the sample, these could correspond to multiple DWs found in similar tubes using synchrotron XMCD, but other interpretations are possible as well.

In Fig. 8.23 we can see another tube from the sample. Again the top image features EFM image, this time taken with -1.5 Hz setpoint, sample bias 1400 mV. The top image is a constant height MFM now with lift 0 nm (we tried also 30 nm, but the signal was quite weak). Even though the lift is lower than for the first tube, it seems that the real tip-sample distance is higher (note different setpoint) as we do not see much contrast in our tube. In both cases the tube should have several domains and we should evidence the stray field from the domains walls separating them. Also in both Fig. 8.22 and Fig. 8.23, the EFM (top one) image displays weaker contrast at the very ends of the tubes. From SEM images one can see that the diameter at the end decreases, forming a cigar-shaped structure, thus leading to weaker signal.

Contrast pattern differs from the first tube. Here we see bright contrast on the left, dark contrast of the similar magnitude (vs background) close to the right end and significantly weaker dark contrast at the very end. This contrast is rather puzzling as without it we could think that the tube is rather axially magnetized and there is some defect at the end.

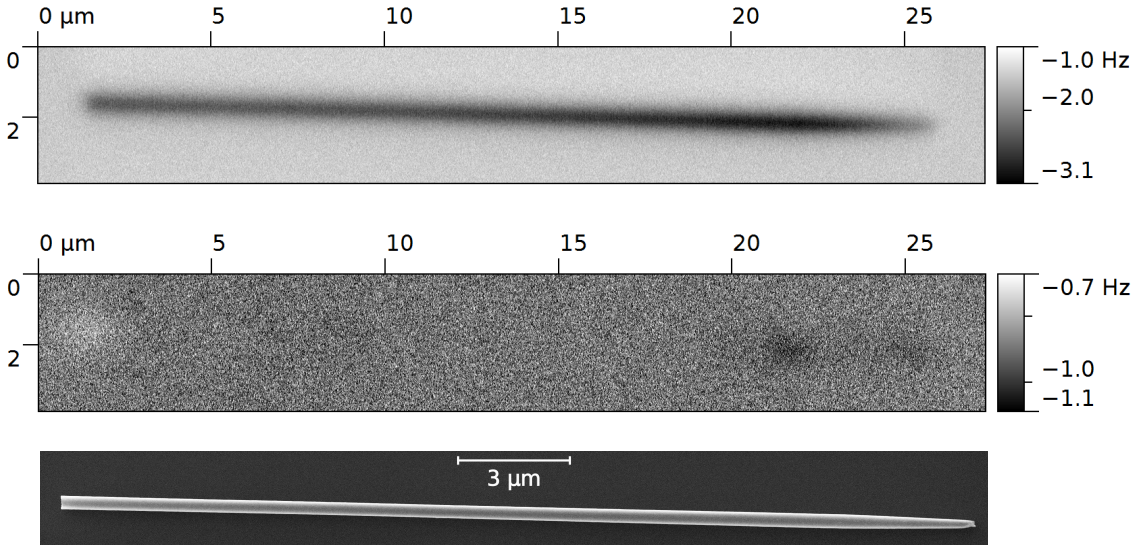

Fig. 8.23: CoNiB aged tube 2. From top: electric force microscopy for sample localization, constant height MFM, and electron microscopy image of the tube.

These are just preliminary measurements that could be further refined (+more tube measured). As we tried to be cautious, we know that we have a safety margin as for the tip sample distance and we can go closer (e.g. setting lower = more negative setpoint, and smaller lift – even negative) and benefit from increased signal and spatial resolution. This could help us to assign the contrast to magnetic configuration with help of other measurements (STXM, electron holography). As currently we have MFM measurements of only 2 tubes, with very different patterns. Still showing that there seems to be some considerable change of the magnetic state of the tubes through time.

Further, one may try also a so-called dual-PLL MFM, so called bimodal MFM [222, 223]. In this non-contact technique the cantilever is driven at two frequencies at the same time – primary and first overtone. The overtone is used for z-feedback and monitors topography, whereas primary is more sensitive to long range magnetic interaction. In addition, it is possible to compensate the CPD non only based on one point of the sample, but by performing Kelvin force probe microscopy [184] we can do the compensation at every point of our image. However, both mentioned methods increase the complexity of the experiment. Also to the best of our knowledge, the bimodal MFM was employed so far for topography features having height max 70 nm and our tubes with 300 nm could be a considerable challenge. In the worst case, one may try classical two pass tapping technique with the lift mode.

8.4 Comparison with nanotubes with smaller diameters

Aside from larger diameter tubes, we also tried to investigate CoNiB NTs with diameters in the range 100-200 nm. We used both NTs from TU Darmstadt and our own NTs.

Fig. 8.24a shows XMCD-PEEM image of SS125 CoNiB NT with diameter of 100 nm. The X-ray beam propagation direction is along the tube. As strong magnetic contrast is observed, we conclude that the tube is axially magnetized (or at least with strong axial component of he magnetization). This trend, preference for axial magnetization for smaller diameter has been already discussed (e.g. Fig. 3.2). The azimuthal state is unfavourable due to exchange energy increasing rapidly with decreasing tube radius R (diameter): $E_{\mathrm{ex}} \propto A_{\mathrm{ex}}/R^2$; with A_{ex} being the exchange constant. Note that not only is the tube diameter smaller, but also the shell thickness is reduced (Fig. 8.24b).

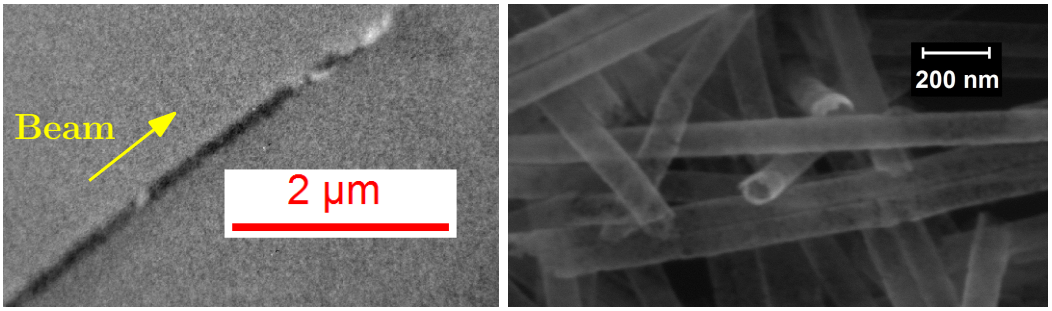

(a) XMCD, beam parallel (b) SEM, courtesy of S. Schaefer

Fig. 8.24: CoNiB nanotubes (SS125) with diameter of 100 nm. a) XMCD-PEEM image of a single nanotube (length 5 µm) with beam along the tube axis, revealing axial magnetization in the tube. Bright contrast at the top right tip corresponds to the shadow where the contrast is opposite to that on the tube surface. Other brighter parts can result from a particular magnetic texture, but here we suppose that they come just from defects as the tube wall is quite thin, also having some holes inside. b) Scanning electron microscopy image of a bundle of such tubes on a Si substrate, image courtesy of Sandra Schaefer.

SS124 CoNiB NTs with diameter of 150 nm had even thinner tube walls with multiple holes in the tube shell. X-ray absorption spectroscopy showed that they are quite oxidized with degree of oxidation increasing for thinner shells. As the thickness decreases, the deposited layer is not so compact; it is granular and containes holes and other defects that facilitate the oxidation. Consistently, for these tubes we

obtained only very weak and poor magnetic contrast (mainly using STXM, but some MFM trial on Ntegra microscope with partial compensation of the electrostatic contribution were done as well).

For CoNiB tubes prepared in our laboratory (diameter 100-200 nm, length $<$ 7 µm, shell thickness around 40 nm) we obtained MFM images with opposite magnetic charges at the tube ends, suggesting significant axial magnetization component (Fig. 8.25). There is also weaker alternating contrast along the tube. This may be either artefact (noise instabilities?), or it is possible that some intermediate magnetic state between fully axial and azimuthal magnetization (e.g. helical magnetization) is present.

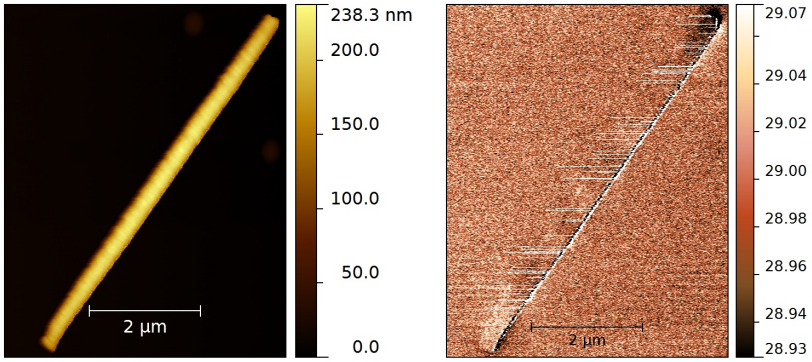

(a) (b)

Fig. 8.25: Atomic and magnetic force microscopy investigation of electroless deposited CoNiB nanotubes from Institut Néel (diameter 200 nm). (a) topography, (b) magnetic contrast (phase/°). The clearly opposite magnetic poles (bright/dark) at the ends of the tube suggest axial magnetization. On the other hand, there is also some alternating contrast along the tube. However, it is weaker and might originate from electrostatic interaction and/or processing of the image or it might be just an artefact. Scalebar length is 2 µm. Probe with a 20 nm CoCr layer.

9 DOMAIN WALLS IN TUBES WITH AZIMUTHAL DOMAINS

As we have multiple magnetic domains in our CoNiB tubes (diameter of 300 nm; for domains see Fig. 8.5), we will now focus on domain walls separating the azimuthal domains. Information on the DW type and structure is one of the keys to determine the mobility of a DW subjected to magnetic field and more importantly to spin-transfer torques [224]. We will start with an overview of possible DWs, we will continue with experimental observation. Further, we will provide more information on the DWs.

9.1 Theoretical considerations

A simplified view of DWs between azimuthal domains can be obtained by imagining the tube unrolled into a flat strip (see Fig. 9.1). Two successive azimuthal domains with opposite circulation turn into a thin film with in-plane magnetization and a 180° DW parallel to magnetization in the domains. Note that the magnetic configuration at opposite ends of such unrolled film has to be the same (periodic boundary condition) and that there are some difference highlighted in the next section. As was already discussed in section 3.2.2, for long nanotubes we may expect DWs of Bloch (radial magnetization) or Néel type (axial magnetization), named in analogy to thin films. Further, a cross-tie wall with axial magnetization components and vortex+anti-vortex pairs can be considered.

We could model all these walls by micromagnetic simulations in tubes with different geometries (diameter and shell thickness) and imposed preferred azimuthal direction for the magnetization. Examples of the resulting configurations follow: Bloch and Néel wall in Fig. 9.2 and Fig. 9.3, and cross-tie wall in Fig. 9.4. Aside from these some combinations of geometry and imposed anisotropy led to strange magnetic configurations that could be analogues of asymmetric Néel and asymmetric Bloch walls in thin films.

9.2 Bloch versus Néel walls in magnetic nanotubes

In thin films, the domain wall (DW) type, Bloch vs Néel, depends mainly on the film thickness. The transition is reported around 20-40 nm for 180° DWs and magnetically-soft films. However, it can be affected by an additional magnetic anisotropy, such as magnetocrystalline [66]. We found a similar trend in the micromagnetic simulations of our nanotubes with azimuthal domains, where Néel-like

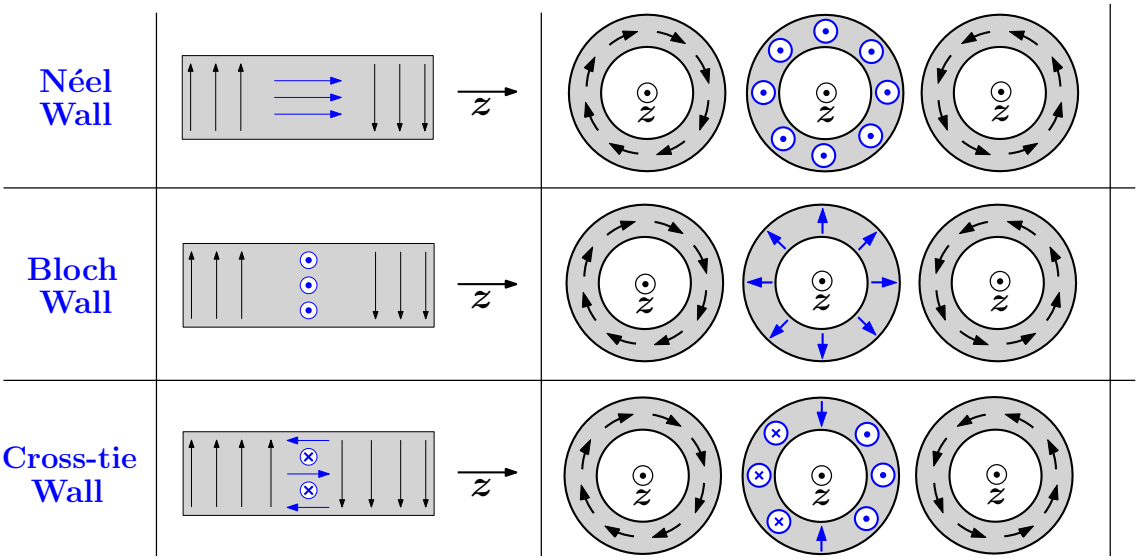

Fig. 9.1: Scheme of domain walls in nanotubes with azimuthal domains. Left: Scheme of idealized walls in unrolled tubes/thin film elements. Right: cross-sections of a tube with two opposite azimuthal domains and the wall in the middle. The nanotube axis lies along z.

DWs are favoured for small tube wall thickness and Bloch-type DWs for larger ones. We expect the DW structure to be influenced by diameter as well. As in the simulations we promote the azimuthal domains by defining the tube axis as a hard axis (uniaxial effective anisotropy), Bloch walls are preferred for larger anisotropy constants. A more systematic study of geometries with a different way of promoting the azimuthal magnetization (*azimuthal easy axis*) could be done to build a phase diagram of the DWs.

Aside from modelling of small tubes (diameter 50 nm) we performed micromagnetic simulations [203] for tubes with diameter 120 nm, tube wall thickness 30 nm and length of 1000 nm. The end charges are removed in the calculation of the dipolar field, to mimick an infinitely-long structure. We suppose permalloy-like material with an effective uniaxial anisotropy with hard axis along the tube (making effectively azimuthal direction the easy axis) and anisotropy constants 30 kJ/m^3 and 100 kJ/m^3, for which Néel and Bloch walls are obtained as a relaxed states, respectively. The simulation provides results similar to the ones for smaller tubes, only the extent of Bloch-like DWs with respect to the tube diameter is smaller (it might be also caused by the anisotropy values considered here). For these reasons and qualitative-only comparison, in the further discussion we will use tubes with the smaller diameter, for the sake of clarity and saving the computation resources.

For a better visualization of the micromagnetic configuration of Bloch and Néel DWs, we display the tube outer surface as if unrolled (Fig. 9.3).

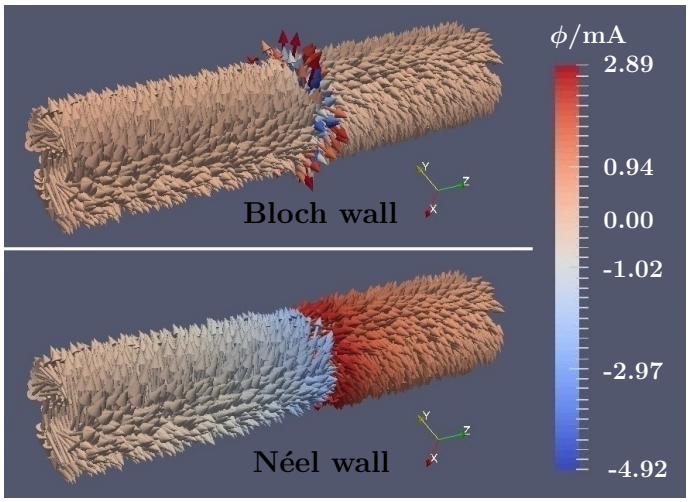

Fig. 9.2: Micromagnetic modelling of Bloch and Néel wall in a tube with two opposite azimuthal domains. Example for tube diameter of 120 nm, shell thickness 30 nm, length 1000 nm, and cell size < 4 nm. The effective anisotropy constants (hard axis along the tube) are 30 kJ/m^3 and 100 kJ/m^3 for obtaining Néel and Bloch walls, respectively. Colouring reflects magnetic charges whose spatial extent is significantly larger for the Néel wall. For better view on the magnetization consult unrolled maps in Fig. 9.3.

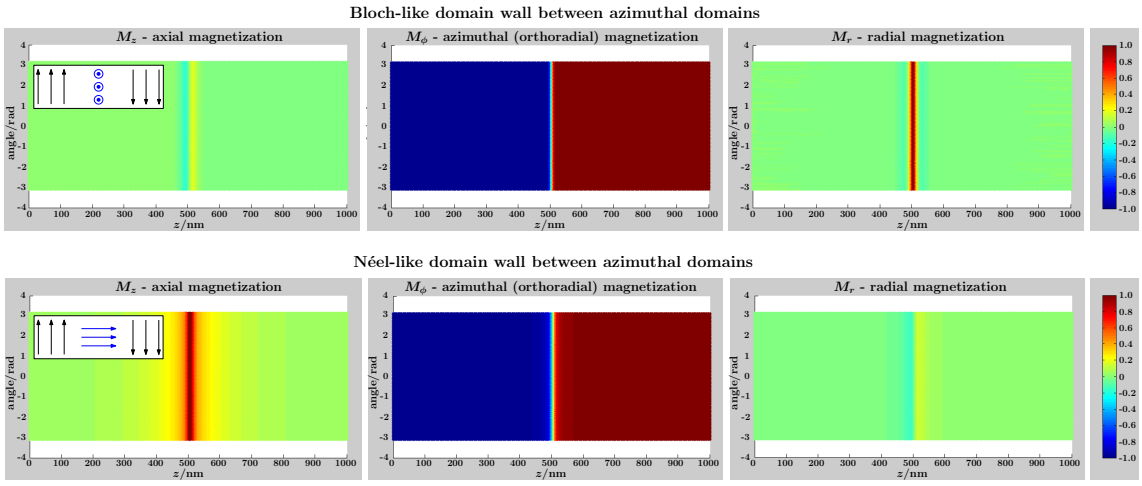

Fig. 9.3: Unrolled maps of magnetization for Bloch (top) and Néel (bottom) DWs in between two azimuthal flux-closure domains. The maps feature the three components of magnetization of the outer surface for a tube with diameter of 120 nm and tube wall thickness of 30 nm. The effective anisotropy constants (hard axis along the tube) are 30 kJ/m^3 and 100 kJ/m^3 for obtaining Néel and Bloch walls, respectively. The domain walls are located in the middle of the maps, in between two azimuthal flux-closure domains with opposite curling sense, which can be seen on the M_ϕ map – opposite sign on either side of the wall. Insets in M_z panels show corresponding idealized Bloch and Néel walls in thin films / unrolled tubes.

Note that maps are very similar for the inner surface. The maps show the three cylindrical components of magnetization: M_z (axial direction), M_ϕ (azimuthal direction), and M_r (radial direction). Unlike for smaller diameters, the Bloch wall is associated with a weak (but non-negligible) bipolar axial component of magnetization, and the Néel wall with a weak bipolar radial component. These, which do not occur for flat thin films, result from the rolled geometry and the bipolar line of charge, which breaks the symmetry between the inner versus outer surface. Note that in general Bloch walls are narrower than Néel walls, the latter giving rise to dipolar field similar to walls between axially-magnetized domains. Tails indeed arise in the latter due to the dipolar line of charges of opposite sign found on either side of the wall (Fig. 9.3), implying a longitudinal dipolar field, while the radial distribution of charges in Bloch walls does not contribute to a longitudinal component of dipolar field in the limit of thin-wall tubes.

Thus, even though the azimuthal domains produce no magnetic stray field, this is not the case for the walls that separate them. Bloch walls with radial magnetization do generate some stray field. However, the field has a smaller spatial extent and decays faster ($\propto 1/r^4$) due to a quadrupolar nature of the magnetic charges compared to the field from domain walls in between axial domains (e.g. in wires, tubes, strips) - magnetic dipoles (field $\propto 1/r^3$), or even monopolar behaviour in some cases.

Note on cross-tie walls in magnetic nanotubes

In our simulations and discussion of domain wall types between azimuthal domains we have also considered analogy of cross-tie walls from flat thin films. In Fig. 9.4 we mention an example of such wall in a small diameter permalloy-like tube (diameter 50 nm, length 200 nm, shell thickness 10 nm, cell size 1 nm, OOMMF) with one vortex-antivortex pair. The azimuthal magnetization in domains is favoured by defining varying easy axis along the tube perimeter with effective anisotropy constant 50 kJ/m^3. Larger number of pairs could be obtained for different anisotropy strength and geometry (e.g. larger number possible for bigger diameter) – see also [93, 94].

9.3 Experimental observation and discussion

In order to determine the DW configuration in our CoNiB tubes we relied on XMCD-PEEM. We considered again the tubes with the X-ray beam both along and perpendicular to their axis (e.g. Fig. 8.4) and compared experimental images with a

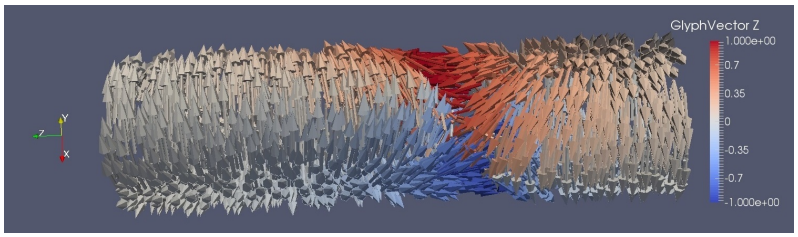

(a) view on antivortex

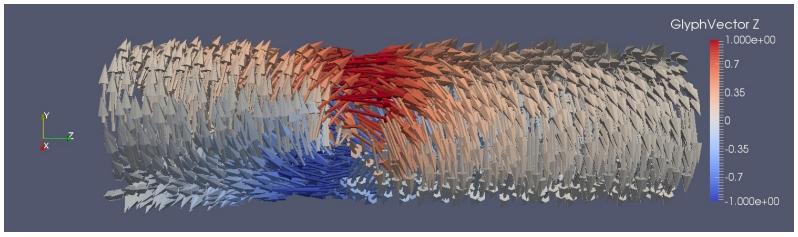

(b) view on vortex

Fig. 9.4: Micromagnetic simulation of a cross-tie wall in a nanotube with one vortex-antivortex pair. Coloured according to the axial (z) magnetization.

numerical modelling based on micromagnetic simulations and XMCD-PEEM post-processing (see methods). No XMCD contrast is seen with the beam parallel to the tubes, from which we exclude Néel DWs (axial magnetization), also the presence of the cross-tie wall is less likely. Therefore, DWs should be of the Bloch type. This is consistent with the images for the beam now perpendicular to the tube axis (Fig. 9.5).

Here, the domain boundary on the tube surface appears tilted with respect to the tube axis both in the experiment (Fig. 9.5a) and for the simulation with Bloch wall (Fig. 9.5b). While the tilt may be at first sight thought to result from a physical tilt of the wall, it reflects that magnetization in the Bloch DW changes direction from parallel to antiparallel to the X-ray beam when going from the front to the back side of the tube surface. This behaviour can be fully reproduced with the XMCD-PEEM simulations without any physical tilt of the wall. Still we cannot rule out completely the possibility of a small physical tilt (e.g. 5°) or other DW distortions due to possible defects in the tube as these would not be manifested in the images due to the limited spatial resolution. Note also that there is no such tilt of the domain boundary in the shadow (for the beam perpendicular to the tube axis). Again, small (e.g. 5° physical tilts could be hard to distinguish due to limited resolution (30-40 nm) and the fact that the shadow is elongated (approx. 3.6 times the tube diameter due to the X-ray beam incidence angle). Larger physical tilts would lead to changes in the images that are not observed in the experiment.

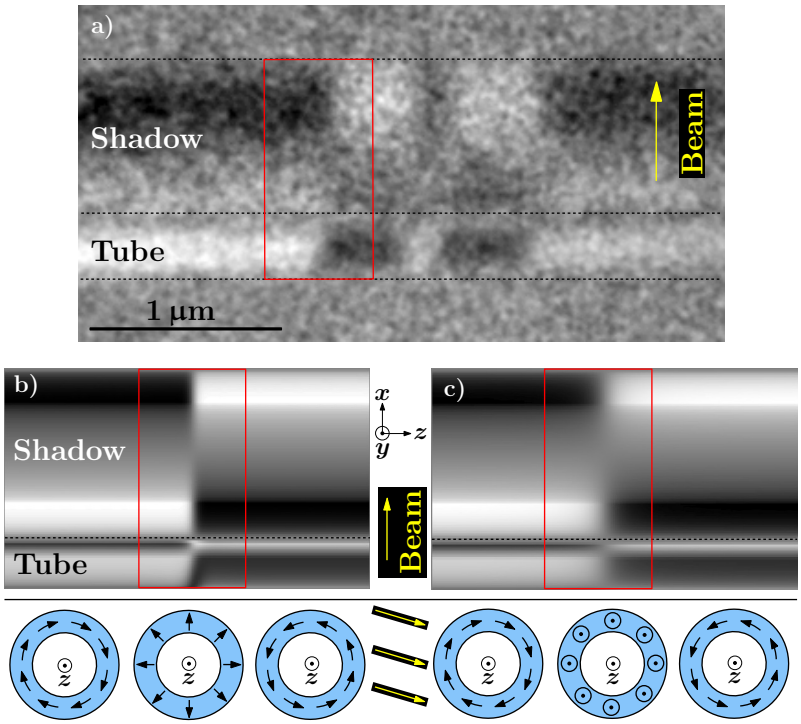

Fig. 9.5: Domain walls between flux-closure domains: experiment vs simulation. a) Experimental XMCD-PEEM with the beam perpendicular to the CoNiB tube (diameter around 300 nm, shell thickness 30 nm, length 30 µm). Five azimuthal domains are featured; the red rectangle highlights an area with one domain wall. Simulation of XMCD-PEEM contrast for b) Bloch and c) Néel walls. Schematic tube cross-sections below the simulations show the magnetization in domains and the domain wall (in the middle of the tube) respectively. Note that in the experiment part of the shadow is covered by the structure itself. The simulations are based on small-diameter tubes (50 nm, shell thickness 10 nm, cell size 2 nm) with imposed hard axis along the tube axis to favour the azimuthal magnetization (otherwise tube with such geometry would be axially magnetized). The X-ray absorption coefficient is the one for 80% Co.

In addition, from the micromagnetic point of view (supported also by numerical modelling) there is no clear reason for tilting the domain wall as this leads to a penalty in exchange energy and there is no other gain (e.g. in dipolar energy) even when considering multiple domain walls. This is also given by the form of anisotropy considered here. Physically tilted (surface) domain boundaries have been reported in amorphous microwires with helical anisotropy and axial magnetization component [225]. However, as no axial magnetization is detected in the presented case, such case is unlikely. On the other hand, the azimuthal anisotropy may become weaker for example upon sample ageing. This may result in tube sections with some axial magnetization component and more complex magnetic configurations. This we partially observed with STXM and electron holography for some oxidized tubes (aged for 1 year).

In the majority of cases, the tilt is in the same direction for all walls in a given tube. As the domains alternate, this means that the DW contrast at the tube front and back alternates between successive DWs. Therefore, the radial magnetization points alternatively inwards and outwards (alternating domain wall *polarity*). This case is shown in a simulation in Fig. 9.6a, while Fig. 9.6b shows the case with DWs having the same radial component. The former allows a better closure of the flux and as a result is found to be of lower energy, which may explain its predominance in the experiments.

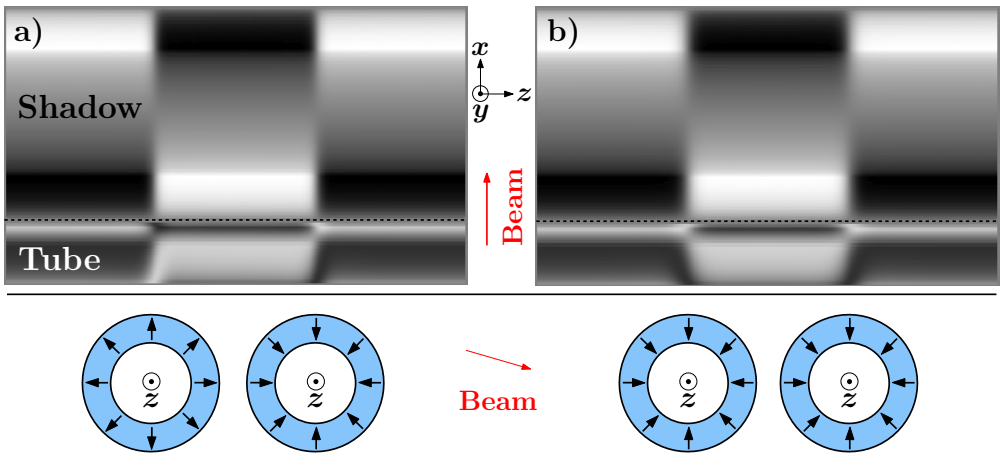

Fig. 9.6: Simulated XMCD-PEEM contrast for two Bloch DWs separating three azimuthal domains with alternating circulation. DWs with (a) opposite and (b) same radial components (*polarity*). Simulations are based on small tubes (diameter 50 nm, tube wall thickness 10 nm) and only partially relaxed micromagnetic configurations (not necessarily stable for this geometry). Still it reflects well the main qualitative differences between the two configurations.

We performed also modelling of both XMCD-PEEM and electron holography

contrast for cross-tie walls (Fig. S3), but it does not correspond to our measurements (in XMCD-PEEM there is no tilt of domain boundary as for Bloch wall). Other features than the tilt in XMCD-PEEM with transverse beam might be difficult to spot in the experiment due to limited spatial resolution, however they should be resolved in electron holography (resolution of few nm), still we have not observed phase maps matching the cross-tie walls (compare images in section 8.3.5 and Fig. S3).

9.4 Non-zero XMCD-PEEM contrast for the beam "along" the tube axis

Sometimes we use a potentially misleading notation *beam parallel to the tube* for the beam lying in the plane defined by the tube (long) axis and normal to the substrate. The word *parallel* may lead to wrong expectations as for the XMCD-PEEM contrast. Even though the dominant beam component is parallel to the tube axis (and thus perpendicular to the magnetization in most cases), one should not forget that the beam arrives at 16 ° with respect to the substrate and also the tube axis (Fig. 9.7).

Therefore, for the tube with the azimuthal magnetization, the contrast in images with the beam *along* the tube is non-zero with the maximum ($\approx 28\,\%$ of the contrast for the magnetization parallel to the beam; $\sin 16\,^\circ$) reaching when the magnetization is perpendicular to the substrate. This happens at the opposite sites along the whole tube as can be seen in an example of a tube with 2 azimuthal domains separated by a Néel wall (Fig. 9.8). It is also visible in the shadow behind the tube surface. Note that contrast in the shadow is inverted with respect to the tube surface, as usually.

The fact, that in the experiments we observe almost zero contrast, is probably given by the small spatial extent of such contrast (comparable to the tube wall thickness), which may be too small with respect to the experimental resolution. At least this is the case for SS53 tubes with tube wall thickness around 30 nm, while the resolution of the XMCD-PEEM is rather 30-40 nm. Further limitation is the angular efficiency of photoelectron collection, which decreases quite rapidly for photoelectrons travelling off-normal (vs supporting substrate). Moreover, the contrast close to the edges of the tube can be smeared out in case of non-ideal drift correction. However, it should be observable for tubes with larger wall thickness and/or nanowires. This is illustrated on a simulation involving a 50-nm-diameter nanowire with 3 azimuthal domains (Fig. 9.9). Similar image is expected also for a larger diameter wire.

Thus event-though some XMCD-PEEM contrast can arise for the beam being aligned with the tube, we will allow ourself to disregard it as it is expected to be

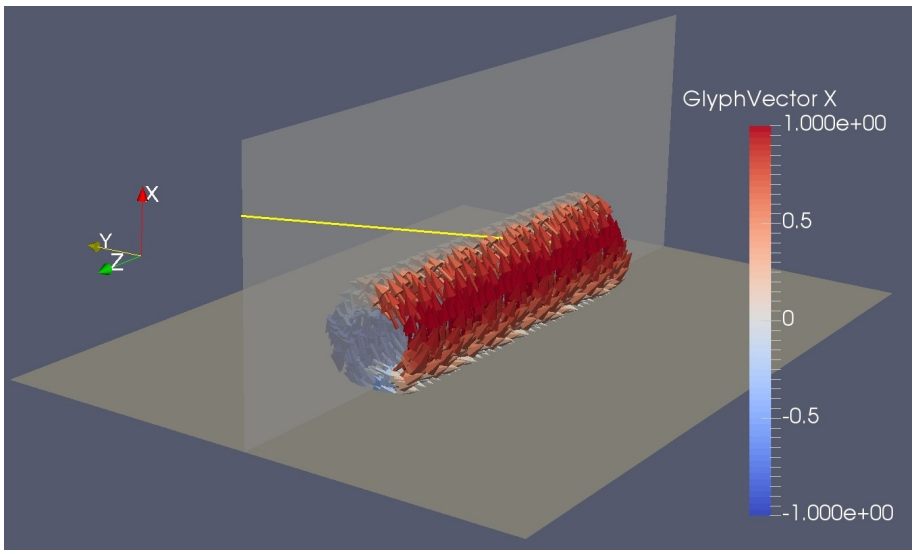

Fig. 9.7: Scheme of a X-ray beam arriving *parallel* to the tube. The yellow line depicts the propagation direction of the beam. The beam arrives at 16 ° with respect to the substrate and it is so wide that it irradiates the whole tube as well as the substrate. On top of the tube with the azimuthal magnetization, there is no projection of the magnetization to the beam direction. However, at both sides of the tube, the magnetization lies out-of-plane with respect to the substrate and thus there is some projection to the beam direction. Magnetization arrows are coloured according to the out-of-plane magnetization; non-zero surface out-of-plane magnetization will contribute to the contrast in a XMCD-PEEM image.

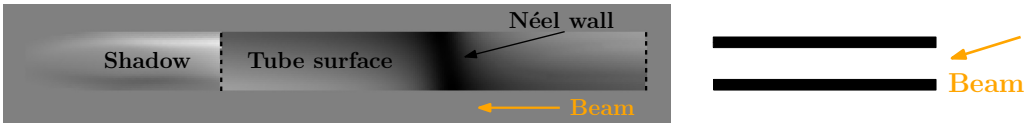

Fig. 9.8: XMCD-PEEM simulation for the beam along the tube with two azimuthal domains separated by a Néel-like domain wall giving a strong contrast in the wall area as the DW magnetization is along the tube. Weak contrast close to the top/bottom edges of the tube can be observed. Simulation is based on a small tube (diameter 50 nm). A small side-view scheme is to the right of the XMCD-PEEM image as a reminder that the beam arrives 16° with respect to the supporting surface.

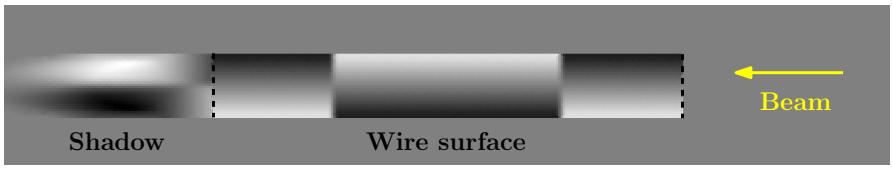

(a) Simulated XMCD-PEEM

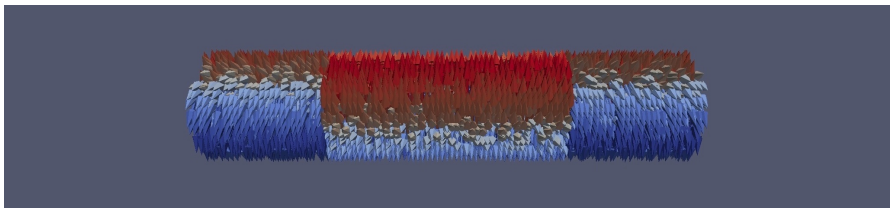

(b) Magnetic configuration

Fig. 9.9: Simulation of a solid nanowire with three azimuthal domains. (a) XMCD-PEEM simulation with beam along (16° with respect to the supporting surface) the wire axis. (b) Corresponding magnetic configuration, arrows are coloured according to a transverse normalized magnetization component (M_y, -1..1). Note that this is a crude non-relaxed magnetic configuration. Therefore, it cannot describe properly what happens at the domain boundaries.

weak and most likely cannot be resolved with current instrumentation.

Part IV

Results & Discussion
Multilayered nanotubes

So far we have been dealing with single-shell magnetic nanotubes. In view of obtaining enhanced magnetic properties and going towards devices based on nanotubes, we now study more complex geometries. Namely we look at magnetic trilayers in tubular geometry: two magnetic layers separated by a non-magnetic spacer. We provide both micromagnetic modelling and experiments on such core-shell structures.

Multilayered thin films with various magnetic and non-magnetic layers (spacers) are crucial in current spintronics. In curved, cylindrical geometry this implies coaxial magnetic tubes with a spacer in between. To the best of our knowledge, this geometry has not been considered before in the literature. The first translation of trilayered physics into tubular structures we aimed at was synthetic antiferromagnets (SAFs). Synthetic antiferromagnets and ferrimagnets are formed by two magnetic layers separated by a very thin (a few nanometres or even less) non-magnetic spacer such as Ru. For certain spacer thickness, an antiparallel alignment of magnetization in the two layers can be established through the RKKY interaction [50].

Here we focus on two axially-magnetized shells separated by a thicker spacer such as 10 nm, because at the moment reliable fabrication of compact thinner layers is too challenging in the tubular geometry, at least by (electro)chemistry that we employ in the nanotube synthesis. Therefore, as a first step, our aim is to explore whether we can achieve antiparallel ordering just through magnetostatic interaction through the magnetic charges at tube ends of tubes with axial magnetization (or possibly domain walls). Later one could investigate the micromagnetics and dynamics of domain walls in a such systems. In other words, we want to combine SAF with domain walls in magnetic nanotubes which are predicted to propagate at very high speed under both magnetic field and current without repeated transformations (and Walker breakdown).

In chapter 10 we focus on micromagnetic modelling of trilayered tubes with the spacer and in chapter 11 we show experimental realization and investigation of a similar multilayer system in tubular geometry. However, with slightly different focus as for the physics.

10 TRILAYERED TUBES: MODELLING OF SYNTHETIC FERRIMAGNETS

Here, we will address only modelling of SAF-like systems with thicker spacer (further on we will use this notation) in the tubular geometry. For simulations we will use a micromagnetic approach and we will neglect the contributions of the spacer (like effects at the interfaces, induced moments, RKKY or orange-peel coupling, ...), i.e. we will consider it as a free space (vacuum) separating two magnetic permalloy layers. This approximation is reasonable for larger spacer thickness, but would fail for low spacer thickness (in particular $< 1\,\mathrm{nm}$) – still we do not consider such low thickness. The numerical simulations presented in this chapter were done before the experimental realization of multilayered tubes to outline the physics and suitable geometry.

Note, that in our first simulations the total magnetic moments of both magnetic tubes are not fully compensated (difference between two shells is approximately 80% for smaller and 34% for the larger tubular SAF presented here), therefore we should speak rather about synthetic ferrimagnet systems in these cases. This is caused by a different cross-section and thus volume for the two layers related to the limitation given by the size of the discretization volume and cell size (cube or tetrahedron edge). Majority of the magnetization configurations shown in this chapter is coloured according to the magnetization component along the tube axis (z).

Even though finite elements simulations in FeeLLGood [202, 203] are more suitable for curved geometries, the preparation of the geometry and proper meshing is not as straightforward as initialization of the simulation in OOMMF [201], which is more versatile. Therefore, our first test were conducted in OOMMF. Later, we will present results obtained in finite elements as well.

10.1 Simulations in OOMMF

As pointed above, we model our system with two coaxial permalloy nanotubes separated by a spacer – here vacuum. We approximated our geometry with 1nm cubes. This leads to (numerically) rough "curved" surfaces, with a slightly exaggerated example depicted in Fig. 10.1 (a). As we consider permalloy layers, we neglect both magnetocrystalline anisotropy and magnetostriction. Other parameters follow:

- length L=200 nm; spacer thickness (in between the tubes) $s = 10\,\mathrm{nm}$
- outer tube: external radius R_2=25 nm, tube wall thickness t_2=5 nm
- inner tube: external radius R_1=10 nm, tube wall thickness t_1=5 nm

- cell size 1 nm, damping $\alpha = 0.1$
- exchange stiffness $A = 13\,\mathrm{pJ/m}$, spontaneous magnetization $M_\mathrm{s} = 860\,\mathrm{kA/m}$

We started the simulation with a random magnetization direction in each cell. When following the evolution of the system, first, magnetization was aligned along the common axis for the outer tube, followed by the inner tube. However, two domains separated by a transverse wall were formed in the inner tube [consult Fig. 10.1 (b)]. A similar evolution was observed also for a similar geometry modelled in finite elements (see below). Later on, the domain wall moves slightly towards the end of the structure with the parallel magnetization in both shells (left end in Fig. 10.1b). Therefore, the antiparallely-aligned part (lower energy) extends and we expect the wall to be annihilated, even though this has not happened so far during several tens of thousands of steps. Note slight curling at the ends for the outer tube; we see only slight tilting of the magnetization at the ends for the smaller tube as the curling is not favoured due to a large exchange energy penalty for such tiny tube diameter. Both these features seems to be consistent with the phase diagram for single-shell NTs: geometry of the outer tube lies in the mixed state part of the diagram (but close to the uniform state), whereas the inner tube would be completely uniform (F) state (see Fig. 3.2).

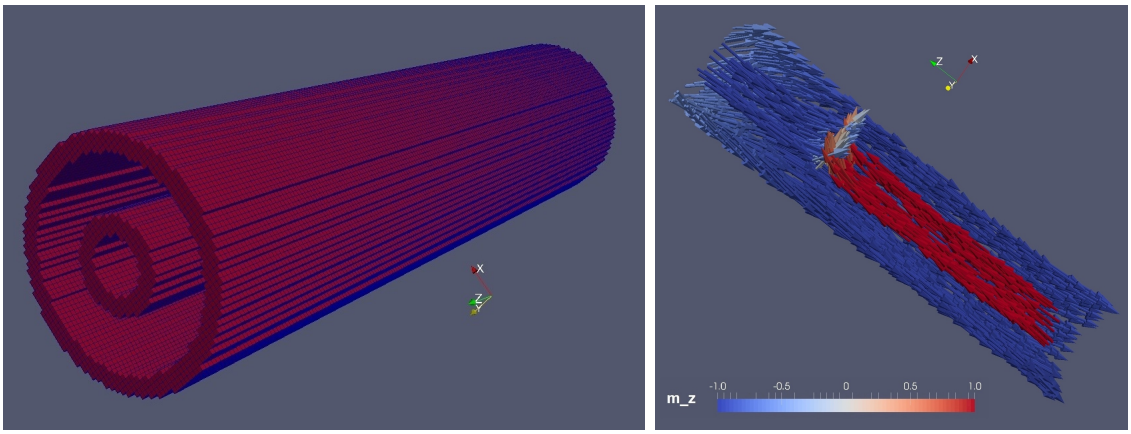

(a) example of coaxial tubes' geometry (b) SAF with a domain wall

Fig. 10.1: Tubular SAF in OOMMF (outer diameter 50 nm, shell thickness 5 nm, cell size 1 nm). (a) example of the geometry (coaxial tubes): the representation of curved surfaces with cubes is far from ideal. Note that the depicted example does not reflect exactly the geometry used in the simulations as 5 instead of 3-4 cells (shown here) were used for the tube wall. The (over)simplification comes from the visualization in ParaView. (b) Simulated magnetization (not completely relaxed) in the SAF with a transverse domain wall inside the inner tube. Only one half of the structure is shown, in order to have a better view on the magnetization in both tubes.

Even though the OOMMF geometry is rather a poor approximation of curved surfaces, the preliminary simulation shows that indeed one may achieve antiparallel alignment of magnetization in coaxial magnetic NTs based on the dipolar coupling. In other words, the magnetization is along the common tubes' axis and mostly antiparallel to the magnetization in the other tube. This will be further explored with micromagnetic simulations in finite elements.

10.2 Simulations in FeeLLGood

For the finite elements scheme our model is the same as above, i.e. we suppose two permalloy tubes with a vacuum spacer and following parameters:

- maximum element size size = 4 nm, damping $\alpha = 1$
- exchange stiffness $A = 13\,\mathrm{pJ/m}$, spontaneous magnetization $\mu_0 M_\mathrm{s} = 1\,\mathrm{T}$
- finite structures, charges at ends not removed

We perform first trials on tubes with a moderate diameter (external diameter of 50 nm) that are closer to the OOMMF simulations above. Later we consider a larger system with outer diameter of 250 nm, which is closer to magnetic tubes we have already used in our experiments and which may serve as a basis for the tubular SAF. In both cases three main initial micromagnetic configurations were considered:

- (pseudo)random (boost library) – random $\vec{M}$ at each node (Fig. 10.3)
- (axial) antiparallel – $\vec{M}$ in one tube opposite to the other one
- (axial) parallel – $\vec{M}$ along the same direction in both tubes

If not stated otherwise, (anti)parallel refers to an axial magnetization (along the tube). Later we tested also azimuthal magnetization with same (parallel) and opposite (antiparallel) curling sense (chirality) in both tubes.

10.3 Tubular SAF – smaller diameter (50 nm)

As in case of the OOMMF simulation we started our exploration with a smaller system, the geometrical and simulations parameters are summarized below:

- length L=400 nm; spacer thickness (in between the tubes) $s = 5\,\mathrm{nm}$
- outer tube: external radius R_2=25 nm, tube wall thickness t_2=5 nm
- inner tube: external radius R_1=15 nm, tube wall thickness t_1=5 nm
- max cell size 4 nm, damping parameter $\alpha = 1$ (for fast convergence)
- exchange stiffness $A = 13\,\mathrm{pJ/m}$, saturation magnetization $\mu_0 M_\mathrm{s} = 1\,\mathrm{T}$

As stated above, we performed micromagnetic simulations for 3 different initial configurations, the results with initial and relaxed state and its energy are summarized in Tab. 10.1. Initial and relaxed states are captured in Figures 10.2 and

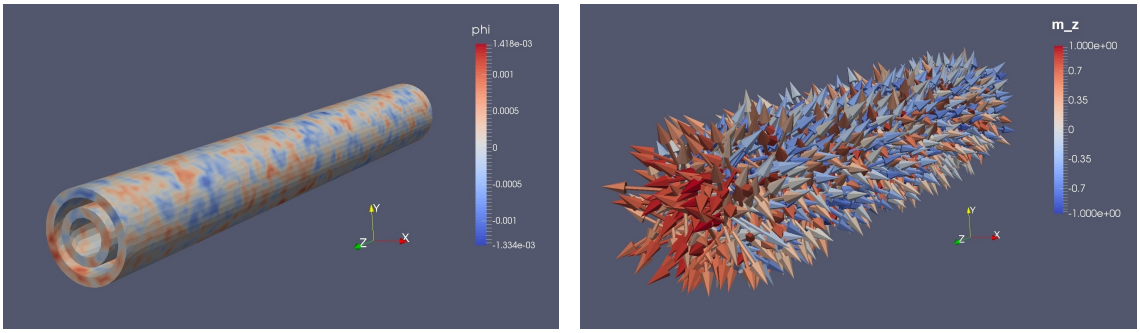

(a) Magnetic scalar potential in amps (b) Magnetization vector

Fig. 10.2: Illustration of a random initial micromagnetic configuration on SAF multilayered tubes. Magnetization at each node is assigned using a pseudorandom number generator. (a) scalar magnetic (pseudo)potential (in amps), (b) magnetization depicted with normalized vectors pointing randomly in all directions.

10.3 (initial $\vec{M}$: random), 10.4 (initial $\vec{M}$: antiparallel) and 10.5 (initial $\vec{M}$: parallel). From now on, only one half of the structure (cut through the common tube axis) will be displayed in order to have a clear picture of magnetization in both tubes.

Tab. 10.1: Summary of simulations of tubular SAF – smaller system in FeeLLGood: length L=400 nm, outer and inner tube diameter D_2=50 nm and D_1=30 nm respectively, tube wall thickness and spacing $t_2 = t_1 = s = 5$ nm.

Initial state	**Relaxed state**	**Relaxed energy**	Reference
random	antiparallel	$4.13{\cdot}10^{-18}$ J	Fig. 10.3
antiparallel	antiparallel	$4.13{\cdot}10^{-18}$ J	Fig. 10.4
parallel	parallel	$8.84{\cdot}10^{-18}$ J	Fig. 10.5

The initially random magnetization evolves in a very similar way to the OOMMF case described above, only a vortex-like wall (Fig. 10.3) is present in the inner tube (diameter of 30 nmm instead of 20 nm for the OOMMF simulation).

Both random and antiparallel initial configuration resulted in the antiparallel axial magnetization in the two tubes having basically the same energy. The only difference is the end curling which can have either same or opposite sense at both tube ends. Recall that in a single-shell tube there should not be any preference for the curling sense at the end [79]. Note that the end curling is clearly observed only for the outer tube with larger diameter; it looks like there is only inward or outward tilting of the magnetization for the inner tube (diameter 30 nm) – in Landeros phase diagram (Fig. 3.2) such tube would be in the uniform axial state.

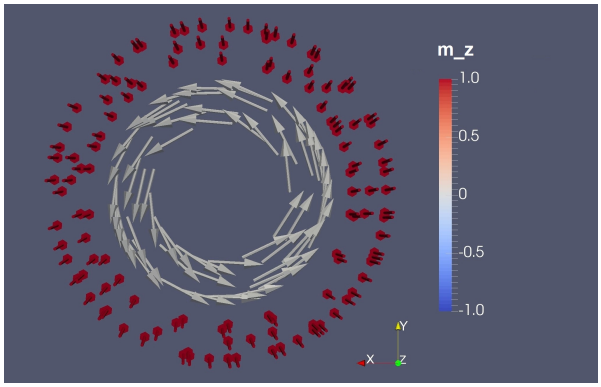

(a) Slice of intermediate state – vortex-like wall

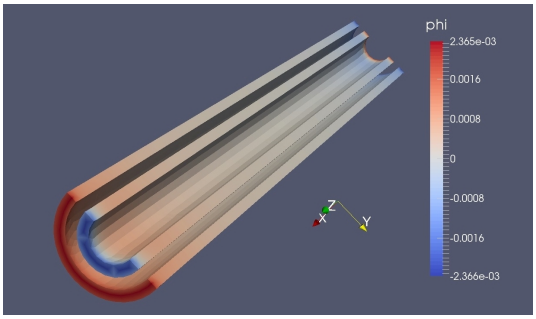

(b) Relaxed – magnetic scalar potential/A

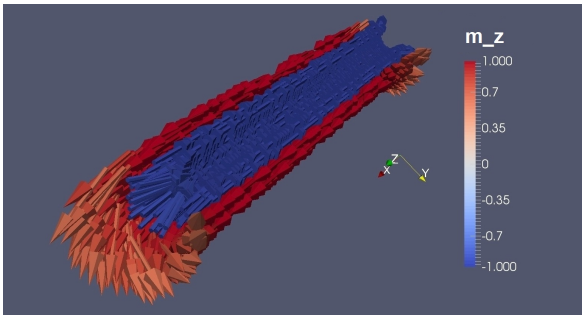

(c) Relaxed state – magnetization

Fig. 10.3: Small tubular SAF system (outer diameter 50 nm): random initial magnetization (depicted in Fig. 10.2). (a) Slice of the tubes in an intermediate state with a vortex-like wall in the inner shell; the outer one is uniformly magnetized. After relaxation, antiparallel state is established: (b) scalar magnetic potential (reflects also magnetic charges – at ends) and (c) magnetization.

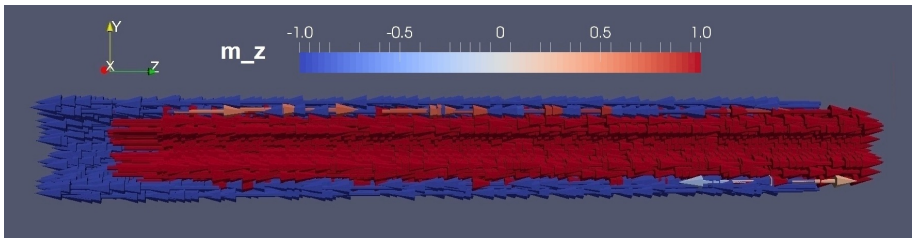

(a) Initial state

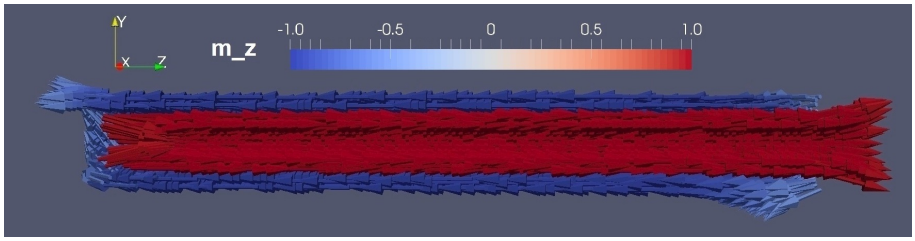

(b) Relaxed state

Fig. 10.4: Small tubular SAF system (outer diameter 50 nm): antiparallel initial configuration.

The structure with initially parallel alignment of the magnetization kept this arrangement, only curling/tilt of magnetization developed at the ends as discussed above. However, the energy of the relaxed state is more than two times higher than for the antiparallel alignment. Similar ratio of energies is found also in flat thin films [226]. The antiparallel state is preferred, while the parallel one may exist as a metastable state.

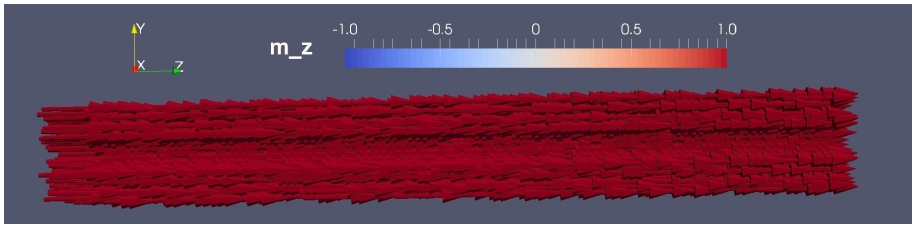

(a) Initial state – magnetization

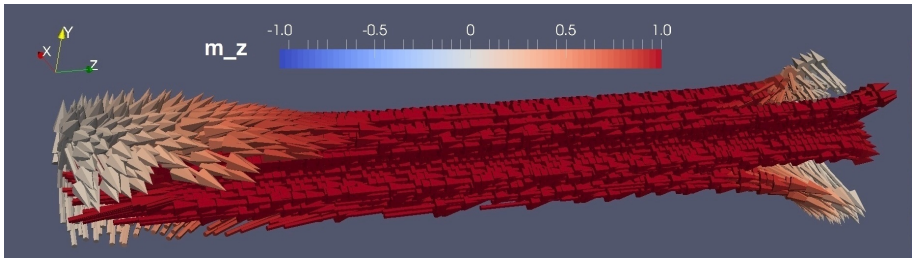

(b) Relaxed state – magnetization

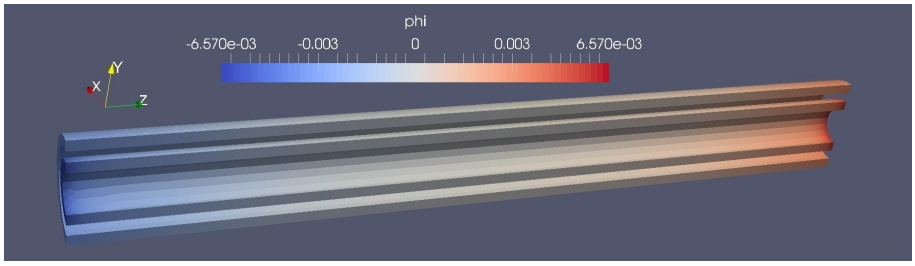

(c) Relaxed state – magnetic scalar potential/A (resulting from charges)

Fig. 10.5: Small tubular SAF system (outer diameter 50 nm): parallel initial configuration.

10.3.1 Simulated contrast for electron holography

We performed also crude simulations of expected magnetic phase maps for electron holography on tubular SAF. We used relaxed tubular SAF configuration discussed above – parallel [Fig. 10.5(b)] and antiparallel [Fig. 10.4(b)] magnetization in the two nanotubes. Fig. 10.6 shows that a clear difference between parallel and antiparallel states can be observed in the electron holography. In other words it should be possible to distinguish the two states using electron holography. Note that in our case [Fig. 10.6 (a)] the two tubes do not have the same cross-section and thus they do not compensate fully each other due in terms of magnetic moment. The full compensation would lead to the same potential and thus phase outside the structure – i.e. same level both on the left and right of Fig. 10.6a-b.

10.4 Tubular SAF – larger diameter (250 nm)

The simulations on the smaller system (both OOMMF and FeeLLGood) showed that the magnetization in two coaxial tubes with a spacer can be in the antiparallel state, thus forming a synthetic ferrimagnet. Now we will explore larger systems consisting of tubes with larger diameter (250 nm), which is closer to our electroless tubes (SS53 NiCoB tubes) used in the synchrotron experiments. The geometry and simulation parameters are given below:

- length L=2000 nm; spacer thickness (in between the tubes) $s = 15$ nm
- outer tube: external radius R_2=125 nm, tube wall thickness t_2=15 nm
- inner tube: external radius R_1=95 nm, tube wall thickness t_1=15 nm
- max cell size 4 nm, damping parameter $\alpha = 1$ (for fast convergence)
- exchange stiffness $A = 13$ pJ/m, spontaneous magnetization $\mu_0 M_s = 1$ T

Aside from random and axial (anti)parallel initial configuration we also simulated azimuthal magnetization (curling everywhere) with either same or opposite sense in the two coaxial tubes. The results are gathered in Tab. 10.2.

As in the case of smaller tubes, the random and antiparallel initial configuration evolved to antiparallel alignment, now with the end curling present in both tubes. Note that again the sense of the end curling varies, it can be either the same at both ends or the opposite [Fig. 10.7 (a)-(b)].

Fig. 10.8 shows how the magnetization looks like when we consider only the outer shell (diameter of 250 nm). The curling extends almost along the whole length of the tube (2 microns), therefore one may argue if this is an axially magnetized tube with extended end curling or azimuthally magnetized tube with a Néel wall . . . The extend of both end curling seems to be similar to models presented by Wyss et al. [79] (maybe our is slightly larger). Note that in our NiFeB tubes the end curling

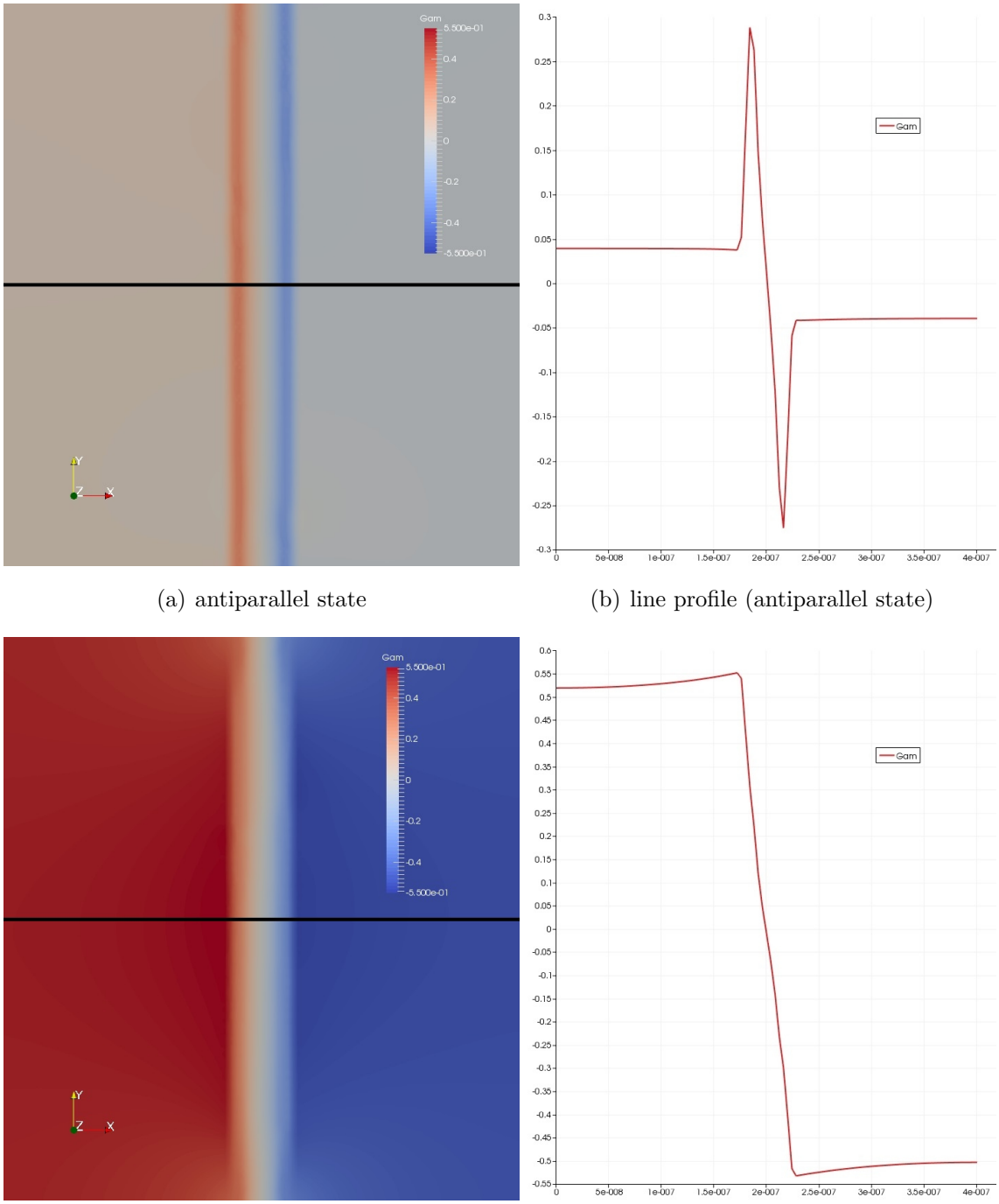

(a) antiparallel state

(b) line profile (antiparallel state)

(c) parallel state

(d) line profile (parallel state)

Fig. 10.6: Crude electron holography magnetic phase maps (Gam in rads) on SAF tubes. (a) antiparallel state [see Fig. 10.4(b)], (c) parallel state [consult Fig. 10.5(b)]. Note that in (a) the 2 tubes do not have the same cross-section and thus they do not compensate fully each other as for the stray field. Still only small magnetic induction can be seen outside the structure. (c) and (d) depicts line section of both maps across the tubes (black line).

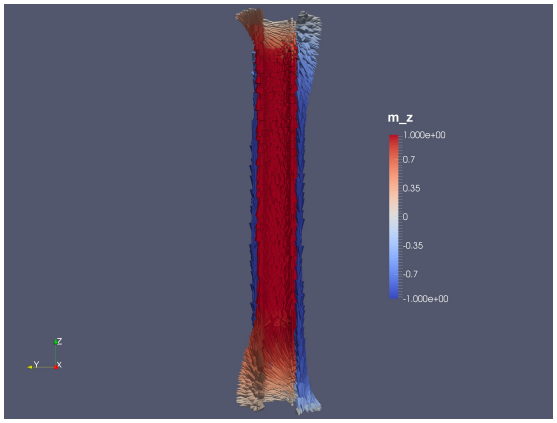

(a) **Initial $\vec{M}$: random** – relaxed

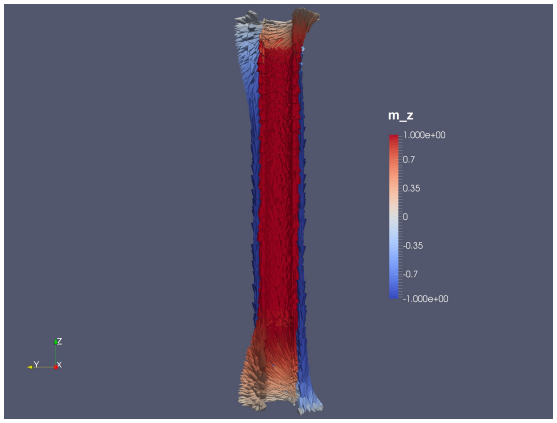

(b) **Initial $\vec{M}$: antiparallel** – relaxed

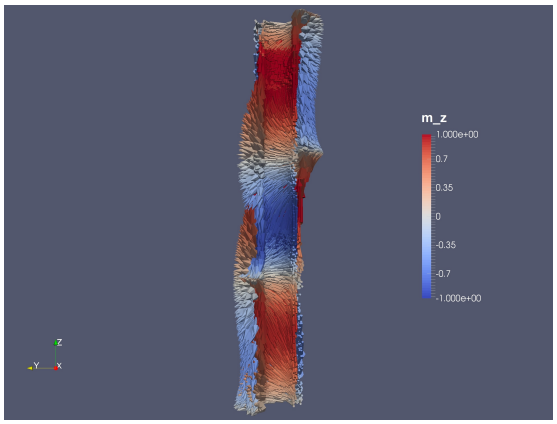

(c) **Initial $\vec{M}$: parallel** – 40k iterations

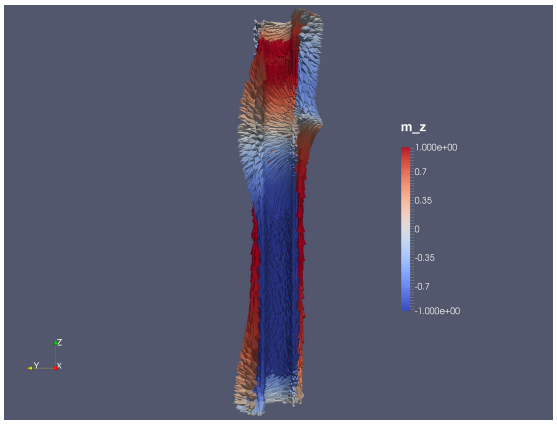

(d) **Initial $\vec{M}$: parallel** – 120k iterations

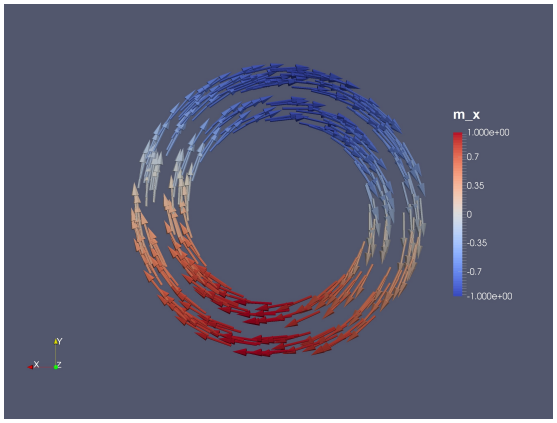

(e) **Initial $\vec{M}$: parallel** – 40k iterations – bottom DW slice

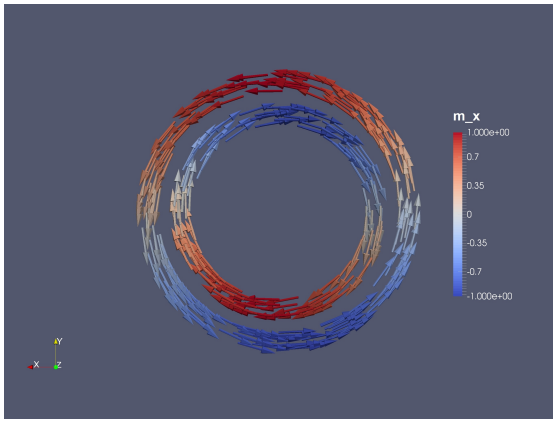

(f) **Initial $\vec{M}$: parallel** – 120k iterations – top DW slice

Fig. 10.7: Larger coaxial tubes with a spacer with various initial configurations. Except for azimuthal magnetization, (a)-(c) all cases evolve towards axial antiparallel alignment of the magnetization in both tubes. (c)-(d) in case of initially parallel state, antiparallel domain were formed separated by coupled domain walls with either (e) same or (f) opposite chirality.

Tab. 10.2: Summary of simulations of tubular SAF – larger system in FeeLL-Good: length L=2000 nm, outer and inner tube diameter D_2=250 nm and D_1=190 nm respectively, tube wall thickness and spacing $t_2 = t_1 = s = 15$ nm.

Initial state	Relaxed state	Relaxed energy
azimuthal – same chirality	azimuthal – same chirality	$4.90 \cdot 10^{-17}$ J
azimuthal – opposite chirality	azimuthal – opposite chirality	$4.90 \cdot 10^{-17}$ J
random	axial antiparallel	$2.00 \cdot 10^{-17}$ J
axial antiparallel	axial antiparallel	$2.00 \cdot 10^{-17}$ J
axial parallel	axial antiparallel domains[†]	[◇]

[†] After few thousands iterations 3 antiparallel domains were established. Much later one moved towards the end of the structure and annihilated, the other one remains even after 160 k iterations. The total micromagnetic energy (dipolar+exchange) is higher than mono-domain antiparallel state, as expected.
[◇] Energy around $3.61 \cdot 10^{-17}$ J after $137 \cdot 10^3$ iterations (=several months).

was mostly not present. Still it is clear that SAF geometry promotes the axial magnetization even for large diameters and short tubes [compare with Fig. 10.7 (a)-(b)].

The simulation with initially parallel alignment of the magnetization is more interesting for large tubes (but there is also the effect of larger spacer). Instead of staying parallel as for small tubes, 3 antiparallel domains separated by coupled vortex-like walls were established [Fig. 10.7(c)]. The domain walls are present in both tubes at the same location and they have either same [Fig. 10.7(e)] or opposite chirality [Fig. 10.7(f)]. Later the domain walls with the same chirality moved to the end of the structure and annihilated. The other couple (opposite chirality) of domain walls moved only slightly and still persist [Fig. 10.7(d)] even after almost 140 thousands iterations and there is almost no change in the magnetization (close to a convergence condition).

As for the azimuthal magnetization (no anisotropy introduced), both simulations ended quickly keeping the initial configuration. Independent of chirality, the total magnetic energy is the same and it is significantly larger than axial antiparallel configuration that is the most energetically favourable. Still it could be a metastable state – to be further investigated. Azimuthal magnetization in both tubes, either with same or opposite chirality, looks like domain wall slices in Fig. 10.7 (e) and (f), just this state is present along the whole structure.

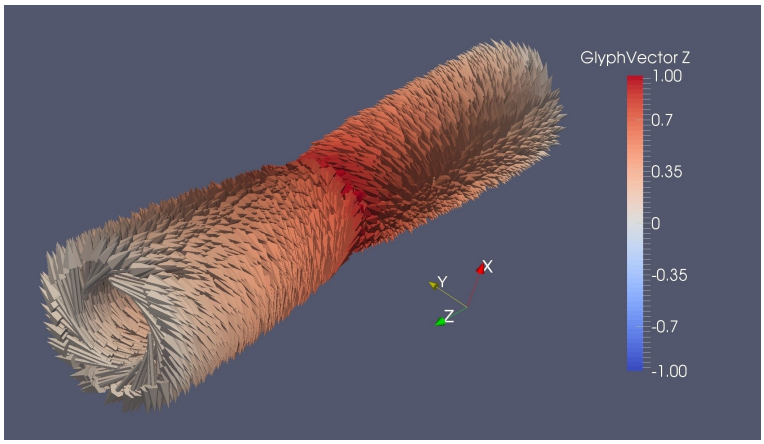

Fig. 10.8: Micromagnetic configuration when considering only the outer tube from our coaxial tube stack. Unlike in the SAF geometry, the curling extends almost along the whole length of the tube (2 microns).

10.5 Summary of tubular synthetic ferrimagnet modelling

Micromagnetic simulations suggest that it should be possible to realize synthetic antiferromagnet (ferrimagnet) in tubular geometry with interesting physics ahead. These tubular SAFs can serve as a one of the key elements in 3-dimensional spintronics. Further, simulations of electron holography phase maps demonstrated a sizeable difference in phase between parallel and antiparallel alignment in the both tubes. Therefore, the electron holography can be used for confirmation of presence of the SAF configuration. However, further experimental studies would be done rather utilizing magnetic circular dichroism (polarized X-rays or in future also electrons) with shell formed from different elements to probe separately the magnetization in the tubes. Our preliminary work can be further extended also with consideration of proper SAF (with thin Ru spacer).

11 TRILAYERED TUBES: EXPERIMENTS

In the previous chapter we probed with micromagnetic simulations the possibility of obtaining synthetic ferrimagnets in tubular geometry through dipolar coupling and thicker non-magnetic spacer (e.g. 10 nm). Here we show experimental realization of such trilayers. In the following sections we provide structural, chemical and mainly magnetic investigation of the multilayered tubes. Note that the focus as for physics is different as one of our magnetic layers (CoNiB) displays similar azimuthal anisotropy to single-layered tubes discussed in chapter 8. Therefore, we will focus on obtaining (exchange) decoupled magnetic layers. Still we will also briefly discuss how one could obtain the tubular SAF.

11.1 Structural and chemical analysis

In our case, we used electroless plating (see section 4.4.3) to prepare the multilayered system such as in Fig. 11.1. We used different elemental composition of the layers, so that we could disentangle the magnetization in each magnetic layer by utilizing the element specificity of the synchrotron X-ray magnetic microscopy (XMCD-PEEM).

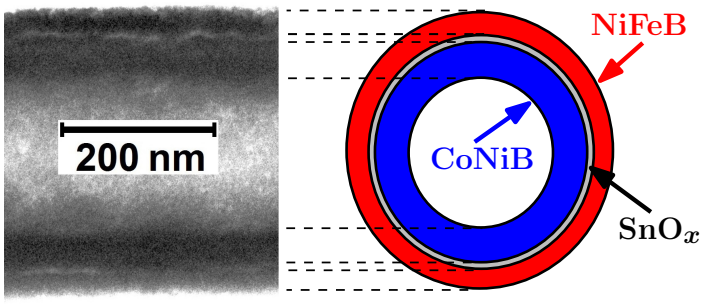

Fig. 11.1: Multilayered tube with a non-magnetic (oxide) spacer. Experimental realization (left) – transmission electron microscopy of a tube segment (electrons arrive perpendicular to the tube axis). The oxide spacer appears as a brighter line in the tube wall. Scheme to the right highlights the different layers of the tube.

At TU Darmstadt, S. Schaefer prepared several samples with different tube lengths, different non-magnetic spacers and their (chemical) modification for the subsequent deposition of the inner magnetic layer. Two main spacers were tested – metallic (Pd) and insulating (SnO_x), yielding multilayered tubular stacks NiFeB/Pd/-CoNiB (sample SS147) and NiFeB/SnO_x/CoNiB (sample SS148).

Fig. 11.2 displays electron microscopy and chemical mapping of a set of two multilayered tubes from the SS148 sample, dispersed on a TEM grid. The left tube contains all three layers (NiFeB, SnO_x, and CoNiB) whereas the other one lacks the

inner CoNiB layer. Transmission electron microscopy shows that proper multilayered tubes are thick, with the total tube wall thickness around 90 nm. The SnO_x spacer is represented by a bright line in the otherwise dark tube wall (Fig. 11.2a, left tube). The measured thickness of the layers from the TEM images (higher magnification) is as follows (deviation up to ±5 nm, except SnO_x – rather larger thickness):

- **outer shell**: NiFeB approx 30 nm
- **spacer**: SnOx approx 10 nm (may be underestimated see below)
- **inner shell**: CoNiB approx 50 nm

Due to the large thickness of the metallic layers, the SnOx (bright line) may be underestimated; up to 20 nm thickness is expected from typical deposition rates (1 nm/h) for SnO_x using the chemical bath deposition. As for the chemical mapping with EDX, we can clearly see the presence of outer NiFeB (Fe) for both tubes; the inner CoNiB (Co) is only in the left tube. Unfortunately, we cannot see a well-localized spacer: Sn appears everywhere as it is also used for modification of the tube surface after deposition of each layer. Delocalized Sn presence is also caused by a large interaction volume (for 20 keV primary beam energy). Spacer from a different material would be more easy to detect, e.g. TiO_2 that can be prepared in very similar way as SnO_x [170].

Regarding the SS147 sample, no clear sign of Pd was detected with EDX, indicating that it may have been replaced during the deposition of the inner layer that was in some cases thicker than expected. Sometimes particles (most likely Sn) can be seen inside the tubes. In several other tubes, the Pd spacer turned out to be inhomogeneous or completely missing. Therefore, in order to get a metallic spacer, different metal should be selected, such as copper. Alternatively, one can use a different fabrication technique, such as ALD that enables also deposition of pure metals [133].

Better results were obtained for the SnO_x, but even here significant portion of tubes was without the inner CoNiB core. This is caused mainly by blocked pore extremities as the membrane is polished after each deposition step. This may lead to obstruction of the pore openings. Only 2 out of 6 series of samples had significant amount of tubes with the inner CoNiB layer and only one sample had tubes with both magnetic layers separated by the continuous spacer (SS148). The yield of multilayered tubes could be significantly increased when using porous alumina templates. Here the excessive growth can be removed by ion beam etching instead of the mechanical polishing. Ion etching could not be used in our case as polycarbonate membranes are slightly burnt during the process (at least in our machine). In addition, ion etching can be performed just after the activation of the alumina membrane with Pd seeds – this would remove the catalysts and thus prevent the

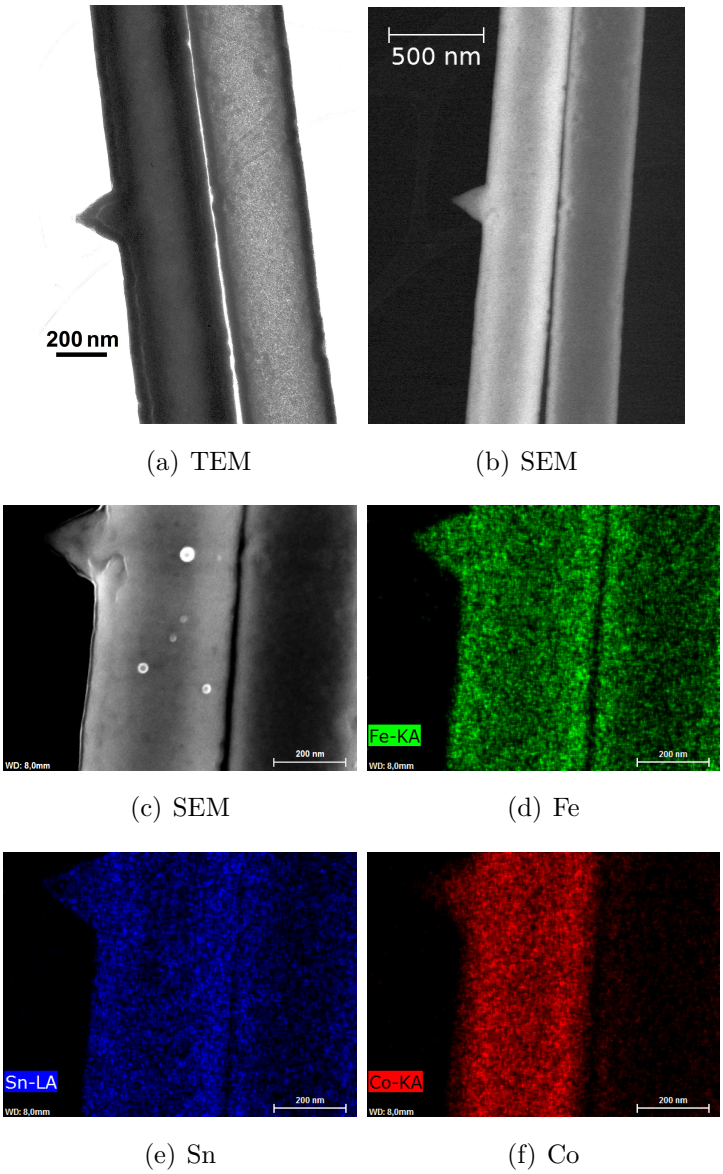

(a) TEM (b) SEM

(c) SEM (d) Fe

(e) Sn (f) Co

Fig. 11.2: Electron microscopy and chemical mapping of two SS148 tubes side-by-side. (a) Transmission electron microscopy, courtesy of Laurent Cagnon. (b) Scanning electron microscopy (SEM) image with backscattered electrons – reflecting the tube wall thickness and partially also the atomic number of elements. (c) SEM – detail close to a protrusion defect. (d)-(f) EDX maps for different elements in the (c) area (Fe, Sn, and Co respectively). The left tube has all the layers whereas the right one only the outer NiFeB and most likely also the SnO_x spacer (see discussion in the text), but it lacks the inner CoNiB shell. The diameter of Co is significantly smaller than that of Fe and also than the tube diameter in (c) – consistent with CoNiB being the inner layer. The SnO_x oxide spacer can be seen in (a) as a brighter line in the tube wall separating two darker regions – metallic layers (easier to spot on the left side of the tube, but present on both). Scalebars: (b) 500 nm, otherwise 200 nm.

unwanted metal deposition on top/bottom of the template. Last but not least, ordered arrays with tunable outer diameter and distance among tubes, would be more interesting for a potential device.

In the following, we will focus mainly on the sample SS148 with tubes having all the three layers.

11.2 XMCD-PEEM imaging

For the synchrotron experiments we dispersed the tubes on multiple Si substrates. Prior to the beamtime, using EDX we identified on each substrate several tubes containing elements from all layers: Fe, Sn, and Co. Additional tubes suitable for the investigation were determined directly at the Nanospectroscopy beamline (synchrotron Elettra) by utilizing X-ray absorption spectroscopy around Co-L_3 edge (i.e. tubes with inner CoNiB layer).

11.2.1 Demagnetized state

Prior to the imaging, the tubes were AC demagnetized in the transverse direction using an electromagnet. Fig. 11.3 displays XMCD-PEEM images of a SS148 multilayered tube with a complete insulating spacer separating the two magnetic layers, outer NiFeB and inner CoNiB. Imaging at both at Fe-L_3 (outer layer) and at Co-L_3 (inner layer) edges was performed to probe separately both magnetic layers. The magnetic patterns are completely different, indicating that the spacer is thick enough and continuous, so that it successfully allows the (exchange-)decoupling of the two magnetic layers. The outer NiFeB layer is uniformly axially magnetized similar to single NiFeB tubes. On the other hand, the inner CoNiB tube features several domains. To reveal the nature of these domains we performed more refined imaging with the beam almost perpendicular to the tube and adjusted settings so that almost the full shadow is visible. It turned out that these are azimuthal (Fig. 11.4c). Therefore, with a proper spacer both layers display magnetization similar to single-shell tubes of the same material and geometry. In Fig. 11.3 (left) one can also see even the non-magnetic SnO_x spacer – the grey line in the white NiFeB shadow close to its bottom rim.

Fig. 11.5 displays an example of a tube from SS147 sample where the non-magnetic spacer (now Pd) was not continuous or even completely missing. The two magnetic layers appear to be exchange-coupled: they feature the same contrast pattern along the whole tube (here only a part close to the end is shown) for both layers, i.e. for images at both Fe-L_3 and Co-L_3 edges. The gradual change in the contrast in the shadow suggests azimuthal magnetization in both layers.

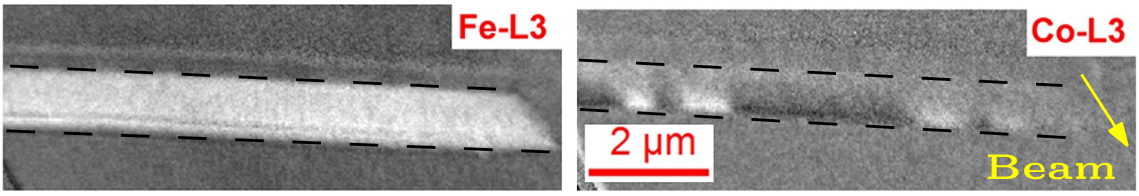

Fig. 11.3: NiFeB/SnO$_x$/CoNiB – decoupled magnetic layers (SS148 sample). In both images, shadow area at given absorption edge is highlighted with a dashed line. Here, the extent of the shadow, reflects the tube diameter. Thus, it is smaller at Co edge, as CoNiB is the inner layer (smaller diameter). The information from the tube surface is weak due to the imaging conditions being optimized for the shadow and also in case of the inner layer no surface magnetic signal is expected. The outer NiFeB layer is uniformly magnetized along the tube axis (uniform transverse magnetization is highly unlikely without external magnetic field). Note also the grey line in the white shadow close to its bottom rim – this is the non-magnetic SnO$_x$ spacer. On the other hand, the inner CoNiB layer (smaller extent of the shadow) displays a completely different magnetization pattern with multiple domains. These are azimuthal as in a single CoNiB tube case (with similar geometry) as can be seen in Fig. 11.4c.

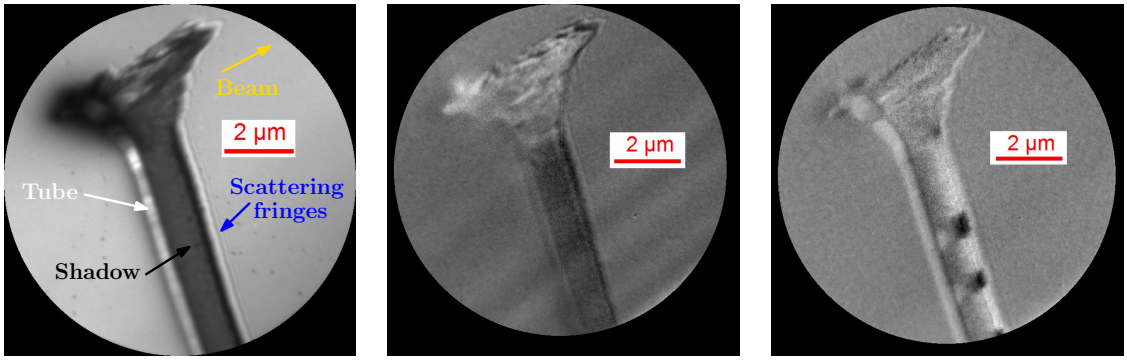

(a) XPEEM Fe-L$_3$ (b) XMCD-PEEM Fe-L$_3$ (c) XMCD-PEEM Co-L$_3$

Fig. 11.4: Images of a SS148 multilayered tube (NiFeB/SnO$_x$/CoNiB). (a) PEEM image @ Fe-L$_3$showing the tubular character. (b) XMCD-PEEM @ Fe-L$_3$ with uniform contrast and magnetization, and (c) XMCD-PEEM @ Co-L$_3$ with a clear contrast change in the shadow indicating presence of azimuthal domains. Microscope settings are adjusted for better collection of photoelectrons from the shadow (substrate surface). The defect at the tube end (top) is caused by the mechanical polishing of the membrane with tubes which may lead to tube opening being blocked, filled with both magnetic and non-magnetic particles. The presence of this defect does not disturb the magnetization and decoupling of both layers in other parts of the tube.

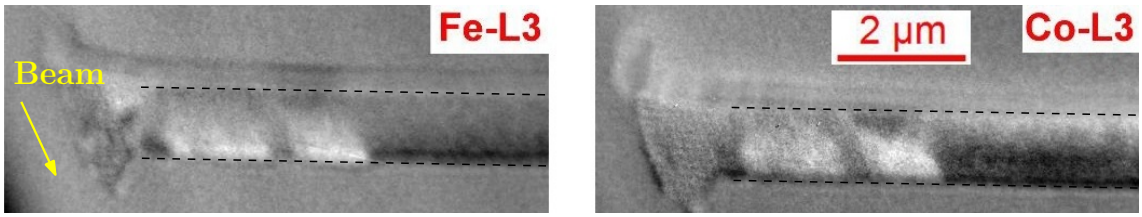

Fig. 11.5: NiFeB/Pd(incomplete)/CoNiB – coupled magnetic layers (SS147 sample). XMCD-PEEM images Fe-L_3 and Co-L_3 edge, respectively. Arrow depicts the beam direction; the approximate shadow extent is marked by dashed lines. The gradual change in the contrast in the shadow suggests azimuthal magnetization in both layers. Tube end displays similar defect as in Fig. 11.4.

Multiple tubes were investigated on both SS147 and SS148 samples, yielding very similar images to the ones presented here.

11.2.2 Switching by field pulses

Aside from the imaging of the tubes in a demagnetized state, we also inspected the tubes after applying magnetic field with direction close to along the tube axis. Similar to single shell SS53 CoNiB tubes, the magnetization could be manipulated with very low magnetic fields. A detailed inspection and testing revealed that the problem lay in a current source supplying current for the coil. Before delivering the desired current (field) value, there was a spike of 5 A (around 100 mT, width in ms). More information can be found in the methods section 5.1.1.

Despite the nuisance, field pulse revealed also very interesting behaviour not observed under DC field. From our previous imaging under axial field, we know that the azimuthal magnetization in single shell CoNiB tubes rotates towards the axis, but otherwise no dramatic changes happen: at most (dis)appearance of a few domains. Here the situation was very different. The axial magnetization in the NiFeB layer was switched to opposite, remaining in the single domain state, which can be expected after applying field larger than the coercivity. The azimuthal domains in the CoNiB layer were switched as well. The azimuthal domains stayed at exactly the same place, just the curling sense switched in all domains to the opposite. We repeated the switching with alternating the direction of the field several times. Further, we verified that the contrast inversion is not caused by the instrument-related issues, nor processing of the images. Same behaviour was observed also for single shell SS53 CoNiB tubes. This behaviour is surprising, especially its reproducibility, especially as the field magnitude (approx. 100 mT should saturate both tubular layers along the field direction.)

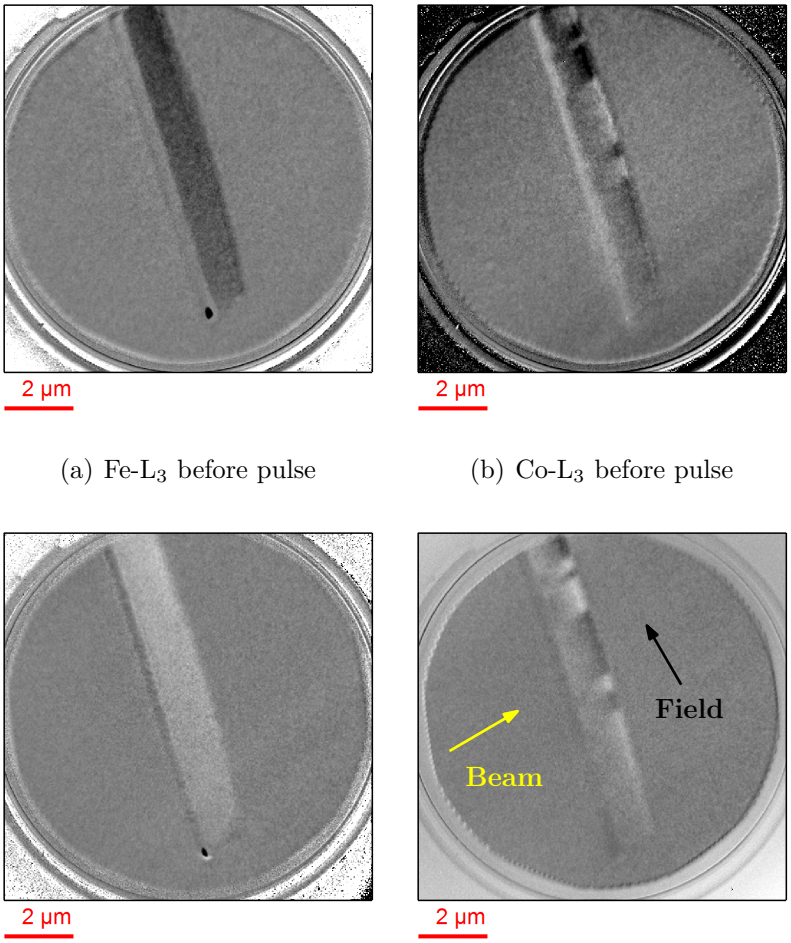

(a) Fe-L_3 before pulse

(b) Co-L_3 before pulse

(c) Fe-L_3 after pulse

(d) Co-L_3 after pulse

Fig. 11.6: Switching of magnetization by field pulses in multilayered NiFeB/SnO_x/CoNiB tubes. (a)-(b) initial state for both layers: NiFeB with uniform axial magnetization and CoNiB with azimuthal domains. (c)-(d) after the pulse not only the NiFeB layer is switched, but also the azimuthal domains in CoNiB have opposite circulations. The field is applied perpendicular to the beam direction.

We do not have a proper understanding of the mechanism, but it could be interesting to probe this circulation switching further with controlled pulses (magnitude, duration, ramp). Influence of local defects even weak, cannot be excluded. It should be noted that in our case the field is not applied exactly along the tube axis, but at some angle which could be also an important factor.

11.2.3 Magnetization switching with quasistatic DC field

Thanks to a great effort of the Nanospectroscopy beamline staff, the problem with the current and thus field spike could be solved. Therefore, we could probe the magnetization switching, now after applying DC pulse field with a well-defined duration (0.5 s = quasistatic) and magnitude. We started with saturating the tube along one direction (negative field values) and then we applied field with increasing value in the opposite direction. After the field application, we took images at zero field for both Fe-L_3 and Co-L_3 edges to map the XMCD-PEEM contrast in the both magnetic shells. Our investigation is summarized in Fig. 11.7. Note that even though we would like to apply the field directly along the tube axis, we are restricted to field directions with some angle vs tube axis. The reason is the instrumental setup: applied field is always perpendicular to the beam direction. As we want to have some information on both tubes, i.e. both on axial and transverse components of magnetization, the beam cannot arrive directly perpendicular to the tube (zero projection of axial magnetization). Therefore we select a compromise with some misalignment (differs from tube to tube as all tubes does not have exactly the same orientation on the substrate).

Again we focus on the shadow (reminder: tube in the shadow is stretched by a factor of 3.6 along the beam direction) as no information about the inner shell can be retrieved from the tube surface. The outer NiFeB shell is initially uniformly magnetized. Upon applying field of increasing values, magnetization reversal starts at the tube end. The domain boundary seems to be rather complex and its shape evolves with the field history (Fig. 11.7, left column). Another puzzling aspect is that the XMCD-PEEM contrast level close to the left end is very similar to the background level (neither bright, nor dark). This could indicate that in this region magnetization is mostly perpendicular to the beam, so (anti)parallel to the field direction. As from the image itself we cannot determine, whether the magnetization is parallel or antiparallel in this region, we cannot elucidate the pattern. E.g. whether it involves a transverse wall with an azimuth neither parallel, not perpendicular to the beam. The state after 15 mT is particularly puzzling, clearly a state with a domain with magnetization neither axial, nor azimuthal.

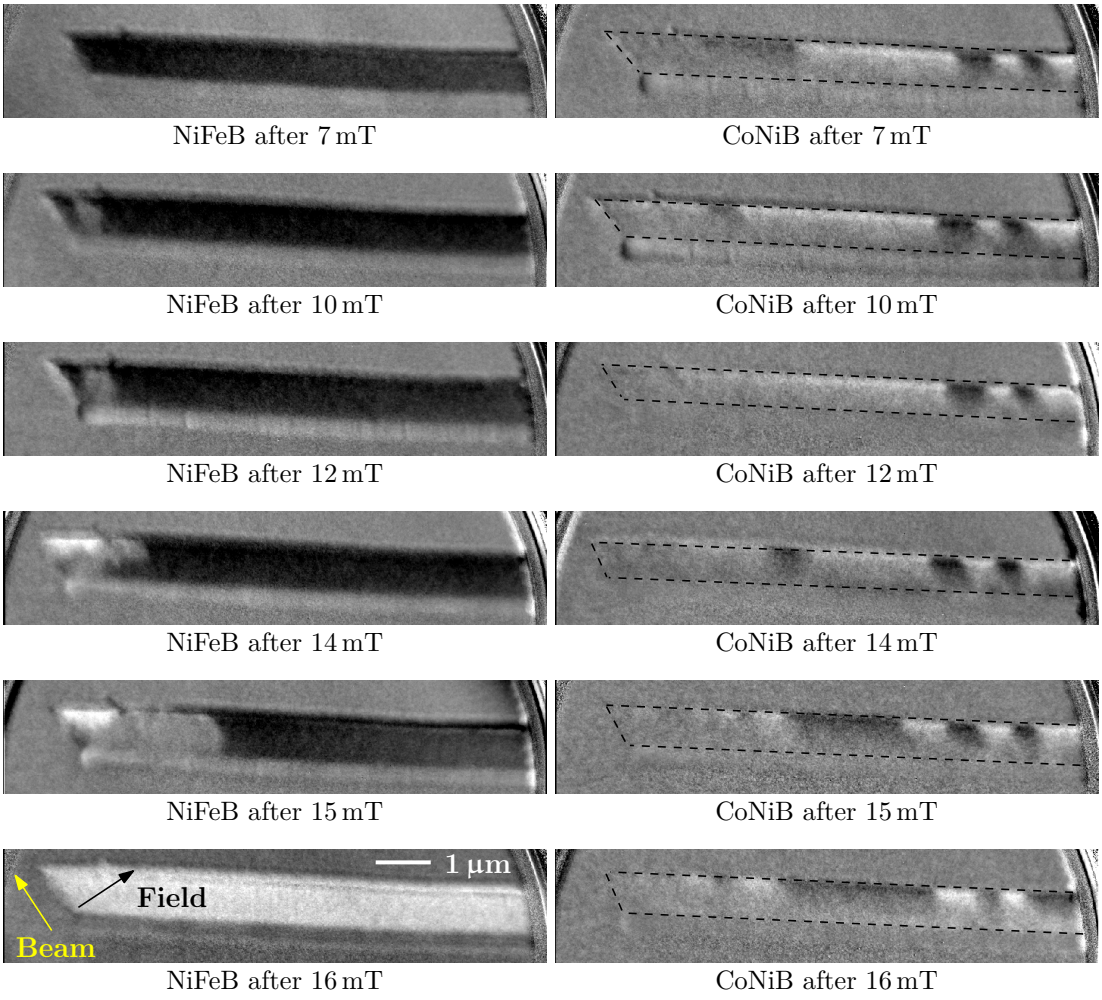

Fig. 11.7: Manipulation of magnetization by a DC field in multilayered NiFeB/SnO_x/CoNiB tubes. First, the tube is saturated in one direction with negative field, then we apply magnetic field in the opposite direction (positive), always perpendicular to the beam direction (imposed by the cartridge design). The approximate extent of the CoNiB shadow is marked with dashed lines.

The magnetic configuration that propagates during the reversal (especially after 14 mT) is not just a domain wall expected in tubes with axial magnetization (transverse, or rather vortex-like wall for such big diameter as in Fig. 3.5). Complex magnetic (induction) patterns were observed also for single shell NiFeB tubes (SS123) by electron holography (see section 8.3.3). This might be the combined effect of a larger diameter (400 nm outer diameter), material, and the field deviating from the axial direction. The magnetization reversal is completed after 16 mT. Few other multilayered tubes were investigated for the NiFeB reversal, the switching field is in the range 10-20 mT (again field with a small deviation from the axial direction). As we have also tubes with missing inner CoNiB shell, we made a reference measurement on a tube with NiFeB layer only. The switching occurred at 12 mT (partial reversal started at 5 mT). Therefore, it seems that the presence of CoNiB layers does not affect (significantly) the outer NiFeB layer. Another interesting point is that the NiFeB shell does not display curling state (small azimuthal domain) at the end which is expected in axially magnetized tubes, especially with such a large diameter.

So far we focused on the outer shell. Let us now turn back to the inner CoNiB shell with azimuthal magnetization (Fig. 11.7 right column). There are some changes in the CoNiB layer as well: azimuthal domains appear and disappear, some of them switch, but there is no clear correlation with the reversal in the NiFeB shell. This is caused most likely by the spacer being too thick (10-20 nm) and also the presence of the flux-closure domains in the CoNiB layer.

We performed also the switching in the opposite direction, obtaining similar behaviour with the partly unresolved domain boundary in the NiFeB shell.

To conclude this part, we could obtain the first preliminary experimental images of a magnetization reversal in the tubes. NiFeB reverses its axial magnetization by nucleation and propagation of a complex magnetic structure. This is most likely caused by the combination of large diameter, material, and the field not being applied directly along the tube axis. Last but not least, we cannot rule out some influence of the inner CoNiB layer.

11.3 Magnetometry

After the synchrotron investigations, we tried to measure global hysteresis loops of arrays of multilayered tubes still in the membranes (templates). The idea was to check whether we could spot some differences for arrays of tubes as regards the presence and quality of the non-magnetic spacer separating the two magnetic layers (stack: NiFeB/spacer/CoNiB). We compared samples SS147 (NiFeB/CoNiB,

Pd spacer is discontinuous or even in many cases completely missing) and SS148 (NiFeB/SnO_x/CoNiB where at least some tubes have a good spacer leading to decoupling of the two magnetic layers). VSM-SQUID loops are featured in Fig. 11.8. The porosity of membranes is very low, similar to SS53 CoNiB tubes (see Fig. 8.10b). Therefore, we expect dipolar interactions among tubes to be rather weak – this could enable us to get information about average single (multilayered) tube.

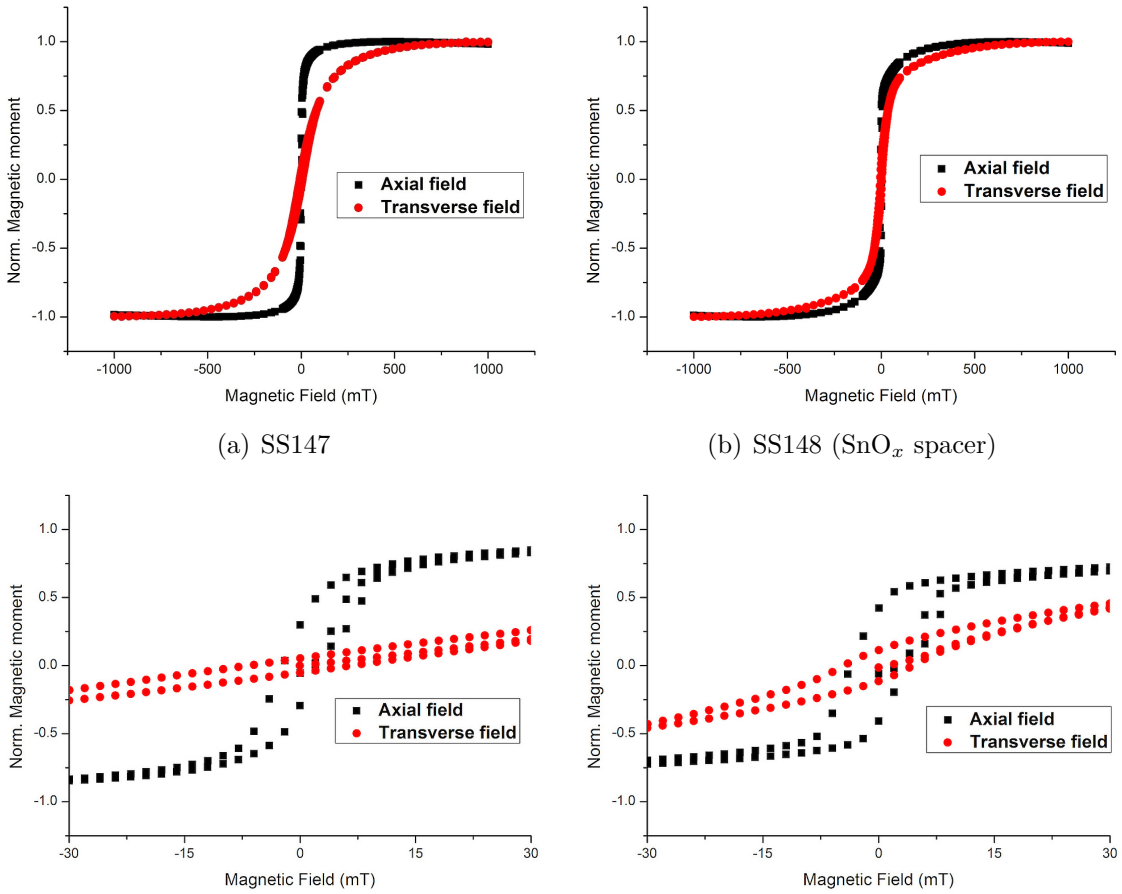

(a) SS147

(b) SS148 (SnO_x spacer)

(c) SS147 – detail

(d) SS148 (SnO_x spacer) – detail

Fig. 11.8: Magnetometry on arrays of multilayered tubes. (a), (c) SS147 NiFeB/-CoNiB, the Pd spacer is either completely missing, or at least discontinuous in many cases. (b), (d) SS148 containing some NiFeB/SnO_x/CoNiB with a good spacer, leading to decoupling of the two magnetic layers.

For SS148 the loops are similar for the field parallel and perpendicular to the tube axis with both directions being rather soft. This can be consistent with the two magnetic layers having different magnetization patterns. For NiFeB layer with axial magnetization the axial direction is the easy axis and from measurement on single shell CoNiB tubes we know that these are reoriented toward the axis within 25 mT.

Easy reorientation in transverse field is also understandable due to the presence of CoNiB with azimuthal anisotropy (transverse to tube axis).

For SS147 (magnetic layers in direct contact), XMCD-PEEM suggested that both layers are coupled and have azimuthal magnetization. Again easy axial reorientation can within 25 mT seems reasonable. However, it is strange that the axial loops are more squared than for SS148 and mainly that the transverse direction appear so hard.

The deviations from the expected behaviour could be partially caused by a non-proper removal of the film on top and bottom of the template with the tubes, and/or slightly bent membrane with the tubes. Also some of SS148 tubes have only the outer layer.

To conclude this part: we cannot clearly tell the quality of the spacer just from the global measurements in this case. Situation should be better for two magnetic layers with both having axial magnetization (e.g. for smaller diameters below 100 nm, or both layers from NiFeB) where two distinct switching events should occur.

11.4 Annealing and towards synthetic ferrimagnets

We also tried to image annealed SS148 multilayered tubes to get axial magnetization in both layers and possibly explore (anti)parallel alignment of magnetization in both layers modelled in the previous chapter. Unfortunately, the spacer was either damaged during the treatment, or the temperature was too low to recover axial magnetization in the CoNiB layer. Here one can use spacer from different material and of smaller thickness (possibly done by atomic layer deposition), or rather change the composition of both magnetic layers to have the axial magnetization from the beginning. One may think of e.g. NiFeB/SnO_x/NiFeB layer that should be feasible to fabricate and with preferred axial magnetization direction for both layers. One would be still able to distinguish between parallel and antiparallel configuration, but the layers could not be resolved independently. The easiest way might be keeping the same chemical composition and just decreasing the diameter, as CoNiB nanotubes with smaller diameter (e.g. 100 nm) were found to be axially magnetized (see section 8.4). Such downscaling is challenging, but feasible as both at TU Darmstadt and in our laboratory we could fabricate nanotubes with diameters around 100 nm (80 nm at TU Darmstadt).

Further, spacers with smaller thickness and from different materials could be of interest for investigation of magnetoresistance effects; SnO_x that was employed in

our case is a conductive oxide (similar to indium tin oxide – ITO), thus one could prefer either better metal, or insulating oxide (depending on the application). We used SnO_x for the ease of fabrication, but other spacers can be fabricated using atomic layer deposition or solution-based methods.

11.5 Summary of investigation of multilayered tubes

We studied multilayered tubes with two magnetic layers with different chemical composition separated a non-magnetic spacer (metallic or insulating), more precisely NiFeB/(Pd)/CoNiB (SS147 sample) and NiFeB/SnO_x/CoNiB (SS148 sample) stacks.

In all cases the CoNiB layer resembled single-layered CoNiB tubes with similar diameter (e.g. SS53 sample): it contained multiple azimuthal domains. For SS147 (NiFeB/CoNiB), the outer NiFeB layer displayed the same magnetization pattern, i.e. both layers were exchange-coupled due to the missing/damaged spacer. SS148, with SnO_x spacer, displayed exchange-decoupled layers, where outer NiFeB was axially magnetized and the inner CoNiB exhibited azimuthal magnetization. We observed effect of both pulse and quasistatic magnetic field on the tubes. Short high field value (100 mT, ms duration) pulses led to switching of magnetization in both layers with azimuthal domains surprisingly staying at the same place, just reversing the circulation sense. Quasistatic field of increasing value resulted in the reversal of the outer NiFeB shell by a propagation of a strange magnetic configuration (not properly understood). Some changes occurred also for the CoNiB layer – (dis) appearance and extension of some domains, but nothing clearly related to changes in the NiFeB shell.

Next steps could include the realization of a system with axial magnetization in both layers (towards SAFs) and downscaling of the system, which is challenging, but feasible as both at TU Darmstadt and in our laboratory we could fabricate nanotubes with diameters as small as 100 nm (80 nm at TU Darmstadt).

12 CONCLUSION & PERSPECTIVE

We successfully fabricated nanotubes from several ferromagnetic materials by electrochemical methods in nanoporous templates. Namely we prepared NiCo nanotubes (diameter 70-90 nm), Ni nanotubes (diameter around 60 nm) and nanostructures with alternating wire (solid) and tube (hollow) segments. Further, we obtained CoNiB and NiFeB electroless deposited tubes (diameters 80-400 nm) as well as multilayered tubes from our collaborators in TU Darmstadt. Aside from these, we fabricated similar CoNiB nanotubes by the same technique (diameters 100-200 nm).

We investigated all these nanostructures with electron microscopy (scanning/-transmission) and in some cases also with atomic force microscopy. Aside from the morphology and topography investigation, we performed chemical analysis using energy-dispersive X-ray spectroscopy. In addition, we have some preliminary chemical analysis from our collaborators (CEMES, Toulouse and Spintec, Grenoble) by electron energy loss spectroscopy. The key magnetic investigation was conducted with a combination of various magnetic microscopies: electron holography, magnetic force microscopy, and mainly X-ray magnetic circular dichroism microscopies (XMCD-PEEM and STXM). These were complemented with magnetometry on arrays and single structures. Our findings are supported by micromagnetic simulations and numerical modelling of XMCD-PEEM images.

Electroless-deposited CoNiB and NiFeB tubes

In electroless-deposited CoNiB tubes (diameter around 300 nm), the XMCD-PEEM imaging and comparison with the numerical modelling revealed series of well-defined domains with azimuthal magnetization separated by Bloch-type walls (radial magnetization in the core). These flux-closure domains generate weak and very short-ranged stray fields, while being separated by narrow domain walls, significantly narrower than the tube diameter. The domain wall density is as high as 5/µm. Assuming just the geometry, these long (up to 30 µm) tubes should be axially magnetized. Thus, an additional contribution of magnetic anisotropy has to be present in order to favour alignment of magnetization along the azimuthal direction (i.e. easy axis for the azimuthal and hard axis for the longitudinal direction). The azimuthal anisotropy may originate from the growth-induced strain and/or grain shape. We cannot also rule out the effect of rapid template dissolution.

When magnetic field is applied along the tube axis, the magnetization gradually rotates towards the axial direction. Thanks to STXM imaging under such field we could extract the strength of the anisotropy corresponding to an effective anisotropy constant of approximately $10\,\mathrm{kJ/m^3}$. The anisotropy strength could be tailored

through annealing or material composition. I.e. after annealing at around 450°C, the magnetization is axial and can be switched with several mT applied along the tube axis.

$(Ni_{80}Fe_{20})B$ tubes of similar geometry prepared in the same way are axially-magnetized even in the as-deposited state. Unlike CoNiB (significant negative magnetostriction), NiFeB exhibits almost zero (tiny positive) magnetostriction. On this basis we put forward the magnetoelastic origin of azimuthal domains in the CoNiB tubes. We observed a switching of the magnetization in NiFeB tubes with magnetic field and the displacement of a domain boundary. In electron holography experiments complex phase maps were observed which we attribute to the large tube diameter (sometimes almost 400 nm) and field having significant transverse component with respect to the tube axis.

Another way how to obtain axial magnetization is to reduce the diameter. CoNiB nanotubes with diameter around 100 nm display longitudinal magnetization, both in XMCD-PEEM and magnetic force microscopy imaging. Even though there might be some anisotropy present, the exchange energy for azimuthal magnetization would be too high. Thus, axial magnetization is preferred.

Some nanotubes, mainly electroplated ones (NiCo, Ni) with thin shells (< 15 nm) could not be investigated properly by magnetic microscopies due to a very low signal resulting from the (partial) oxidation of the material. Such thin nanotubes should be sandwiched in between protective layers, e.g. few nanometres of silica/hafnia deposited by atomic layer deposition, or titania prepared by chemical bath deposition.

Aside from focusing on nanotubes we also probed more complex geometries: nanoelements with wire and tube segments and multilayered tubes (core-shell structures).

Twires

Nanoelements with alternating nanowire and nanotube parts (outer diameter around 60 nm) had very sharp wire/tube transitions (mostly gradual transition is reported in the literature) with multiple tube segments with lengths even above 2 µm (longer than found in the literature). Unfortunately, the structure proved to be quite challenging for the first magnetic microscopy imaging. Small diameter with low Ni magnetic moment gave weak magnetic signal for nanowire parts, not speaking of the tubular segments. In more sensitive XMCD-PEEM we had problems with localizing suitable structures as well as with the limited spatial resolution and image analysis due to a high curvature. Yet, with slightly larger structures (thicker) containing Fe or Co (higher magnetic moment), one may test experimentally numerical

and theoretical predictions regarding these intriguing structures combining wire and tube segments.

Multilayered tubes (core-shell structures)

For potential (spintronic) devices (e.g. sensors), one would need to use multilayered tubes (core-shell structures), not just simple tubes. Along this line, in collaboration with TU Darmstadt we prepared multilayered tubes with two different magnetic layers separated by a non-magnetic spacer (NiFeB/SnO_x/CoNiB). Thanks to the element specificity of XMCD-PEEM we could probe separately each magnetic layer. These were found to be exchange-decoupled. Anisotropy of each individual shell prevailed. Therefore, CoNiB had azimuthal domains, whereas NiFeB axial magnetization. Further, we probed switching of the tubes by magnetic field. With static magnetic field we saw reversal of NiFeB through the nucleation and propagation of a domain boundary. There were also some changes in CoNiB, but these could not be clearly correlated with NiFeB state except for the effect of stray field emanating from a domain wall in the NiFeB layer. More interesting were experiments with field pulses when the field was applied with some angle versus the common tube axis. To our surprise, not only NiFeB switched, but also circulation of all domains in CoNiB was reversed.

Aside from experiments we also run micromagnetic simulations of multilayered tubes with a thicker spacer (e.g. 10 nm). Here we could demonstrate antiparallel ordering of axially-magnetized domains in both magnetic layers through dipolar interaction as well as obtain some intriguing coupled vortex-like walls in both tubes.

Despite providing only preliminary results in some cases, we believe that we have shown versatility of magnetic nanotubes. Through changing the composition, geometry or annealing one can obtain domains almost á la carte: azimuthal or axial ones with both being useful. Especially azimuthal domains are interesting owing to the magnetic flux-closure that could be exploited in magnetic sensors or in devices based on dense arrays of elements. Both hollow nature and azimuthal domains would significantly decreases interaction between these elements and unwanted cross-talk. Properties and viability of tubes can be further enhanced by preparing core-shell structures / tubular multilayers.

Perspective

Nanotubes with azimuthal domains

CoNiB tubes with azimuthal domains and many domain walls may open the way for the experimental study of domain wall motion in nanotubes as well as novel phenomena predicted in curved geometries. Our CoNiB tubes with azimuthal domains could be a good system for experimental test of recent theoretical predictions of the non-reciprocity of spin-wave propagation in magnetic nanotubes [35, 36]. In both cases (DWs & spin waves), the intermediate challenge would be to control the size and number of azimuthal domains as the simpler system would be easier for fundamental investigations. Later one could think of designing new magnonics wave-guides utilizing core-shell structures with inner core having segments from different (ferromagnetic) materials forming a magnonic crystal. One can also consider the CoNiB tubes with flux-closure domains and very narrow domain walls as a building block of the racetrack memory as array of such structures would have smaller cross-talk and it would be easier to fabricate than vertical strips. As for the miniaturization of the tubes, one could prepare azimuthal domains in even smaller nanotubes by tuning the geometry and material. However, we do not expect that one can go significantly below 100 nm-diameter for high aspect ratio nanotubes, while keeping the azimuthal magnetization.

Multilayered tubes

We have demonstrated possibility of fabrication of multilayered tubes with a thick non-magnetic spacer. The further development could focus on effects already known from flat multilayers, but not implemented so far in the curved tubular geometry. I.e. on the Spin Hall effect and the Dzyaloshinskii-Moriya interaction in magnetic nanotubes with e.g. Pt core (bilayer). As already outlined in the introduction, one can also combine effective DMI interaction arising from the curvature with the one coming from interfaces with heavy metals/oxides. Further, one can realize tubular version of synthetic antiferromagnets and trilayers for giant or tunnel magnetoresistance elements that are important for various sensors. These would require continuous spacer (such as our SnO_x), however, with smaller thickness (few nm instead of 10-20 nm). Such thin spacer layer could be prepared by atomic layer deposition, which can provide both insulators and metals. Longer term challenge could be again the miniaturization (decrease of diameter) of the tubular structures. For sure one could prepare several of the above-mentioned structure by deposition of layers on (vertical) pillars, but here we have in mind rather preparation of large vertical arrays of such structures in ordered porous templates.

Tubular magnetic racetrack memory

Now we briefly return to the idea of the domain wall memory proposed by IBM [2]. The proposal gradually evolved from simple permalloy tracks towards more complex heterostructures (multilayers) and shifting of DWs by electric current instead of magnetic field.

Until the racetrack memory 4.0 based on synthetic antiferromagnetic (SAF) strips [5], the issues of dipolar interaction among the magnetic tracks was not properly addressed. This is partially caused by the fact that most experiments were performed utilizing 2D tracks on flat substrates, where dipolar fields are short-ranged especially for ultrathin films with perpendicular magnetization. This is no longer the case for the 3D concept, where longer-ranged dipolar fields arise. Even though the concept of SAF has been demonstrated on a flat substrate, the idea about making such tracks vertical to have a proper 3D device is rather vague. It was admitted that fabrication of vertical tracks is "outstanding challenge" [5]. The possible solution put forward by Parkin is atomic layer deposition of vertical strips. However, fabrication of such 3D multilayered strips utilizing ALD or other techniques does not seem to be viable. In addition there are still some question-marks regarding the material properties (especially magnetic ones) of the ALD layers that tend to be very granular.

Here we propose racetrack memory based on magnetic nanotubes. First, even simple tubes with axially-magnetized domains (i.e. analogy of Parkin's racetrack 1.0) could be of interest for racetrack or other devices as it has been shown that interaction among tubes in arrays is significantly smaller than for solid wires (with the same diameter and spacing) [215]. In our work we experimentally show that the CoNiB tubes can sustain many azimuthal domains even for long tubes. These flux-closure domains significantly reduce the dipolar interactions among closely spaced tracks as DWs bear no net magnetic charge. In addition, the DWs separating such domains in our tubes are very narrow, significantly smaller than the tube diameter itself (see Fig. 8.6). Further, as regards the fabrication, vertical arrays of tubes have been already synthesized in (ordered) porous templates by chemical methods by many groups, while array of vertical strips remains on a paper.

Therefore, for the tubular racetracks one can either utilize tubes with single magnetic layer having azimuthal magnetization, or one can even return to the Parkin's idea of SAF layers, however, in the form of multilayered tubes, not flat strips. Unlike vertical strips, one can fabricate SAF in tubular geometry by combining electrochemistry (e.g. electroless plating as shown in our work) for the magnetic layers and atomic layer deposition for the non-magnetic Ru spacer, or maybe the whole structure can be realized by ALD using direct deposition of metals [133]. In case of

tubular SAF, we are no longer considering azimuthal domains, but rather axial or radial ones (magnetization perpendicular to the tube surface). Therefore, one could possibly realize vertical SAF this way and even in the tubular geometry, opening ways to study new and enhanced phenomena predicted for curved geometries.

In our work we investigated similar multilayered system: we obtained two magnetic layers separated by a non-magnetic spacer (chapter 11). Therefore, the synthesis of vertical array of multilayered tubes is feasible. In the future, the tubular SAF could be realized by making thinner spacers and possibly employing different materials.

We have been concerned with magnetic nanotubes, cylindrical structures with a hollow core. The curvature and the core give them interesting properties that could be possibly exploited in 3D spintronics, be it solid state memory, advanced sensors or magnonics crystals for spin waveguides, all based on (arrays of vertical) multilayered tubes or core-shell nanowires.

BIBLIOGRAPHY

[1] Parkin, S. Shiftable magnetic shift register and method of using the same (2004). URL http://www.google.com/patents/US6834005. US Patent 6,834,005.

[2] Parkin, S. S., Hayashi, M. & Thomas, L. Magnetic domain-wall racetrack memory. *Science* **320**, 190–194 (2008).

[3] Suto, H. *et al.* Three-dimensional magnetic recording using ferromagnetic resonance. *Jpn. J. Appl. Phys.* **55**, 07MA01 (2016). URL http://stacks.iop.org/1347-4065/55/i=7S3/a=07MA01.

[4] Okamoto, S., Kikuchi, N., Furuta, M., Kitakami, O. & Shimatsu, T. Microwave assisted magnetic recording technologies and related physics. *J. Phys. D: Appl. Phys.* **48**, 353001 (2015). URL http://stacks.iop.org/0022-3727/48/i=35/a=353001.

[5] Parkin, S. & Yang, S.-H. Memory on the racetrack. *Nat. Nanotechnol.* **10**, 195–198 (2015).

[6] Vázquez, M. (ed.) *Magnetic nano-and microwires: design, synthesis, properties and applications*, vol. 80 of *Woodhead Publishing Series in Electronic and Optical Materials* (Woodhead Publishing, 2015).

[7] Streubel, R. *et al.* Magnetism in curved geometries. *J. Phys. D: Appl. Phys.* **49**, 363001 (2016). URL http://stacks.iop.org/0022-3727/49/i=36/a=363001.

[8] Fernández-Pacheco, A. *et al.* Three-dimensional nanomagnetism. *Nat. Commun.* **8**, 15756 (2017).

[9] Baraduc, C., Chshiev, M. & Dieny, B. Spintronic phenomena: Giant magnetoresistance, tunnel magnetoresistance and spin transfer torque. In *Giant Magnetoresistance (GMR) Sensors*, 1–30 (Springer, 2013). URL https://doi.org/10.1007/978-3-642-37172-1_1.

[10] Thomas, L. & Parkin, S. *Current induced domain-wall motion in magnetic nanowires*, vol. 2 - Micromagnetism of *Handbook of Magnetism and Advanced Magnetic Materials*, chap. Magnetic configurations in small elements, magnetization processes and hysteretic properties (John Wiley & Sons, Ltd, 2007). URL http://dx.doi.org/10.1002/9780470022184.hmm210.

[11] Wegrowe, J.-E., Kelly, D., Franck, A., Gilbert, S. E. & Ansermet, J.-P. Magnetoresistance of ferromagnetic nanowires. *Phys. Rev. Lett.* **82**, 3681–3684 (1999). URL http://link.aps.org/doi/10.1103/PhysRevLett.82.3681.

[12] Wernsdorfer, W. *et al.* Nucleation of magnetization reversal in individual nanosized nickel wires. *Phys. Rev. Lett.* **77**, 1873 (1996).

[13] Bran, C. *et al.* Spin configuration of cylindrical bamboo-like magnetic nanowires. *J. Mater. Chem. C* **4**, 978–984 (2016). URL http://dx.doi.org/10.1039/C5TC04194E.

[14] Biziere, N. *et al.* Imaging the fine structure of a magnetic domain wall in a Ni nanocylinder. *Nano Lett.* **13**, 2053–2057 (2013).

[15] Da Col, S. *et al.* Observation of Bloch-point domain walls in cylindrical magnetic nanowires. *Phys. Rev. B* **89**, 180405 (2014).

[16] Thiaville, A. & Nakatani, Y. *Domain-Wall Dynamics in Nanowires and Nanostrips*, 161–205 (Springer Berlin Heidelberg, Berlin, Heidelberg, 2006). URL http://dx.doi.org/10.1007/10938171_5.

[17] Yan, M., Kákay, A., Gliga, S. & Hertel, R. Beating the Walker limit with massless domain walls in cylindrical nanowires. *Phys. Rev. Lett.* **104**, 057201 (2010).

[18] Son, S. J., Reichel, J., He, B., Schuchman, M. & Lee, S. B. Magnetic nanotubes for magnetic-field-assisted bioseparation, biointeraction, and drug delivery. *J. Am. Chem. Soc.* **127**, 7316–7317 (2005).

[19] Li, X.-Z., Wu, K.-L., Ye, Y. & Wei, X.-W. Controllable synthesis of Ni nanotube arrays and their structure-dependent catalytic activity toward dye degradation. *CrystEngComm* **16**, 4406–4413 (2014).

[20] Usov, N., Zhukov, A. & Gonzalez, J. Domain walls and magnetization reversal process in soft magnetic nanowires and nanotubes. *J. Magn. Magn. Mater.* **316**, 255–261 (2007).

[21] Sun, C. & Pokrovsky, V. L. Magnetic properties of a long, thin-walled ferromagnetic nanotube. *J. Magn. Magn. Mater.* **355**, 121 – 130 (2014). URL http://www.sciencedirect.com/science/article/pii/S0304885313009049.

[22] Yan, M., Andreas, C., Kákay, A., García-Sánchez, F. & Hertel, R. Fast domain wall dynamics in magnetic nanotubes: Suppression of Walker breakdown and Cherenkov-like spin wave emission. *Appl. Phys. Lett.* **99**, 122505 (2011).

[23] Kimling, J. *et al.* Photoemission electron microscopy of three-dimensional magnetization configurations in core-shell nanostructures. *Phys. Rev. B* **84**, 174406 (2011). URL http://link.aps.org/doi/10.1103/PhysRevB.84.174406.

[24] Pitzschel, K. *et al.* Magnetic reversal of cylindrical nickel nanowires with modulated diameters. *J. Appl. Phys.* **109**, 033907 (2011). URL https://doi.org/10.1063/1.3544036.

[25] Sekhar, M. C. *et al.* Helical domain walls in constricted cylindrical nife nanowires. *Appl. Phys. Lett.* **101**, 152406 (2012). URL https://doi.org/10.1063/1.4758469.

[26] Ivanov, Y. P., Chuvilin, A., Lopatin, S. & Kosel, J. Modulated magnetic nanowires for controlling domain wall motion: Toward 3D magnetic memories. *ACS Nano* **10**, 5326–5332 (2016).

[27] Davis, D. M. *et al.* Magnetoresistance in electrodeposited CoNiFe/Cu multilayered nanotubes. *Electrochem. Solid-State Lett.* **9**, C153–C155 (2006). URL http://esl.ecsdl.org/content/9/9/C153.abstract. http://esl.ecsdl.org/content/9/9/C153.full.pdf+html.

[28] Pitzschel, K. *et al.* Controlled introduction of diameter modulations in arrayed magnetic iron oxide nanotubes. *ACS Nano* **3**, 3463–3468 (2009).

[29] Philippe, L. & Michler, J. A kinetic model enabling controlled electrosynthesis of stacked metallic nanotubes and nanowires. *Small* **4**, 904–907 (2008).

[30] Neumann, R. F. *et al.* Tailoring the nucleation of domain walls along multi-segmented cylindrical nanoelements. *Nanotechnology* **26**, 215701 (2015). URL http://stacks.iop.org/0957-4484/26/i=21/a=215701.

[31] Rohan, J. F. *et al.* Coaxial metal and magnetic alloy nanotubes in polycarbonate templates by electroless deposition. *Electrochem. Commun.* **10**, 1419 – 1422 (2008). URL http://www.sciencedirect.com/science/article/pii/S1388248108003020.

[32] Emori, S., Bauer, U., Ahn, S.-M., Martinez, E. & Beach, G. S. Current-driven dynamics of chiral ferromagnetic domain walls. *Nat. Mater.* **12**, 611–616 (2013).

[33] Belmeguenai, M. *et al.* Interfacial Dzyaloshinskii-Moriya interaction in perpendicularly magnetized Pt/Co/AlO_x ultrathin films measured by brillouin

light spectroscopy. *Phys. Rev. B* **91**, 180405 (2015). URL https://link.aps.org/doi/10.1103/PhysRevB.91.180405.

[34] Hertel, R. Curvature-induced magnetochirality. *SPIN* **03**, 1340009 (2013). URL http://dx.doi.org/10.1142/S2010324713400092.

[35] Otálora, J. A., Yan, M., Schultheiss, H., Hertel, R. & Kákay, A. Curvature-induced asymmetric spin-wave dispersion. *Phys. Rev. Lett.* **117**, 227203 (2016). URL http://link.aps.org/doi/10.1103/PhysRevLett.117.227203.

[36] Otálora, J. A., Yan, M., Schultheiss, H., Hertel, R. & Kákay, A. Asymmetric spin-wave dispersion in ferromagnetic nanotubes induced by surface curvature. *Phys. Rev. B* **95**, 184415 (2017). URL https://link.aps.org/doi/10.1103/PhysRevB.95.184415.

[37] Chan, K. T., Doran, C., Shipton, E. G. & Fullerton, E. E. Core-shell structured nanowire spin valves. *IEEE Trans. Magn.* **46**, 2209–2211 (2010).

[38] Dyakonov, M. I. Spin hall effect. *arXiv:1210.3200* (2012).

[39] Hirsch, J. E. Spin hall effect. *Phys. Rev. Lett.* **83**, 1834–1837 (1999).

[40] Hu, C. D. The Dzyaloshinskii-Moriya interaction in metals. *J. Phys. Condens. Matter* **24**, 086001 (2012). URL http://stacks.iop.org/0953-8984/24/i=8/a=086001.

[41] Kronmüller, H. & Parkin, S. (eds.) *Fundamentals and Theory*, vol. 1 of *Handbook of Magnetism and Advanced Magnetic Materials* (Wiley, 2007).

[42] Blundell, S. *Magnetism in condensed matter*. Oxford master series in condensed matter physics (Oxford, 2001).

[43] Coey, J. M. D. *Magnetism and magnetic materials* (Cambridge University Press, 2010).

[44] MacDonald, A. & Tsoi, M. Antiferromagnetic metal spintronics. *Phil. Trans. R. Soc. A* **369**, 3098–3114 (2011).

[45] Jungwirth, T., Marti, X., Wadley, P. & Wunderlich, J. Antiferromagnetic spintronics. *Nat. Nanotechnol.* **11**, 231–241 (2016).

[46] Stanciu, C. D. *et al.* Ultrafast spin dynamics across compensation points in ferrimagnetic GdFeCo: The role of angular momentum compensation. *Phys. Rev.*

B **73**, 220402 (2006). URL https://link.aps.org/doi/10.1103/PhysRevB.73.220402.

[47] Kim, K.-J. *et al.* Fast domain wall motion induced by antiferromagnetic spin dynamics at the angular momentum compensation temperature of ferrimagnets. *arXiv:1703.07515* (2017).

[48] Oh, S.-H. *et al.* Coherent terahertz spin-wave emission associated with ferrimagnetic domain wall dynamics. *arXiv:1706.00549* (2017).

[49] Faure-Vincent, J. *et al.* Interlayer magnetic coupling interactions of two ferromagnetic layers by spin polarized tunneling. *Phys. Rev. Lett.* **89**, 107206 (2002).

[50] Bruno, P. Theory of interlayer exchange interactions in magnetic multilayers. *J. Phys. Condens. Matter* **11**, 9403 (1999). URL http://stacks.iop.org/0953-8984/11/i=48/a=305.

[51] Yang, S.-H., Ryu, K.-S. & Parkin, S. Domain-wall velocities of up to 750 $\mathrm{m\,s^{-1}}$ driven by exchange-coupling torque in synthetic antiferromagnets. *Nat. Nanotechnol.* **10**, 221–226 (2015).

[52] Yang, S.-H. & Parkin, S. Novel domain wall dynamics in synthetic antiferromagnets. *J. Phys. Condens. Matter* **29**, 303001 (2017). URL http://stacks.iop.org/0953-8984/29/i=30/a=303001.

[53] Lepadatu, S. *et al.* Synthetic ferrimagnet nanowires with very low critical current density for coupled domain wall motion. *Sci. Rep.* **7**, 1640 (2017).

[54] Hubert, A. & Schäfer, R. *Magnetic domains: The Analysis of Magnetic Microstructures* (Springer, 2009), 3rd edn.

[55] Guimarães, A. P. *Principles of Nanomagnetism*. NanoScience and Technology (Springer, 2009).

[56] Fruchart, O. Lecture notes on nanomagnetism. PDF (2016). Available from http://fruchart.eu/olivier/lectures/nanomagnetism-2016-11-04.pdf, [Accessed 2017-04-30].

[57] Sandratskii, L. M. Insight into the Dzyaloshinskii-Moriya interaction through first-principles study of chiral magnetic structures. *Phys. Rev. B* **96**, 024450 (2017). URL https://link.aps.org/doi/10.1103/PhysRevB.96.024450.

[58] Bogdanov, A. & Hubert, A. Thermodynamically stable magnetic vortex states in magnetic crystals. *J. Magn. Magn. Mater.* **138**, 255 – 269 (1994). URL http://www.sciencedirect.com/science/article/pii/0304885394900469.

[59] Rohart, S. & Thiaville, A. Skyrmion confinement in ultrathin film nanostructures in the presence of Dzyaloshinskii-Moriya interaction. *Phys. Rev. B* **88**, 184422 (2013). URL https://link.aps.org/doi/10.1103/PhysRevB.88.184422.

[60] Goussev, A., Robbins, J., Slastikov, V. & Tretiakov, O. A. Dzyaloshinskii-Moriya domain walls in magnetic nanotubes. *Phys. Rev. B* **93**, 054418 (2016).

[61] Stöhr, J. & Siegmann, H. C. (eds.) *Magnetism: From Fundamentals to Nanoscale Dynamics*, vol. 152 of *Solid-State Sciences* (Springer, 2006).

[62] Ralph, D. C. & Stiles, M. D. Spin transfer torques. *J. Magn. Magn. Mater.* **320**, 1190–1216 (2008).

[63] Garello, K. *et al.* Symmetry and magnitude of spin-orbit torques in ferromagnetic heterostructures. *Nat. Nanotechnol.* **8**, 587–593 (2013).

[64] Safeer, C. *et al.* Spin–orbit torque magnetization switching controlled by geometry. *Nat. Nanotechnol.* **11**, 143–146 (2016).

[65] Abert, C., Bruckner, F., Vogler, C. & Suess, D. Efficient micromagnetic modelling of spin-transfer torque and spin-orbit torque. *AIP Adv.* **8**, 056008 (2018). URL https://doi.org/10.1063/1.5006561.

[66] Xu, F. *et al.* Enhanced film thickness for Néel wall in soft magnetic film by introducing strong magnetocrystalline anisotropy. *Sci. Rep.* **6** (2016).

[67] Forster, H. *et al.* Micromagnetic simulation of domain wall motion in magnetic nano-wires. *J. Magn. Magn. Mater.* **249**, 181–186 (2002). URL http://www.sciencedirect.com/science/article/pii/S0304885302005280. International Workshop on Magnetic Wires.

[68] Hertel, R. Computational micromagnetism of magnetization processes in nickel nanowires. *J. Magn. Magn. Mater.* **249**, 251–256 (2002).

[69] Han, D.-S. *et al.* Magnetic domain-wall motion by propagating spin waves. *Appl. Phys. Lett.* **94**, 112502 (2009). URL http://dx.doi.org/10.1063/1.3098409.

[70] Wang, W. *et al.* Magnon-driven domain-wall motion with the Dzyaloshinskii-Moriya interaction. *Phys. Rev. Lett.* **114**, 087203 (2015). URL https://link.aps.org/doi/10.1103/PhysRevLett.114.087203.

[71] Moretti, S., Raposo, V., Martinez, E. & Lopez-Diaz, L. Domain wall motion by localized temperature gradients. *Phys. Rev. B* **95**, 064419 (2017). URL https://link.aps.org/doi/10.1103/PhysRevB.95.064419.

[72] Bryan, M. T., Dean, J. & Allwood, D. A. Dynamics of stress-induced domain wall motion. *Phys. Rev. B* **85**, 144411 (2012). URL https://link.aps.org/doi/10.1103/PhysRevB.85.144411.

[73] Dean, J. *et al.* A sound idea: Manipulating domain walls in magnetic nanowires using surface acoustic waves. *Appl. Phys. Lett.* **107**, 142405 (2015). URL http://dx.doi.org/10.1063/1.4932057.

[74] Schryer, N. L. & Walker, L. R. The motion of 180° domain walls in uniform dc magnetic fields. *J. Appl. Phys.* **45**, 5406–5421 (1974).

[75] Hagelberg, F. *Magnetism in Carbon Nanostructures* (Cambridge University Press, 2017).

[76] Escrig, J., Landeros, P., Altbir, D., Vogel, E. & Vargas, P. Phase diagrams of magnetic nanotubes. *J. Magn. Magn. Mater.* **308**, 233–237 (2007).

[77] Landeros, P., Suarez, O. J., Cuchillo, A. & Vargas, P. Equilibrium states and vortex domain wall nucleation in ferromagnetic nanotubes. *Phys. Rev. B* **79**, 024404 (2009). URL http://link.aps.org/doi/10.1103/PhysRevB.79.024404.

[78] Chen, A., Usov, N., Blanco, J. & Gonzalez, J. Equilibrium magnetization states in magnetic nanotubes and their evolution in external magnetic field. *J. Magn. Magn. Mater.* **316**, e317 – e319 (2007). URL http://www.sciencedirect.com/science/article/pii/S0304885307002466. Proceedings of the Joint European Magnetic Symposia.

[79] Wyss, M. *et al.* Imaging magnetic vortex configurations in ferromagnetic nanotubes. *Phys. Rev. B* **96**, 024423 (2017). URL https://link.aps.org/doi/10.1103/PhysRevB.96.024423.

[80] Li, D., Thompson, R. S., Bergmann, G. & Lu, J. G. Template-based synthesis and magnetic properties of cobalt nanotube arrays. *Adv. Mater.* **20**, 4575–4578 (2008).

[81] Landeros, P. *et al.* Reversal modes in magnetic nanotubes. *Appl. Phys. Lett.* **90**, 102501 (2007). URL `http://scitation.aip.org/content/aip/journal/apl/90/10/10.1063/1.2437655`.

[82] Bachmann, J. *et al.* Size effects in ordered arrays of magnetic nanotubes: Pick your reversal mode. *J. Appl. Phys.* **105**, 07B521 (2009). URL `http://dx.doi.org/10.1063/1.3074109`.

[83] Allende, S., Escrig, J., Altbir, D., Salcedo, E. & Bahiana, M. Angular dependence of the transverse and vortex modes in magnetic nanotubes. *Eur. Phys. J. B* **66**, 37–40 (2008).

[84] Albrecht, O. *et al.* Experimental evidence for an angular dependent transition of magnetization reversal modes in magnetic nanotubes. *J. Appl. Phys.* **109**, 093910 (2011).

[85] Allende, S. & Arias, R. Transverse domain wall propagation in modulated cylindrical nanostructures and possible geometric control. *Phys. Rev. B* **83**, 174452 (2011).

[86] Otálora, J., Lopez-Lopez, J., Vargas, P. & Landeros, P. Chirality switching and propagation control of a vortex domain wall in ferromagnetic nanotubes. *Appl. Phys. Lett.* **100**, 072407 (2012).

[87] Yan, M., Andreas, C., Kákay, A., García-Sánchez, F. & Hertel, R. Chiral symmetry breaking and pair-creation mediated walker breakdown in magnetic nanotubes. *Appl. Phys. Lett.* **100**, 252401 (2012).

[88] Yang, J. *et al.* Characteristic dynamic modes and domain-wall motion in magnetic nanotubes excited by resonant rotating magnetic fields. *Phys. Rev. B* **94**, 024425 (2016).

[89] Otálora, J., López-López, J., Núñez, A. & Landeros, P. Domain wall manipulation in magnetic nanotubes induced by electric current pulses. *J. Phys.: Condens. Matter* **24**, 436007 (2012).

[90] Yang, J., Yoo, M.-W. & Kim, S.-K. Spin-wave-driven high-speed domain-wall motions in soft magnetic nanotubes. *J. Appl. Phys.* **118**, 163902 (2015).

[91] López-López, J., Cortés-Ortuño, D. & Landeros, P. Role of anisotropy on the domain wall properties of ferromagnetic nanotubes. *J. Magn. Magn. Mater.* **324**, 2024–2029 (2012).

[92] Lee, D., Cohen, R. E. & Rubner, M. F. Heterostructured magnetic nanotubes. *Langmuir* **23**, 123–129 (2007).

[93] Betancourt, I., Hrkac, G. & Schrefl, T. Micromagnetic simulation of domain wall dynamics in permalloy nanotubes at high frequencies. *J. Appl. Phys.* **104**, 023915 (2008).

[94] Streubel, R. *et al.* Magnetic microstructure of rolled-up single-layer ferromagnetic nanomembranes. *Adv. Mater.* **26**, 316–323 (2014). URL `http://dx.doi.org/10.1002/adma.201303003`.

[95] Chen, A., Gonzalez, J. & Guslienko, K. Domain walls confined in magnetic nanotubes with uniaxial anisotropy. *J. Magn. Magn. Mater.* **324**, 3912 – 3917 (2012). URL `http://www.sciencedirect.com/science/article/pii/S0304885312005410`.

[96] Daub, M., Knez, M., Goesele, U. & Nielsch, K. Ferromagnetic nanotubes by atomic layer deposition in anodic alumina membranes. *J. Appl. Phys.* **101**, 09J111 (2007).

[97] Proenca, M. *et al.* Magnetic interactions and reversal mechanisms in Co nanowire and nanotube arrays. *J. Appl. Phys.* **113**, 093907 (2013).

[98] Vansteenkiste, A. *et al.* The design and verification of MuMax3. *AIP Adv.* **4**, 107133 (2014).

[99] Richardson, D. & Rhen, F. M. F. Increasing the magnetization of electrolessly deposited Ni–B nanotubes. *IEEE Trans. Magn.* **51**, 1–4 (2015).

[100] Pathak, S., Hong, J., Chaudhary, J. & Sharma, M. Magneto-optical Kerr effect characterization of electrodeposited Y-junction magnetic nanostructures. *J. Appl. Phys.* **117**, 17A751 (2015). URL `http://dx.doi.org/10.1063/1.4918952`.

[101] Tabasum, M. R. *et al.* Magnetic force microscopy investigation of arrays of nickel nanowires and nanotubes. *Nanotechnology* **25**, 245707 (2014). URL `http://stacks.iop.org/0957-4484/25/i=24/a=245707`.

[102] Wang, T., Wang, Y., Li, F., Xu, C. & Zhou, D. Morphology and magnetic behaviour of an Fe_3O_4 nanotube array. *J. Phys.: Condens. Matter* **18**, 10545–10551 (2006).

[103] Li, F. S. *et al.* Fabrication and magnetic properties of FeCo alloy nanotube array. *J. Appl. Phys.* **101**, 014309 (2007). URL http://dx.doi.org/10.1063/1.2405729.

[104] Kozlovskiy, A. *et al.* Study of Ni/Fe nanotube properties. *Nucl. Instrum. Methods Phys. Res., Sect. B* **365**, 663 – 667 (2015). URL http://www.sciencedirect.com/science/article/pii/S0168583X15009635. Swift Heavy Ions in Matter, 18-21 May, 2015, Darmstadt, Germany.

[105] Wang, Z. K. *et al.* Spin waves in nickel nanorings of large aspect ratio. *Phys. Rev. Lett.* **94**, 137208 (2005). URL https://link.aps.org/doi/10.1103/PhysRevLett.94.137208.

[106] Nguyen, T. & Cottam, M. Spin-wave excitations in ferromagnetic nanotubes. *Surf. Sci.* **600**, 4151 – 4154 (2006). URL http://www.sciencedirect.com/science/article/pii/S0039602806004870.

[107] González, A., Landeros, P. & Núñez, Á. S. Spin wave spectrum of magnetic nanotubes. *J. Magn. Magn. Mater.* **322**, 530 – 535 (2010). URL http://www.sciencedirect.com/science/article/pii/S0304885309010117.

[108] Buchter, A. *et al.* Reversal mechanism of an individual Ni nanotube simultaneously studied by torque and SQUID magnetometry. *Phys. Rev. Lett.* **111**, 067202 (2013). URL https://link.aps.org/doi/10.1103/PhysRevLett.111.067202.

[109] Diehle, P., Caron, J., Kovács, A., Ungermann, J. & Dunin-Borkowski, R. E. Towards electron holographic tomography of three-dimensional magnetization distributions in ferromagnetic nanotubes (2015). URL http://www.rafaldb.com/posters/pics2015/04g.pdf. Presented at the 3rd International Conference on Frontiers of Aberration Corrected Electron Microscopy "PICO 2015", Kasteel Valsbroek, The Netherlands. Available from http://www.rafaldb.com/posters/pics2015/04g.pdf [accessed 2017-04-04].

[110] Ruffer, D. *et al.* Magnetic states of an individual Ni nanotube probed by anisotropic magnetoresistance. *Nanoscale* **4**, 4989–4995 (2012). URL http://dx.doi.org/10.1039/C2NR31086D.

[111] Baumgaertl, K. *et al.* Magnetization reversal in individual Py and CoFeB nanotubes locally probed via anisotropic magnetoresistance and anomalous Nernst effect. *Appl. Phys. Lett.* **108** (2016). URL http://scitation.aip.org/content/aip/journal/apl/108/13/10.1063/1.4945331.

[112] Jia, C.-J. *et al.* Single-crystalline iron oxide nanotubes. *Angew. Chem. Int. Ed.* **44**, 4328–4333 (2005). URL http://dx.doi.org/10.1002/anie.200463038.

[113] Mertig, M., Kirsch, R. & Pompe, W. Biomolecular approach to nanotube fabrication. *Appl. Phys. A* **66**, S723–S727 (1998).

[114] Khan, A. A. *Tobacco Mosaic Virus (TMV) as a Nanoscaffold for Inorganic Assemblies*. Ph.D. thesis, University of Basque Country (2012).

[115] Apel, P. Y. & Dmitriev, S. Micro-and nanoporous materials produced using accelerated heavy ion beams. *Adv. Nat. Sci.: Nanosci. Nanotechnol.* **2**, 013002 (2011).

[116] Masuda, H. *Highly Ordered Nanohole Arrays in Anodic Porous Alumina*, 37–55 (Springer, Boston, MA, 2005). URL http://dx.doi.org/10.1007/0-387-25193-6_3.

[117] Vogel, E. E., Vargas, P., Altbir, D. & Escrig, J. 14 - magnetic nanotubes. In Sattler, K. D. (ed.) *Handbook of nanophysics: nanotubes and nanowires*, 14–1–14–13 (CRC press, 2010).

[118] Ye, Y. & Geng, B. Magnetic nanotubes: Synthesis, properties, and applications. *Crit. Rev. Solid State Mater. Sci.* **37**, 75–93 (2012). URL http://dx.doi.org/10.1080/10408436.2011.613491.

[119] Proenca, M., Sousa, C., Ventura, J. & Araújo, J. 24 - Electrochemical synthesis and magnetism of magnetic nanotubes. In Vázquez, M. (ed.) *Magnetic Nano- and Microwires*, Woodhead Publishing Series in Electronic and Optical Materials, 727 – 781 (Woodhead Publishing, 2015). URL http://www.sciencedirect.com/science/article/pii/B9780081001646000242.

[120] Huang, Y.-C. *et al.* Fabrication and magnetic properties of 100-nm-scaled permalloy nanotube arrays. *J. Vac. Sci. Technol., B* **30**, 06FF07 (2012). URL http://dx.doi.org/10.1116/1.4762843.

[121] Wang, X. W., Yuan, Z. H. & Fang, B. C. Template-based synthesis and magnetic properties of Ni nanotube arrays with different diameters. *Mater. Chem. Phys.* **125**, 1–4 (2011).

[122] Atalay, F. *et al.* The effect of back electrode on the formation of electrodeposited CoNiFe magnetic nanotubes and nanowires. *Appl. Surf. Sci.* **256**, 2414 – 2418 (2010). URL http://www.sciencedirect.com/science/article/pii/S0169433209015220.

[123] Proenca, M., Sousa, C., Ventura, J., Vazquez, M. & Araujo, J. Distinguishing nanowire and nanotube formation by the deposition current transients. *Nanoscale Res. Lett.* **7**, 280 (2012). URL `http://www.nanoscalereslett.com/content/7/1/280`.

[124] Bao, J. *et al.* Template synthesis of an array of nickel nanotubules and its magnetic behavior. *Adv. Mater.* **13**, 1631–1633 (2001).

[125] Fukunaka, Y., Motoyama, M., Konishi, Y. & Ishii, R. Producing shape-controlled metal nanowires and nanotubes by an electrochemical method. *Electrochem. Solid State Lett.* **9**, C62–C64 (2006).

[126] Li, Y. L. *et al.* Fabrication and magnetic properties of free-standing Ni nanotube arrays with controllable wall thickness. *Appl. Phys. Lett.* **100**, 052402 (2012). URL `http://dx.doi.org/10.1063/1.3681136`.

[127] Schaefer, S. *et al.* NiCo nanotubes plated on Pd seeds as a designed magnetically recollectable catalyst with high noble metal utilisation. *RSC Adv.* **6**, 70033–70039 (2016).

[128] Richardson, D. & Rhen, F. M. Investigation of the electroless deposition process of magnetic nanostructures. *ECS Trans.* **64**, 39–48 (2015).

[129] Wang, W., Li, N., Li, X., Geng, W. & Qiu, S. Synthesis of metallic nanotube arrays in porous anodic aluminum oxide template through electroless deposition. *Mater. Res. Bull.* **41**, 1417–1423 (2006).

[130] Richardson, D. & Rhen, F. The diverse nanostructure of electroless plated CoNiFeB alloy: thin film, nanotubes and nanoparticles. *Phys. Procedia* **75**, 1158–1166 (2015).

[131] George, S. M. Atomic layer deposition: An overview. *Chem. Rev.* **110**, 111–131 (2010). URL `http://dx.doi.org/10.1021/cr900056b`.

[132] Miikkulainen, V., Leskelä, M., Ritala, M. & Puurunen, R. L. Crystallinity of inorganic films grown by atomic layer deposition: Overview and general trends. *J. Appl. Phys.* **113**, 2 (2013).

[133] Lim, B. S., Rahtu, A. & Gordon, R. G. Atomic layer deposition of transition metals. *Nat. Mater.* **2**, 749–754 (2003).

[134] Rüffer, D. *et al.* Anisotropic magnetoresistance of individual CoFeB and Ni nanotubes with values of up to 1.4% at room temperature. *APL Mater.* **2**, 076112 (2014).

[135] Pereira, A., Palma, J. L., Denardin, J. C. & Escrig, J. Temperature-dependent magnetic properties of Ni nanotubes synthesized by atomic layer deposition. *Nanotechnology* **27**, 345709 (2016).

[136] Xu, Y., Xue, D. S., Fu, J. L., Gao, D. Q. & Gao, B. Synthesis, characterization and magnetic properties of Fe nanotubes. *J. Phys. D: Appl. Phys.* **41**, 215010 (2008). URL `http://stacks.iop.org/0022-3727/41/i=21/a=215010`.

[137] Hua, Z. *et al.* Metal nanotubes prepared by a sol-gel method followed by a hydrogen reduction procedure. *Nanotechnology* **17**, 5106 (2006). URL `http://stacks.iop.org/0957-4484/17/i=20/a=011`.

[138] Mendach, S., Podbielski, J., Topp, J., Hansen, W. & Heitmann, D. Spin-wave confinement in rolled-up ferromagnetic tubes. *Appl. Phys. Lett.* **93**, 262501 (2008).

[139] Streubel, R. *et al.* Retrieving spin textures on curved magnetic thin films with full-field soft X-ray microscopies. *Nat. Commun.* **6** (2015).

[140] Fan, H. J., Gösele, U. & Zacharias, M. Formation of nanotubes and hollow nanoparticles based on Kirkendall and diffusion processes: A review. *Small* **3**, 1660–1671 (2007). URL `http://dx.doi.org/10.1002/smll.200700382`.

[141] Pablo-Navarro, J., Magén, C. & de Teresa, J. M. Three-dimensional core–shell ferromagnetic nanowires grown by focused electron beam induced deposition. *Nanotechnology* **27**, 285302 (2016).

[142] Chen, J. Y., Ahmad, N., Shi, D. W., Zhou, W. P. & Han, X. F. Synthesis and magnetic characterization of Co-NiO-Ni core-shell nanotube arrays. *J. Appl. Phys.* **110**, 073912 (2011). URL `http://dx.doi.org/10.1063/1.3646491`.

[143] Chen, Y. *et al.* Preparation and magnetic properties of Cu-Ni core-shell nanowires in ion-track templates. *J. Wuhan Univ. Technol.-Mat. Sci. Ed.* **30**, 665–669 (2015).

[144] Chong, Y. T. *et al.* Multilayered core/shell nanowires displaying two distinct magnetic switching events. *Adv. Mater.* **22**, 2435–2439 (2010).

[145] Rathmell, A. R., Nguyen, M., Chi, M. & Wiley, B. J. Synthesis of oxidation-resistant cupronickel nanowires for transparent conducting nanowire networks. *Nano Lett.* **12**, 3193–3199 (2012).

[146] Khan, U. *et al.* Magnetic response of hybrid ferromagnetic and antiferromagnetic core–shell nanostructures. *Nanoscale* **8**, 6064–6070 (2016).

[147] Javed, K. *et al.* Enhanced exchange bias and improved ferromagnetic properties in permalloy–$BiFe_{0.95}Co_{0.05}O_3$ core–shell nanostructures. *Sci. Rep.* **5** (2015).

[148] Irfan, M. *et al.* Controllable synthesis of ferromagnetic–antiferromagnetic core–shell NWs with tunable magnetic properties. *Nanoscale* (2017). URL `http://dx.doi.org/10.1039/C7NR01471F`.

[149] Wang, Q., Wang, G., Han, X., Wang, X. & Hou, J. G. Controllable template synthesis of Ni/Cu nanocable and Ni nanotube arrays: A one-step coelectrodeposition and electrochemical etching method. *J. Phys. Chem. B* **109**, 23326–23329 (2005). URL `http://dx.doi.org/10.1021/jp0530202`.

[150] Liu, Z. *et al.* Exploiting finite size effects in a novel core/shell microstructure. *J. Appl. Phys.* **103**, 064313 (2008). URL `http://scitation.aip.org/content/aip/journal/jap/103/6/10.1063/1.2844286`.

[151] Li, X. *et al.* Fabrication and magnetic properties of Ni/Cu shell/core nanocable arrays. *J. Phys. Chem. C* **114**, 6914–6916 (2010).

[152] Ozel, T., Bourret, G. R. & Mirkin, C. A. Coaxial lithography. *Nat. Nanotechnol.* **10**, 319–324 (2015).

[153] Jamet, S. *et al.* Quantitative analysis of shadow X-ray magnetic circular dichroism photoemission electron microscopy. *Phys. Rev. B* **92**, 144428 (2015). URL `http://link.aps.org/doi/10.1103/PhysRevB.92.144428`.

[154] Arshad, M. S. *et al.* Angular dependence of the coercivity in electrodeposited Co–Pt nanostructures with a tube–wire morphology. *IEEE Trans. Magn.* **50**, 1–4 (2014).

[155] Neumann, R. *et al.* Domain wall control in wire-tube nanoelements. *Appl. Phys. Lett.* **102**, 202407 (2013).

[156] Espejo, A. *et al.* Current-driven vortex domain wall motion in wire-tube nanostructures. *Appl. Phys. Lett.* **106**, 132405 (2015).

[157] Salazar-Aravena, D., Corona, R., Goerlitz, D., Nielsch, K. & Escrig, J. Magnetic properties of multisegmented cylindrical nanoparticles with alternating magnetic wire and tube segments. *J. Magn. Magn. Mater.* **346**, 171–174 (2013).

[158] Salazar-Aravena, D., Palma, J. L. & Escrig, J. Angular dependence of the magnetic properties of cylindrical nanostructures with wire–tube morphology. *Mater. Res. Express* **1**, 026112 (2014).

[159] Salazar-Aravena, D., Palma, J. & Escrig, J. Magnetostatic interactions between wire-tube nanostructures. *J. Appl. Phys.* **117**, 193905 (2015).

[160] Riveros, A., Salazar-Aravena, D. & Escrig, J. Theoretical investigation on the magnetostatic interaction between two wire-tube nanostructures. *J. Magn. Magn. Mater.* **428**, 452 – 456 (2017). URL `http://www.sciencedirect.com/science/article/pii/S0304885316319850`.

[161] Losic, D. & Santos, A. *Nanoporous Alumina* (Springer, 2015).

[162] Schlesinger, M. & Paunovic, M. (eds.) *Modern electroplating* (John Wiley & Sons, 2010), 5th edn.

[163] Bard, A. J. & Faulkner, L. R. *Electrochemical methods: Fundamentals and applications* (Wiley, 2001), 2nd edn.

[164] Tourillon, G., Pontonnier, L., Levy, J.-P. & Langlais, V. Electrochemically synthesized Co and Fe nanowires and nanotubes. *Electrochem. Solid-State Lett.* **3**, 20–23 (2000). URL `http://esl.ecsdl.org/content/3/1/20.abstract`.

[165] Zhang, X. *et al.* Comparative study in fabrication and magnetic properties of FeNi alloy nanowires and nanotubes. *J. Magn. Magn. Mater.* **331**, 162 – 167 (2013). URL `http://www.sciencedirect.com/science/article/pii/S0304885312009365`.

[166] Zhang, H., Zhang, X., Zhang, J., Li, Z. & Sun, H. Template-based electrodeposition growth mechanism of metal nanotubes. *J. Electrochem. Soc.* **160**, D41–D45 (2013). URL `http://jes.ecsdl.org/content/160/2/D41.abstract`.

[167] Zhang, B. *Amorphous and Nano Alloys Electroless Depositions* (Elsevier, 2015), 1st edn.

[168] Shacham-Diamand, Y., Osaka, T., Okinaka, Y., Sugiyama, A. & Dubin, V. 30 years of electroless plating for semiconductor and polymer micro-systems. *Microelectron. Eng.* **132**, 35–45 (2015). URL `http://www.sciencedirect.com/science/article/pii/S0167931714003694`. Micro and Nanofabrication Breakthroughs for Electronics, MEMS and Life Sciences.

[169] Watanabe, T. *Nano plating* (Elsevier, 2004).

[170] Antoni, M. *et al.* Electrocatalytic applications of platinum-decorated TiO_2 nanotubes prepared by a fully wet-chemical synthesis. *J. Mater. Sci.* **52**, 7754–7767 (2017).

[171] Kulyk, N., Cherevko, S. & Chung, C.-H. Copper electroless plating in weakly alkaline electrolytes using DMAB as a reducing agent for metallization on polymer films. *Electrochim. Acta* **59**, 179 – 185 (2012). URL http://www.sciencedirect.com/science/article/pii/S001346861101588X.

[172] Muench, F., Oezaslan, M., Svoboda, I. & Ensinger, W. Electroless plating of ultrathin palladium films: self-initiated deposition and application in microreactor fabrication. *Mater. Res. Express* **2**, 105010 (2015). URL http://stacks.iop.org/2053-1591/2/i=10/a=105010.

[173] Stöhr, J. & Siegmann, H. *Magnetism: From Fundamentals to Nanoscale Dynamics*, vol. 152 of *Springer Series in Solid-State Sciences*, chap. 9–10 (Springer, 2006).

[174] Joachim Stöhr webpage: Magnetic dichroism and spectroscopy. Available from https://www-ssrl.slac.stanford.edu/stohr/xmcd.htm, [Accessed 2017-06-27].

[175] Fischer, P. & Ohldag, H. X-rays and magnetism. *Rep. Prog. Phys.* **78**, 094501 (2015). URL http://stacks.iop.org/0034-4885/78/i=9/a=094501.

[176] Locatelli, A. & Bauer, E. Recent advances in chemical and magnetic imaging of surfaces and interfaces by XPEEM. *J. Phys. Condens. Matter* **20**, 093002 (2008). URL http://stacks.iop.org/0953-8984/20/i=9/a=093002.

[177] Cheng, X. M. & Keavney, D. J. Studies of nanomagnetism using synchrotron-based X-ray photoemission electron microscopy (X-PEEM). *Rep. Prog. Phys.* **75**, 026501 (2012).

[178] Eaton, P. & West, P. *Atomic force microscopy* (Oxford University Press, 2010).

[179] Hopster, H. & Oepen, H. P. (eds.) *Magnetic microscopy of nanostructures.* NanoScience and Technology (Springer, 2005).

[180] Staňo, M. *Characterization of magnetic nanostructures by magnetic force microscopy.* Master's thesis, Brno University of Technology (2014). URL https://www.vutbr.cz/www_base/zav_prace_soubor_verejne.php?file_id=86694.

[181] Digital Instruments. *Magnetic Force Microscopy* (1996). Support Note No. 229, Rev. B.

[182] Albrecht, T. R., Grütter, P., Horne, D. & Rugar, D. Frequency modulation detection using high-Q cantilevers for enhanced force microscope sensitivity. *J. Appl. Phys.* **69**, 668–673 (1991). URL http://dx.doi.org/10.1063/1.347347.

[183] Weigert, S., Dreier, M. & Hegner, M. Frequency shifts of cantilevers vibrating in various media. *Appl. Phys. Lett.* **69**, 2834–2836 (1996). URL https://doi.org/10.1063/1.117334.

[184] Nonnenmacher, M., O'Boyle, M. P. & Wickramasinghe, H. K. Kelvin probe force microscopy. *Appl. Phys. Lett.* **58**, 2921–2923 (1991). URL http://dx.doi.org/10.1063/1.105227.

[185] Berlin, J. Analysis of boron with energy dispersive X-ray spectrometry. *Imaging & Microscopy* **13**, 19–21 (2011). URL https://www.bruker.com/fileadmin/user_upload/8-PDF-Docs/X-rayDiffraction_ElementalAnalysis/Microanalysis_EBSD/Articles/Repr_I_M_boron.pdf.

[186] Völkl, E., Allard, L. F. & Joy, D. C. *Introduction to electron holography* (Springer, 1999).

[187] Lichte, H. & Lehmann, M. Electron holography – basics and applications. *Rep. Prog. Phys.* **71**, 016102 (2008).

[188] Kasama, T., Beleggia, M. & Dunin-Borkowski, R. E. *Electron holography of magnetic materials* (INTECH, 2011).

[189] McCartney, M. R. & Smith, D. J. Electron holography: Phase imaging with nanometer resolution. *Annu. Rev. Mater. Res.* **37**, 729–767 (2007).

[190] Sanchez, A. & Ochando, M. A. Calculation of the mean inner potential. *J. Phys. C: Solid State Phys.* **18**, 33 (1985). URL http://stacks.iop.org/0022-3719/18/i=1/a=011.

[191] Signoretti, S. *Electron holography for the analysis of magnetic and electric microfields in nanostructured systems*. Ph.D. thesis, Naturwissenschaften ETH Zürich (2003).

[192] Tonomura, A., Matsuda, T., Endo, J., Arii, T. & Mihama, K. Holographic interference electron microscopy for determining specimen magnetic structure

and thickness distribution. *Phys. Rev. B* **34**, 3397–3402 (1986). URL `https://link.aps.org/doi/10.1103/PhysRevB.34.3397`.

[193] Dunin-Borkowski, R. E. *et al.* Off-axis electron holography of magnetic nanowires and chains, rings, and planar arrays of magnetic nanoparticles. *Microsc. Res. Tech.* **64**, 390–402 (2004).

[194] Wolf, D. *et al.* 3D magnetic induction maps of nanoscale materials revealed by electron holographic tomography. *Chem. Mater.* **27**, 6771 (2015).

[195] Tanigaki, T. *et al.* Three-dimensional observation of magnetic vortex cores in stacked ferromagnetic discs. *Nano Lett.* **15**, 1309–1314 (2015).

[196] Beeli, C., Doudin, B., Ansermet, J.-P. & Stadelmann, P. Study of Co, Ni and Co/Cu nanowires: magnetic flux imaging by off-axis electron holography. *J. Magn. Magn. Mater.* **164**, 77–90 (1996).

[197] Col, S. D. *et al.* Nucleation, imaging, and motion of magnetic domain walls in cylindrical nanowires. *Appl. Phys. Lett.* **109**, 062406 (2016). URL `http://dx.doi.org/10.1063/1.4961058`.

[198] Bran, C. *et al.* Direct observation of transverse and vortex metastable magnetic domains observed in cylindrical nanowires. *arXiv:1705.04615* (2017).

[199] Bochmann, S. *et al.* Preparation and physical properties of soft magnetic nickel-cobalt nanowires with modulated diameters. *In preparation* (2017).

[200] Višňovský, S. *Optics in Magnetic Multilayers and Nanostructures.* Optical Science and Engineering (CRC Press, 2006).

[201] Donahue, M. J. & Porter, D. G. *OOMMF Users's Guide, Version 1.0.* National Institute of Standards and Technology, Gaithersburg, MD (1999). Intragency Report NISTIR 6376.

[202] Alouges, F., Kritsikis, E., Steiner, J. & Toussaint, J.-C. A convergent and precise finite element scheme for Landau–Lifschitz–Gilbert equation. *Numer. Math.* **128**, 407–430 (2014).

[203] FeeLLGood webpage. Available from `http://feellgood.neel.cnrs.fr`, [Accessed 2017-04-04].

[204] ovf2vtk webpage. Available from `http://www.southampton.ac.uk/~fangohr/software/ovf2vtk/`, [Accessed 2017-03-13].

[205] ParaView webpage. Available from http://www.paraview.org/, [Accessed 2016-05-18].

[206] Vaysset, A. *Micromagnetic modelling of spin-transfer-driven magnetisation dynamics in nanopillars*. Ph.D. thesis, Université de Grenoble (2013).

[207] Jamet, S. *Étude des parois de domaines dans les nanofils magnétiques*. Ph.D. thesis, Université Grenoble Alpes (2015). In English.

[208] Scalfmm webpage. Available from http://scalfmm-public.gforge.inria.fr/doc/, [Accessed 2017-03-14].

[209] Geuzaine, C. & Remacle, J.-F. Gmsh: A 3-D finite element mesh generator with built-in pre-and post-processing facilities. *Int. J. Numer. Methods Eng.* **79**, 1309–1331 (2009).

[210] FreeCAD. Available from http://www.freecadweb.org/, [Accessed 2016-05-18].

[211] Boost C++ libraries. Available from http://www.boost.org/ [Accessed 2016-09-21].

[212] Nakajima, R., Stöhr, J. & Idzerda, Y. Electron-yield saturation effects in L-edge X-ray magnetic circular dichroism spectra of Fe, Co, and Ni. *Phys. Rev. B* **59**, 6421 (1999).

[213] Geng, J., Jefferson, D. A. & Johnson, B. F. Exploring the structural complexities of metal–metalloid nanoparticles: The case of Ni·B as catalyst. *Chem. Eur. J.* **15**, 1134–1143 (2009).

[214] Saxena, A., Dandoloff, R. & Lookman, T. Deformable curved magnetic surfaces. *Physica A* **261**, 13–25 (1998).

[215] Velázquez-Galván, Y. *et al.* Dipolar interaction in arrays of magnetic nanotubes. *J. Phys. Condens. Matter* **26**, 026001 (2014). URL http://stacks.iop.org/0953-8984/26/i=2/a=026001.

[216] Konč, M. *et al.* Temperature dependence of the magnetization and of the other physical properties of rapidly quenched amorphous CoB alloys. *IEEE Trans. Magn.* **30**, 524–526 (1994).

[217] Dieny, B. & Chshiev, M. Perpendicular magnetic anisotropy at transition metal/oxide interfaces and applications. *Rev. Mod. Phys.* **89**, 025008 (2017). URL https://link.aps.org/doi/10.1103/RevModPhys.89.025008.

[218] O'Handley, R. C. *Modern magnetic materials* (Wiley, 2000).

[219] Vlasák, G., Jergel, M. & Duhaj, P. Compositional dependence of magnetostriction of amorphous Co-Fe-B and Co-Ni-B alloys. *Mater. Sci. Eng.* **99**, 109–112 (1988).

[220] Yamasaki, J., Fukunaga, H. & Narita, K. Anisotropic magnetoresistance in transition metal-boron amorphous alloys. *J. Appl. Phys.* **52**, 2202–2204 (1981).

[221] Vock, S. *et al.* Magnetic vortex observation in FeCo nanowires by quantitative magnetic force microscopy. *Appl. Phys. Lett.* **105** (2014). URL `http://scitation.aip.org/content/aip/journal/apl/105/17/10.1063/1.4900998`.

[222] Li, J. W., Cleveland, J. P. & Proksch, R. Bimodal magnetic force microscopy: Separation of short and long range forces. *Appl. Phys. Lett.* **94**, 163118 (2009).

[223] Schwenk, J. *et al.* Bimodal magnetic force microscopy with capacitive tip-sample distance control. *Appl. Phys. Lett.* **107**, 132407 (2015).

[224] Khvalkovskiy, A. V. *et al.* Matching domain-wall configuration and spin-orbit torques for efficient domain-wall motion. *Phys. Rev. B* **87**, 020402 (2013). URL `https://link.aps.org/doi/10.1103/PhysRevB.87.020402`.

[225] Stupakiewicz, A. *et al.* Direct imaging of the magnetization reversal in microwires using all-MOKE microscopy. *Rev. Sci. Instrum.* **85**, 103702 (2014). URL `http://dx.doi.org/10.1063/1.4896758`.

[226] Fruchart, O. & Diény, B. Magnetostatics of synthetic ferrimagnet elements. *J. Magn. Magn. Mater.* **324**, 365 (2011).

[227] Midgley, P. An introduction to off-axis electron holography. *Micron* **32**, 167–184 (2001).

[228] Snoeck, E. *et al.* Quantitative magnetization measurements on nanometer ferromagnetic cobalt wires using electron holography. *Appl. Phys. Lett.* **82**, 88–90 (2003).

LIST OF ABBREVIATIONS

e.g.	*exempli gratia*, for example
i.e.	*id est*, that is (GB), *c'est à dire* (FR)
3D	Three-dimensional
AFM	Atomic Force Microscopy
ALD	Atomic Layer Deposition
BPW	Bloch Point Wall
CE	Counter Electrode
DC	Direct Current (also static mode)
DMAB	DiMethylAmine Borane
DMI	Dzyaloshinskii-Moriya Interaction
DW	Domain Wall
EDX	Energy-Dispersive X-ray Spectroscopy
HDD	Hard Disc Drive
GMR	Giant MagnetoResistance
IBM	International Business Machines Corporation
LLG	The Landau-Lifschitz-Gilbert (equation)
MFM	Magnetic Force Microscopy
MOKE	Magneto-Optical Kerr Effect
NT	NanoTube
NW	NanoWire
OOMMF	Object-Oriented MicroMagnetic Framework
PEEM	PhotoEmission Electron Microscopy
RE	Reference Electrode
SAF	Synthetic AntiFerromagnet

SCE	Saturated Calomel Electrode
SEM	Scanning Electron Microscopy
STXM	Scanning Transmission X-ray Microscopy
TEM	Transmission Electron Microscopy
TMR	Tunneling MagnetoResistance
TW	Transverse Wall
VlW	Vortex-like Wall
WE	Working Electrode
XAS	X-ray Absorption Spectroscopy
XMCD	X-ray Magnetic Circular Dichroism

LIST OF APPENDICES

A HOW TO DAMAGE YOUR (NANO)TUBE

Most of the time authors show their best results. In this short section we will show the opposite – complete failures. Or to be more positive as everything depends on the point of view and how you sell your work, the alternative heading may go as follows: micro and nanomachining using local probe, focused laser, and high voltage. At least some of these could be in principle done on purpose and exploited.

A.1 Nanomachining using AFM

In our first atomic force microscopy scans of magnetic tubes with diameters 300-400 nm, we had some problems just with acquiring topography images. From time to time, holes were created in the tube during the tapping AFM (Fig. S1). Too fast scan speed ($>>$ 10 µms) led even to cutting the tube into several pieces. Slower scan ($<$ 5 µms) with higher z (vertical direction) feedback prevented from similar issues. Another possible solution is a truly non-contact measurement.

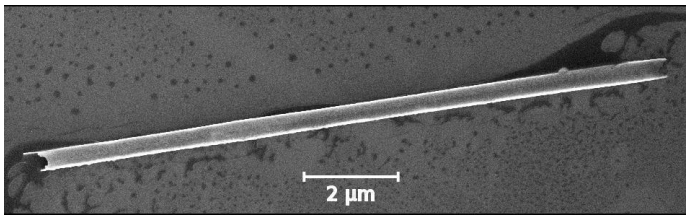

(a) Before AFM

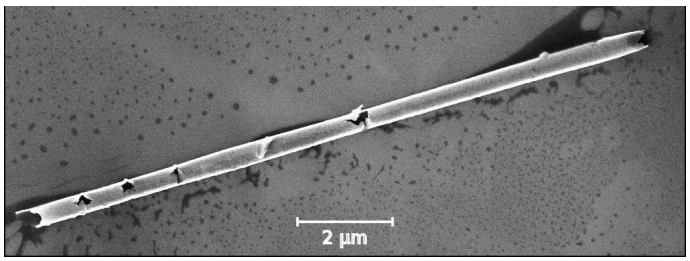

(b) After AFM

Fig. S1: Cutting tubes with atomic force microscopy. Magnetic tube with shell thickness 20 nm (a) before and (b) after tapping atomic force microscopy.

A.2 Laser cutting with micrometric precision

During magneto-optical experiments with focused laser, prolongated exposure (at least several minutes) to laser power of 3 mW or higher led to severe damage of the

investigated tubes (Fig. S2 and S3). Note that such laser powers are sometimes used for measurement of thin films where the thermal contact with the substrate is much better than in case of our tubes. It is necessary to state that some of our tubes were exposed to X-rays during synchrotron XMCD-PEEM investigation which could possibly make them more susceptible to the laser beam.

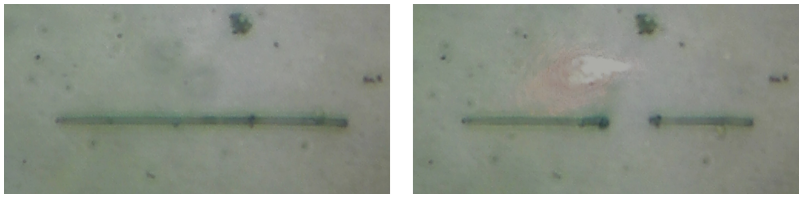

Fig. S2: Cutting tubes using focused laser beam (aka magnetooptics). Left: before, right: after several min of laser beam exposure (spot size 1 µm, power around 3 mW). Original tube length slightly below 30 µm, laser spot on the image is defocused.

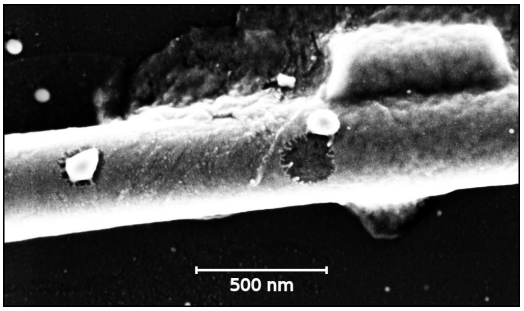

Fig. S3: Burning well-positioned holes using focused laser beam (magnetooptics) with a sample on a piezostage.

A.3 Big task requires big instrument

In case you want prepare a nice crater in your Si substrate, grill your tubes and splash some melted Si around, you can apply for beamtime at synchrotron. You insert your not ideally clean sample into UHV and apply 20 kV between your sample and electron microscope objective. Results may resemble Fig. S4.

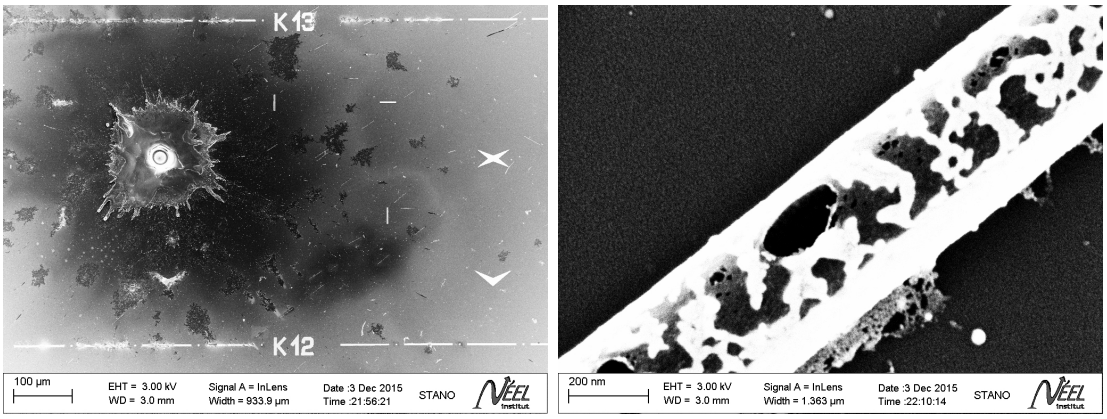

(a) Sample overview (b) Detail of a tube

Fig. S4: Sample affected by electric discharge during XMCD-PEEM measurement. (a) Overview image with a crater in the Si substrate, (b) detail of a partially melted tube.

B ELECTRON HOLOGRAPHY

B.1 Electrostatic interaction constant c_E

In vacuum we express the electron velocity as

$$v = \frac{p\mathrm{c}}{E}\mathrm{c} = \frac{p\mathrm{c}}{E_\mathrm{k} + E_0}\mathrm{c}, \tag{B.1}$$

with electron momentum $p = \frac{1}{\mathrm{c}}\sqrt{E_\mathrm{k}^2 + 2E_\mathrm{k}E_0}$, c the speed of light in vacuum, E the total electron energy involving kinetic energy E_k and rest energy $E_0 = \mathrm{m}_0\mathrm{c}^2$, where m_0 represents the rest mass of the electron.

Then inserting (B.1) into c_E definition we obtain:

$$\mathrm{c}_E = \frac{\mathrm{e}}{\hbar}\frac{1}{v} = \frac{\mathrm{e}}{\hbar}\frac{E_\mathrm{k} + E_0}{\sqrt{E_\mathrm{k}^2 + 2E_\mathrm{k}E_0}}\frac{1}{\mathrm{c}} = \frac{2\pi\mathrm{e}}{\mathrm{h}}\frac{\sqrt{E_\mathrm{k}^2 + 2E_\mathrm{k}E_0}}{\mathrm{c}}\frac{(E_\mathrm{k} + E_0)}{E_\mathrm{k}^2 + 2E_\mathrm{k}E_0} = 2\pi\mathrm{e}\frac{p}{\mathrm{h}}\frac{(E_\mathrm{k} + E_0)}{E_\mathrm{k}^2 + 2E_\mathrm{k}E_0}. \tag{B.2}$$

Here we got rid of the square root in the denominator, using $p = \frac{1}{\mathrm{c}}\sqrt{E_\mathrm{k}^2 + 2E_\mathrm{k}E_0}$ and $\mathrm{h} = 2\pi\hbar$. If we recall the de Broglie wavelength (of the electron):

$$\lambda = \frac{\mathrm{h}}{p}, \tag{B.3}$$

with $\lambda = \frac{\mathrm{h}}{p}$ (h is the Planck constant and p the electron momentum), we can get expression which is used in literature on electron holography [227]:

$$\mathrm{c}_E = \frac{2\pi\mathrm{e}}{\lambda}\frac{(E_\mathrm{k} + E_0)}{E_\mathrm{k}^2 + 2E_\mathrm{k}E_0}. \tag{B.4}$$

Note that in some (review) articles on electron holography - e.g. Kasama [188] and McCartney [189] (but also many others), the expression (B.4) is given **without elementary charge e**. But without this constant the expression makes no sense, as both dimensions and order of magnitude are incorrect and inconsistent with values and dimension of the c_E, even with value+dimension provided in these articles just one line below the formula - e.g. [188]. Midgley's review [227] provides the correct expression including elementary charge.

The formula without e works only when energies are expressed as voltages, i.e. E/e, this might be convenient in practical use as one just puts there accelerating voltage instead of energy (e.g. 300 kV) and 511 kV instead of electron rest energy E_0.

Now we will consider the value of c_E for electron energy of 300 keV used in our electron holography experiments at CEMES Toulouse.

The relativistic relation between energy and momentum is:

$$E^2 = (E_\mathrm{k} + E_0)^2 = p^2\mathrm{c}^2 + \mathrm{m}_0^2\mathrm{c}^4. \tag{B.5}$$

From the relativistic relation (B.5) we can express momentum $p = \frac{1}{\mathrm{c}}\sqrt{E_\mathrm{k}^2 + 2E_\mathrm{k}E_0}$ and insert it into (B.3) in order to obtain an expression for the wavelength in terms of energies:

$$\lambda = \frac{\mathrm{hc}}{\sqrt{E_\mathrm{k}^2 + 2E_\mathrm{k}E_0}}. \tag{B.6}$$

For accelerating voltage of 300 kV we get electron wavelength $\lambda_{300\,\mathrm{kV}} = 1.97\,\mathrm{pm}$ which is in accordance with the literature. Inserting this value into (B.4) we obtain:

$$\mathrm{c}_{300\,\mathrm{keV}} = 6.5262 \cdot 10^6\ \mathrm{rad}/(\mathrm{V}\cdot\mathrm{m}).$$

This is consistent with the literature [188, 228]. Values of the c_E parameter for other energies are plotted in Fig. S1.

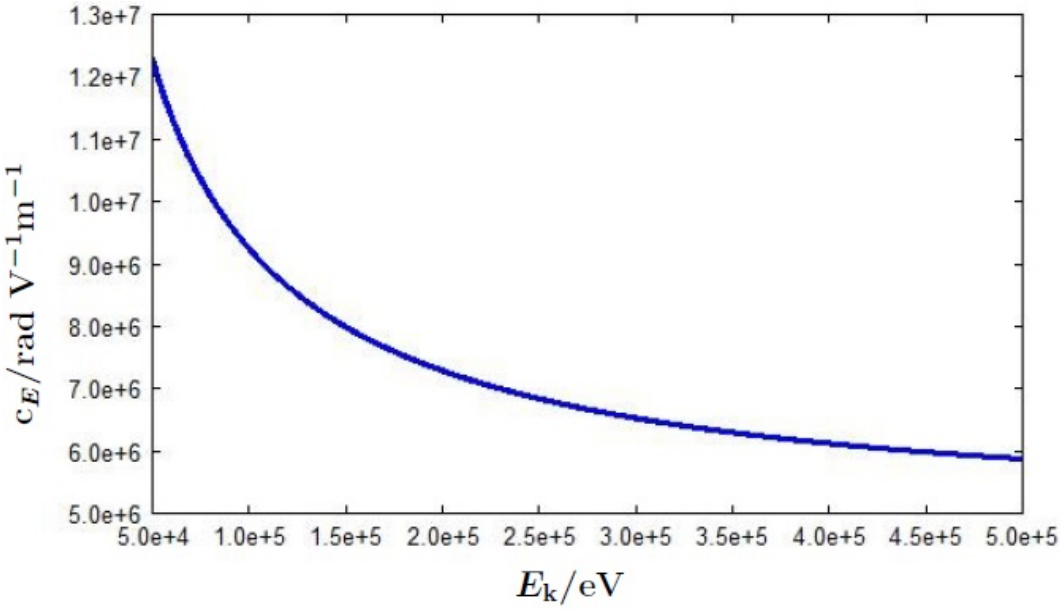

Fig. S1: Dependence of the c_E parameter on electron energy.

B.2 Electrostatic contribution of a tube

As has been mentioned in the methods, our current simulation code cannot cope with hollow tubes as regards the electrostatic contribution to the phase maps. Still the same (simple) model used for wires should hold: the electrostatic part is proportional to the sample thickness or better to say the path travelled through the sample. For a tube with outer radius R and shell thickness t, the path across the tube (in line profile with coordinate $x \in -R..R$ across the tube) should read:

$$p = \begin{cases} 2\left(\sqrt{R^2 - x^2} - \sqrt{(R-t)^2 - x^2}\right) & \text{if } x \le R - t \\ p = 2\left(\sqrt{R^2 - x^2}\right) & \text{if } R - t < x \le R \end{cases}$$

Comparison of the simple analytical model (MIP 25 V, diameter 250 nm, shell thickness 30 nm) and experimental line profile for the electrostatic contribution to the phase is given in Fig. S2.

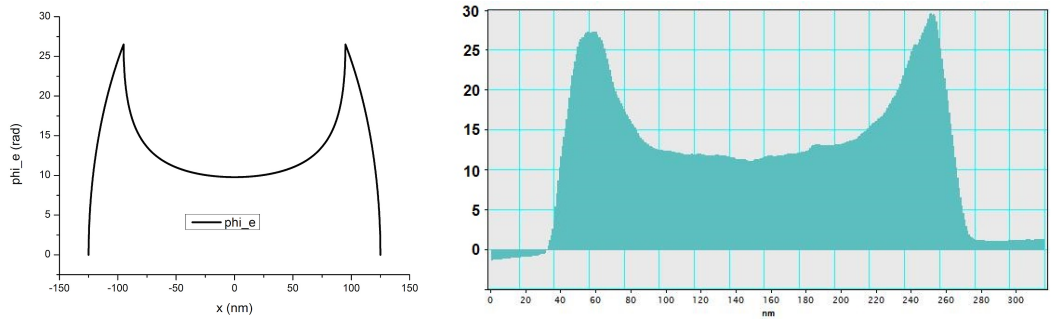

(a) analytics – simple model (b) from experiment

Fig. S2: Electrostatic contribution for a tube: simple analytical model vs phase reconstructed from experiment. Line cross-section across the tube.

Even though the geometry is slightly different, the simple model performs rather well. Therefore, one can either extend the numerical computation code or add this analytical contribution to the simulated magnetic phase map (not done here).

B.3 Contrast modelling for domain walls in tubes between azimuthal domains

In the electron holography phase maps we expected no signal from the azimuthal domains, due to the magnetic flux-closure and thus cancellation of the magnetic phase contribution when going through the top and bottom part of the tube shell having opposite magnetization. The only magnetic signal should come from the domain walls. A crude simulation of the magnetic contribution originating from Néel, Bloch, and cross-tie-like domain walls is featured in Fig. S3.

The Néel wall should give rise to contrast already obtained on nanowires with axial magnetization, only more spatially localized. Therefore, it should be visible even without removing the electrostatic contribution.

On the other hand, the Bloch wall give rise to quadrupole contrast that is much weaker (6 times weaker) than for the Néel wall in the same tube geometry. Most likely such signal is invisible in the experiment without removing the electrostatic part (see Fig. S4 for simulation with and without the electrostatic part).

In the two above-mentioned cases the signal does not depend on the rotation of the tube due to the symmetry of the magnetic configurations. This is not the case

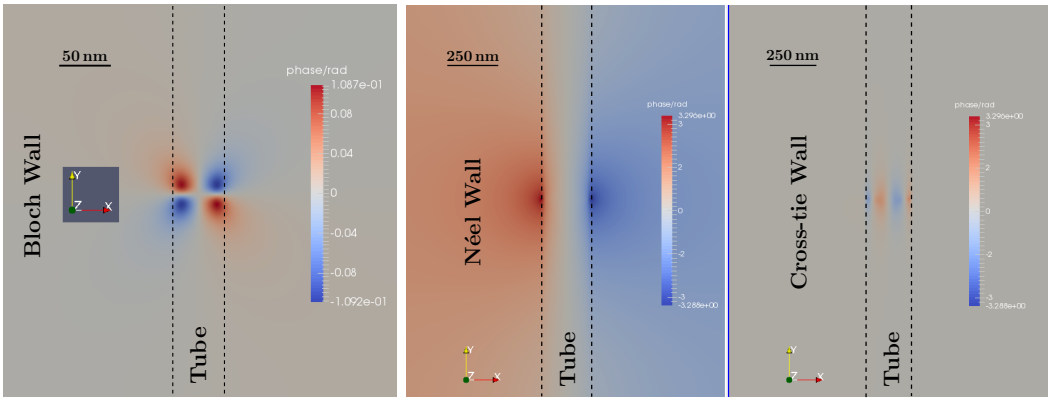

Fig. S3: Crude electron holography simulations of the magnetic phase maps (no electrostatic contribution) for Bloch, Néel and cross-tie walls in between 2 opposite azimuthal domains in a tube. Note that the Bloch wall was prepared in a smaller tube and the contrast range is different as well (for the same geometry, the Bloch wall gives 6 times weaker contrast than the Néel one).

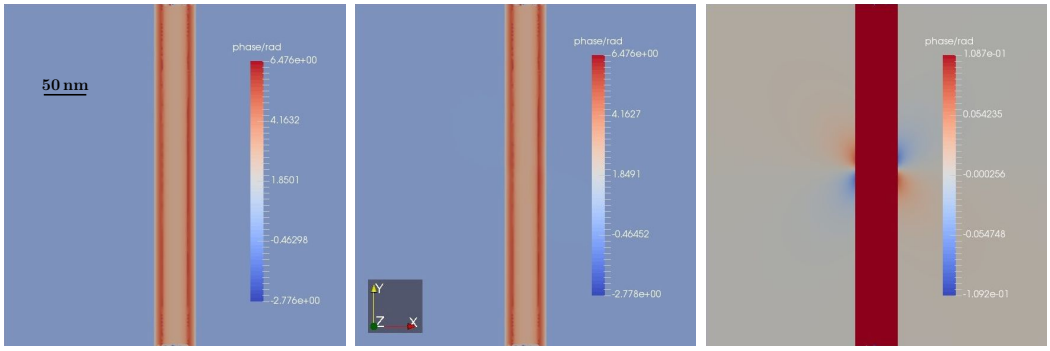

(a) electrostatic only (b) electrostatic+magnetic (c) electrostatic+magnetic

Fig. S4: Simulation of electron holography phase map with electrostatic contribution for Bloch wall (radial magnetization) in between 2 opposite azimuthal domains in a tube (for magnetic part only see in Fig. S3a). (a) Electrostatic part only. The highest phase shift is close to tube edges where the electron path travelled through the tube is the longest; the spatial extent corresponds roughly to the tube wall (shell) thickness. (b) and (c) depict both electrostatic and magnetic parts scaled to (a) full range of the phase, (b) small range around zero. The electrostatic part dominates and in experiment one cannot probably clearly see the weak magnetic signal without removing the electrostatic contribution. Even here it is almost impossible to spot a small difference between (a) and (b).

for the cross-tie wall. In addition, here the contrast may depend on the number of vortex-antivortex pairs (here 4, smaller amount is found in tubes with smaller

diameter).

B.4 Electron holography on NiCo nanowires with modulated diameter

We consider here diameter-modulated $Ni_{60}Co_{40}$ nanowires. These have been introduced in the short tutorial about electron holography imaging – section 5.4.4. We intend to use the investigation of diameter-modulated nanowires as a step towards performing similar measurements on tubes, later also with modulated-diameter.

In the ground state, such nanowires are axially magnetized (aside from curling at the wire ends and diameter modulations). A typical nanowire geometry with diameter modulations has been already shown in Fig. 5.10. Two types of domain walls (DWs) may exist in such nanowires: transverse or Bloch point wall (see Fig. 2.4). We remind the readed that the diameter modulation is intended for easier nucleation and trapping of a DW in the thin section of the wire. After few initial trials, we performed most of the experiments on one nanowire displayed in Fig. S5. This wire has around 120 nm in diameter in the central thin section. Later, we probed other NiCo nanowires, where we could nucleate even multiple DWs.

B.4.1 Domain wall nucleation and displacement

After applying an out-of-plane field pulse of 1 T (width of few s) with a slight tilt (around -8 °), we successfully nucleated a DW, which was located at the P1 site (see location in Fig. 5.10). Then, applying smaller fields of 30 mT (out-of-plane, along the beam) with different component along wire given by the sample tilt, we were able to move the DW to P2 and then repeatedly with the same field (tilt) values between pinning sites P2 (tilt during field application: -18 °) and P3 (tilt during field application: +9 °. Therefore, there is a small component along the wire, but the field has significant component transverse to the wire axis. An example of the DW pinned at P3 site is given in Fig. S6. As the initial sample needed for DW nucleation was -8 ° and when going above or below the tilt, the magnetization was switched we assume that the wire is initially already slightly tilted and at -8 ° the wire is perpendicular to the beam. In such case the both tilts for DW displacement corresponds to approx. 10 °, which result in 5 mT applied along the wire axis (but 30 mT total magnitude).

When we tried to reach again the P1 site, we gradually increased the sample tilt while keeping constant excitation of the objective lenses (producing still 30 mT). After the depinning, the DW went through the smooth diameter modulation and

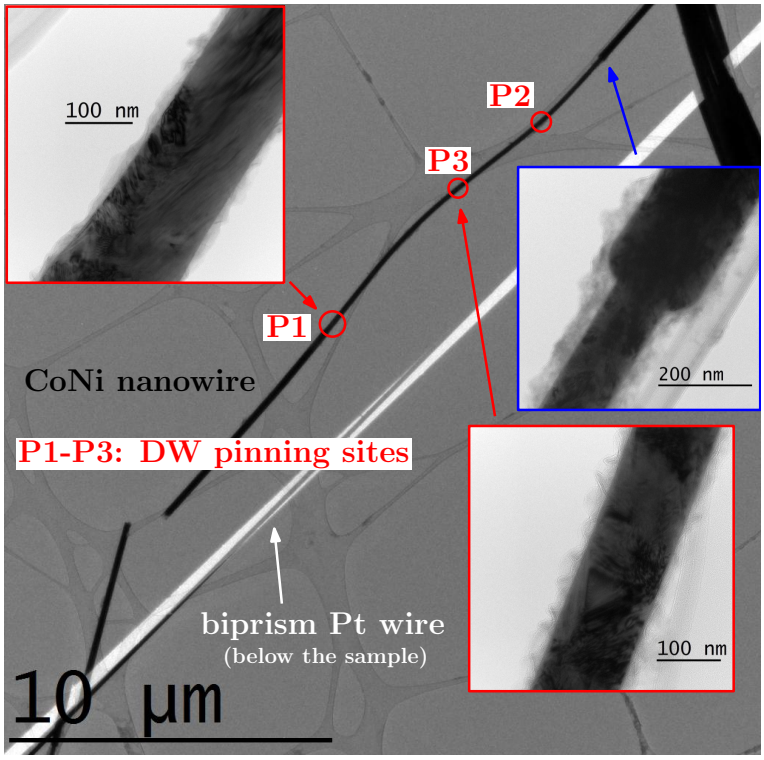

Fig. S5: TEM image of the NiCo nanowire sample with pinning sites (P1-P3) for a domain wall. A magnetic domain wall was repeatedly nucleated at P1 site and then moved back and forth many times between pinning sites P2 and P3. Insets show higher magnification images of the regions of interest (pinning sites, diameter modulation).

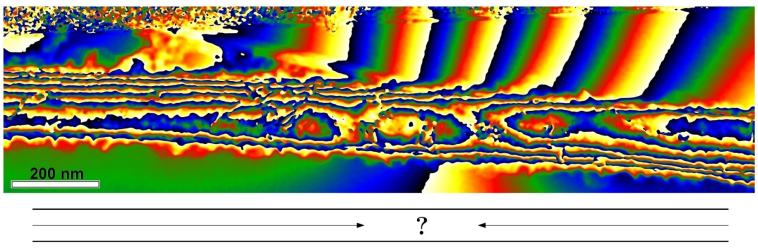

Fig. S6: Electron holography phase map (both magnetic and electrostatic part) of the nanowire with a domain wall (P3 site). The DW location is in between regions with the contour lines concentrated on opposite sides of the wire – recall Fig. 5.12 from our small electron holography tutorial. The position is also indicated by the stray field (outside the wire). It is not easy to determine the domain wall configuration just from the map itself.

then annihilated at the left wire end (complete magnetization reversal). With the same field sequence as at the beginning we re-nucleated the DW at P1 and shifted it again many times between P2 and P3 sites. Unfortunately, the diameter modulations were not very efficient in trapping the DW except for the smooth modulation. Here the DW was trapped rather due to a small notch (structural defect, see Fig. S7a) than the diameter change. In general, the DW pinning was stronger at local defects like a triangular grain at P3 site from Fig. S5. Therefore, after applying sufficiently high field to depin the DW, the wall moved either to another local defect, or went through the diameter modulation and annihilated. This might be improved by enhancing the material quality (lowering strength of natural pinning sites, e.g. by annealing) and changing the modulation geometry (more abrupt change in diameter).

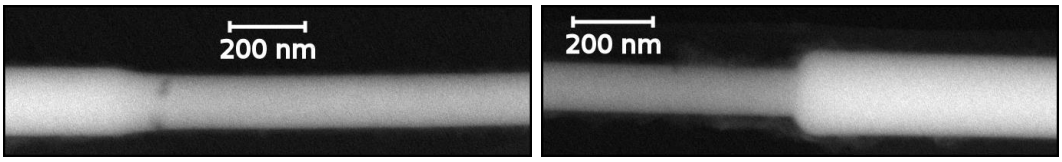

(a) Smooth diameter modulation (b) Sharp diameter modulation

Fig. S7: NiCo nanowire – diameter modulations with a structural defect at the smooth modulation. Scanning electron microscopy with backscattered electron detection. The thicker wire part appear brighter, whereas the defects – notches (missing material) are dark in the image – this is the P1 area.

B.4.2 Domain wall identification

While localization of the DW position is easy, the determination of its type and magnetic configuration can be difficult. We did numerical modelling of nanowires with both TW and BPW for comparison with the experimental images. The electron phase shift maps for the wire with a DW and their numerical modelling are summarized in Fig. S8. The electrostatic part which may make the DW identification more difficult can be either removed experimentally or included in the simulations. The first option paves the way towards quantitative matching of the DW pattern but it is time consuming from the experimental point of view. On the other hand, even with a rather simple model for the electrostatic part we can reproduce the experiment numerically without this nuisance. The experimental magnetic phase shift is slightly smaller than in the simulations; we attribute this to a reduced path-integrated magnetic induction due to surface oxidation. Quantitative agreement for both magnetic and electrostatic contributions is possible yet difficult due to the model simplicity

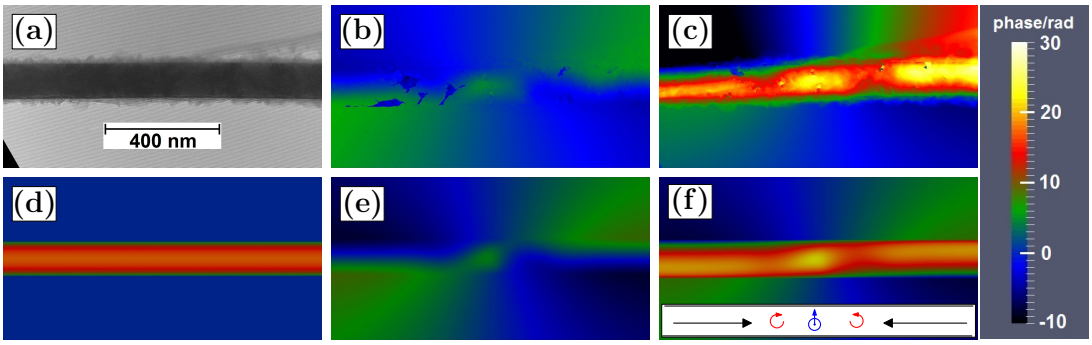

Fig. S8: Electron holography – experiment (top) vs simulations (bottom). (a) hologram (wire+interference fringes); experimental phase maps: (b) magnetic only and (c) electrostatic+magnetic. Simulated phase: (d) electrostatic only, (e) magnetic only and (f) both contributions with a scheme of the magnetization pattern. Here the azimuth of the core of the transverse wall is in-between in-plane and out-of-plane (beam) direction. There is a curling with opposite sense of circulation on either side of the wall due to the large wire diameter (120 nm).

and electrostatic contributions arising from an inhomogeneous supporting carbon film, defects and crust of impurities on the wire (Fig. S8a).

In all our experiments so far, we identified the transverse wall with various orientation (azimuth). Fig. S9 and Fig. S10 show that depending on this azimuth, the same DW type (TW) produces different magnetic phase maps.

The question arises, whether one is able to unambiguously distinguish a BPW from a TW with an a priori unknown azimuth. The more challenging case is when the azimuth of the TW is aligned with the electron beam direction as the phase is not sensitive to the magnetic induction pointing along the beam. Even in this case we can distinguish a BWP and from a TW thanks to an additional curling that has opposite sense at either side of the TW – this has been already reported in [14]. For the BPW the curling sense is the same on both sides of the wall. Note that different magnetic configurations can produce very similar phase maps, e.g. BPW and ideal TW without curling pointing along the beam (exist only for small diameters [15] – not our case). Therefore, ideally one should acquire images for at least a few tilts to avoid the misinterpretation.

In few cases we were in doubt regarding distinguishing BPW and TW. Therefore, we performed imaging with tilted sample – always ±tilt (e.g. $\pm X\,^{\circ}$). This should give us some information on the out-of-plane magnetic induction. The phase maps for BPW should look the same (at least the magnetic part) when tilting the sample along the wire axis (rotating the wire), just due to the BPW symmetry. Tilting the wire with respect to the axis perpendicular to the wire could also allow to determine the curling sense. In all cases transverse wall with various core magnetization

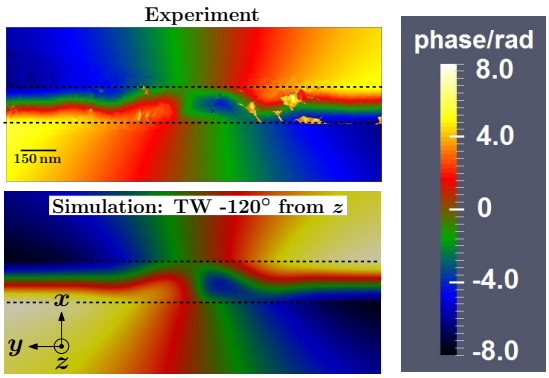

Fig. S9: Magnetic phase maps for a transverse domain wall: experiment (top, diameter) vs simulation (bottom). Dashed lines show the approximate wire position.

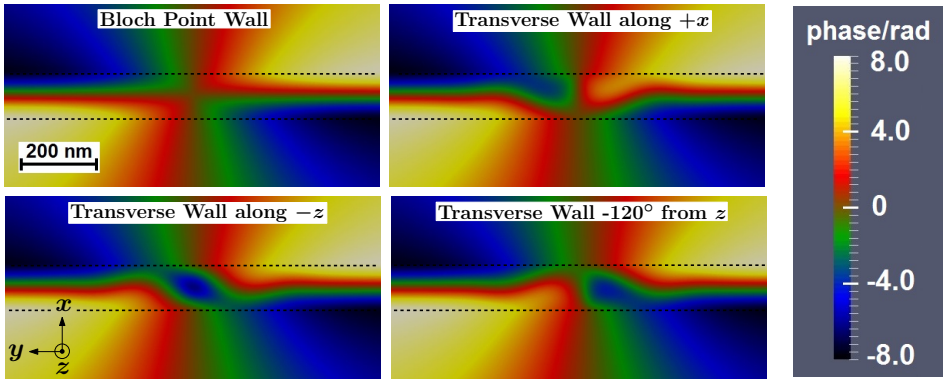

Fig. S10: Simulated magnetic phase maps for Bloch point wall and transverse wall with different azimuths (orientations) for the latter. The transverse wall can give rise to very different phase maps depending on the magnetization direction in the domain wall core. Similar effect may also happen if the angle between the wire and the electron beam changes (tilted sample). Dashed lines show the approximate wire extent.

orientation was found.

B.4.3 Summary of electron holography on modulated nanowires

In case of CoNi nanowires, the magnetic signal related to opposite axial magnetization was distinguishable even without removing the electrostatic contribution. The stray field was observed emanating both from diameter modulation (Fig. 5.12) as well as from a DW (Fig. S6). Electron holography together with simulations enables identification of the type of DW and determination of its structure. Our simulations of the electron holography phase maps shows very good agreement with the experiment (Fig. S8). Both magnetic and electrostatic contributions to the phase shift can be modelled and even simple electrostatic model (phase proportional to thickness times constant MIP) gives satisfactory results. We evidenced the transverse wall with the orientation of the transverse magnetization sometimes changed after the wall displacement with the magnetic field.

We were able to reproduce nucleation, shifting (back and forth among several pinning sites) and annihilation of the DW. The diameter modulations were not efficient in stopping the domain wall – the wall was pinned rather on local defect (e.g. notches). Better material quality and more abrupt diameter change are required. Different approach can be followed as well – e.g. with segments from different materials [26] or tube-wire elements discussed in the min text.

We benefited from the experience and familiarity with the technique in further investigation of magnetic tubes. In future, we hope to apply similar sample preparation, domain wall nucleation and manipulation also to diameter modulated nanotubes.

C FEELLGOOD – MAGNETIC STATE INITIALIZATION

Below we give an example of a script used for building initial magnetic configuration for FeeLLGood micromagnetic simulations. In this particular case it is state with two azimuthal domains having opposite circulation of magnetization, separated by an ideal Bloch-like domain wall (radial magnetization).

```
#include "fem.h"

// Initial distribution of magnetization
// tube along z, with z=0 being its centre
// 2 azimuthal domains separated by a Bloch-like domain wall

void init_distrib(Fem &fem)
{
const int NOD = fem.NOD;
int chir; // auxiliary for sense of azimuthal curling

for (int i=0; i<NOD; i++){
   Node &node = fem.node[i];
   double x = 2.*(node.x-fem.cx)/fem.lx; // x in -1..1]
   double y = 2.*(node.y-fem.cy)/fem.ly; // y in -1..1]
   double z = 2.*(node.z-fem.cz)/fem.lz; // z in -1..1]
   double a=0.1; // initial extent of the wall along z
   double u0, u1, u2; // auxiliary for M_x, M_y, M_z
   double teta=atan2(y,x);

// define opposite chirality for the 2 azimuthal domains
if (z>0) {chir=1;}
else {chir=-1;}

// radial magnetization in the wall (i.e. around z=0)
if (abs(z)<a {
   u0 = x; // M_x
   u1 = y; // M_y
   u2 = 0; // M_z
             }
// azimuthal magnetization in the domains
```

```
else {
   u0 = (-1)*chir*sin(teta);  // M_x
   u1 = chir*cos(teta);   // M_y
   u2 = 0;       // M_z
     }

// norm for normalization of the magnetization vector
   double norme=sqrt(u0*u0+u1*u1+u2*u2);

// asign normalized magnetization vector to nodes
   node.u[0] = u0/norme;
   node.u[1] = u1/norme;
   node.u[2] = u2/norme;
   node.phi  = 0;
   } // end for
} //
```

D INTRODUCTION (FRANÇAIS)

La recherche en magnétisme aux petites dimensions (le micro et nanomagnétisme) a accompagné la révolution dans le stockage de données de capacité toujours croissante (par ex. disques durs, HDD), de nouveaux capteurs magnétiques (pour des besoins d'orientation, de mesure de rotation et vitesse). Ceci s'est fait en se concentrant principalement sur les films minces, les nanoparticules et plus récemment nanofils.

En 2004, S. Parkin de IBM [1] a proposé un concept de mémoire à l'état solide non volatile (Mémoire racetrack, Fig. 1.1) basé sur l'existence et le déplacement de parois de domaines magnétiques (DW) dans des nanopistes [2]. Une telle mémoire serait rapide, robuste (non sensible aux coupures de courant, sans mouvement mécanique de pièces), avec une consommation d'énergie modérée et dans le cas de grands réseaux de pistes verticales, la perspective de densité de stockage élevée.

Récemment, d'autres types de mémoires tendent à exploiter la troisième dimension (par exemple la mémoire flash, consistant maintenant en quelques dizaines de couches empilées). Des tentatives existent pour les disques dur avec quelques (2-3) couches d'enregistrement, qui pourraient bientôt arriver sur le marché. Cependant, la mémoire racetrack reste encore dans les laboratoires, voire simplement un concept. En effet, IBM et de nombreux autres groupes ont apporté la preuve de concept racetrack sur la base de bandes magnétiques planaires réalisées par lithographie, et ont contribué à la compréhension fondamentale du déplacement de parois de domaine. Cependant, même dans un article récent [5], S. Parkin admet qu'aller en 3D est un défi considérable, principalement du point de vue de la fabrication.

Plus récemment, des études ont été menées sur des nanofils cylindriques préparés par des méthodes (électro)chimiques [6]. Au-delà des nanofils cylindriques, il est maintenant évoqué d'autres géométries incurvées (l'étude de l'interaction de courbure et du magnétisme) [7] ainsi que des nano-aimants en 3D (nanomagnétisme tridimensionnel) [8]. Il s'agit pour l'instant essentiellement de propositions et concepts, avec très peu de réalisations expérimentales, même sous forme d'ébauches. Ces deux aspects (Fig. 1.2) possèdent des recouvrement et apportent de nouveaux défis, promettant de nouvelles configurations magnétiques, de la physique, et possiblement une plus grande densité surfacique de composants dans les dispositifs.

Nanofils et nanotubes magnétiques

En nanomagnétisme et spintronique, le déplacement de parois de domaines magnétiques a été principalement étudié en bandes planaires préparées par lithographie [5, 10]. Cependant, les nanotubes (NT) et nanofils cylindriques (NWs) fabriqués

sous forme de réseaux verticaux par des méthodes dites bottom-up, sont plus appropriés pour la conception de dispositifs de stockage à haute densité avec l'architecture 3D en termes de synthèse de structures très profondes.

Dix ans après la proposition initiale de mémoire racetrack, l'attention est passée des expériences sur des réseaux étendues de nanofils cylindriques, à la physique du nanofil isolé. Cette dernière a été abordée par le transport électronique [11], la magnétométrie [12], et l'imagerie magnétique [13] apportant les premières confirmations expérimentales de parois de domaines spécifiques aux nanofils cylindriques [14, 15]. Ces nanofils pourraient fournir un système modèle pour l'étude du déplacement de parois sous champ magnétique [16] ou sous un courant polarisé en spin [17], avec notamment une vitesse très rapide prédite ($> 1\,\mathrm{km/s}$) [17]. Cependant, les parois dans les nanofils magnétiquement doux sont de type tête-à-tête ou queue-à-queue en raison de l'aimantation axiale dans les domaines. Ces parois sont intrinsèquement associées à une importante charge monopolaire magnétostatique. Le champ de fuite à longue portée qui en résulte pourrait induire des interactions indésirables (couplages entre parois et entre fils) dans le cas de réseaux denses. Une solution pour contourner ce problème repose sur des matériaux artificiels, appelés matériaux antiferromagnétiques synthétiques et qui ne génèrent pas de champ de fuite. Mais, alors que le concept a été démontré pour les nanostructures 2D et est utilisé dans les dispositifs commerciaux [5], l'implémentation 3D n'a pas encore été réalisée pour des raisons de difficulté de synthèse.

Les nanotubes magnétiques, moins étudiés que la simple géométrie des nanofils, ont été rapportés principalement dans le cadre de la biomédecine [18] et de la catalyse [19]. Cependant, leurs propriétés magnétiques individuelles restent largement méconnues. Pourtant, la théorie et les simulations prédisent une physique similaire des nanotubes, par rapport aux nanofils cylindriques [20, 21], y compris un mouvement de parois rapide ($> 1\,\mathrm{km/s}$) sans instabilité de Walker [22]. De plus, en termes de nouvelle physique et de nouveaux dispositifs, les nanotubes semblent être plus appropriés que les nanofils solides. En effet, leurs propriétés magnétiques pourraient être ajustées en modifiant l'épaisseur de la coquille du tube, et des architectures plus complexes peuvent être élaborées à partir de structures cœur-coquille [23]. Ceux-ci sont analogues aux multicouches en spintronique 2D (spin-electronics), comme les couches magnétiques séparées par une fin intercalaire non magnétique pour obtenir des effets de magnétorésistance [9], des antiferromagnétiques synthétiques, du couplage d'échange etc.

En outre, comme cela a déjà été fait pour les nanofils [24–26], on peut ajuster les propriétés magnétiques et la fonctionnalité des dispositifs potentiels en modifiant les propriétés le long des tubes (les modifications pourraient également être utilisées pour la définition des bits dans la mémoire racetrack):

- matériau: composition, segments de différents éléments [27], dopage, irradiation ...
- changement géométrique: modulation de diamètre sous forme de protrusions, ou constrictions [28], entailles-défauts, éléments tube-fils (avec des segments de fils et tubes) [29, 30]
- structures cœur-coquille [23] / multicouches [31].

Pourquoi les nanotubes magnétiques?

Dans ce travail, nous nous intéressons uniquement aux propriétés magnétiques et aux applications possibles des nanotubes en spintronique. En dehors de ceux-ci, les tubes ont d'autres propriétés intéressantes pour différents domaines, par ex. grande surface – utile pour la catalyse. Par ailleurs, les surfaces interne et externe peuvent être fonctionnalisées et/ou des molécules peuvent être stockées à l'intérieur du tube. Les nanotubes magnétiques peuvent apporter des phénomènes nouveaux ou améliorés en raison de leur géométrie, une topologie différente par rapport aux films plans, et la possibilité de créer des structures et des dispositifs plus complexes à base de nanotubes multicouches (Fig. 1.3).

Les tubes apportent une autre possibilité radicalement nouvelle: la courbure qui leur est associée a été prédite comme conduisant à la brisure de la symétrie d'inversion, liée au fait que les surfaces interne et externe sont distinctes. Cela ne se produit pas pour un film plat parfait, mais seulement pour les multicouches – couche magnétique prise en sandwich entre deux couches différentes (non magnétiques). Par conséquent, à cet égard, un tube magnétique (surface courbe) apporte la fonctionnalité de certaines hétérostructures en couches minces. Dans les systèmes plans comme les films Pt/Co/AlO_x (avec une couches de Co ultramince et donc une aimantation perpendiculaire), la brisure de la symétrie d'inversion est associée à la promotion des textures magnétiques chirales, à la propagation rapide des parois de domaines magnétiques [32] et à la non-réciprocité de propagation des ondes de spin [33]. Des phénomènes similaires devraient en effet se produire dans le cas de nanotubes magnétiques (couche magnétique unique, aucune couche supplémentaire nécessaire): la courbure induit la magnétochiralité [34], l'anisotropie s'apparantant à une interaction dite Dzyaloshinskii-Moriya [7]. Récemment, des prédictions théoriques de la non-réciprocité de la propagation des ondes de spin dans les tubes ont été faites [35, 36].

Une question ouverte et passionnante est de savoir si l'on pourrait combiner des effets provenant à la fois de la courbure et des interfaces avec différents matériaux et rendre les effets (par exemple, l'interaction Dzyaloshinskii-Moriya) encore

plus forts. La combinaison de telles structures cœur-coquilles avec modification des propriétés le long des structures comme indiqué ci-dessus (par exemple matériau, géométrie) pourrait conduire a par exemple, de nouveaux guides d'ondes magnoniques (ondes de spin). Certaines structures cœur-coquilles ont déjà été réalisés, par exemple des vannes de spin [37]. Cependant, la plupart des empilement pertinents n'a pas encore été synthétisée: les matériaux antiferromagnétiques synthétiques, les structures à métaux lourds (Pt) exploitant l'effet Hall de spin [38, 39] et l'interaction Dzyaloshinskii-Moriya [40] . . . Au-delà de la physique nouvelle, des réseaux verticaux de tels nanotubes multicouches pourraient permettre le transfert de la spintronique 2D vers la 3D et rendre ainsi les dispositifs spintroniques plus compétitifs.

Les chimistes et les spécialistes des matériaux savent fabriquer une grande variété de nanostructures à partir de différents matériaux et de différentes formes y compris les nanotubes magnétiques, les tubes multicouches et les nanofils cœur-coquilles. Cependant, la caractérisation de telles structures est très souvent faite par des mesures globales, typiquement par magnétométrie sur des réseaux ou faisceaux de telles structures. D'un autre côté, les physiciens peuvent imager et mesurer des nanostructures isolées, mais jusqu'à présent, ils se sont concentrés principalement sur des éléments en couches minces préparées par lithographie, qui leur est un outil habituel. Dans ce travail, nous bénéficions de ces deux mondes. L'auteur lui-même est un hybride d'ingénieur, de physicien et de chimiste. Nous profitons également d'une collaboration avec des chimistes experts et des spécialistes des matériaux de l'Université de Darmstadt, en particulier Sandra Schaefer.

Organisation du manuscrit

Le manuscrit présenté comporte 4 parties:

- I: Théorie et état de l'art
- II: Méthodes et instrumentation
- III: Résultats et discussion – Nanotubes magnétiques
- IV: Résultats et discussion – Nanotubes multicouches

Nous commencerons donc par un examen de l'historique théorique et des informations de ce qui a déjà été fait dans le domaine des nanostructures magnétiques allongées, et en particulier des nanotubes. La partie II décrit les techniques que nous avons utilisées dans nos études, ainsi que certaines informations connexes. Enfin, les résultats (les expériences et modélisation numérique) sont abordés dans les parties III et IV; la partie III se concentre sur les nanotubes magnétiques et la dernière sur des structures cœur-coquilles plus avancées (tubes multicouches).

E CONCLUSION (FRANÇAIS)

Nous avons fabriqué avec succès des nanotubes à partir de plusieurs matériaux ferromagnétiques par des méthodes électrochimiques dans des gabarits nanoporeux. A savoir, nous avons préparé des nanotubes de NiCo (diamètre 70-90 nm), des nanotubes de Ni (diamètre aux environs de 60 nm) et des nanostructures avec des segments alternés sous forme de fil (plein) et de tube (creux). De plus, nous avons obtenu des tubes par dépôt autocatalytique: CoNiB et NiFeB (diamètres 80-400 nm) ainsi que des tubes multicouches de nos collaborateurs de TU Darmstadt. En plus de ceux-ci, nous avons fabriqué nous-mêmes des nanotubes CoNiB, par la même technique (diamètres 100-200 nm).

Nous avons étudié toutes ces nanostructures à l'aide de la microscopie électronique (à balayage / en transmission) et, dans certains cas, de la microscopie à force atomique. En plus de l'étude de la morphologie et de la topographie, nous avons effectué une analyse chimique en utilisant la spectroscopie à rayons X à dispersion d'énergie. De plus, nous avons quelques analyses chimiques préliminaires de nos collaborateurs (CEMES, Toulouse et Spintec, Grenoble) par la spectroscopie de perte d'énergie des électrons. L'étude magnétique, aspect clé de ce travail, a été menée avec une combinaison de diverses microscopies magnétiques: l'holographie électronique, la microscopie à force magnétique, et surtout les microscopies de dichroïsme circulaire magnétique de rayons X associé à la microscopie à émission de photoelectrons (XMCD-PEEM) ou microscopie à rayons X en transmission à balayage (STXM). Ceux-ci ont été complétés par la magnétométrie sur des réseaux de tubes et sur des structures isolées. Nos résultats sont étayeés par des simulations micromagnétiques et la modélisation numérique d'images XMCD-PEEM.

Tubes CoNiB et NiFeB déposés par voie chimique

Dans les tubes CoNiB préparés par dépôt autocatalytique (diamètre autour de 300 nm), l'imagerie XMCD-PEEM et la comparaison avec la modélisation numérique ont révélé des séries de domaines magnétiques bien définis avec aimantation azimutale, séparés par des parois de domaines de type Bloch (aimantation radiale). Ces domaines à fermeture de flux magnétique génèrent des champs de fuite faibles et à courte distance, tout en étant séparés par des parois étroites, significativement plus étroites que le diamètre du tube. La densité de parois de domaine peut atteindre 5/µm. Si l'on ne tenait compte que de la géométrie, ces tubes longs (jusqu'à 30 µm de longueur) devraient être aimantés axialement. Ainsi, une contribution supplémentaire de l'anisotropie magnétique doit être présente afin de favoriser l'alignement de l'aimantation le long de la direction azimutale (c'est-à-dire l'axe facile pour l'axe

azimutal et l'axe difficile pour la direction longitudinale). L'anisotropie azimutale pourrait provenir de la déformation induite par la croissance et / ou de la forme du grain (microstructure). Nous ne pouvons pas non plus exclure l'effet de la dissolution rapide du gabarit.

Lorsqu'un champ magnétique est appliqué le long de l'axe du tube, l'aimantation tourne progressivement vers la direction axiale. Grâce à l'imagerie STXM sous un tel champ, nous avons pu extraire la force de l'anisotropie, correspondant à une constante d'anisotropie effective d'environ de $10\,\mathrm{kJ/m^3}$. La valeur de l'anisotropie a pu être adaptée par recuit ou variation de la composition du matériau. En particulier, après recuit à environ 450 °C, l'aimantation est axiale et peut être renversée avec plusieurs mT appliquées le long de l'axe du tube.

Les tubes NiFeB de géométrie similaire préparés de la même manière sont aimantés axialement même sans traitement (comme recuit effectué pour les tubes CoNiB). Contrairement à CoNiB (magnétostriction négative significative), NiFeB présente une magnétostriction presque nulle (faiblement positive). Sur cette base, nous mettons en avant l'origine magnétoélastique des domaines azimutaux dans les tubes CoNiB. Nous avons observé le renversement d'aimantation des tubes NiFeB sous un champ magnétique et le déplacement d'une paroi de domaine. Dans les expériences d'holographie électronique, nous avons observé des cartes de phase complexes que nous attribuons à un grand diamètre de tube (parfois près de 400 nm) et à un champ ayant une composante transversale significative par rapport à l'axe du tube.

Une autre façon d'obtenir une aimantation axiale est de réduire le diamètre. Les nanotubes de CoNiB d'un diamètre d'environ 100 nm montrent une aimantation longitudinale, à la fois en XMCD-PEEM et en imagerie par microscopie à force magnétique. Même s'il peut y avoir une certaine anisotropie azimutale, l'énergie d'échange associée à l'aimantation azimutale serait trop élevée et donc une aimantation axiale est préférée.

Certains nanotubes, principalement préparées par dépôt électrolytique (NiCo, Ni) avec des parois minces ($< 15\,\mathrm{nm}$), n'ont pas pu être étudiés correctement par des microscopies magnétiques en raison du très faible signal résultant de l'oxydation (partielle) du matériau. De tels nanotubes minces devraient être encapsulés par des couches protectrices, par ex. quelques nanomètres de silice / hafnia déposés par dépôt par couche atomique (ALD), ou de l'oxyde de titane préparé par dépôt chimique en bain.

Outre la focalisation sur les nanotubes, nous avons également étudié des géométries plus complexes: des nanoéléments avec des segments de fil et de tube et des tubes multicouches (structures cœur-coquilles).

Nanostructures tube-fils

Les nanoéléments avec des segments composés de nanofils et nanotubes alternés (diamètre extérieur d'environ 60 nm) présentaient des transitions tube/fil très nettes (des transitions progressives font l'essentiel des rapports de la littérature) avec plusieurs segments de tubes de longueur supérieure à 2 µm (plus long que dans la littérature). Malheureusement, la structure s'est avérée très difficile pour la première imagerie par microscopie magnétique. Un petit diamètre avec un moment magnétique faible de Ni a donné un faible signal magnétique pour les parties de nanofils, sans parler des segments tubulaires, où nous n'avons pas pu conclure. Dans le cas du XMCD-PEEM (plus sensible), nous avons rencontré des problèmes de localisation de structures ainsi qu'une résolution spatiale limitée et une analyse d'image rendue complexe en raison d'une forte courbure. Cependant, avec des structures légèrement plus grandes (plus épaisses) contenant Fe ou Co (moment magnétique plus élevé), on pourrait tester expérimentalement des prédictions numériques et théoriques concernant ces structures intrigantes combinant des segments de fils et de tubes.

Tubes multicouches (structures cœur-coquilles)

Pour les dispositifs potentiels (spintroniques, par exemple les capteurs), il faudrait utiliser des tubes multicouches (structures coeur coquilles), et pas seulement des tubes simples. Dans cet objectif, en collaboration avec TU Darmstadt, nous avons préparé des tubes multicouches avec deux couches magnétiques différentes séparées par un intercalaire non magnétique (NiFeB / SnOx / CoNiB). Grâce à la sensibilité en élément du XMCD-PEEM, nous avons pu étudier séparément chaque couche magnétique. Celles-ci ont été trouvées découplées du point de vue de l'interaction d'échange. L'anisotropie de chaque couche prédominait, donc le CoNiB présentait des domaines azimutaux, alors que l'aimantation axiale a été identifiée dans la couche de NiFeB. En outre, nous avons sondé le renversement d'aimantation dans les tubes, par champ magnétique. Sous un champ magnétique quasistatique, nous avons observé le renversement de la couche NiFeB par nucléation et propagation d'une paroi de domaine; des changements sont apparus dans le CoNiB, mais ceux-ci ne pouvaient pas être clairement corrélés avec l'état de la couche de NiFeB, sauf pour l'effet du champ de fuite émanant d'une paroi de domaine dans la couche de NiFeB. Des expériences avec des impulsions de champ se sont révélées instructives, lorsque le champ a été appliqué avec un certain angle par rapport à l'axe du tube. À notre grande surprise, non seulement la couche NiFeB a été renversée, mais aussi la circulation de tous les domaines azimutaux de CoNiB a été inversée.

Mis à part les expériences, nous avons également effectué des simulations micromagnétiques de tubes multicouches avec un espaceur plus épais (par exemple 10 nm). Ici, nous avons pu démontrer l'alignement antiparallèle des domaines aimantés axialement dans les deux couches magnétiques par interaction dipolaire, ainsi que l'obtention de parois de domaines de type vortex couplées des dans les deux tubes.

En dépit du caractère préliminaire dans certains cas de nos résultats, nous pensons avoir montré la polyvalence des nanotubes magnétiques. En modifiant la composition, la géométrie ou le recuit, il est possible d'obtenir des domaines presque à la carte: azimutaux ou axiaux, les deux étant utiles. Les domaines azimutaux, en particulier, sont intéressants en raison de la fermeture de flux magnétique qui pourrait être exploitée dans des capteurs magnétiques ou dans des dispositifs basés sur des réseaux d 'éléments denses. La nature creuse et les domaines azimutaux réduiraient significativement l'interaction entre ces éléments et les interférences indésirables. Les propriétés et la viabilité des tubes peuvent être encore améliorées en préparant des structures cœur-coquille / multicouches tubulaires.

Nous nous sommes focalisés sur des nanotubes magnétiques, des structures cylindriques avec un coeur vide. La courbure et l'absence de matière sur l'axe donnent des propriétés intéressantes qui pourraient être exploitées en spintronique 3D, que ce soit pour des mémoires à l'état solide, des capteurs avancés ou des cristaux magnoniques pour les guides d'ondes de spin, le tout basé sur (des réseaux verticaux de) tubes multicouches ou des nanofils coeur coquille.